AN EXPERIMENTAL AND THEORETICAL STUDY OF PILE FOUNDATIONS EMBEDDED IN SAND SOIL

AMEER ASHOUR JEBUR

A thesis submitted in partial fulfilment of the

requirements of Liverpool John Moores University

for the degree of Doctor of Philosophy

April 2018

Statement of Authorship

The research documented in this thesis was conducted at Liverpool John Moores University, Department of Civil Engineering. I hereby declare that, except where specific reference is made to the work of others, this is my work and has not been submitted for a degree at another university.

Ameer Ashour Jebur

Liverpool John Moores University, UK

April 2018

Abstract

This study aimed to examine the load carrying capacity of model instrumented piles embedded in sand soil, and to develop and verify reliable, highly efficient predictive models to fully correlate the non-linear relationship of pile load-settlement behaviour using a new, self-tuning artificial intelligence (AI) approach. In addition, a new methodology has been developed, in which the most effective pile bearing capacity design parameters can be precisely determined. To achieve this, a series of comprehensive experimental pile load tests were carried out on precast concrete piles, steel closed-ended piles and steel open-ended piles, comprised of three slenderness ratios of 12, 17 and 25, using an innovative calibrated testing rig, designed and manufactured at Liverpool John Moores University. The model piles were tested in a large pile testing chamber at a range of different densities of sand; loose (18%), medium (51%) and dense (83%). It is worth noting that novel structural fibres were utilised and optimised for different volume fractions to enhance the mechanical performance of concrete piles.

The obtained results revealed that the higher the values of the of the pile effective length, Lc (embedded length of pile), sand density, and the soil-pile angle of shearing resistance, the higher the axial load magnitudes to reach the yield limit. This can be attributed to the increase in the end bearing point and mobilised shaft resistance. In addition, the plastic mechanism occurring in the surrounding soil was identified as the leading cause for the presence of nonlinearity in the pile-load tests.

Furthermore, a new enhanced self-tuning supervised Levenberg-Marquardt (LM) training algorithm, based on a MATLAB environment, was introduced and applied in this process. The proposed algorithm was trained after conducting a comprehensive statistical analysis, the key objectives being to identify and yield reliable information from the most effective input parameters, highlight the relative importance "*Beta values*" and the statistical significance "*Sig values*" of each model input variable (IV) on the model output.

To assess the accuracy and the efficiency of the employed algorithm, different measuring performance indicators (MPI), suggested in the open literature, were utilised. Common statistical performance indexes, i.e., root mean square error (RMSE), Pearson's moment correlation coefficient (p), coefficient of determination (R), and mean square error (MSE) for each model were determined. Based on the graphical and numerical comparisons between the experimental and predicted load-settlement values, the results revealed that the optimum models of the LM training algorithm fully characterised load-settlement response with remarkable agreement. Additionally, the proposed algorithm successfully outperformed the conventional approaches, demonstrating the feasibility of the current study.

New design charts have been developed to calculate the individual contribution of the most significant pile bearing capacity design parameters "the earth pressure coefficient (K) and the bearing capacity factor (N_q)". The improved approach takes into account the change in sand relative density, pile material type, and the pile slenderness ratios. It is therefore a significant improvement over most conventional design methods recommended in the existing design procedures, which do not consider the influence of the most significant parameters that govern the pile bearing capacity design process.

Acknowledgements

I would like to express my sincere gratitude and appreciation to my principal supervisor, Dr. William Atherton, and my supervision team Professor Rafid AL Khaddar and Dr. Edward Loffill for their supervision, professional support, endless encouragement, invaluable guidance, and for facilitating my progress throughout the period of my study at Liverpool John Moores University, Liverpool, UK.

I would like to extend my thanks to the technical staff of the Civil Engineering Department, in particular Malcolm Feegan, who provided expertise and great assistance for the experimental programme of work.

The authors would like to thank the External Examiner Prof. W. H. Craig, and the Internal Examiners Prof. D. Al-Jumeily and Dr M. Sadique for their thoughtful review and the constructive feedback, which helped to improve the quality of the thesis.

My acknowledgment and great apperception goes to the Iraqi Ministry of Higher Education and Scientific Research, the Iraqi Cultural Attaché in London and the University of Wasit for the grant provided to carry out this research.

I wish to express my extreme gratitude to my family, in particular my beloved mother and father for their continuous care, motivation and support. Finally, I owe my thanks to my wife Mrs. Zeinab Al Attar, my lovely boys Mohammed and Hassan, as without their understanding, patience and continued encouragement it would have been difficult for me to successfully finish my PhD thesis.

Ameer Ashour Jebur

Liverpool John Moores University, UK

April 2018

Dedication

This thesis is dedicated to my father and mother.

To my brothers and sisters for their support.

To my wife, for her continuous help, endless support, and sacrifice over these years.

To my lovely sons Mohammed and Hassan who make the world a much happier place.

Sincerely,

Ameer Ashour Jebur

Liverpool John Moores University, UK

April 2018

Awards and Recognitions

No.	Award Name	Events and Awarding Body	Year
1	Best Paper	ICCBE 2016: 18TH International Conference on Civil and Building Engineering, London, UK.	May 2016
2	Best Poster	Edge Hill University: Cutting Edge Postgraduate Conference Poster Prize Winner	April 2017
3	Best Paper (3rd runner up)	The 3rd BUiD Annual Doctoral Research Conference 2017. British University in Dubai, Dubai.	May 2017
4	Certificate of Excellence	Awarded by the Ambassador of the Republic of Iraq in the UK, and the Iraqi Student Society in the UK.	March 2017
5	Recognition Award and appreciation certificate	Awarded by the Executive Dean of the Faculty of Engineering and technology, LJMU, during the Faculty research week.	May 2017
6	Associate Fellow of the Higher Education Academy	UK Professional Standards Framework for teaching and learning support in higher education. Higher Education Academy Board, UK.	January 2016
7	Medal of Excellence	Awarded by the Iraqi Minister of Higher Education and Scientific Research at University College London, UK.	January 2018

List of Contents

List of Figures

List of Tables

List of Abbreviations

AI	Artificial Intelligence
ANN	Artificial Neural Network
ASTM	American Society for Testing and Materials
AEA	Air Entraining Agent
BSI	British Standards Institution
CI	Confidence Interval
CIRP	Constant Incremental Rate of Penetration
CPT	Cone Penetration Test
DLT	Dynamic Load Test
DV	Dependent Variable
EH	Error Histogram
FRC	Fibre Reinforced Concrete
IV	Independent Variable
LM	Levenberg-Marquardt
MAE	Mean Absolute Error
MD	Mahalanobis Distance
MLT	Maintained Load Test
MLP	Multi-layer Perceptron
MPI	Measuring Performance Indicator
MRT	Multiple Regression Technique
MSE	Mean Square Error
NN	Neural Network

OCR	Overconsolidation Ratio
PE	Processing Element
PLR	Plug Length Ratio
PIV	Particle Image Velocity
PTFE	Polytetrafluoroethylene
RMSE	Root Mean Square Error
S.D.	Standard Deviation
SEM	Scanning Electronic Microscopy
SSE	Sum Square Error
TO	Tinius Olsen
USCS	Unified Soil Classification System

Nomenclature

Roman alphabet

A_{tip}	Cross-sectional area of the pile tip
A_b	Pile base area
A_S	Pile shaft area interfacing
Beta value	Relative importance
b	Bias value
C_c	Coefficient of curvature
CEM-II	Portland cement type II
COO_1	Cook's distance
C_u	Coefficient of uniformity
C, A	Constant parameters
C_p	Pile perimeter
C_s	An empirical factor
c'	Effective cohesion of the soil
d	Pile diameter
d_{10}	Effective grain size
d_{50}	Mean grain size diameter
D_r	Sand relative density
d_k	Desired output of the neuron
$d_{p,m}$	Predicted output vectors
E	Young's modulus of the pile

EA	Pile axial rigidity
e_{max}	Void ratio of the sand in the loosest state
e_{min}	Void ratio of the sand in the densest state
$e_{p,m}$	Error of training process at output m when applying pattern p
E_k	Last total error
E_{k+1}	Current total error
E_s	Young's modulus of the soil
$\bar{f}$	Derivation of the activation function
f_c'	Concrete compressive strength
$f\left(I_j\right)$	Applied transfer function
G_s	Specific gravity
g	Gradient vector
h_i	Hidden neuron output
h_j	Actual output of hidden neuron
I	Influence factor for a rigid pile in a deep layer of soil
I_0	Settlement-influence factor for pile compressibility
I_j	Node activation level
$I_p, I_{\boldsymbol{ps}}$	Empirical factors
I_i	Identity matrix
J	Jacobian matrix
K	Earth pressure coefficient
k	Number of output neurons
K_o	Coefficient of earth pressure at rest
K_u	Coefficient of uplift pile capacity

L	Pile length
Lc	Pile effective length (embedded length of pile)
Lc/d, lc/d	Pile slenderness ratio
Logsig	Logarithmic sigmoid transfer function
m_u	Marquardt adjustment parameter
N_q	Bearing capacity factor
n, N	Number of independent variables
$o_{p,m}$	Observed output vectors
O'	Prediction value of dependent variable
p	Pearson's moment correlation coefficient
P	Pile applied load
purelin	Linear transfer function
P_{wp}	Load carried at the pile head
P_{ws}	Load carried by skin resistance
P_i	Computational values
$\bar{P}$	Mean of the predicted values
Q_T	Total pile capacity
$Q_{ult(uplift)}$	Ultimate uplift capacity
q_b	Portion of the vertical stress of the pile (end bearing resistance)
q_p	An empirical factor
q_s	Portion of the shear stress of the pile (shaft unit friction)
R	Coefficient of determination
R_h	Influence parameter for finite-depth of layer on a rigid base
R_k	Pile compressibility correction factor

R_p	An empirical factor
radbas	Radial basis transfer function
R_v	Poisson’s ratio correction factor
SF	Macro synthetic structural fibre type 1
Sig value	Statistical significance
SP	Poorly graded
S	Pile total settlement
T_i	Targeted values
tansig	Tangent sigmoid transfer function
$\bar{T}$	Mean of the targeted values
u	Pore water pressure
w/c	Water-cement ratio
w_{ij}	Connection weight
w_k	Value of the same weight at previous step
w_{k+1}	Weight value at a certain iteration +1
w_{pile}	Pile weight
XT	Micro synthetic structural fibre type 2
x_i	Input signal
y_k	Independent output

Greek alphabet

α	Momentum term
γ_{max}	Maximum dry unit weight of sand
γ_{min}	Minimum dry unit weight of sand

γ	Sand unit weight
∇w	Increment of the weight vector
$\Delta w_{jk}(n-1)$	Previous weight correction
δ	Soil-pile interface friction angle
δ_{peak}	Peak interface friction angle
$\delta_{critical}$	Critical state interface friction angle
δ_k	Back propagation error
η	Learning rate
θ_j	Bias on hidden neuron
μ	Combination function
μ_s	Soil-pile coefficient of friction
υ	Poisson's ratio
$\boldsymbol{\xi}$	Skin friction distribution influence factor
σ'	Normal effective stress on the failure plane
σ'_t	Vertical effective stress at the tip of the pile
σ'_v	Average vertical effective stress
σ	Total stress
τ_{si}	Skin friction unit along the length of the pile
τ_f	Soil shear stress on the failure plane
$\emptyset'$	Effective angle of friction
$\emptyset$	Angle of friction
$\emptyset_{peak}$	Peak angle of friction
$\emptyset_{critical}$	Critical state angle of friction

CHAPTER 1

General Introduction

1.1 Introduction

Pile foundations are slender structural elements, underneath superstructures, extensively utilised as load transferring systems and settlement controls at construction sites encountering undesirable bearing capacity of soil at shallow depth. Load carrying capacity is achieved via the contribution of end bearing capacity, shaft frictional resistance or a combination of both from inappropriate subsurface soil strata to stiff and reliable bearing strata (Letsios et al., 2014; Jebur et al., 2016; Jebur et al., 2018b). Examples of superstructures incorporating such deep foundations are skyscrapers, bridges, offshore platforms and transmission towers, tall chimneys, wharfs and jetties. Urbanisation and limited space availability are of global concern. However, additional loads from modern structures (piled structures) are widely expected. Furthermore, it has been stressed in the literature that deep foundations are the safest and the most economical solution to overcome most foundation problems (Tomlinson and Woodward, 2014). Piles may also resist uplift pressure from transmission towers, wind turbines, waves, ship impact, dry docks utilisation, and pumping stations, which are constructed below normal ground level utilising shaft skin friction resistance and/or suction developed in the adjoining soil zone of influence (Nazir and Nasr, 2013; Faizi et al., 2015).

In the last few years, there has been considerable debate regarding the current piling analysis and design methods (Ismail et al., 2013; Momeni et al., 2014; Nejad and Jaksa, 2017; Jebur et al., 2018b). This can probably be attributed to the lack of accurate, reliable and comprehensive methodologies, the use of different hypotheses, and pre-conditions associated with the most conventional pile capacity design procedures. Moreover, the mechanism involved in pile-soil interaction in the effective soil zone (elastic-plastic) and the subsequent load-settlement conditions are still a matter of discussion and an area of active research in the field of geotechnical engineering. The main sources of uncertainties are induced from material properties (soil and/or pile stiffness), soil shear strength parameters, pile type, site conditions, initial boundary conditions, load transfer method (end bearing point, suction and/or skin friction) interpretation, and soil stress history. Therefore, searching for a rigorous scientific methodology is crucial to ensure appropriate structural integrity and serviceability performance in different situations.

Over more recent years, the scientific community working on artificial intelligence (AI) has experienced a strong resurgence of interest via exploring state-of-art artificial neural network (ANN) technology. Academic research and development of different neural network (NN) algorithms as efficient, cost effective, and reliable data-driven tools have repeatedly been used over a wide range of applications in the field of civil engineering without the need for precondition or arbitrary assumptions (Majeed et al., 2013; Morfidis and Kostinakis, 2017). Nowadays, the applicability of artificial neural networks (ANNs), "*a bio-inspired computational tool whose configuration has been acknowledged based on biological human brain and its central nervous system (Ahmadi et al., 2016)*" is fully recognised and they have been applied successfully to solve many engineering problems, such as materials modelling (Mohammadi and Ashour, 2016) hydrologic and hydraulic modelling problems (Kabiri-Samani et al., 2011; Jaeel et al., 2016) offshore structures implementation (Kabiri-Samani et al., 2011), structures modelling (Morfidis and Kostinakis, 2017), pavement design application (Mirabdolazimi and Shafabakhsh, 2017), and geotechnical modelling (Alkroosh and Nikraz, 2014). Furthermore, the AI is succinctly able to correlate the relationships between a set of independent variables and the desired model output(s) of each objective system via their unique characteristic mathematical structures.

1.2 Research Aim and Objectives

The contribution to knowledge can be summarised in three main points. Firstly, the innovative use of physical laboratory models to investigate and assess the bearing capacity of different slenderness ratios (Lc/d) using instrumented piles (precast reinforced concrete, steel open-ended, and steel closed-ended), which penetrated in three sand densities and were subjected to uplift and compression loading system. It should be noted that two types of new structural fibres have been optimised using different fibre percentages (0.5, 0.75, 1, 1.25, 1.5, 1.75) by concreate volume and used in the concrete pile, the key objective is to minimise the need for steel mesh reinforcement, increase pile mechanical performance subjected to a wide range of load by increasing the ductility, and to enhance the concrete efficiency in harsh environments. Secondly, the feasibility of a new supervised, self-tuning computational intelligence approach, enhanced by a comprehensive statistical analysis, was examined to develop and train predictive models to fully capture non-linear pile performance subjected to a wide range of loads. The derived method offers a reliable, high efficiency and simple-to-use method to overcome the main limitations associated with the classical artificial neural methods (i.e., slow rate of convergence, performance analysis during the learning process, the necessity of tuning training parameters after each application, and becoming trapped in the local minima). Finally, load-settlement curves were analysed to develop new design charts to individually highlight the contribution of pile bearing capacity design parameters "*bearing capacity factor* (N_q) *and earth pressure coefficient* (K)" on total pile capacity. Moreover, for verification purposes, comparisons have been made between the developed design charts and the published work cited by the author.

Specific objectives were to:

1. Undertake an experimental investigation using physical scale models to conduct a series of comprehensive tests to examine bearing capacity and associated settlement of precast concrete piles, steel closed-ended piles, and steel open-ended piles, subjected to uplift and compression loads, having three slenderness ratios of 12, 17, and 25. This permitted the exploration of the behaviour of rigid and flexible piles in three relative densities of sand, D_r; of loose, medium and dense.
2. Explore the addition of a new type of structural fibre, promising economic and environmental advantages, which can be used to enhance the mechanical performance of the concrete pile.
3. Perform a comprehensive statistical analysis using Multiple Regression Technique (MRT) to identify the most influential model input parameters by determining "*Beta values*", to highlight the contribution of each parameter by calculating the statistical significance "*Sig values*", of identified independent variables (IVs), and to check and assess the reliability of the studied dataset by checking the presence of outliers, and data size. It is noteworthy that this objective was achieved using SPSS-24 package.

4. Examine the feasibility of an optimised supervised, self-tuning Levenberg-Marquardt (LM) training algorithm, based on a MATLAB environment to fully map the non-linear pile-load settlement response for different types of model piles when subjected to a wide range of compression and uplift loads.
5. Compare the results obtained in this study with the commonly used pile bearing capacity design procedures.

The Iraqi Regional Government has largely invested in people, including the work on this project, to build a well-educated workforce, which will contribute to the delivery of the vast existing and planned infrastructure projects supported by deep foundations. Urbanisation and limited space is one of the present challenges worldwide, particularly in developing countries, including Iraq. As a result, safe and cost effective design and analysis procedures are to be produced for deep piled structures.

1.3 Thesis Outline

The thesis is comprised of seven chapters and eight appendices that cover different important aspects of the research. The introductory chapter (chapter one), details the background on the use and development of pile foundations. It also defines the scope and the thesis aim and objectives.

Chapter 2: details background of two main stages of the literature review. Stage I shows a review of literature on deep foundations and stage II presents a review of literature on the artificial neural network (ANN) concept and the proposed use of the LM training algorithm.

Chapter 3: discusses the research methodology, and experimental technique followed in the experimental study.

Chapter 4: presents and discusses the bearing capacity of the various types of piles driven in three sand densities, subjected to compression loads. The reliability and efficiency of the employed LM trained algorithm with reference to the experimental pile-load tests has also been examined. In addition, graphical comparisons have been made between the LM approach and most conventional design procedures.

Chapter 5: covers the results and discussion for the described pile types embedded in sandy soil under an uplift loading system. In addition, the superiority of the LM algorithm has been also been demonstrated in this chapter by comparing its predictions results using unseen dataset with targeted values and with the results reported by the most design methods.

Chapter 6: shows performance analysis of the various types of model piles. Moreover, numerical comparisons between the results of the current study and the results suggested by the conventional pile bearing capacity design methods have been presented and discussed.

The final chapter 7: includes the concluding summary for the current study. Study limitations and recommendations for further research are also made in this chapter.

CHAPTER 2

Background Study I: A Review of Pile Foundations

2.1 Introduction

As a starting point, it is important to review the methods of pile classification, factors affecting pile design, pile-testing procedures, and the influence of pile installation on the shear strength parameters. A review of the existing pile bearing design approaches is outlined. Furthermore, previous numerical and experimental studies concerning pile-bearing capacity are also discussed. The assessment of the behaviour of different types of piles (steel open-ended, steel closed-ended and concrete) with a wide range of slenderness ratios is complex, and is core to research in the field of geotechnical engineering. The study of pile design continues to hold the attention of engineers with a series of studies and seminars held across the world each year.

2.2 Pile Foundations Design Approaches

One of the key functions of piles is to transfer the applied load from the heavy structure to the subsurface through end bearing capacity and developed shaft friction. To ensure structural integrity and serviceability and a pile settlement does not deform beyond an acceptable level, piles must be designed in an appropriate way and have the ability to carry and transfer the applied load to the deep and stiff bearing strata without causing geotechnical failure between soil-pile interactions; pile settlement must be within the design limit. In order to enable the precise evaluation of pile bearing capacity and allowable settlement, the current design methods must be suitably rigorous. Ultimate pile bearing capacity can be developed in three ways (Shaia, 2013). Firstly, ultimate pile capacity can be delivered from the skin frictional resistance developed between the soil-pile interactions (Figure 2.1a). Secondly, pile-bearing capacity can be largely provided by the end bearing (Figure 2.1b). Thirdly, pile mobilised capacity can be gained from the contribution of both (skin friction and end bearing) as illustrated in Figure 2.1c in various percentages (Tschuchnigg and Schweiger, 2015). Bearing capacity of a pile under compression load consists of two main components and can be determined using the following general expressions (Equation 2.1 and 2.2) (Ebrahimian and Movahed, 2016). After literature survey, it is worth noting that for a pile subjected to compression load, the influence of pile weight (w_{pile}) on pile capacity is ignored since it has a relatively insignificant influence on pile ultimate capacity. While, for a pile tested under uplift load, the pile weight (w_{pile}) can be taken into consideration when calculating the ultimate uplift capacity of a single vertical pile as expressed in Equation 2.2 (Meyerhof, 1976).

$$Q_T = q_b A_b + \sum q_s A_S \tag{2.1}$$

$$Q_{ult(uplift)} = \sum q_s A_S + w_{pile} \tag{2.2}$$

where: Q_T is total pile capacity, q_b and q_s are, respectively, the portions of the vertical stress of the pile (end bearing resistance) and the shear stress of the pile (shaft unit friction). A_b is the pile cross-sectional area at the tip and A_S is the pile shaft area interfacing with the soil layer. $Q_{ult(uplift)}$ is the ultimate uplift capacity, w_{pile} is the pile weight.

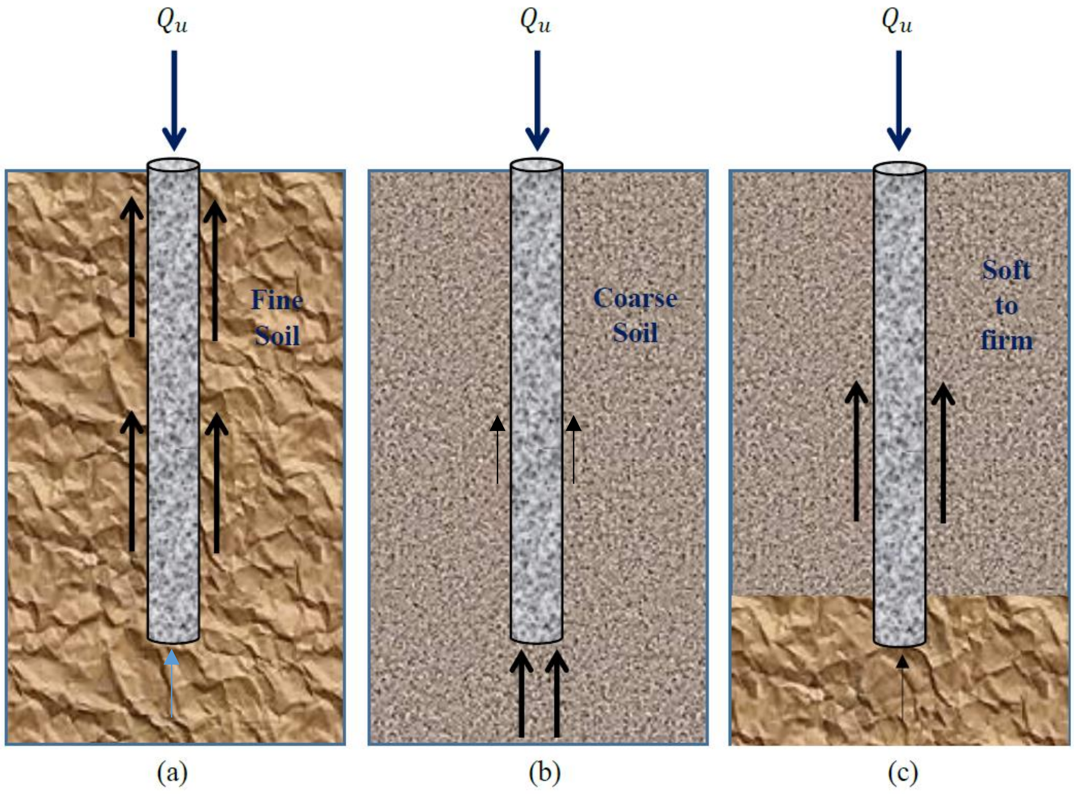

Figure 2-1: Schematic diagram showing pile bearing capacity contributions, (a) friction pile, (b) end bearing pile, (c) combination of both skin friction and end bearing.

2.2.1 Total Stress Design Approach

According to the site investigation, if the in-situ soil geotechnical properties are classified as a fine grained soil such as clay and silty clay, the pile foundations are likely to be designed using a total stress approach (Tomlinson and Woodward, 2014; Das, 2015; American Petroleum Institute, 2007). It has been stressed that a pile penetrated in fine soils tends to attribute its maximum bearing capacity from pile shaft friction resistance with the contacted soil in the adjoining zone of influence (the extent to which the soil mass will be influenced due to pile installation and its varies with pile installation method and the relative density of the soil) (Poulos and Davis, 1980; Gaaver, 2013). It is inferred from the relevant studies that the zone of influence is principally within a range of 3 to 8 times the pile diameter (Kishida, 1963; Robinsky and Morrison, 1964). These piles can be classified as skin friction piles (Igoe et al., 2011; Peiris et al., 2014) . The general governing equations to predict the unit shaft resistance of a pile can be determined in the skin friction term as given in in the following equations:

$$q_s = C_p \sum_{i=1}^{n} \tau_{si} \ \mathrm{Lc} \tag{2.3}$$

$$\tau_{si} = \mathrm{K}\, \sigma'_v \tan \delta \tag{2.4}$$

in which the parameter $C_p$stands for pile perimeter, τ_{si} is the skin friction along the length of the pile, Lc is the pile effective length (embedded length of pile), K is the earth pressure coefficient, σ'_v is the average vertical effective stress, and δ is the soil-pile interface friction angle.

The angle of friction, which is typically mobilised at the soil-pile interface can be determined utilising different techniques, i.e. direct shear box testing (Paik and Salgado, 2003; Jebur et al., 2016). Alternatively, it has been cited by Fleming et al. (2009) that the interface friction angle, δ is equal to the in-situ soil critical state of friction angle.

The earth pressure coefficient (K), however, is influenced by different parameters (i.e. soil density, method of pile installation, coefficient of earth pressure at rest, K_o and soil stress history). The K coefficient can also be determined, according to the pile slenderness ratio and sand relative density based on the conventional design charts suggested by Broms (1964); Poulos and Davis (1980) and American Petroleum Institute (1993).

2.2.2 Effective Design Approach

It has been stated by Tomlinson and Woodward (2014) that an effective design method is normally used when the soil type is classified as coarse grained soil. This type of pile could be classified as a point bearing pile in comparison to the skin friction pile. Understanding the principles and the theory of the effective stress in soil mechanics is essential. This idea was first studied by Terzaghi (1951): *"… All measurable effects of a change of stress, such as compression, distortion and a change of shearing resistance are due exclusively to changes of effective stress. The effective stress* (σ') *is related to total stress and pore water pressure as explained by* $\sigma = \sigma' + u$*"*.

Any sample of soil can be considered as a compressible skeleton of solid small particles consisting of two phases when soil voids are filled with water. The soil shear strength is determined by the arising frictional forces during slip at the soil particles (Burland, 1973). These frictional forces are normally a function of the transmitted normal stress by the soil skeleton rather than the soil total stress.

In the effective stress design approach, the pile attributes its maximum capacity to the end bearing point. The following general formula is use to predict the pile end bearing capacity in coarse soil.

$$q_b = \sigma'_t \, \mathrm{N}_q \tag{2.5}$$

in which the term σ'_t stands for the vertical effective stress at the tip of the pile, N_q is the bearing capacity parameter. It should be noted that the pile bearing capacity parameter can be predicted using a series of design charts proposed by American Petroleum Institute

(1993), Poulos and Davis (1980), Coyle and Castello (1981), and Tomlinson and Woodward (2014).

2.3 Pile Bearing Capacity Testing Methods

There are several procedures to determine pile-bearing capacity. These methods are identified by the testing time, the resulted strain percentage, and the type of system loading. Tests with long duration and high loads are normally adopted for the evaluation of pile load capacity. In addition, the method of low capacity and small-induced strain is used to evaluate the pile capacity subjected to cyclic loads and dynamic high strain loads.

2.3.1 Constant Incremental Rate of Penetration (CIRP)

Early studies on this method of pile testing were first conducted by Whitaker (1963). In this method, the required load to advance a pile in the desired soil depth must be monitored until either pile physical failure or the maximum required pile capacity is reached (American Society for Testing and Materials, 2013). The test objective is to obtain the maximum pile bearing capacity, especially for piles being designed for use in cohesive soils and their capacity is mainly developed from the shaft resistance within the contacted soil in the adjoining zone of influence (the extent to which the soil mass will be influenced due to pile installation and its varies with pile installation method and the relative density of the soil) (Poulos and Davis, 1980; Gaaver, 2013). It is inferred from the relevant studies that the zone of influence is principally within a range of 3 to 8 times the pile diameter (Kishida, 1963; Robinsky and Morrison, 1964). Furthermore, the constant incremental rate of penetration (CIRP) test takes about a maximum of 3 hours. However, the ground reaction may overestimate the maximum pile bearing capacity due to high-applied load in such a small period of time. The CIRP technique has been used by many researchers to investigate the pile bearing capacity. Nazir and Nasr (2013) conducted an experimental study to examine the ultimate pull-out capacity for model piles embedded in sandy soil. Sixty two pile-load tests of model steel piles penetrated in sandy soil at three densities loose, medium and dense were conducted in a calibrated chamber. The steel model piles had different slenderness ratios ranging from 7.5 to 30. The results revealed that the pile pull-out capacity increased with increases of batter angle. The results also indicated that the circular steel model piles had more resistance than the rectangular and square model piles.

2.3.2 Maintained Load Test (MLT)

In this method, the load is subjected to the pile in discrete units. The load is maintained until the settlement rate is not more than 0.25 mm/h. The next load increment will be applied once the indicated period of time has elapsed and the pile settlement is less than the specified limits (0.25 mm/h). The full test normally takes about 48 hours (American Society for Testing and Materials, 2013). The MLT is preferable to determine the load-displacement curve for a pile subjected to 200% of the anticipated working load. Rajasvaran (2007) studied the pile bearing capacity using MLT together with pile driving analyses methods. It has also been reported that the maintained load test is more accurate in determining and interpreting the pile load-settlement behaviour.

2.3.3 Dynamic Load Test (DLT)

Determining the pile bearing capacity using the dynamic load test (DLT) dates back to the 19th century. Testing of piles by dynamic load testing is widely adopted because of its efficiency and cost effectiveness. A specific combustion chamber must be provided to apply a rapid load at pile head, which produces a shock pulse with a short period. This type of test is likely to be conducted on high strength precast concrete driven piles. The pile head has to be protected from damage during the applied loading. To avoid concentrations of the stress at a pile head, grout cement needs to be applied to the pile surface at the point of the applied load. It is worth mentioning that the pile-time set-up effect can be ignored when using the dynamic load test procedure (Handley et al., 2006).

2.4 General Factors Influencing Pile Design

Generally, there are various factors that play a substantial role in pile design and analysis, for instance, soil bearing capacity, load types (dynamic, static), method of pile installation and pile material. Below are the main factors that influence the pile design process:

2.4.1 Bearing Capacity Factor

One of the most significant factors that affects and needs to be considered in the pile foundations design process is the bearing capacity factor (N_q). N_q could be estimated using a series of conventional design charts proposed in the geotechnical literature. Meyerhof (1976) takes into consideration the angle of friction to evaluate the N_q parameter as shown in Table 2.1. Values of the estimated N_q along with the soil friction angle (Ø) can also be determined based on a study proposed by Tomlinson and Woodward (2014), as depicted in Figure 2.2. It can be noted that the bearing capacity factor increased with the increasing of the angle of friction (Ø), with a range of pile slenderness ratio of 5, 20 and 70, and reach its maximum value at Ø of about 41°.

Table 2-1: Interpolated values of N_q values, according to Meyerhof (1976).

Soil friction angle (Ø)	**N_q**	**Soil friction angle (Ø)**	**N_q**
20	12.4	33	96.0
21	13.8	34	115.0
22	15.5	35	143.0
23	17.9	36	168.0
24	21.4	37	194.0
25	26.0	38	231.0
26	29.5	39	276.0
27	34.0	40	346.0
28	39.7	41	420.0
29	46.5	42	525.0
30	56.7	43	650.0
31	68.2	44	780.0
32	81.0	45	930.0

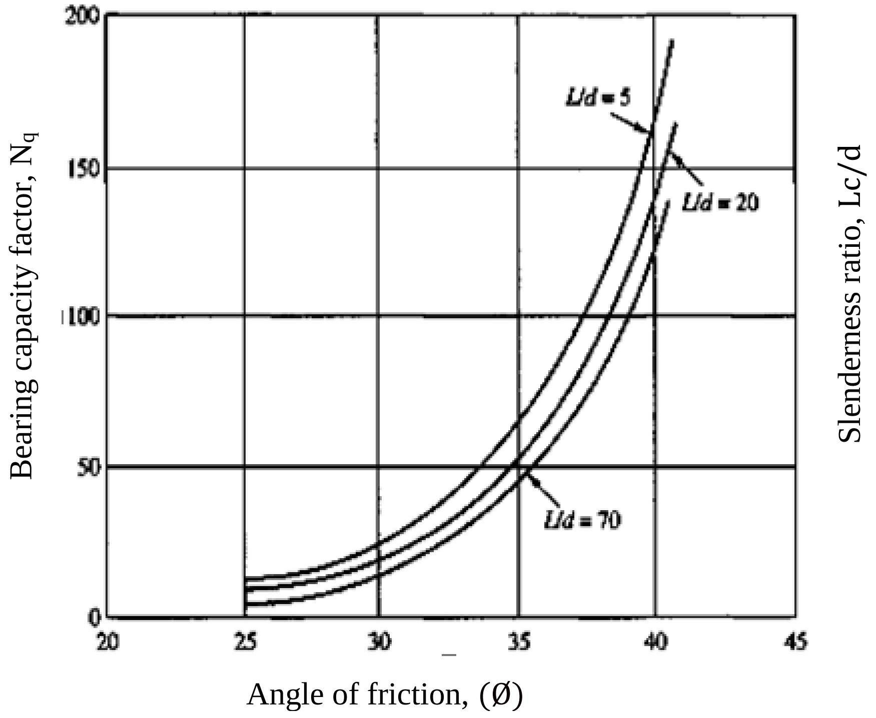

Figure 2-2: Schematic diagram of the bearing capacity factor (Tomlinson and Woodward, 2014), permission to reuse this figure has been granted by Taylor and Francis.

Table 2.2 also reported the predicted values of the N_q factor for piles penetrated in sand soil with three relative densities, suggested by the American Petroleum Institute (1987).

Table 2-2: Bearing capacity factor based on the American Petroleum Institute (1984).

Sand Relative Density, D_r	**Bearing Capacity Factor, N_q**
Dense	40
Medium	12-40
Loose	9-12

Another design chart (Coyle and Castello, 1981), was suggested to find the N_q factor as a function of soil friction angle and pile slenderness ratio as shown Figure 2.3. The plot compares the trend of the N_q values with the variation of Lc/d for different values of angle of friction (Ø). It can be observed that the parameter N_q, for different values of Ø, is slightly increases with increasing values of Lc/d and reaches a maximum value at Lc/d equals to 20. For all values of Ø, the increase in Lc/d, after a value of 20, leads to a reduction in N_q towards a minimum value at Lc/d of about 65. The results also revealed that a similar trend also occurs for higher values of Ø. Therefore, this leads to the conclusion that the ratio of Lc/d has less significant influence on the parameter N_q in comparison with the sand relative density.

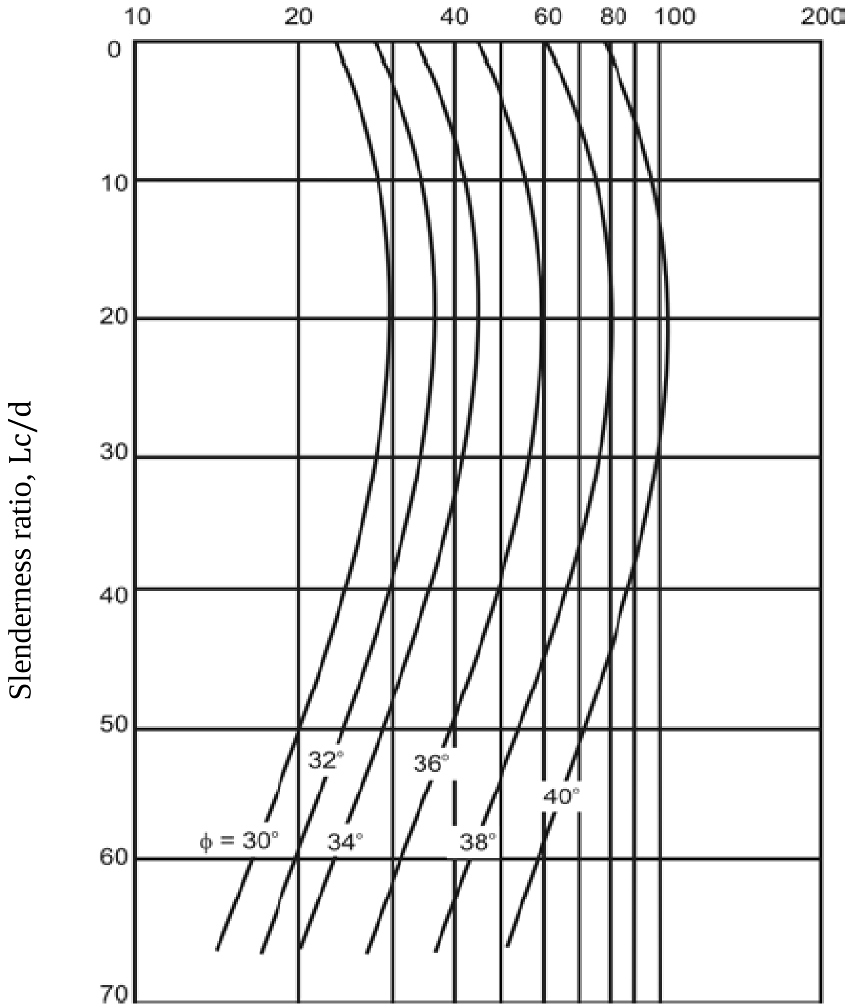

Figure 2-3: Schematic diagram of variation of pile bearing capacity, N_q and angle of friction, $\emptyset$ with pile slenderness ratio (Coyle and Castello, 1981), permission to reuse this figure has been granted by ASCE library.

2.4.2 Earth Pressure Coefficient

The coefficient of the earth pressure (K) is highly effected by the soil stress state before and after pile installation (Jeffrey, 2012). It has been demonstrated that the soil around the pile is normally compacted, especially when the method of pile installation is by the displacement method. The column of the soil displacement is equal to the pile volume in the case of closed-ended piles (large displacement pile) and equal the net thickness of pile diameter in the case of the open-ended piles (small displacement pile) (Tomlinson and

Woodward, 2014). The increase in the soil stress state leads to an increase in the angle of friction as a consequence of increasing the earth pressure factor. Table 2.3 proposed by Das (2015) can be used to predict the K coefficient for different pile installation methods.

Table 2-3: Lateral earth pressure coefficient according to Das (2015).

Method of pile installation	**Lateral earth pressure coefficient, K**
High displacement driven pile	$1 - \sin\emptyset \; to \; 1.8 * 1 - \sin\emptyset$
Low displacement driven pile	$1 - \sin\emptyset \; to 1.4 * 1 - \sin\emptyset$
Bored pile	$1 - \sin\emptyset$

Kulhawy (1984) also studied the effect of pile installation on the lateral earth pressure coefficient. The results of the study are given in the following equations:

$$K_o = 1 - \sin\emptyset' \tag{2.6}$$

$$K_o = 1 - \sin\emptyset' * OCR^{\sin\emptyset'} \tag{2.7}$$

where: K_o is the coefficient of earth pressure at rest, OCR stands for overconsolidation ratio, $\emptyset'$ is the effective angle of friction.

Moreover, the lateral earth pressure factor can also be assessed based on the method of pile installation and often stated as a function of K_o as detailed in the following table.

Table 2-4: Lateral earth pressure coefficient according to Kulhawy (1984).

Pile Classification	**K/K_o**
Non displacement pile	0.75-1.0
Large displacement pile	1-2
Small displacement pile	0.75-1.25

2.4.3 Soil-Pile Angle of Interface Friction

The angle of the interface friction (δ) between the soil and the model pile is also an important factor in the design and analysis of pile foundations (Gaaver, 2013) . The pile-soil interface depends purely on the pile materials and the initial sand relative density (Ramasamy et al., 2004; Jebur et al., 2016). The magnitude of the interface friction angle can be determined from the direct shear test. Kulhawy (1984) carried out an experimental study on a model pile penetrated in sand. It has been demonstrated that the effect of the soil-pile interface is a function of the pile material, as shown in the table 2.5, where μ_s is equal to $tan\ \delta$.

Table 2-5: Soil-Pile coefficient of friction according to Kulhawy (1984).

Pile materials	**Surface roughness**	**Soil-pile coefficient of friction (μ_s)**
Steel	Rough	0.8-1.0
Steel	Smooth	0.7-0.9
Concrete	Rough	1.0
Concrete	Smooth	0.8-1.0
Timber	All	0.5-0.8

Another experimental study (Jeffrey, 2012) was carried out to find the relationship between the soil-pile interface friction angle and sand relative density. The results are presented in Table 2.6.

Table 2-6: Soil-Pile angle of interface friction based on Jeffrey (2012).

Materials roughness	**Loose sand**		**Medium sand**		**Dense sand**	
	δº peak	**δº critical**	**δº peak**	**δº critical**	**δº peak**	**δº critical**
Rough concrete	29.7	25.7	40.5	28.6	48.4	34.5
Smooth concrete	27.1	23.7	30.8	24.1	37.2	24.5

2.5 Outline of Pile Settlement Prediction Methods

2.5.1 Introduction

In this section, a review has been made covering most conventional pile settlement design procedures proposed by: Poulos and Davis (1980), Vesic (1977), and Das (1995). It is worth mentioning that although the suggested approaches have been subjected to strong criticism because of their empirical nature and poor predictive efficiency when tested with experimental studies, the proposed methods below have remained popular due to their simplicity and ease of application (Igoe et al., 2011). Elastic methods are based on the hypothesis that the pile is acted upon by a system of constant shear stress around its shaft, due a point load on a linearly elastic, semi-infinite soil profile but this the shear stress is vary (increases) with increasing pile effective length, which could mainly be attributed due to an increase in the overburden pressure. Whereas the pile end bearing is acted upon by uniform pressures. These approaches are applicable to circumstances where the linear deformation of soil behaviour is considered acceptable.

2.5.2 Poulos and Davis (1980) Method

Poulos and Davis (1980) proposed a framework and reported that the following empirical equations can be utilised to predict pile total settlement (S) for single model piles subjected to axial load (Equations 2.8 and 2.9):

$$S = \frac{PI}{E_s \mathrm{d}} \tag{2.8}$$

$$I = I_0 R_k R_h R_v \tag{2.9}$$

where: P, d, and E_s are, respectively, pile applied load, pile diameter, and Young's modulus of the soil, I is the influence factor for a rigid pile in a deep layer of soil that involves the layer influence of soil depth, pile compressibility and Poisson's' ratio, R_k is the pile compressibility correction factor. R_h is the influence parameter for finite-depth and R_v is the Poisson's ratio correction factor. These factors could be determined from design charts suggested by Poulos and Davis (1980). In this method, for a rigid pile driven in a semi-infinite soil with 0.5 Poisson's' ratio, I_0 is the only influence parameter needing consideration (Poulos and Davis, 1980). The E_s for each sand relative density used in this study are summarised in Table 2-7, and within the range of the typical E_s values recommended by Kézdi and Rétháti (1974).

Table 2-7: Material properties and empirical factors that are used in the traditional methods.

Sand relative density (D_r %)	Sand Young's modulus (E_s)	Pile slenderness ratio (Lc/d)	I_0	I_{ps}
Loose	10-30 MPa	Lc/d =12	0.17	3.21
Medium	30-50 MPa	Lc/d =17	0.13	3.44
Dense	50-80 MPa	Lc/d =25	0.10	3.75

2.5.3 Vesic (1977) Approach

Vesic (1977) recommended that pile total settlement can be determined from the summation of three components $S_{1,}\ S_2,$ and S_3 by means of the following simplified formula (Equations 2.10, 2.11, and 2.12):

$$S_1 = \frac{\left(P_{wp} + \xi P_{ws}\right)\mathrm{L}}{A_{tip}E} \tag{2.10}$$

$$S_2 = R_p \frac{P_{wp}}{\mathrm{d}q_p} \tag{2.11}$$

$$S_3 = C_s \frac{P_{ws}}{\mathrm{L}q_p} \tag{2.12}$$

where: P_{wp} is the load applied at the pile head, P_{ws} is the load supported by the skin resistance, L is the pile length, **ξ** is the skin friction distribution influence factor, q_p is the portion of the vertical stress of the pile (end bearing resistance) (Meyerhof, 1976) , and R_p is an empirical factor. The coefficient C_s can be determined using the following expressions (Equation 2.13):

$$C_s = \left(0.93 + 0.16\sqrt{\frac{\mathrm{L}}{\mathrm{d}}}\right) R_p \tag{2.13}$$

The factor **ξ** can be assumed to equal 0.5, and the parameter R_p is equal to 0.09, as recommended for cohesionless soil (Poulos and Davis, 1980).

2.5.4 Das (1995) Method

The methodology proposed by Das (1995) is similar to that offered by Vesic (1977) with some modifications in calculating S_2 and S_3. These modifications can be precisely summarised through the following formulas:

$$S_2 = \frac{P_{wp}\mathrm{d}}{A_{tip}E_s}(1-\upsilon^2)I_p \tag{2.14}$$

$$S_3 = \left(\frac{P_{ws}}{C_p\mathrm{Lc}}\right)\left(\frac{\mathrm{d}}{E_s}\right)(1-\upsilon^2)I_{ps} \tag{2.15}$$

$$I_{ps} = 2 + 0.35\sqrt{\frac{\mathrm{Lc}}{\mathrm{d}}} \tag{2.16}$$

where the empirical coefficient (I_p) is equal to 0.88, and C_p is the pile perimeter, and the coefficient I_{ps} can be determined using Equation (2.16) given by Poulos and Davis (1980).

2.6 Uplift Capacity of a Single Pile: Outline of the Existing Predictive Models

2.6.1 Introduction

Piled structures are normally designed to resist large uplift and/or lateral loads due to the effect of wave or wind impact (Tomlinson and Woodward, 2014). Consequently, a tension force will be induced in some of the piles. A few traditional theories, developed by means of a limit equilibrium approach, have been suggested by Das (1983), Truncated cone method, and Meyerhof (1973). It is worth noting that the aforementioned theories are not recommended to be applied in practice due to the differences associated with their assumptions regarding the context and the shape of the failure surface as outlined by

Shanker et al. (2007). In the following sections, for completeness, some of the frequently applied predictive models are briefly documented.

2.6.2 Meyerhof (1973)

An empirical expression to reliably predict the net uplift pile capacity has been suggested by Meyerhof (1973) by assuming that the failed soil mass has an approximately similar shape as suggested for a shallow anchor. Therefore,

$$Q_{ult(uplift)} = \frac{\pi}{2} \mathrm{L}^2\ \mathrm{K}_u \gamma \mathrm{d} \tan \delta \tag{2.17}$$

K_u denotes the coefficient of uplift pile capacity and may change within a wide range and depends mainly on soil properties, method of pile installation and pile type, L is the pile length, d is the pile diameter, γ is the soil unit weight, and δ is the soil-pile interface friction angle.

2.6.3 Truncated cone model

Geotechnical engineers often predict the net pile uplift capacity by assuming a surface of slip as a truncated inverted cone with the sides of enveloping rising at an angle of $\frac{\emptyset}{2}$ from the vertical. Dead weight within the frustum is considered as the pile ultimate capacity, as revealed in the following equation:

$$Q_{ult(uplift)} = \frac{\pi}{3} \mathrm{L}^3 \gamma\ tan^2 \frac{\emptyset}{2} \tag{2.18}$$

L is the pile length, and Ø is the soil angle of shearing resistance.

2.6.4 Das (1983)

Das (1983) suggested an empirical method to predict the pile net uplift ultimate capacity developed within the pile-soil interface. It has been reported that the mobilised skin friction resistance increases linearly with increasing overburden pressure up to the effective pile penetration length. The pile slenderness ratio is a function of the sand relative density, as clearly indicated in the following equations:

$$\frac{\mathrm{Lc}}{\mathrm{d}} = 00156D_r + 3.58 \qquad (for\ D_r \leq 70\%) \tag{2.19}$$

$$\frac{\mathrm{Lc}}{\mathrm{d}} = 14.5 \qquad (for\ D_r \geq 70\%) \tag{2.20}$$

The pile uplift capacity in sand can be summarised as:

$$Q_{ult(uplift)} = 0.5\ P\gamma \mathrm{L}^2 \mathrm{K}_u tan\delta \qquad \text{(if Lc/d} \leq \text{Lc/d)} \tag{2.21}$$

$$Q_{ult(uplift)} = 0.5\ P\gamma\ \mathrm{Lc}^2\ \mathrm{K}_u tan\delta +\ P\gamma\ \mathrm{Lc}\ \mathrm{K}_u tan\delta\ (\mathrm{L} - \mathrm{Lc}) \tag{2.22}$$

The term $Q_{ult(uplift)}$ stands for the ultimate uplift capacity of pile.

Background Study II: A Review of Artificial Neural Networks (ANNs)

2.7 Introduction

Artificial neural networks (ANNs) are computational models, which attempt to mimic the biological structures of the human brain and its nervous system. They have the ability to efficiently implement difficult tasks, such as function approximation, classification, and pattern recognition (Tarawneh, 2017). ANN models comprise of interconnected processing elements (PEs). The PEs receives input signals (values) of ith independent variables (X_{i-1}, X_{i-2},….. X_{i-n}) (see Figure 2.4) from either external sources or adjacent PEs then transfers them to signals in the next layer by means of an activation function. The input layer can be represented by a vector of IVs. In an attepmt to solve problems, the proposed model should be trained. The methods of training can be generally categorised in two types: supervised and non-supervised. Supervised training is based on comparison between the selected inputs and model output. This method of learning is normally formulated as the error function, such as the mean square error between the measured and the predicted values summed over all available data. While, the non-supervised is solely based on the correlations among input data. During the learning process, the outputs of the (i-1)th layer are multiplied by an optimised vector so-called connection weight (w_{ij}), then the latest will be added together with a threshold bias and then summarised before being used as inputs into the next PE in the next ith layer. The PEs in the output and hidden layers can be defined by means of an activation function, which is introduced to the input and produces the value of the ith processing element in the output layer. It should be reported that a bias value does not include an activation function and only has a specific value determined during the process of training along with the value of the synaptic connection weights (Morfidis and Kostinakis, 2017).

On the training process, the values of connection weights and biases are updated in such a fashion that the total error between the targeted and the predicted values is minimised (Erdem, 2015). One fact of significant importance is that, the optimum configuration of these layers is identified utilizing a number of steps. More specifically, these phases can be summarized as: (i) the number of model input parameters, (ii) the optimum number of hidden layers, (iii) the number of model outputs, (iv) the number of processing elements (PEs), (v) the measuring performance indicators, (vi) type of activation function (linear and/or nonlinear). One of the most important features, which plays a key role in the performance of the ANNs, is the type of training algorithm (Xu et al., 2017). Indeed, after the configuration of the model, there are other important aspects which must be clearly defined such as a function of normalisation and the method for dataset division in an attempt to avoid overfitting and to ensure good generalisation ability of the trained network (Hagan et al., 1996) . It is noteworthy that an ANN concept was initially introduced by Rumelhart et al. (1986).

2.8 Functionality of ANN Model

The structure of the ANN has been described by many researchers (Jaeel et al., 2016; Jebur et al., 2018b). ANNs comprise of a number of artificial neurons variously identified as "*processing elements*" *(PEs)*, "*units*" or "*nodes*". In the multi-layer perceptron (MLP) approach, which are the most frequently utilised ANNs in the field of geotechnical engineering, processing elements are typically assembled in layers, consisting of an input layer, an output layer and one or more intermediate layers known as hidden layers (Sitton et al., 2017), as exposed in Figure 2.4.

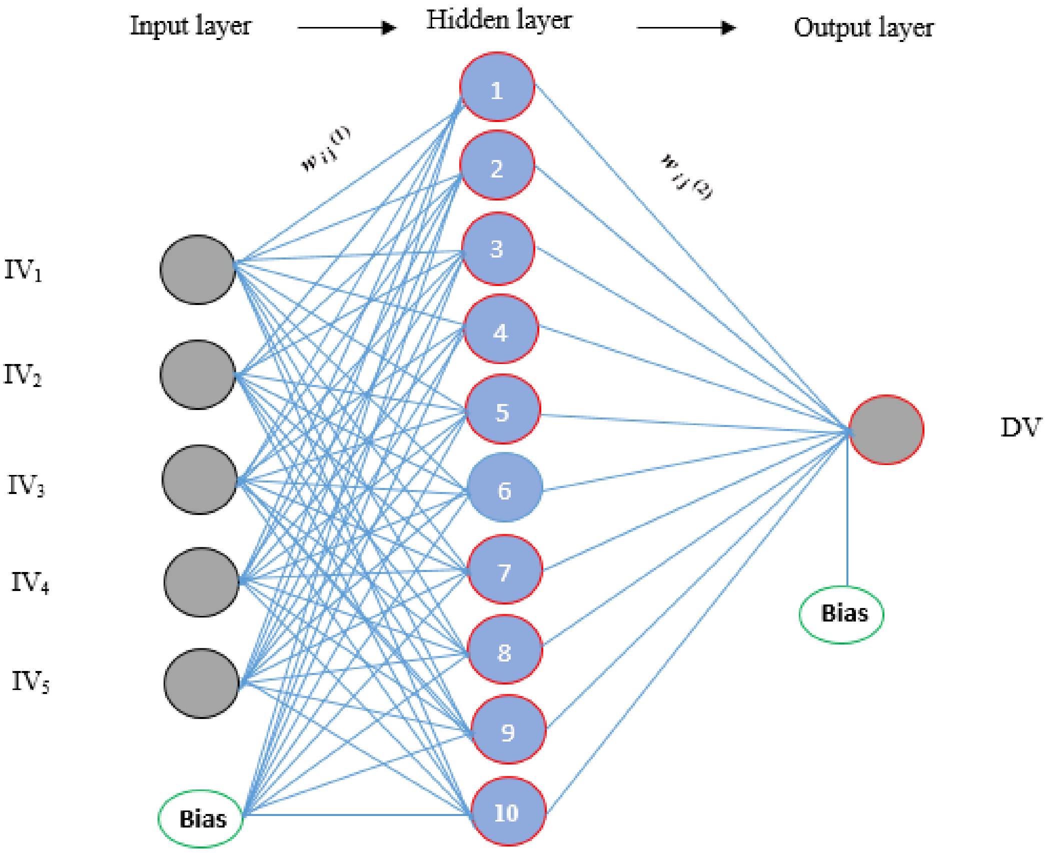

Figure 2-4: Typical structure of ANN model inputs and output variables (Jebur et al., 2018), permission to reuse this figure has been granted by Springer Nature.

The scalar weights determine the connections strength between interconnected nodes (Loria et al., 2015). From other elements, an individual processing unit receives its connections weighted inputs, which are summed and a bias value or threshold unit is either added or subtracted. The bias value is normally assigned to scale the input to a useful range to improve the convergence properties, by minimising the percentage of error between the targeted and the predicted values, of the neural network. The combined values of the independents variables (IVs) processed from the first layer are then passed through a transfer function to produce the output of the processing element. The TF maps a set of independent variables (IVs) to a finite output range. The described process is summarised in Equations 2.23 and 2.24, respectively.

$$I_j = \sum_{i}^{n} w_{ij}^{(1)} IV_i \pm b^{(1)} \tag{2.23}$$

$$y = \sum_{i=1}^{n} w_j^{(2)} \; I_j \pm b^{(2)} \tag{2.24}$$

where: n represents the number of independent variables, I_j denotes the node activation level, the factors $w_{ij}^{(1)}$ and $b^{(1)}$ are the weights and biases values from the inputs and output (hidden) layer, $w_j^{(2)}$ and $b^{(2)}$are the weights and the biases values for layer two.

2.8.1 Transfer Functions

Transfer functions can take a range of forms. The logarithmic sigmoid (logsig), bipolar sigmoid, hyperbolic tangent sigmoid (tansig), linear transfer function (purelin), and radial basis (radbas) transfer functions are the most commonly utilised transfer functions in artificial neural networks. The key objective is to transfer the weighted sum of all signals hitting on the processing element so as to determine its firing intensity (Majdi and Beiki, 2010). The log-sigmoid transfer function is usually utilised when the desired output values are within the limit of 0 and +1, whereas the tan-sigmoid is often utilised when the desired range of output values is between –1 and 1 (Shahin, 2014). The logistic sigmoid and hyperbolic tangent transfer functions are shown in Figure 2.5, and represented by the following Equations:

$$f(I_j) = \frac{1}{1 + e^{-(I_j)}} \tag{2.25}$$

$$f(I_j) = \frac{e^{(I_j)} - e^{-(I_j)}}{e^{(I_j)} + e^{-(I_j)}} \tag{2.26}$$

$$y = \sum_{i=1}^{n} w_i^{(j)} \ f(I_j) \ \pm \ b^{(j)} \tag{2.27}$$

where: $f(I_j)$ is the applied transfer function, factors $w_i^{(j)}$ and $b^{(j)}$ are the synaptic connection weights and biases values from the inputs and output (hidden) layer

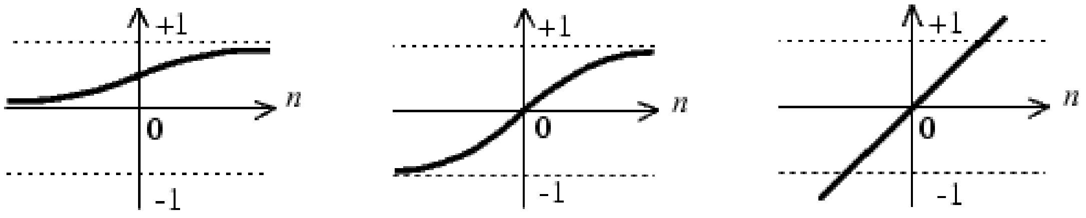

a. Log-Sigmoid b. Tan-Sigmoid c. Linear

Figure 2-5: Forms of commonly used ANN transfer functions.

2.9 ANN Architecture

Artificial neural networks are introduced as parallel computing devices comprising of interconnected units or neurons, where a unit presents a connection point at which data is processed (Feng et al., 2013; Ahmadi et al., 2016). ANN is an interconnected parallel structure comprised of (i) an input layer (ii) hidden layer number(s) (iii) an output layer. The number of neurons in the input and output layers successfully characterise the number of dependent variables to be predicted (Shahin, 2016). Full description of the ANN model architecture is more precisely described in the following sub-sections.

2.9.1 Single Layer Feed-forward Networks

In this type of the ANN structure, a neural network encompasses of one layer of computational processing elements (PEs) (Kriesel, 2011). In attempt to provide this PEs with their input signals, a set of nodes establishes an input layer that acts as middleman between the single layer of neurons and the input layer sources in the surrounding environment. It is crucial to emphasise that no computations are implemented in input nodes (Master, 1993). Two sorts of neurons only are available in this network, as illustrated in Figure 2.6: input neurons that transmit the input signals to the output layer and output neurons that compute their outputs using the same transfer function (Hu et al., 2016). The application of this type of ANN structure can only be strictly of the feed-forward type because both the input and the transfer function flow in one direction, starting from input nodes toward the network output (Han et al., 2017).

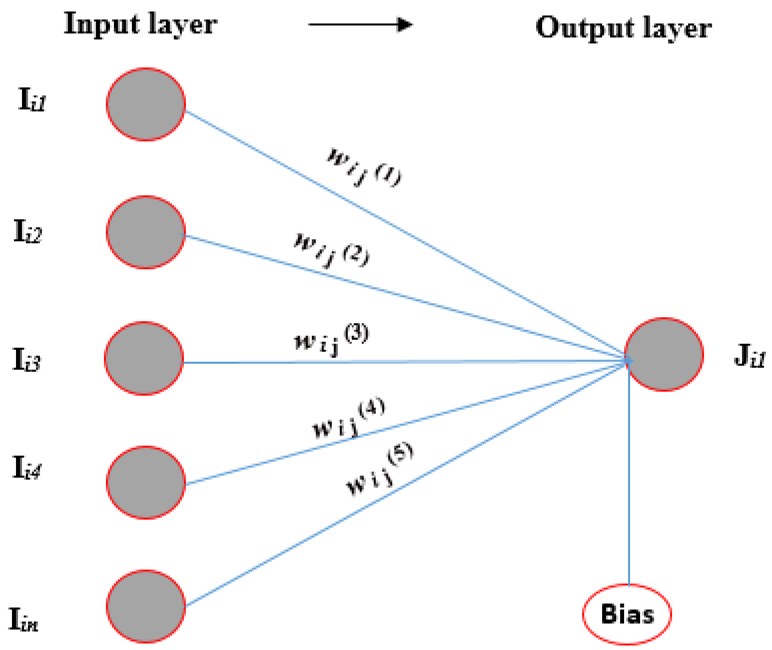

Figure 2-6: Structure of single-layer feed-forward network.

2.9.2 Multilayer Feed-forward Network

Multilayer feed-forward networks are used in an attempt to overcome the limitations and the computational boundaries experienced in single layer networks (Kriesel, 2011). Such networks have an architecture that is simply an updated extension of the previous ANN structure, where one or more layers are introduced between input and output layers. These layers are hidden, thus, named hidden layers. A hidden layer consists of a varied number of disconnected hidden nodes or neurons as shown in Figure 2.7, where each node of a specific layer feeds neurons in the immediate following layer with their input signals (Jaeel et al., 2016).

The activation function in the applied hidden layer units is normally non-linear. The nonlinearity involved between the independents and dependent variables allows for high level interactions between signals of input parameters (Feng et al., 2013). Moreover, the absence of nonlinearity in the ANN network reduces the input-output relationship to that of a single layer. However, two types of different combinations of transfer function can be found in literature: (i) the same type of nonlinear function is utilised in the hidden layers, (ii) a linear transfer function is implemented in the output layers (Deo and Şahin, 2015).

Furthermore, the feedforward ANN is normally fully connected (Juncai et al., 2015), i.e. each neuron in a layer is fully connected to each node in the subsequent layer in the implemented network hierarchy as can be observed in Figure 2.7. while, if either one or two of these connections is missed, the network is partially connected (Al-Janabi, 2006).

In attempt to draw the connectivity patterns for a multilayer feedforward network, a combination of connections matrices is used (Shahin and Jaksa, 2005; Kriesel, 2011; Abdellatif, 2013). In this case, each level of connections between two immediately adjacent layers can be described by a matrix of weights. For a fully connected multilayer feedforward ANN, the set of matrices can be described as follows:

$$w_1 = \begin{bmatrix} w_{i_{1h_1}} & w_{i_{1h_2}} & w_{i_{1h_3}} & w_{i_{1h_4}} \\ w_{i_{2h_1}} & w_{i_{2h_2}} & w_{i_{2h_3}} & w_{i_{2h_4}} \\ w_{i_{3h_1}} & w_{i_{3h_2}} & w_{i_{3h_3}} & w_{i_{3h_4}} \end{bmatrix} \qquad w_2 = \begin{bmatrix} w_{h_{1o_1}} & w_{h_{1o_2}} \\ w_{h_{2o_1}} & w_{h_{2o_2}} \\ w_{h_{3o_1}} & w_{h_{3o_2}} \\ w_{h_{4o_1}} & w_{h_{4o_2}} \end{bmatrix}$$

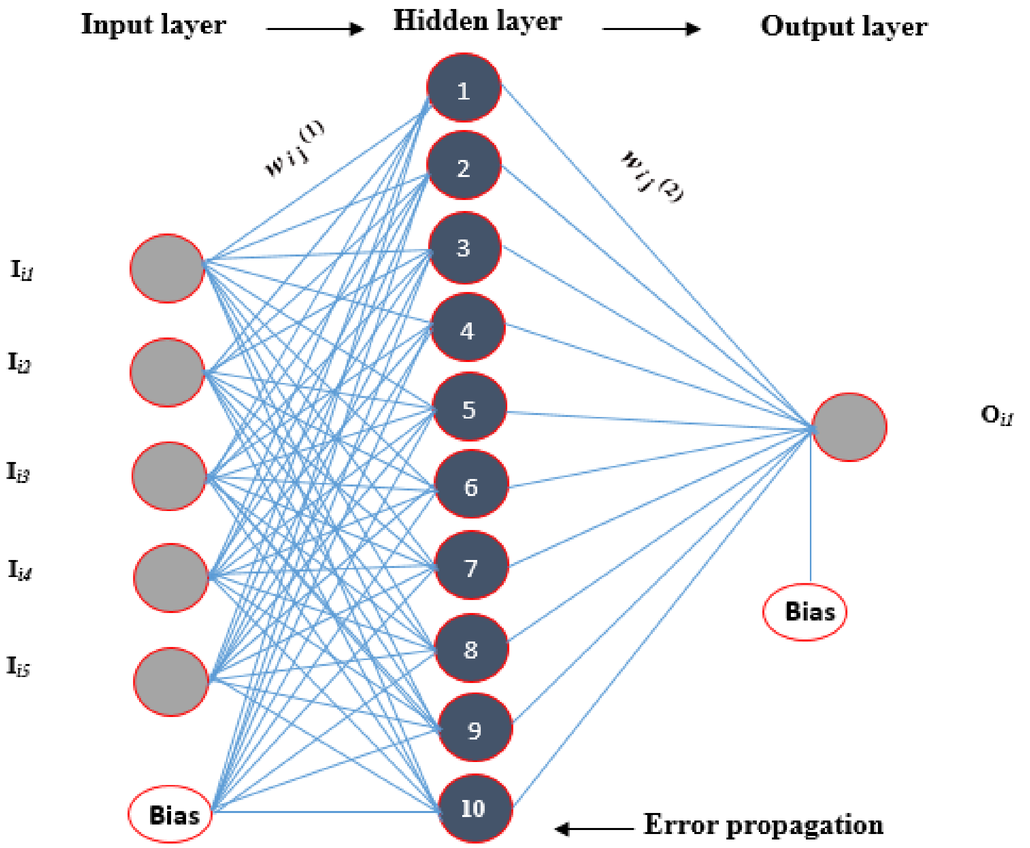

Figure 2-7: Structure of multi-layer feed-forward network (Jebur et al., 2018), permission to reuse this figure has been granted by Taylor and Francis.

2.9.3 Recurrent Network

A recurrent network is normally introduced in the case of a single-layer feed-forward ANN, if the output signals feedback as input that substitute part or all of the input signals (Shahin, 2014). This could also be generalised to cover multilayer feed-forward networks. In other words, a recurrent ANN consists of neurons feeding back their output to serve as new inputs to randomly selected neurons or themselves (Ravuri and Stolcke, 2016). A self-feedback can occur if the output layer of a certain node is fed-back to the same node. Feedback loops are enhanced with delay elements, this is due to the nonlinear environment of the nodes, resulting in a non-linear dynamic behaviour. Model inputs and output signals in a recurrent ANN are presented as x(n) and y(n) respectively in order to reflect the fact of being functions of discrete time variables n (Kriesel, 2011).

2.10 The Error Back-propagation

A variety of ANNs topologies has been developed to solve problems in many applications. One of the most popular and robust ANN configurations is the error back propagation algorithm (Alizadeh et al., 2012; Tarawneh, 2013; Yadav et al., 2014; Mohammed et al., 2017). The error feed-forward back propagation technique has been proven to be a highly efficient tool in modelling non-linear relationships (Feng et al., 2013; Jaeel et al., 2016). The algorithm updates the ANN weights in such a way that the error of the network output is decreased as set in the original goal. An ANN is constructed in such way that each processing element in a specific layer is fully connected to the next layer. Alternatively stated, every single node in the input layer will send its output to every neuron in the middle layer, consequently, every neuron in the input layer will then send its output to every neuron in the model output layer (Nguyen-Truong and Le, 2015).

The multilayer back-propagation ANN learning process comprises of two processing elements passing through the different network layers: a forward pass and backward pass, by computing the gradient for each connection weight and bias utilising the chain rule, as seen in Figure 2.8. During the forward step, the synaptic network weights are all assumed to be fixed, whereas, at the backward pass, the synaptic network weights are adjusted according to an updated error. This iteration procedure is repeated during the training process, which propagates the term of error needed for weight adjustment until the trained network can provide a set of connection weights, which has the input/output mapping that contains the minimum error value. Among the enhancements to the error back-propagation algorithm that have been produced, one method involves the use of the learning rate. The learning rate parameter (η) can be categorised as the factor that initiates the step size that the ANN takes in negative through the weight spaces in attempts to minimize the training error magnitude. The momentum term (α) is another factor that needs to be considered in any ANN training process (Kriesel, 2011). The objective of the α value is to increase the step size when the weight space direction is the same as the previous step direction and vice versa.

2.10.1 The Algorithm of Error in Back-propagation

1. Initialise the network connections weight between the measured and the predicted values;
2. Repeat the following steps until some criteria;
3. Sum up weighted inputs and apply the transfer function to compute the output of hidden layer;

$$h_i = f \sum_{i=1}^{n} (x_i \, w_{ij}) + \theta_j \qquad 2.28$$

h_i= hidden neuron output

x_i= input signal

w_{ij}= connection weight between input neuron i and hidden neuron j

f = the activation function

θ_j= bias on hidden neuron

4. Sum weighted output of hidden layer and apply the activation function to compute the output layer

$$y_k = f \sum_{i=1}^{n} (h_j \, w_{jk}) + \theta_k \tag{2.29}$$

y_k= independent output

w_{ik}= connection weight between hidden nodes j and k

5. Back propagation combinations

$$\delta_k = (d_k - y_k)\bar{f}(\sum j \, h_j w_{jk} + \theta_k) \tag{2.30}$$

$\bar{f}$= the derivation of the activation function

d_k= the desired output of the neuron

6. Calculate of the weight correction term

$$\Delta w_{jk}(n) = \eta \delta_k h_j + \alpha \Delta w_{jk}(n-1) \tag{2.31}$$

$\Delta w_{jk}(n)$= adjustment on connection weight between nodes j and k

η= learning rate

α= momentum term

h_j=actual output of hidden neuron

δ_k = back propagation error

$\Delta w_{jk}(n-1)$= previous weight correction

7. Sum delta input for each hidden unit and calculate error term

$$\delta_j = \sum k\delta_k w_{jk} \ \bar{f}(\sum i x_i \, w_{ij}) \tag{2.32}$$

8. Calculate weight correction term

$$\Delta w_{ij}(n) = \eta \delta_j x_i + \ \alpha \Delta w_{ij}(n-1) \tag{2.33}$$

9. Update weights

$$w_{jk}(new) = w_{jk}(old) + \Delta w_{jk} \tag{2.34}$$

$$w_{ij}(new) = w_{ij}(old) + \Delta w_{ij}$$

10. Compute the sum square error

$$SSE = \frac{1}{2}\sum_{K}(d_k - y_k)^2 \tag{2.35}$$

k= number of output neurons

11. End

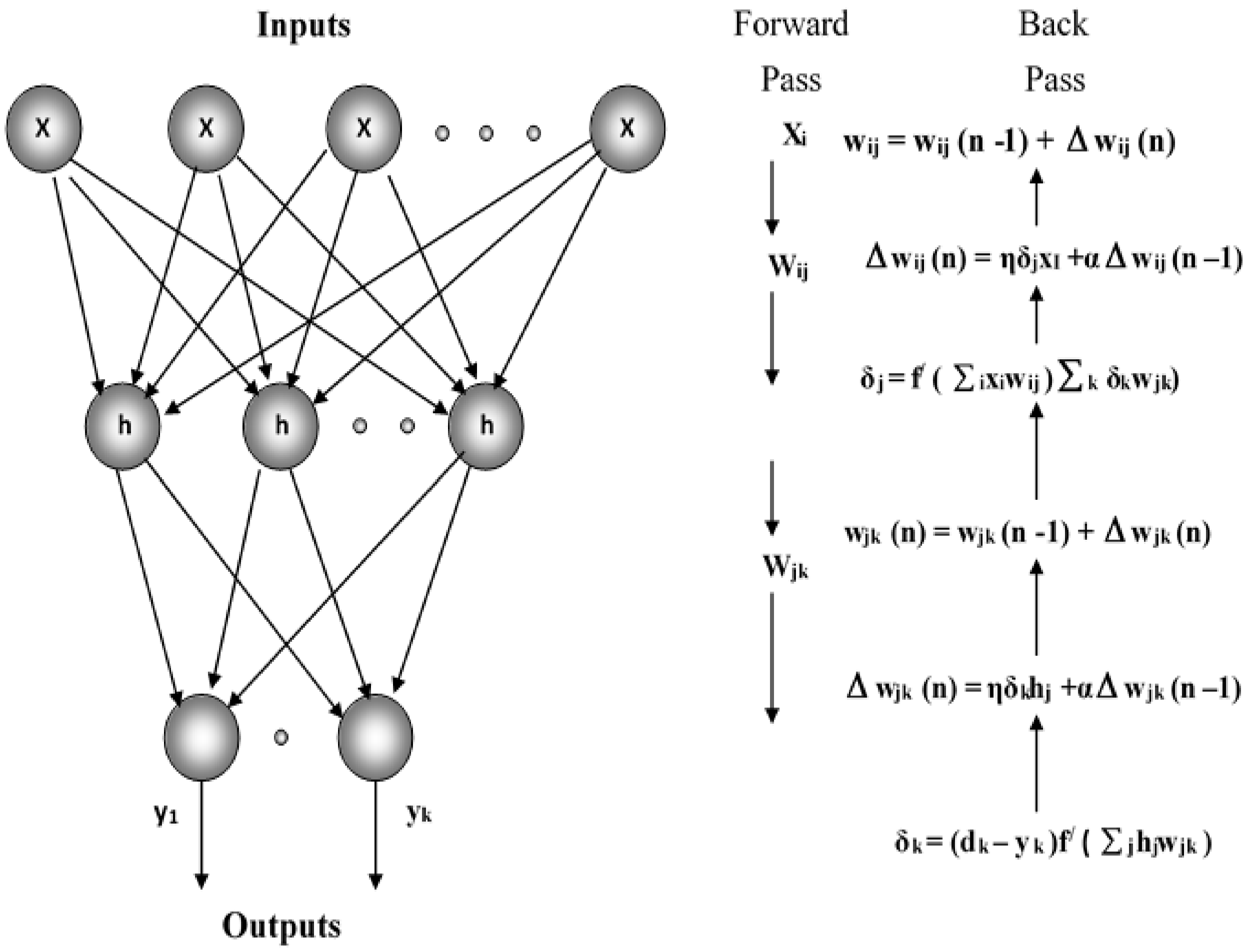

Figure 2-8: Steps to illustrate the back-propagation algorithm error.

2.11 The Levenberg-Marquardt (LM) Training Algorithm

2.11.1 Introduction

The LM training algorithm is one form of the artificial intelligence (AI) concept. The optimisation and training process simply means identification of the optimum ANN model parameters, which are the connection weights, bias, maximum number of hidden neurons and number of hidden layers. It is worth stating that the main target behind the implemented LM algorithms is to minimise the error value between the target and predicted value via adjusting the connection weights that are identified to contribute most to the error (Jebur et al., 2018a). For multi-layer feed-forward, the error function is normally a non-linear function. Consequently, it is not possible to implement an analytical solution for minimising the error percentage to its lowest value. Instead, it is vital to find an algorithm that involves a search through the weight spaces comprising of a succession of steps of the form:

$$w_{k+1} = w_k + \nabla w_k \tag{2.36}$$

where: w_{k+1} denotes weight value at a certain iteration +1, w_k is the value of the same weight at previous step k, ∇w is the increment of the weight vector.

Different types of algorithms found by many scholars in the relevant literature involve different techniques to identify the weight vector increment (Kriesel, 2011). The LM technique has been introduced to overcome the main drawbacks and limitations associated with the conventional approaches and widely cited as an efficient and robust training algorithm across all engineering aspects (Morfidis and Kostinakis, 2017). The LM approach is well documented as achieving a much higher performance by making training 10 to 100 times faster, more reliable, stable, and converging more often (Wilamowski and Yu, 2010; Abdellatif, 2013).

The LM scheme is efficient algorithm but more computationally intensive version of back-propagation. This system was created as an improvement of the Gauss-Newton method, with the target of eliminating the numerical instability associated with the matrix inversion in the latter. In this method, another approximation to the Hessian matrix will be introduced, H denoted as:

$$H = J^T J + \mu I_i \tag{2.37}$$

where: μ is the combination function, I_i is the identity matrix.

J is the Jacobian matrix and could be calculated through a back propagation technique that is less complex than computing the Hessian matrix. The aforementioned matrix contains the first derivatives of the ANN error value with respect to weights and can be defined as:

$$J = \begin{bmatrix} \frac{\partial e_{1,1}}{\partial w_1} & \frac{\partial e_{1,1}}{\partial w2} & \cdots & \frac{\partial e_{1,1}}{\partial w_N} \\ \frac{\partial e_{1,2}}{\partial w_1} & \frac{\partial e_{1,2}}{\partial w_2} & \cdots & \frac{\partial e_{1,2}}{\partial w_N} \\ \cdots & \cdots & \cdots & \cdots \\ \frac{\partial e_{1,M}}{\partial w_1} & \frac{\partial e_{1,M}}{\partial w_2} & \cdots & \frac{\partial w_{1,M}}{\partial w_N} \\ \cdots & \cdots & \cdots & \cdots \\ \frac{\partial e_{P,1}}{\partial w_1} & \frac{\partial e_{P,1}}{\partial w_2} & \cdots & \frac{\partial e_{P,1}}{\partial w_N} \\ \frac{\partial e_{P,2}}{\partial w_1} & \frac{\partial e_{p,2}}{\partial w_2} & \cdots & \frac{\partial e_{P,2}}{\partial w_N} \\ \cdots & \cdots & \cdots & \cdots \\ \frac{\partial e_{P,M}}{\partial w_1} & \frac{\partial e_{P,M}}{\partial w2} & \cdots & \frac{\partial e_{P,M}}{\partial w_N} \end{bmatrix} \tag{2.38}$$

$e_{p,m}$ is error of training process at output m when applying pattern p and is found as

$$e_{p,m} = d_{p,m} - o_{p,m} \tag{2.39}$$

where: $d_{p,m}$ and $o_{p,m}$ are, respectively, the predicted and observed output vectors, p is the pattern index from 1 to N , m is the pattern index, from 1 to $M,$ and N is the weight number.

In addition, the relationship between the Jacobian, J and the gradient vector, g of error, e is defined as:

$$g = J^T e \tag{2.40}$$

$$e = \begin{bmatrix} e_{1,1} \\ e_{1,2} \\ \cdots \\ e_{1,M} \\ \cdots \\ e_{P,1} \\ e_{P,2} \\ \cdots \\ e_{P,M} \end{bmatrix} \tag{2.41}$$

In the current study, the LM algorithm was trained with five input parameters and one output, however, the update rule of the LM algorithm can be illustrated as follows:

$$w_{k+1} = w_k - (J^T J + \mu I_i)^{-1} J_K^T ek \tag{2.42}$$

As a combination of the Gauss-Newton algorithm and the steepest descent algorithm, the LM training algorithm switches between the two algorithms during the training phase (Abdellatif, 2013). Yu and Wilamowski (2011) stated that when the combination coefficient of the training μ is too small, Equation 2.42 is just a Quasi-Newton algorithm. When the μ is large the latest described Equation approximates the steepest descent method. The training or learning process of the LM algorithm is illustrated in Figure 2.9. In this study, the developed model was trained with the help of a MATLAB toolbox version (R2017a) (see Appendix I). The mathematical illustration process between independent input variables and output is clearly defined in Equation 2.43.

$$O' = W_0 + \sum_{j=1}^{m} W_{jg} \left(W_{0j} + \sum_{i=1}^{n} W_{ij} X_i \right) \pm b_i \tag{2.43}$$

where: O' is the prediction value of dependent variable, X_i to X_n is the input values of ith independent variables, w_{ij} and $\pm b_i$ are network connection weights and biases values (see Appendices II to VIII).

An ANN is defined as a generalised network when it generates a resendable output from a set on inputs (testing dataset) that have not been utilised for training dataset (Mareš et al., 2016; Alrashydah and Abo-Qudais, 2018). In the case of a poor or non-generalised model, an ANN could suffer from either over fitting or under fitting (Shahin and Jaksa, 2005; Kriesel, 2011). Indeed, over fitting produces excessive variance, while, under fitting yields excessive bias in the model outputs (Hornik et al., 1989). The early stopping criteria approach was recognised, amongst various procedures, to be the most acceptable method to optimise the generalisation performance of the LM (Yadav et al., 2014). In the data division process, the dataset is divided into two main clusters, training and validation, performance of the training set is verified using the testing dataset. Thus, the method of early stopping requires one more subset between the training and cross-validation sets (not an introduced or unseen data subset during the training process) termed as the testing subset. The typical ANN approach observes the training error only during the training process, but the early stopping criteria observes the validation and the training errors (Kriesel, 2011). Within the early stopping criteria, the process of training is terminated once the mean square error (MSE) between the measured and the predicted values has reached its minimum value.

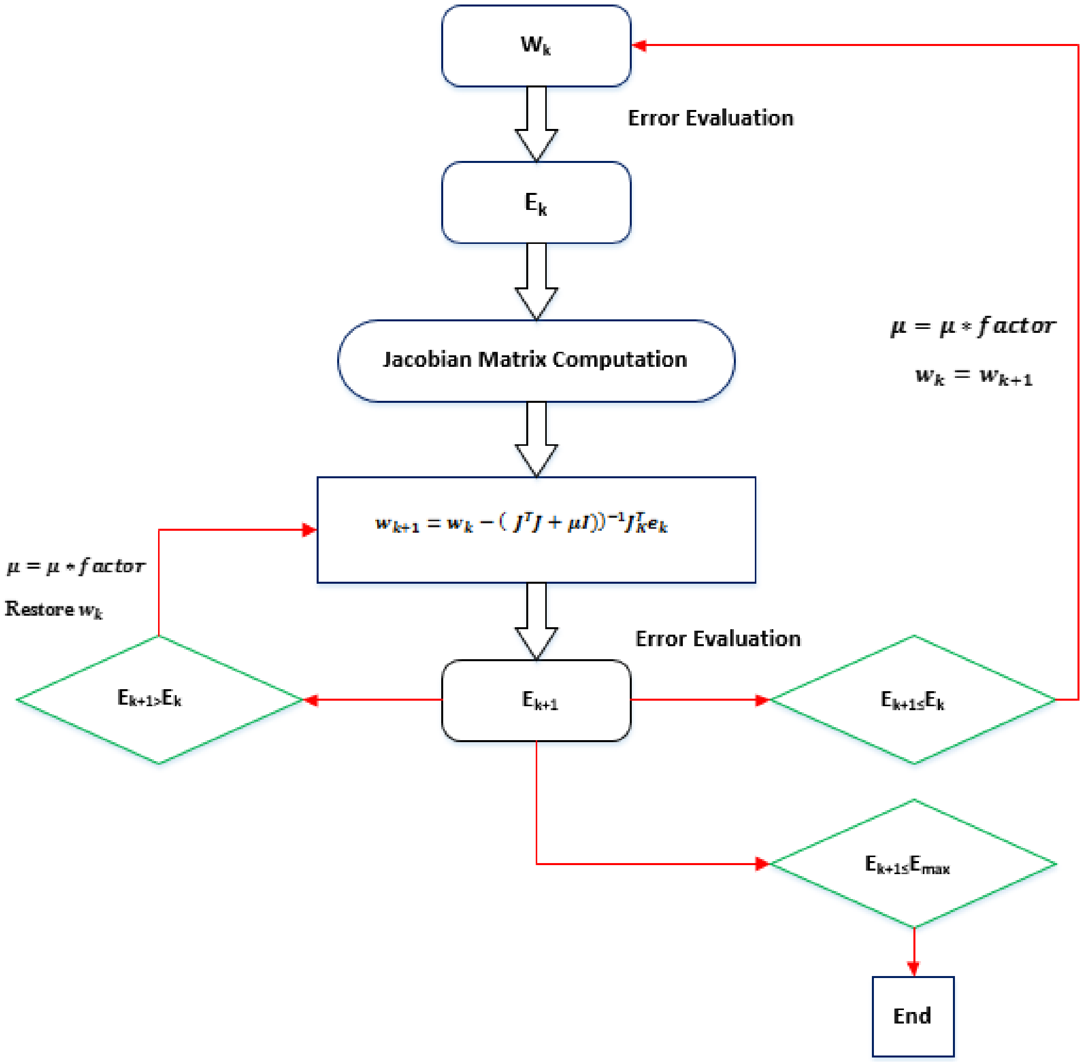

Figure 2-9: Block diagram of the LM training algorithm: w_k is the current weight, w_{k+1} is the next weight, E_{k+1} is the current total error, E_k is the last total error (Jebur et al., 2018), permission to reuse this figure has been granted by Taylor and Francis.

where: w_k denotes the existing weight, w_{k+1} is the subsequent weight, $E_{k+1} and\ E_k$ are the current and last total error respectively.

2.11.2 Determination of the LM Architecture

Determination of the ANN optimum architecture is one of the difficult tasks in network development. Indeed, it requires the selection of the optimum number of layers, selection of the most effective model input parameters, number of hidden layer(s), and the number of nodes in each specific layer. To date, there is no unified theory to determine an optimal ANN optimum topology (Premalatha and Valan, 2016). Basically, in any proposed network, there are two layers representing the input and output variables. One hidden layer is sufficient and can map any continuous function between the model variables (Alrashydah and Abo-Qudais, 2018; Jebur et al., 2018a).

It should be cited that introducing more than one hidden layer leads to substantially slow the process of training and enhances the chance of getting trapped in local minima (Al-Janabi, 2006). Trial-and-error is the promoted method (Stojanovic et al., 2016), which is commonly utilised to optimise the number and connectivity of the hidden layers. It has been suggested by Caudill (1988), that the maximum number of nodes in a single hidden layer could be taken as 2N+1, where N is the number of independent variables. Another approach, suggested by Premalatha and Valan (2016), reveals that the optimum number of the nodes used in the hidden layer is a function of mean square error (MSE) and correlation coefficient (R). Finalisation of the number of neurons can be arrived at when the MSE is minimum value and R numerical value at its upper possible limit.

2.11.3 Model Performance Evaluation

The ANN performance should be assessed once the training process has been successfully accomplished. The objective of the performance evaluation phase is to ensure that the model has the capability to re-generalise within the performance analysis limits set by the training data in a sufficient fashion as would be expected. The acceptable approach that is generally adopted in the relevant literature, is to test the measuring performance of the trained network on a testing data subset (Mareš et al., 2016). If such performance criteria are sufficient, the generalised model can be deemed to be robust. There are many measuring performance indicators documented by many scholars, to such obstacles, the correlation coefficients (R and p), root mean square error (RMSE) and the mean absolute error (MAE) are generally the main statistical performance indicators that are often utilised to evaluate the ANN model efficiency.

The determination coefficient value is a measure that is utilised to find the correlation and the goodness-of-fit between the measured and the predicted value (Hashim et al., 2017a). The following index is suggested by Faber et al. (2011) for R measuring performance between 0.0 and 1.0:

$$|R| \geq 0.8 \text{ strong correlation exists between two sets of variables} \tag{2.44}$$

$$0.2 < |R| < 0.8 \text{ correlation exists between two sets of variables} \tag{2.45}$$

$$|R| \leq 0.2\ weak \text{ correlation exists between two sets of variables} \tag{2.46}$$

- The correlation coefficient (R) to determine the relative correlation between two sets of variables, can be found using Equation 2.47:

$$R = \frac{\sum_{i=1}^{n}(T_i - \bar{T})(P_i - \bar{P})}{\sqrt{\sum_{i=1}^{n}(T_i - \bar{T}_i)^2 \sum_{i=1}^{n}(P_i - \bar{P})^2}} \tag{2.47}$$

- RMSE is the most adaptable criterion to measure the error between the predicted and measured values and has the advantage that a large error value receives greater attention than small errors. While, MSE eliminates the emphasis given to large errors. It should note that both MSE and RMSE are desirable when the assessed output data are continuous or smooth, RMSE and MSE can be calculated as shown in Equations 2.48 and 2.49:

$$RMSE = \sqrt{\frac{1}{N}\sum_{i=1}^{n}|T_i - P_i|} \tag{2.48}$$

$$MSE = \sqrt{\frac{1}{N}\sum_{i=1}^{n}(T_i - \bar{T}_i)^2} \tag{2.49}$$

where N symbolises the dataset number, T_i and P_i are the targeted and computational value, $\bar{P}$ and $\bar{T}$ are the means of the predicted and targeted values.

2.12 Related Studies

There has recently been an increase trend in the number of numerical and experimental studies concerning pile load-settlement behaviour. Among all, (Jeffrey, 2012) developed a comprehensive experimental study to examine the load-settlement responses of different types of model instrumented piles embedded in sand soil and subjected to a wide range of uplift and compression loads. Two types of pile construction methods were used in the experimental programme (replacement and displacement piles). The results revealed that the ultimate pile capacity of the continuous helical displacement piles were similar to that found in the displacement piles. Moreover, the initial sand density has been observed to be highly influenced by the pile type and pile installation method. Comparing the results of different types of piles materials, the continuous helical displacement pile was determined to cause a substantial modification in the sand relative density around the shaft of the pile. Whereas, the sand relative density below the pile base was fond to be highly influenced by displacement piles (concrete and steel). The results also demonstrated that the developed skin friction resistance for displacement and replacement piles were similar. Both displacement and replacement piles develop about 90 % of the ultimate capacity from end bearing resistance.

Gaaver (2013) performed experimental load-displacement tests on steel vertical piles tested in sand soil and subjected to uplift loads. The model piles were tested in three sand relative densities, measuring of dense, medium, and loose with pile-embedded length to diameter ratios of 26, 20, and 14. The results shown that the pile uplift capacity was highly influenced by on the sand properties and pile effective length (embedded length of pile).

Fattah and Al-Soudani (2014) performed experimental study to explore the influence of soil plugs on the pile bearing capacity of steel piles tested in loose sand. Different parameters have been involved in the testing programme, comprising of pile installation technique, pile Lc/d ratio, and soil plug removal with respect to plug length. The results revealed that pile-bearing capacity was influenced by the percentage of plug soil and pile geometry. Two years later, Fattah et al. (2016) carried out another experimental study to examine the bearing capacity of steel piles embedded into three different densities of sand soil; dense, medium, and loose. Different types of model piles with a wide range of slenderness ratios were tested to achieve the intended aim. The results revealed that the ultimate pile capacity increases in parallel with an increase in soil density and plug length ratio (PLR). In light of these test results, an empirical formula created by the authors, which could be used to predict the pile capacity of open-ended steel piles.

Recently, ANNs have been confirmed to be a good modelling technique in various domains including the different speciality areas in geotechnical engineering. An ANN has the capability to deal with complexity and to capture the non-linear functions, adopting the substantial computer capacity to implement extremely iterated work (Cho, 2009). With this respect, Alkroosh and Nikraz (2011) investigated the feasibility of artificial neural network to simulate pile capacity of different types of model pile foundations subjected to axial loads. Three types of ANNs have been developed and trained, one for modelling replacement piles and two models for displacement piles. The models were constructed based on the results of cone penetration tests (CPT). The results demonstrated that the ANN models perform well and have the reliability to predict pile load carrying capacity with some degree of success.

In another study, Momeni et al. (2014) examined the utilisation of hybrid genetic algorithms coupled with ANNs to model pile bearing capacity. A database consisting of 50 pile-loading tests was utilised to develop and learn the proposed ANN model. Four factors were identified as the most influence model input parameters affecting pile capacity, i.e., pile set, drop height, pile geometrical properties, and hammer weight. The results indicated that good agreement was achieved between the measured and the predicted pile bearing capacity values. Recently, Nejad and Jaksa (2017) carried out a study aimed at predicting pile load-settlement of model piles based on a cone penetration test (CPT). Twelve input parameters were used in the input space to develop and train the proposed model. Pile settlement was assigned to be the model dependent variable. The results revealed that the adopted method could be used to predict pile settlement with high accuracy, thus recommending the application of an ANN model as a good tool in predicting pile-settlement behaviour.

Although many researchers have highlighted the use of artificial neural networks (ANNs) in the field of geotechnical engineering, to date, there are still specific gaps in the subject knowledge. The slow rate of convergence, the necessity of adjusting a training constant, and getting trapped in the local minima have been cited as major drawbacks associated with conventional artificial neural networks (Momeni et al., 2014). In addition, the input parameters were selected based on trial and error. In the current study, a new methodology has been presented using a comprehensive experimental pile load test. Additionally, a robust, self-tuning artificial intelligence (AI) approach to fully correlate pile load-carrying capacity and associated settlement of rigid and flexible piles. The choice of input parameters has been discussed using a comprehensive statistical analysis to identify the most efficient input parameters, underline the contribution of each model input parameter, and precisely evaluate the reliability of the dataset being examined.

2.13 Summary

In this chapter, the details of two literature review phases are presented in an effort to provide the reader with a brief review of pile foundations and the feasibility of the computational intelligence schemes in modelling pile-load carrying capacity. Firstly, methods of pile installation were summarised. It has been reported that pile foundations could be categorised in different types, depending on pile installation method, pile geometry and pile materials. Secondly, pile design procedures were presented and it was stated that many variables are involved in the design framework. These were a function of soil type, type of pile installation and factors related to pile functionality such as end bearing capacity and the earth pressure coefficients. Furthermore, in-situ pile bearing capacity testing procedures have also been discussed. A brief review of the conventional methods used to predict pile settlement were also presented. The feasibility of computational intelligence applications has been highlighted and discussed, it has been found that the computational intelligence approaches could be successfully applied to provide a predictive model when the relationships between model inputs and output(s) are non-linear. The topology and the factors affecting the construction and training process of the ANN model have been summarised, it has been revealed that the number of dependent, and independent variables, number of neurons, training method, and size of the dataset are the main parameters affecting the model convergence. Moreover, based on literature, root mean square error (RMSE), mean absolute error (MAE) and the coefficients of determination (Pearson’s R and p) have been selected as the main statistical indicators to test the performance and the generalisation ability of the trained network. The employed self-tuning supervised LM has also been presented and discussed. Finally, a review of some related studies concerning pile foundations have been documented.

CHAPTER 3

Experimental Methodology

3.1 Introduction

This chapter discusses, in detail, the experimental methodology used in this thesis. In the current study, a series of experimental pile-load tests were performed on different types of model piles, with pile slenderness ratios (Lc/d) of 12, 17 and 25, penetrated in three sand relative densities measuring loose (18%), medium (51%) and dense (83%) and subjected to compression and uplift loading systems. The pile load tests were performed using an innovative pile-testing chamber which was designed and manufactured at Liverpool John Moores University. Full-scale in-situ tests are highly preferable. However, such tests are expensive, have a negative environmental impact, and there are uncertainties assigned with the soil stress history. They are time consuming, tedious and as such, pile-load tests have been cited as barriers in determining field pile load carrying capacity (Ornek et al., 2012; Momeni et al., 2014; Baziar et al., 2015). Indeed, a laboratory scale pile-testing programme offers a good solution to overcome the limitations associated with the in-situ testing. However, considering the behaviour at bench scale compared to prototype behaviour is important when conducting any laboratory model testing. Laboratory scale test effects could arise due to both: (i) scale effects because of the localised deformation at the soil-pile interaction and (ii) boundary effects due to soil sample finite size. Therefore, it is worth noting that, in the context of this study, effects of both factors on the performance of the model piles have been addressed prior to the design and manufacture of the pile-testing chamber.

3.2 Development of the Pile Testing Chamber

This section presents, in depth, the manner in which the model pile-testing chamber has been designed and manufactured. In addition, the properties of the test bed and the sand densities preparation methods have also been presented. The physical model was designed and fabricated with overall dimensions of 900mm (in y-direction) x 900mm (in x-direction) with a third dimension (depth) at 3000mm as presented in Figures 3.1 and 3.2, respectively. The experimental set-up was comprised of a pile testing chamber, designed and manufactured by the author and the technical staff at LJMU. The chamber was then used to perform plie load tests for different types of model piles subjected to compression and tension loads. The loading system incorporated a double acting calibrated load cell type (DBBSM S-Beam) having a maximum capacity (compression and uplift) of 10kN. Vertical displacement instrumentation utilised 2 full bridge displacement transducers (strain gauge type), with the loading provided by a hydraulic pump model (Armstrong Lyon Hydraulic, ENERPAC L40N, LTD) connected to double acting hydraulic ram model (ZE3408E-T). A 16-bit resolution data acquisition system was used to monitor pile head load and displacement. The pile testing chamber with its sand bed incorporated a polytetrafluoroethylene (PTFE) sheet with a coefficient friction of less than 0.04 at the sand chamber interface. The pile driving process utilised an adjustable pin with a series of holes along a shaft of maximum length of 1.5m, which permitted incremental driving of the pile under hydraulic loading within the reach (stroke capacity) of the ram (max 400mm). A ball joint arrangement (acting as a universal joint) was used in the loading chain to avoid the transmission of moments under possible minor eccentric loading due to non-exact axial positioning. The data sets during the installation process were not recorded since the pile should be embedded until the desired embedded length has been reached. The pile load-settlement response was then performed to examine pile capacity (the applied load that leads to pile settlement at 10% of the pile diameter (BSI, BS EN 8004:1986).

Ideally, the pile-testing chamber must be large enough so that the chamber edges do not interfere in any major way with the stresses resulting from the pile testing. In experimental pile load testing, limitations on the testing chamber are normally dictated by available space and equipment availabilities. Moreover, the materials of the pile testing rig are found as playing a key role on the concept of the boundary effects and the soil stress distributions in the effective zone. Indeed, high stiffness materials would permit a reduction in the required chamber size to overcome boundary effects limitations in comparison with flexible materials. Nasr (2013), however, reported that if the ratio between the pile testing chamber and the pile diameter is more than 10, the effects of the boundary size could be ignored.

In this research study, the sand chamber is properly scaled down to overcome the issues induced from the chamber boundary influence on the sand stress distribution during the loading process with a ratio of 22.5 between the diameter of the sand box to model pile diameter for all model piles. Robinsky and Morrison (1964) reported that the boundary effect is more predominant within a range of 3-8 times the pile diameter. Whereas, Rao et al. (1998) stressed that, the ratio between the pile diameter and the chamber edge is about 10 to overcome the scale effect limitation. However, the pile diameter used in this study is equal to 40mm (for square and circular sections) and the test tank inside dimensions were (0.9m x 0.9m x 1.25m). Therefore, the minimum required dimension to minimize the scale effect issues must be 840mm (10d + 10d + d). In this study, the inside dimension is 900mm, exceeding the scaling law standards quoted. It is worth noting that Polytetrafluoroethylene (PTFE) has been used, as shown in Figure 3.1, in an effort to reduce the friction between the chamber and the sand test bed, as it has less frictional resistance (0.04) compared to the steel sheet (0.605) (Young and Freedman, 2000). In addition, 20mm sufficiently rigid Perspex sheet was utilised as the front side of the testing chamber and sub-divided into equal segments, as indicated in Figure 3.2. This was to provide a clear viewing area of the sand and to control volume.

Figure 3-1: Pile testing chamber with internal cover of PTFE sheet.

Figure 3-2: Schematic view of the test configuration for the pile testing chamber.

3.3 Sand Properties

This section discusses in detail the properties and the adopted procedure utilised to achieve the required relative sand densities. The sand used in the experimental testing programme is obtained from local supply. It has a relatively small impurity level with a quartz content at about 98%. Based on the Unified Soil Classification System (USCS), the sand being used could be classified as poorly graded (SP). The physical properties of the sand were determined from experimental tests, such as sieve analysis, specific gravity, sand unit weight and direct shear tests, as summarised in Table 3.1. In addition, the sand was composed of sub-rounded particles, as confirmed by scanning electron microscopy (SEM) images shown in Figure 3.3. The physical properties of the sand samples were determined through laboratory tests as per the standard approaches as stated by the BSI (BS EN 1377-7:1990).

The sand packing used in the experimental tests was prepared in three relative densities, D_r of 18%, 51% and 83%. In order to overcome the scale factor issues and to capture the in-situ pile-load test, the influence of the grain size distribution on the combined pile-soil interaction should be maintained. The ratio between the pile diameter and the sand medium diameter (d_{50}) should be 45 (Nunez et al., 1988). It has been stated by Remaud (1999) that the ratio is 60. Taylor (1995) however, reported that the minimum ratio should be 100. In this research, this condition has been met using a sand with the ratio between pile diameter and the sand mean grain size diameter (d/d_{50}) of about 134 as revealed in Figure 3.4, therefore the geotechnical scaling standard condition has been satisfied.

The sand placement technique or the air sand-raining process was observed to play a substantial role in the process of achieving reproducible sand density (Nasr, 2013; Kampitsis et al., 2015). To prepare the loose sand bed, the sand particles were poured into the test chamber utilising a tube delivery system, as proposed by Schawmb (2009). The end of the tube was repeatedly held at a maximum set distance of about 40mm between the sand delivery tube and the surface of the test bed. The medium sand was prepared using an air pluviation technique discussed by Ueno (2001). The sand was controlled by the falling rate at about 800mm above the sand surface with an accuracy of ± 25mm. The medium density of the sand bed was prepared using 2.00mm sieve size according to BSI (BS EN 410-2:2000) along with the use of a mechanical screw-jack as presented in Figure 3.5, and was carried out over 7-8 hours. The sufficiently rigid transparent Perspex sheet (Figure 3.2) with thickness of 18mm was placed in the front of the pile-testing chamber having been marked in equal square grids of 300mm to control the required sand volume during the sand preparation process. The sand top surface was levelled-off using a smooth straight aluminium plate. In addition, the dense sand condition was attained by dividing the testing chamber into four layers, each sand layer was placed with 300mm thickness for each layer and divided into equal segments (300 x 300)mm^2 (see Figure 3.2). subsequently, each sand layer was compacted to obtain the required density, utilising a hand-held vibrator technique, following the procedure detailed by Akdag and Özden (2013).

The sand densities were verified through the use of a small wooden box, (Figure 3.6) made with dimensions of (300 x 300 x 300) mm. With the known weight and volume of the empty wooden box, the specific sand density was defined. The following equation was used in order to establish the different sand test beds.

$$D_r\ (\%) = \frac{\gamma_{max}(\gamma - \gamma_{min})}{\gamma(\gamma_{max} - \gamma_{min})} \tag{3.1}$$

in which the $\gamma_{max}, \gamma_{min},$ and γ are, respectively, the maximum, minimum and sand unit weight (kN/m^3), D_r is the sand relative density.

Table 3-1: Physical properties of the sand.

Index Property	**Value**
Coefficient of uniformity, C_u	1.78
Specific gravity, G_s	2.62
Coefficient of curvature, C_c	1.14
Effective grain size, d_{10} (mm)	0.22
Mean grain size diameter, d_{50} (mm)	0.34
Moisture content, Mc (%)	<0.2
Specific surface area, (mm^2/ml)	94000
Maximum dry unit weight, γ_{max} (kN/m^3)	17.45
Minimum dry unit weight, γ_{min} (kN/m^3)	15.34
Void ratio of the sand in the loosest state, e_{max} (%)	0.709
Void ratio of the sand in the densest State, e_{min} (%)	0.49
Peak angle of friction for loose, medium and dense sand, $\emptyset_{peak}$ (°)	39, 44 and 46
Critical state angle of friction, $\emptyset_{critical}$ (°)	42 and 42.5
Peak sand-concrete interface friction angle, δ_{peak} (°)	28.8, 32.5 and 36
Critical state sand-concrete interface friction angle, $\delta_{critical}$ (°)	31.8 and 33
Peak sand-steel interface friction angle, δ_{peak} (°)	17, 17.7 and 19
Critical state sand-steel interface friction angle, $\delta_{critical}$ (°)	18.5

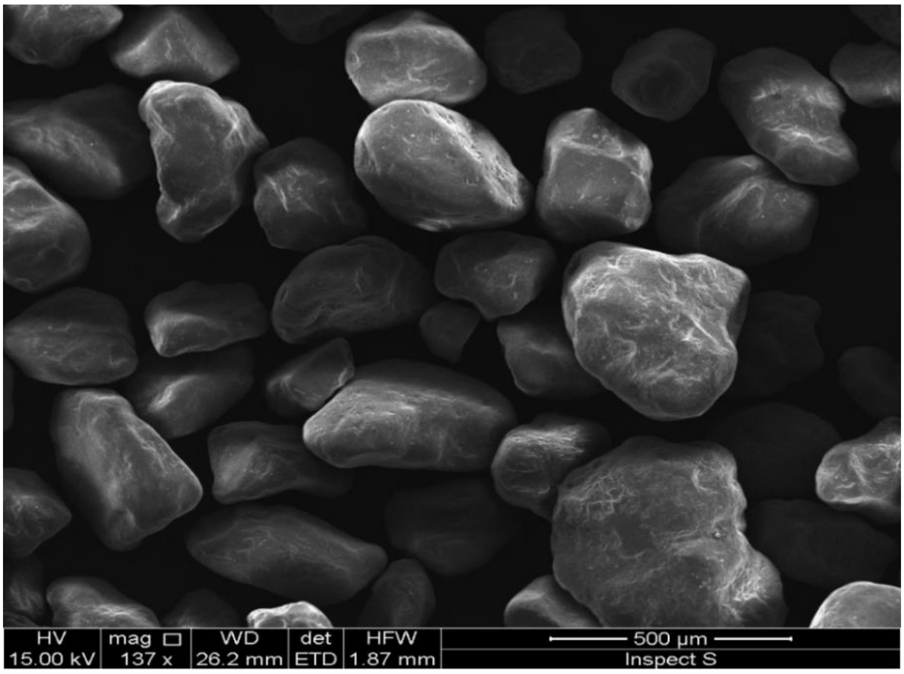

Figure 3-3: Scanning electronic microscopy (SEM) test result for the sand specimen.

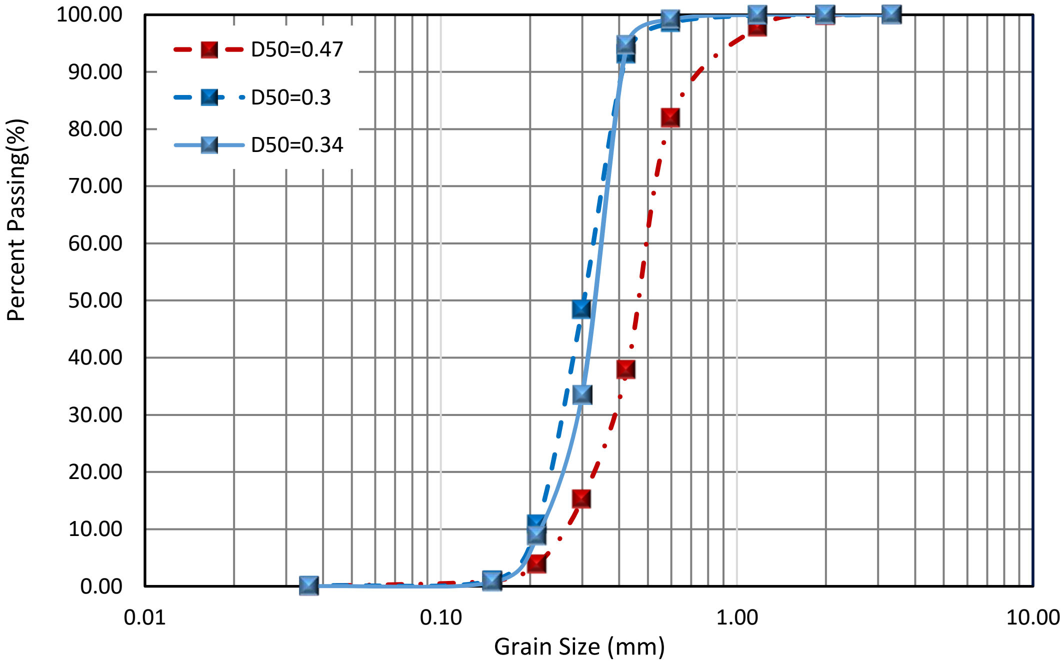

Figure 3-4: Particle size distribution of the sand specimen.

Figure 3-5: Preparation of sand bed by means of pluviation.

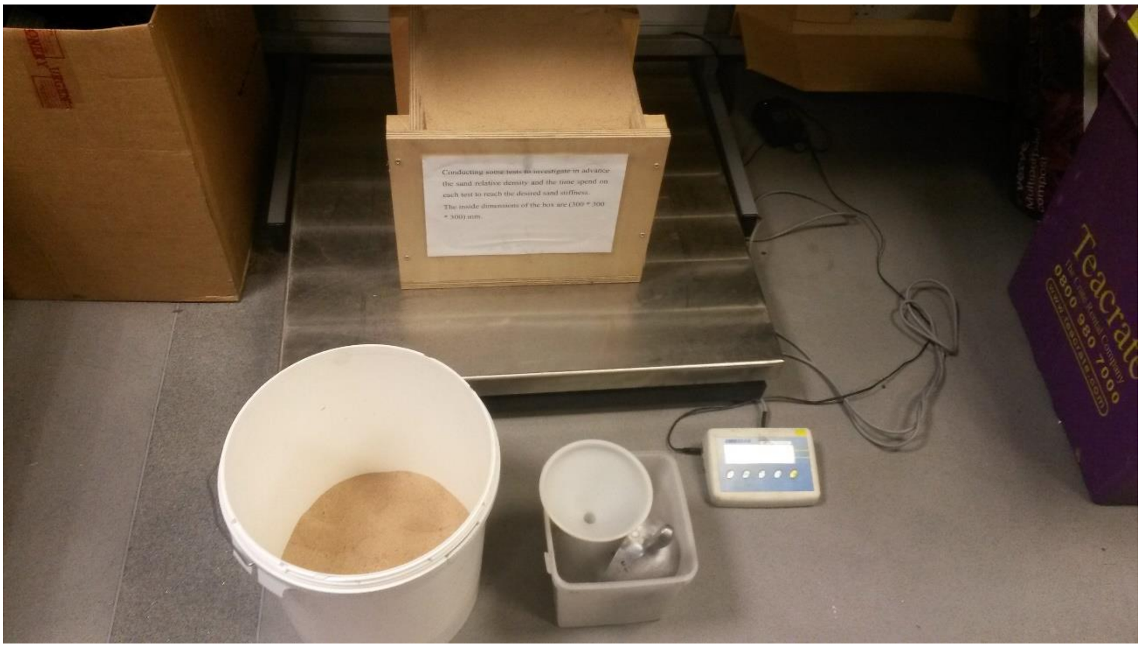

Figure 3-6: Sand density verification.

3.4 Direct Shear Tests of the Sand

Direct shear testing was performed following the technical method described by BSI (BS EN 1377-7:1990) in order to examine the sand shear strength characteristics. The sand bed used throughout the testing programme was uniform sand prepared in different densities with properties as detailed in section (3.3). The laboratory testing programme for the direct shear evaluation was conducted at Liverpool John Moores University, soil mechanics laboratory using a new direct shear box apparatus (Figures 3.7 and 3.8).

In addition to the sand shear strength characteristics, the sand-concrete and sand-steel interface friction angles for different sand relative densities were also determined from the direct shear tests. Applied normal and shear stresses on the adopted sand are evaluated and can be utilised in the determination of the angle of friction using the Mohr-Coulomb definition, as listed in the following equation:

$$\tau_f = \sigma' \tan \emptyset' + c' \tag{3.2}$$

τ_f denotes soil shear stress on the failure plane; $\sigma'$is the normal effective stress on the failure plane; $\emptyset'$ and c' are, respectively, effective angle of friction and effective cohesion of the soil.

3.4.1 Results of Sand Direct Shear Box Test

To reliably clarify the shear behaviour of the sand test bed used in the pile-testing chamber, the results of the direct shear test are presented and discussed in this section. These results were determined from the data (direct shear tests) of the computerised direct shear tests apparatus as shown in Figures 3.7 and 3.8. Figures 3.9 to 3.11 show the profile of shear stresses versus horizontal shear displacement for the three sand relative densities used in the experimental testing programme. The results revealed that the peak and critical state shear values, for the same density of sand, at higher normal stresses are higher than those subjected to low stresses. It can also be observed that the increase in the sand density results in an increase of the peak shearing resistance that could mainly be attributed to an increase in the dilatancy influence for the shearing resistance of the sand being investigated.

With respect to the direct shear test for loose sand, it should be noted that the graphical results in Figure 3.9 show a gradual increase in shear stresses profile as the shear displacement increases and then reaches a plateau without a pronounced peak. It also can be seen that the peak values of the shear stress for the medium sand are about 40kPa, 30kPa, and 23kPa, respectively. Increasing the sand density contributed to an increase of peak shearing resistance. This can be clearly seen form the direct shear test for dense sand with peak shear resistance values of about 44kPa, 33kPa, and 25kPa as revealed in Figure 3.11. The direct shear results also revealed that the critical distribution of the shear stress displays patterns of partially linear relationships for the initial loading stages (elastic zone). Furthermore, the concrete-sand and steel-sand shearing resistances were also induced along the pile effective length. To determine the corresponding angle of interface friction (δ) for each material, direct shear box tests were also performed on sand-concrete and sand-steel for different sand relative densities. Moreover, the results of the peak and critical state shear stresses were graphically presented versus the normal effective stresses, as shown in Figures 3.12, 3.19 and 3.20. A linear relationship can be seen between the normal effective stress and the sand-sand peak and critical state shear stresses. From Figure 3.12, it can also be observed that the sand peak shear stresses for dense sand are higher than those found in loose and medium sand. As stated, this can be attributed to an increase in the influence of the dilatancy for the shear resistance of the dense sand. The angles of internal friction and material interface friction were determined using linear regression, assuming a line of best fit with no cohesion (zero intercept).

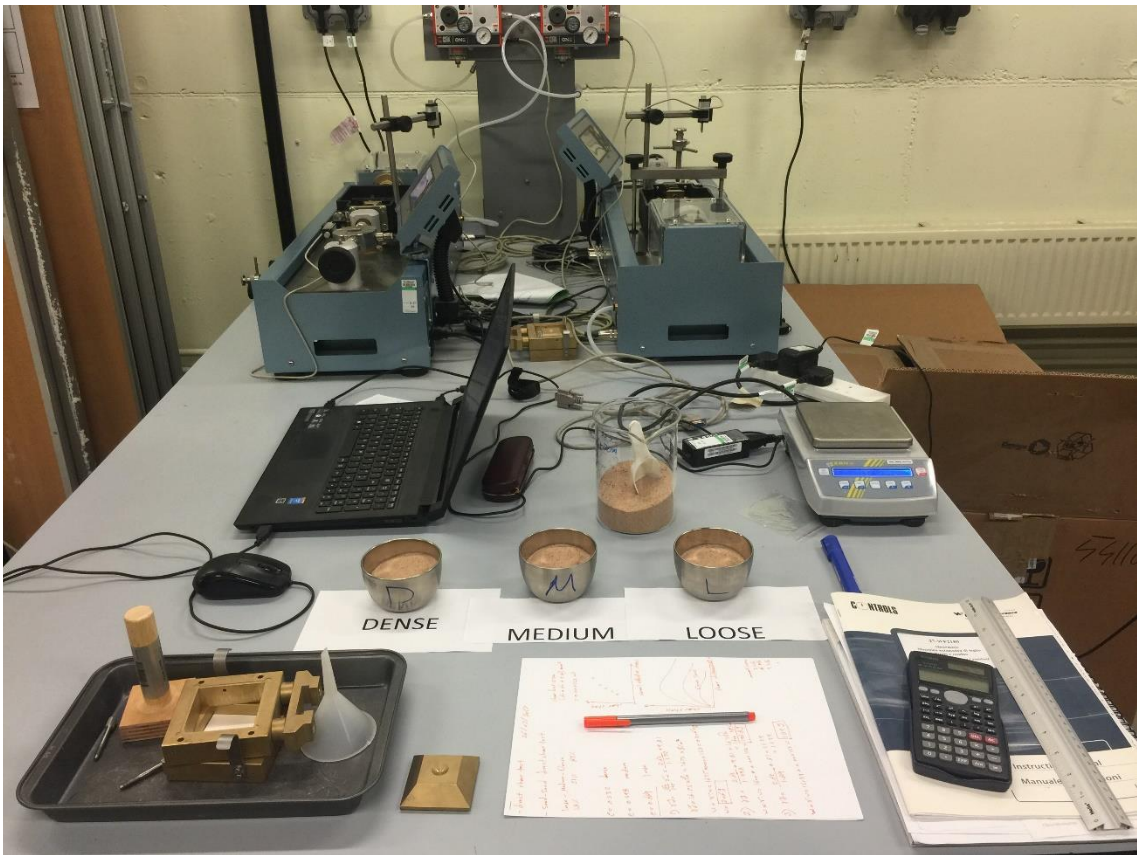

Figure 3-7: Preparation of the sand specimen for shearing tests.

Figure 3-8: Apparatus for the direct shear test.

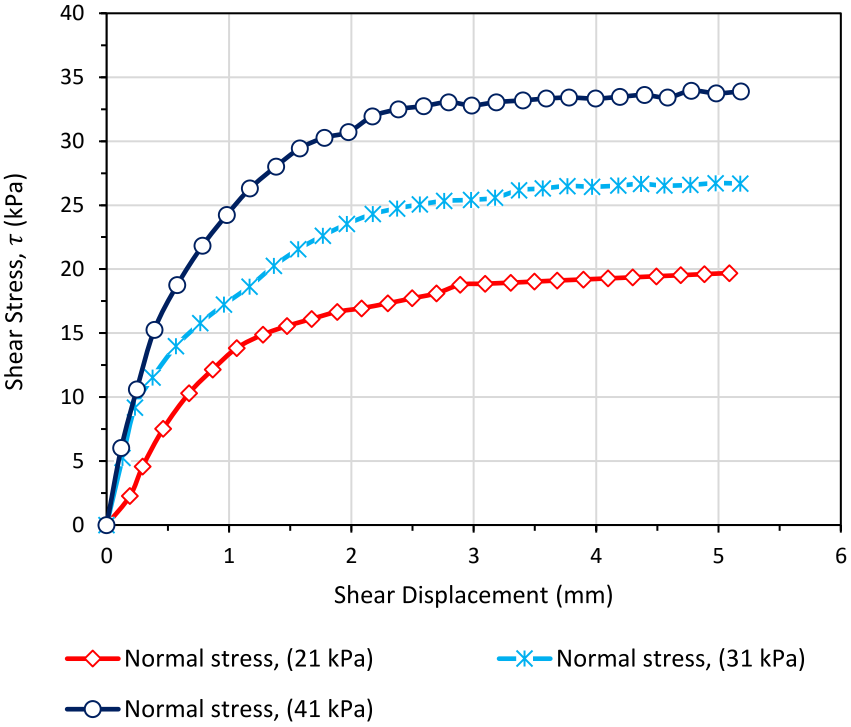

Figure 3-9: Shear stresses versus shear displacements for loose sand.

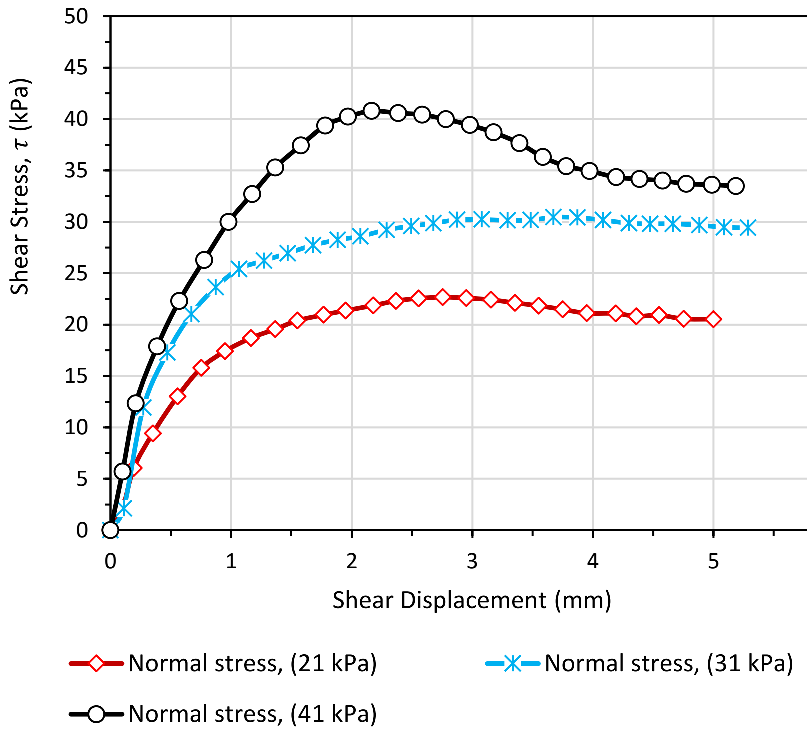

Figure 3-10: Shear stresses versus shear displacements for medium sand.

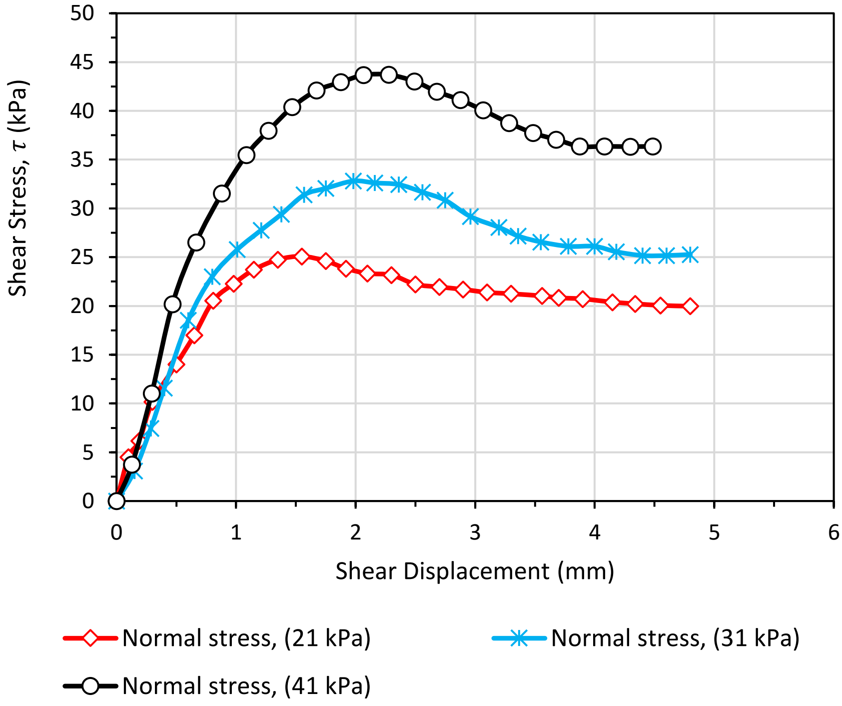

Figure 3-11: Shear stresses versus shear displacements for dense sand.

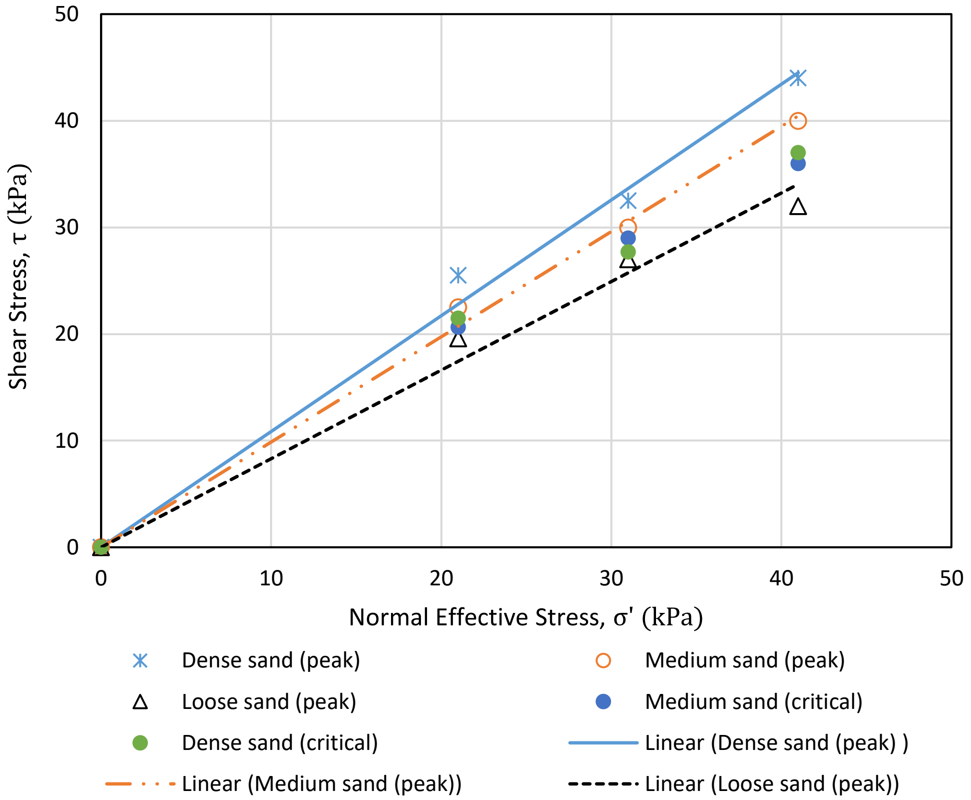

Figure 3-12: Shear stresses versus normal effective stresses for sand-sand interfaces at different relative densities.

Likewise, the interface friction angles between the sand/concrete and sand/steel for different sand densities, have also been experimentally measured using the direct shear test, these summarised in Table 3.1. The sand-concrete and sand-steel shear box tests have been performed by placing a piece of precast concrete block and steel block in the bottom of the shear box and then the tests were carried out in accordance with BSI (BS EN 1377-7:1990). Figures 3.13, 3.14, and 3.15 (sand-concrete interfaces) and Figures 3.16, 3.17, and 3.18 (sand-steel interfaces), depict the results of shear stress against shear displacement for a wide range of relative densities of sand (loose, medium, and dense).

The results revealed that the shear stress profiles in Figures 3.13 and 3.16 are typical for loose sand packing, showing a gradual increase in shear stress with shear displacement, then becoming steady with shearing resistance measuring of 22kPa, 17kPa, and 13kPa for sand-concrete and of 12.7kPa, 9kPa, and 7kPa for sand-steel, respectively, without a pronounced peak. Regarding medium sand, the peak values of the shear resistance are slightly higher than those recorded for the loose sand, giving shear values of 26kPa, 20kPa, and 14.5kPa for sand-concrete and of 13.8kPa, 9.4kPa, and 7.5kPa for sand-steel. Moreover, for dense sand packing, the peak shear resistance is higher than that identified from the loose and medium sand, with notable peak values of 29.5kPa, 23kPa, and 16.5kPa for sand-concrete and of 15kPa, 10.5kPa, and 8kPa for sand-steel, respectively. This could because of an increase in the contribution of dilatancy to the shear resistance of the dense sand. It is worth noting that the values of δ for sand/steel interfaces given in Table 3.1, are slightly lower than commonly stated values owing to the fact that the piles used in the experimental tests were made of steel with a smooth surface.

In addition, the results for sand-concrete and sand-steel for peak and critical state shear stress versus normal effective stress, are shown in Figures 3.19 and 3.20. As expected for dry sand, a linear relationship can be seen between normal effective stress and shear stress values. It can also be observed that the sand peak and critical state values of shear stresses increase with increasing applied effective stress, behaving in the manner anticipated.

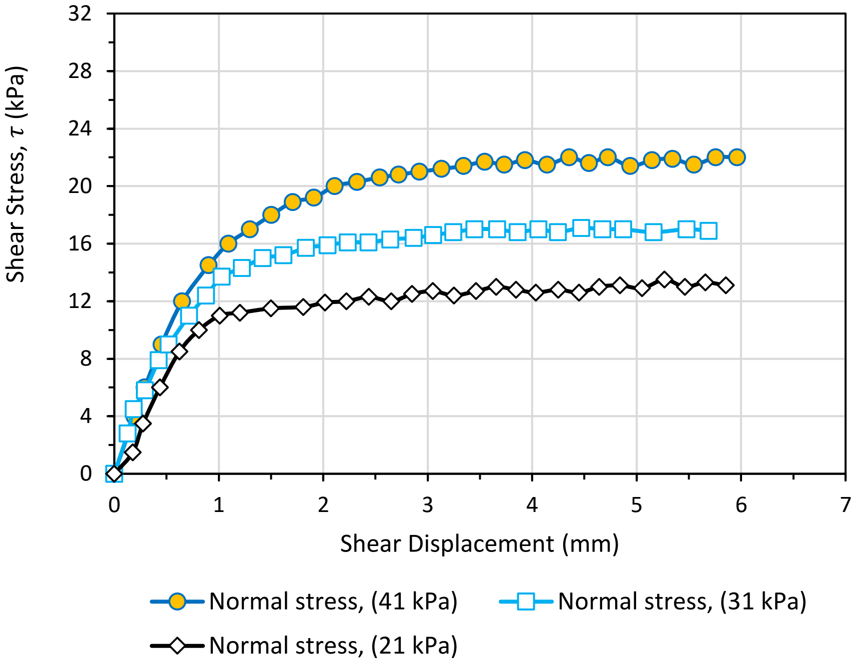

Figure 3-13: Shear stresses versus shear displacements for concrete-loose sand.

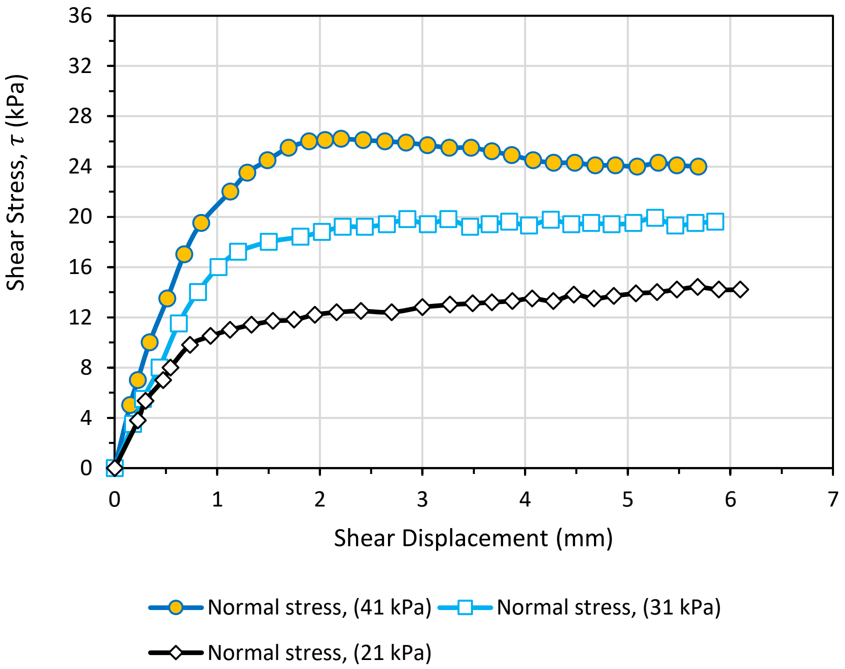

Figure 3-14: Shear stresses versus shear displacements for concrete-medium sand.

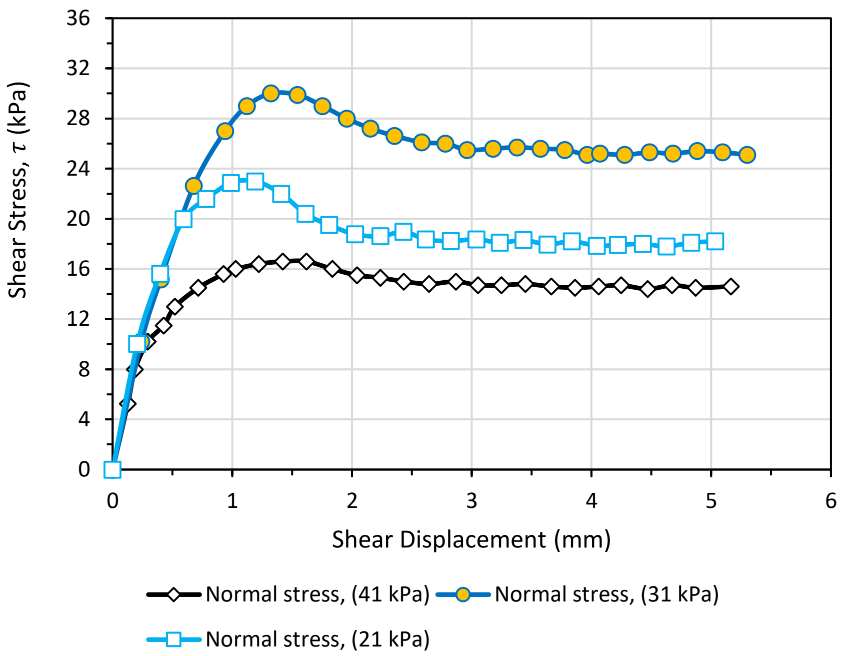

Figure 3-15: Shear stresses versus shear displacements for concrete-dense sand.

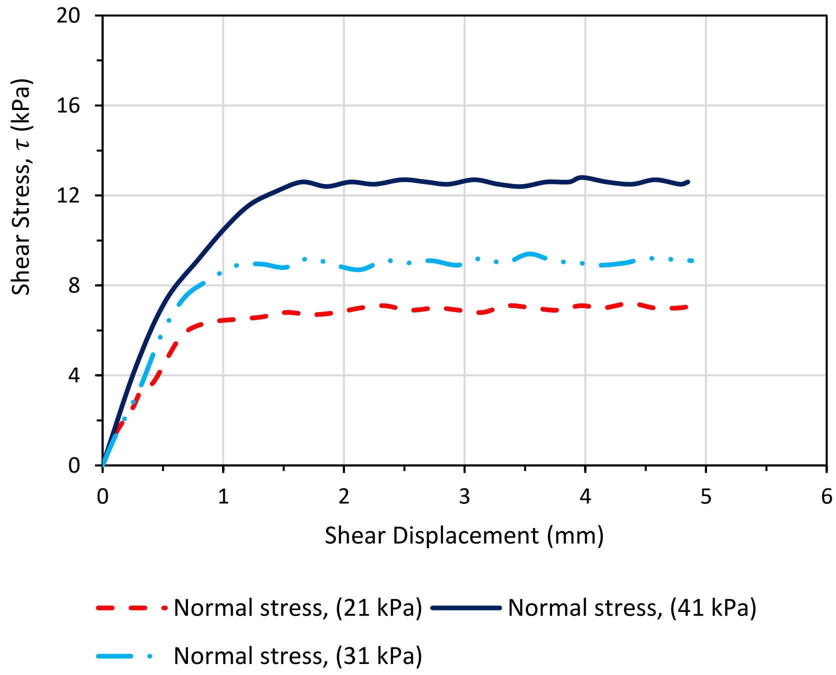

Figure 3-16: Shear stresses versus shear displacements for steel-loose sand.

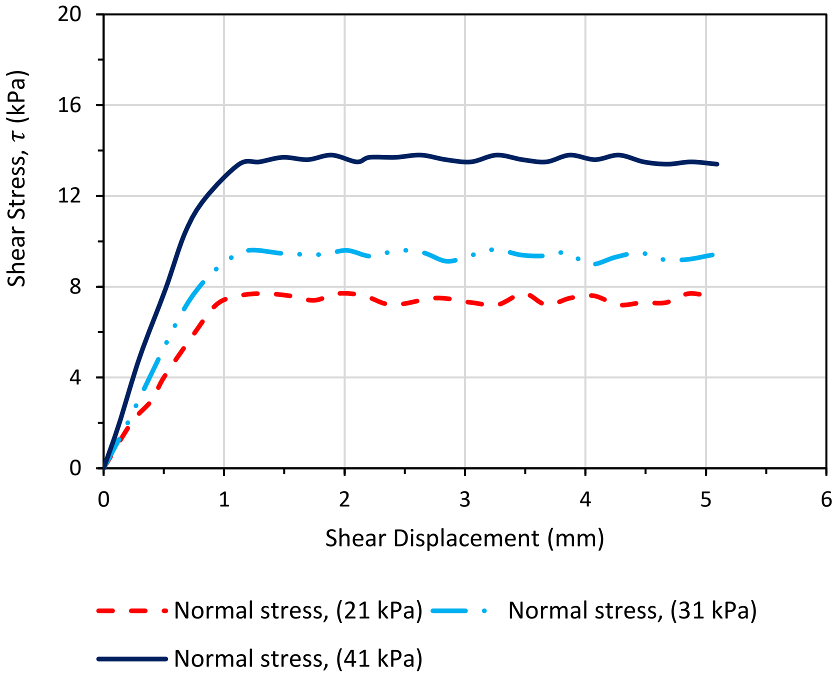

Figure 3-17: Shear stresses versus shear displacements for steel-medium sand.

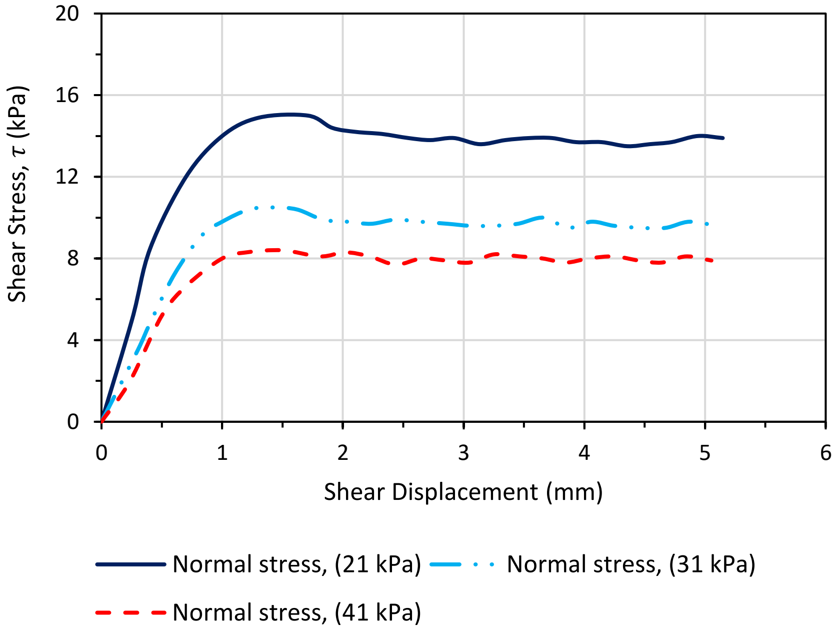

Figure 3-18: Shear stresses versus shear displacements for steel-dense sand.

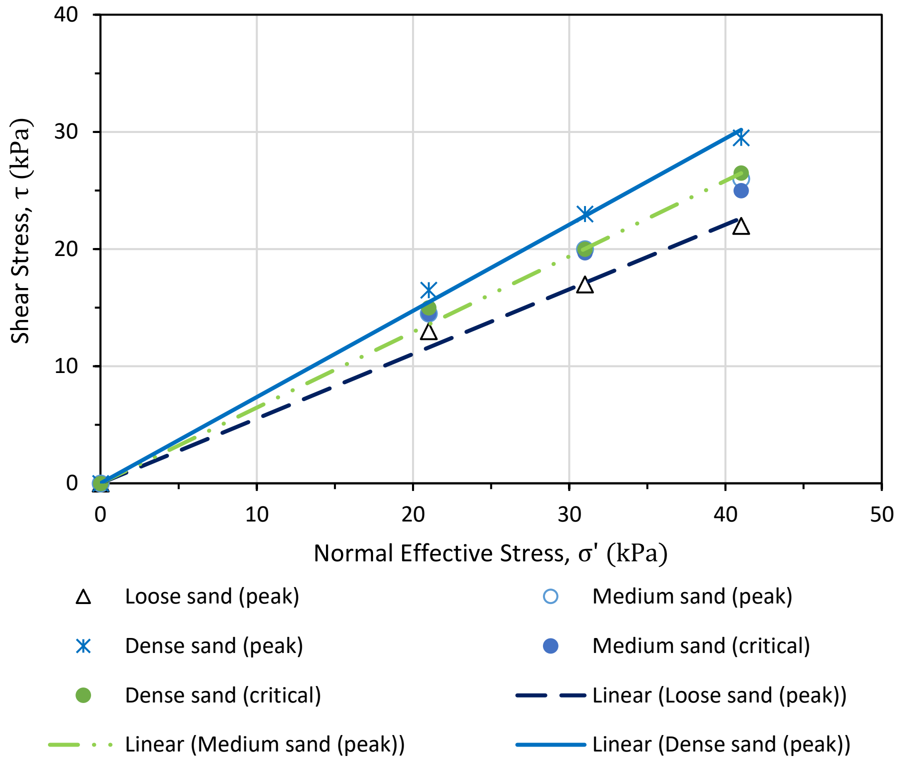

Figure 3-19: Shear stresses versus normal effective stresses for sand-concrete interfaces at different sand relative densities.

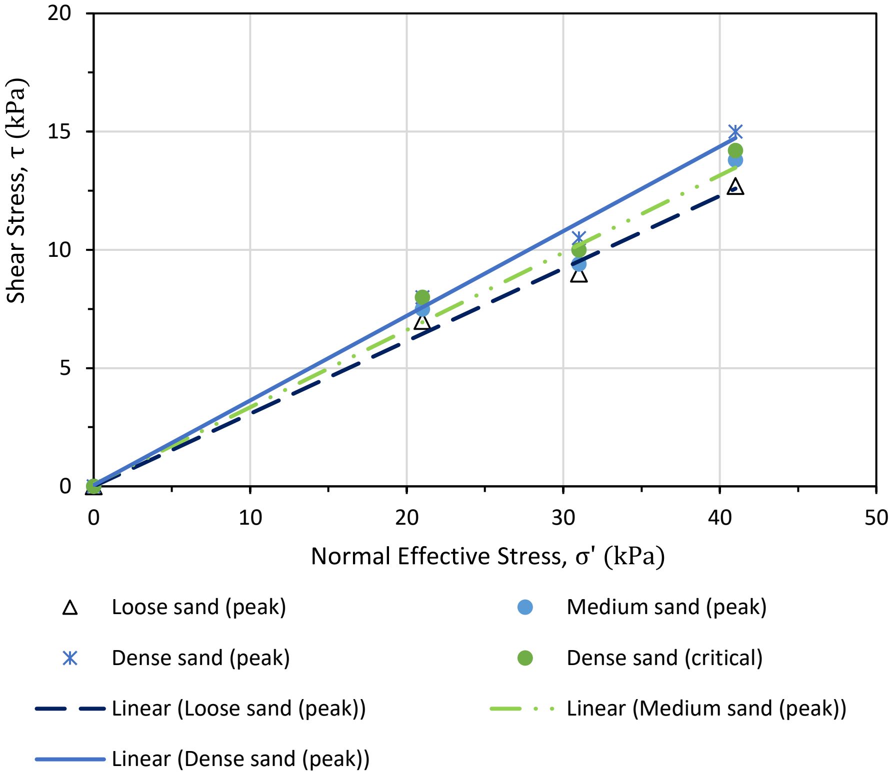

Figure 3-20: Shear stresses versus normal effective stresses for sand-steel interfaces at different sand relative densities.

3.5 Model Piles Specifications and Loading Procedure

The experimental testing programme was designed and performed to examine the uplift and the compression bearing capacity of model piles embedded in cohesionless soil. Precast concrete piles, steel closed-ended, and steel open-ended piles were used with a 40mm square profile for concrete piles and circular profile for steel piles. In addition, the pile embedment length-to-diameter ratios, measuring 12, 17 and 25 were used to investigate the behaviour of rigid and flexible piles (Reddy and Ayothiraman, 2015). The concrete piles were characterised by a Poisson's ratio (ν) of 0.2 and Young's modulus (*E*) = 30GPa. In addition, the steel piles were characterised by a Poisson's ratio of 0.3 and *E*

= 200GPa, which is highly comparable to the suggested material values for steel and concrete as reported by Gere and Timoshenko (1997).

A spirit level with an accuracy of ± 0.5° was used to confirm the pile verticality before each pile-load test. The effective pile lengths (Lc) of 480mm, 680mm and 1000mm were considered plus a freestanding length of 50mm to avoid contact of the soil with the pile cap. This would also confirm that the pile bearing capacity measured from the test was due only to the soil-pile interaction, thus avoiding any contact between the applied load and the soil surface. For the loads mechanically applied to the piles, the compressive and uplift loads were applied at a displacement rate of 1mm/min as specified by Bowles (1992) and within the acceptable ranges specified by BSI (BS EN 8004:1986), using a hydraulic loading system connected to a double acting (compression/tension) manufacturer calibrated load cell, type (DBBSM) having a maximum capacity (uplift and compression) of 10kN. To confirm the accuracy of the adopted load cell, the load cell was also experimentally calibrated by applying known loads (uplift and compression loads) using a Tinius Olsen computerised testing machine (see Figure 3.21), under repeated, static, and sustained loading. The load cell was secured between the loading head and the electric-hydraulic driving system. A double acting electric-hydraulic ram control system, model (ZE3408E-T), assembled at the top of the testing frame, was utilised for pile installation at a controlled driving rate. Moreover, loads were applied directly to an aluminium pile cap of 20mm thickness and 150mm diameter, this was used to confirm that the applied loads were consistently distributed over the pile head. It is worth noting that specific attention was given to minimise load eccentricity, and a spherical ball bearing system, acts as a universal joint, was included in the loading mechanism and utilised on the top of the loading head to overcome eccentricity issues.

A data acquisition system with a resolution of 16-bit has been used to record the applied load and the pile head settlement during the experimental tests. The data logger contains an analogue to digital converter to monitor and receive the experimental signals of pile applied load and corresponding settlement, and an SD memory card to store the results of pile load tests. Then the information stored on the memory card was then transferred to a PC for analysis. Furthermore, two full-bridge strain gauge type displacement transducers of very high-resolution ±0.15 at 150mm stroke capacity were utilised to measure the pile settlement, as depicted in Figure 3.22. A general arrangement of the vertical loading apparatus is illustrated in Figure 3.2.

Furthermore, a mechanical lock has been incorporated in the pile loading system (Figure 3.23). This was designed to ensure the fixity and to ensure pile verticality without tilting during the installation process. Horizontal levels of the pile cap were monitored until reaching final effective length of penetration. For the pile settlement, two magnetic stands were used and secured at the sidewalls of the pile-testing chamber. This was adopted to hold the transducers on the top of the pile cap in pairs so that the influence of bending can be precisely accounted for. The piles were axially loaded with the next load applied when the pile settlement had stabilised. Details of the experimental testing programme are summarised in Tables 3.2, 3.3 and 3.4, respectively.

Table 3-2: Model concrete pile specifications used in the experimental testing programme.

Test ID	Pile Slenderness Ratios (Lc/d)	Diameter (mm)	Sand Density	Test type
C RC1-1	12	40	loose	Compression
C RC1-2	17	40	loose	Compression
C RC1-3	25	40	loose	Compression
C RC1-4	12	40	medium	Compression
C RC1-5	17	40	medium	Compression
C RC1-6	25	40	medium	Compression
C RC1-7	12	40	dense	Compression
C RC1-8	17	40	dense	Compression
C RC1-9	25	40	dense	Compression
T RC1-1	12	40	loose	Uplift
T RC1-2	17	40	loose	Uplift
T RC1-3	25	40	loose	Uplift
T RC1-4	12	40	medium	Uplift
T RC1-5	17	40	medium	Uplift
T RC1-6	25	40	medium	Uplift
T RC1-7	12	40	dense	Uplift
T RC1-8	17	40	dense	Uplift
T RC1-9	25	40	dense	Uplift

Table 3-3: Model steel closed-ended pile specifications used in the experimental testing programme.

Test ID	Pile Slenderness Ratios (Lc/d)	Diameter (mm)	Sand Density	Test type
C SC 1-1	12	40	loose	Compression
C SC 1-2	17	40	loose	Compression
C SC 1-3	25	40	loose	Compression
C SC 1-4	12	40	medium	Compression
C SC 1-5	17	40	medium	Compression
C SC 1-6	25	40	medium	Compression
C SC 1-7	12	40	dense	Compression
C SC 1-8	17	40	dense	Compression
C SC 1-9	25	40	dense	Compression
T SC 1-1	12	40	loose	Uplift
T SC 1-2	17	40	loose	Uplift
T SC 1-3	25	40	loose	Uplift
T SC 1-4	12	40	medium	Uplift
T SC 1-5	17	40	medium	Uplift
T SC 1-6	25	40	medium	Uplift
T SC 1-7	12	40	dense	Uplift
T SC 1-8	17	40	dense	Uplift
T SC 1-9	25	40	dense	Uplift

Table 3-4: Model steel open-ended pile specifications used in the experimental testing programme.

Test ID	Pile Slenderness Ratios (Lc/d)	Diameter (mm)	Sand Density	Test type
C SO 1-1	12	40	loose	Compression
C SO 1-2	17	40	loose	Compression
C SO 1-3	25	40	loose	Compression
C SO 1-4	12	40	medium	Compression
C SO 1-5	17	40	medium	Compression
C SO 1-6	25	40	medium	Compression
C SO 1-7	12	40	dense	Compression
C SO 1-8	17	40	dense	Compression
C SO 1-9	25	40	dense	Compression
T SO 1-1	12	40	loose	Uplift
T SO 1-2	17	40	loose	Uplift
T SO 1-3	25	40	loose	Uplift
T SO 1-4	12	40	medium	Uplift
T SO 1-5	17	40	medium	Uplift
T SO 1-6	25	40	medium	Uplift
T SO 1-7	12	40	dense	Uplift
T SO 1-8	17	40	dense	Uplift
T SO 1-9	25	40	dense	Uplift

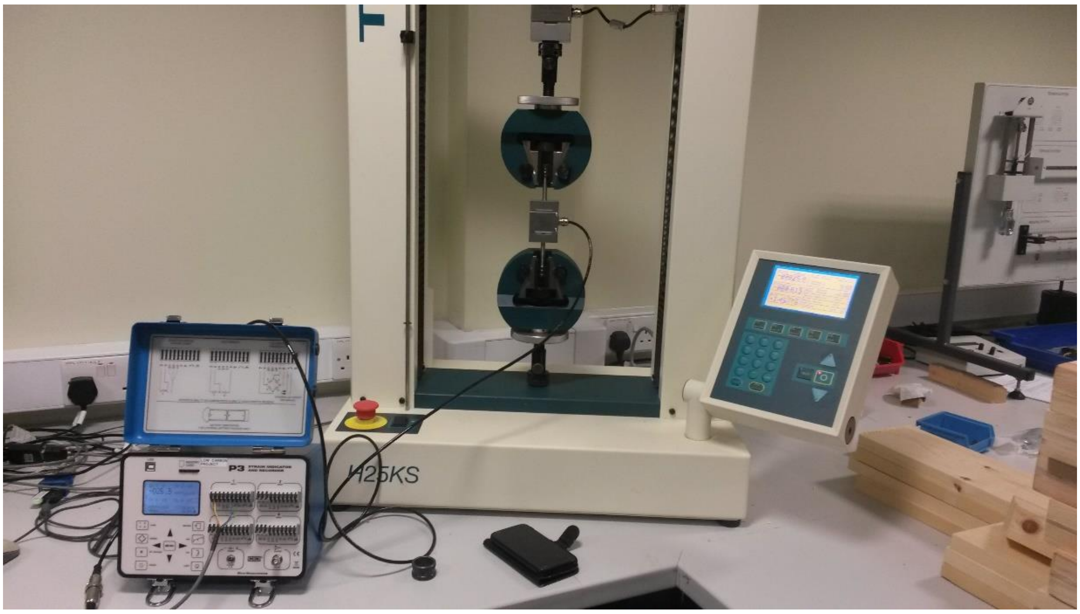

Figure 3-21: Illustrates the load-cell clibration process.

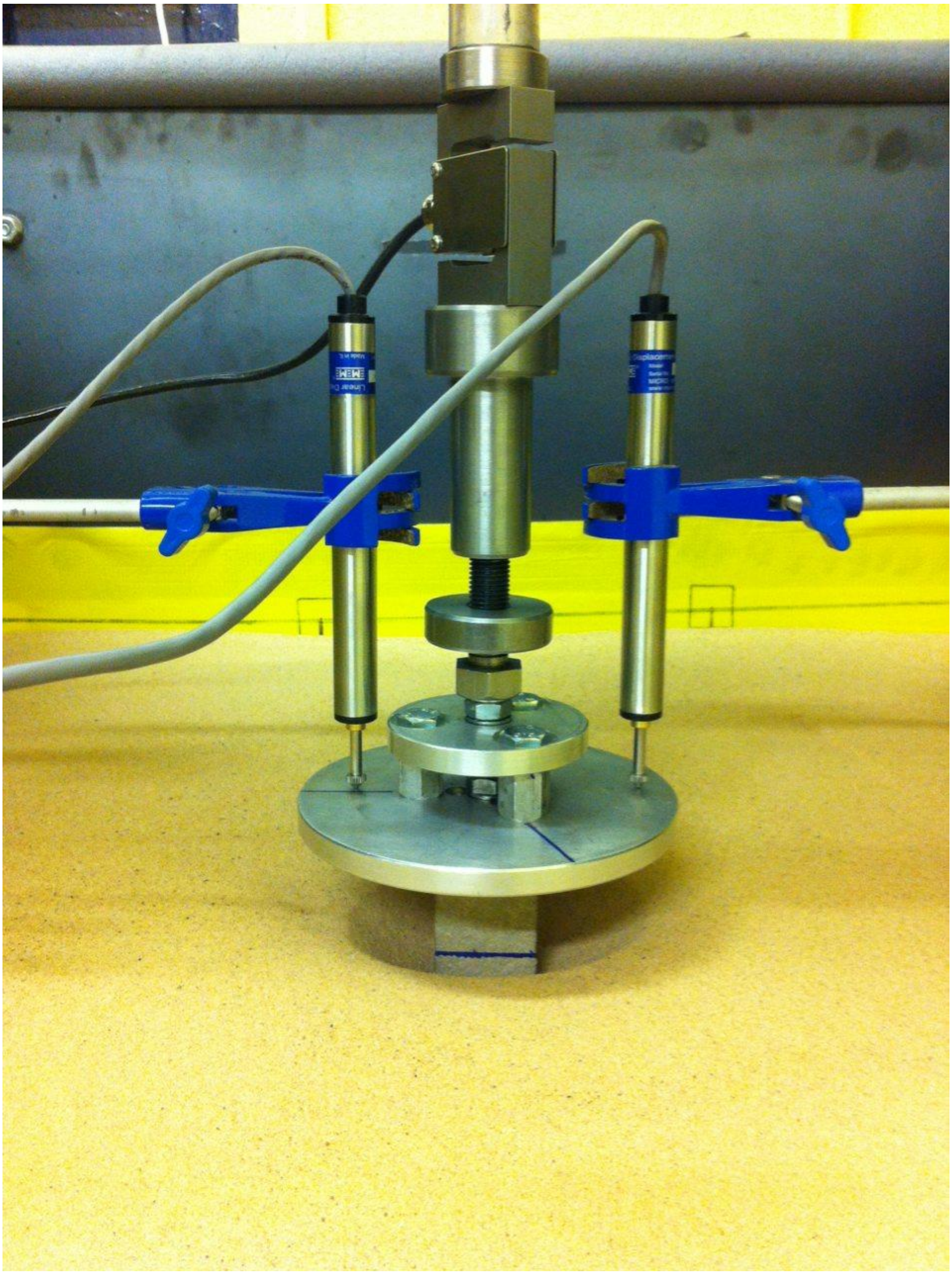

Figure 3-22: Details of pile settlement instrumentation and recording system.

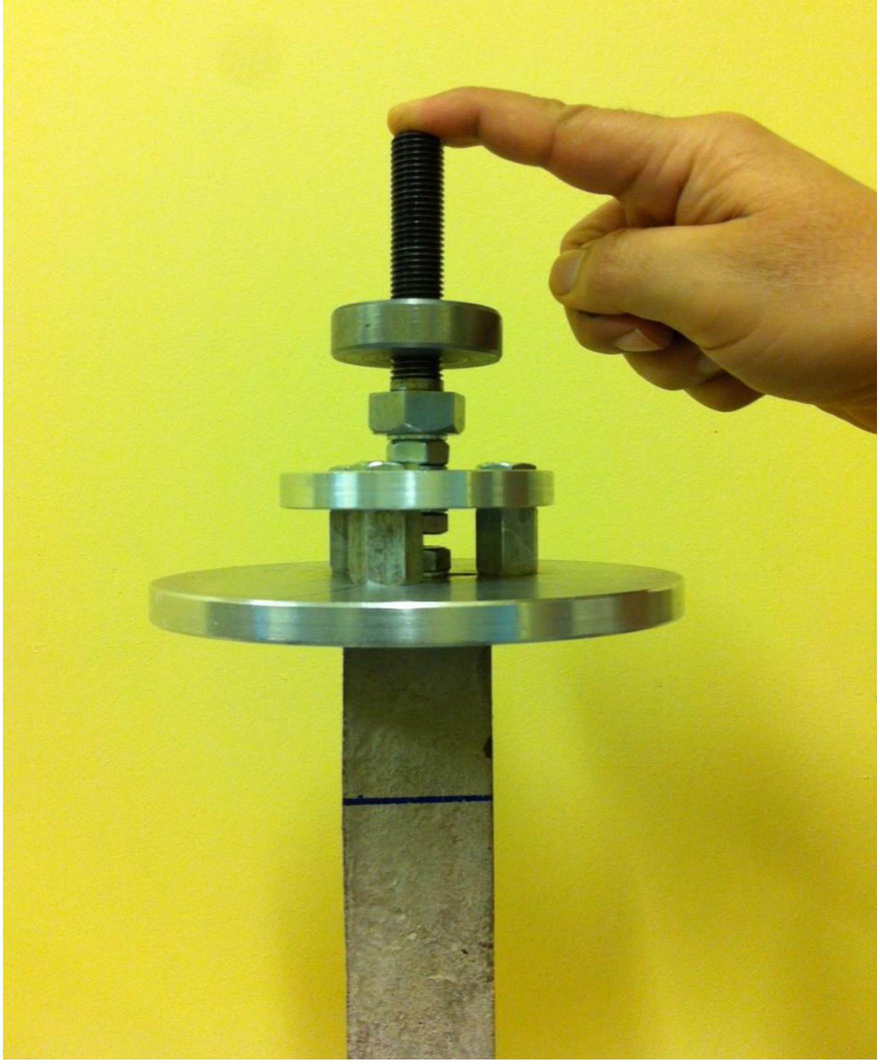

Figure 3-23: Details of the aluminium pile cap used in the loading system.

3.6 Characterisation of Concrete Mix

The concrete mix design for the model concrete piles has been formulated to determine the optimum water-cement ratio (w/c) for the concrete model piles using the compressive strength of concrete cubes(f_c'). The aggregate mixture gradation of the coarse and fine fractions were within the zone of 1-7mm and 0-3mm, respectively. The concrete utilised to formulate the piles has been prepared from Portland cement type II (CEM-II), coarse aggregate, fine aggregate, super-plasticiser, and water using the concrete mixture proportions summarised in Table 3-5. It should be noted that the maximum size of the coarse aggregate specimen is recommended to be one fifth of the smallest concrete structural element (Kosmatka and Panarese, 1994). In this context, the maximum size of the aggregate utilised in the concrete mixture was 7mm, which is less than the critical value (8mm) for a pile with 40mm diameter. This mix design was chosen to establish good workability and compaction of the concrete. Concrete cube specimens with dimensions of (150 x 150 x 150)mm have been prepared to determine the concrete strength development (BSI, BS EN 12390-2:2009). The concrete specimens were demoulded after 24 hours and then cured in water and tested at different curing times of 7, 21, and 28 days (see Table 3-5).

The concrete compressive strength was determined by applying a 0.2 MPa/s loading rate using the controls of compressive strength testing machine as shown in Figure 3.24. The concrete mixture was prepared using a Hobart concrete mixer according to the requirement identified by BSI (BS EN 196-1:2005) for concrete cube preparation. The concrete model piles were prepared using a new adjustable mould with inside dimensions of 40 x 40mm as revealed in Figure 3.25. The adjustable lengths of 530mm, 730mm and 1050mm, respectively were devised according to the concrete pile effective length.

Figure 3-24: Concrete compressive strength apparatus.

Table 3-5: Mix proportions and strength development of the concrete used in the experimental programme.

Material	Mix proportions (kg/m^3)	Compressive strength (MPa)	
Portland cement (CEM-II)	450	f'_{c-7}	21
Coarse aggregate	1050	f'_{c-21}	37
Fine aggregate	850	f'_{c-28}	41
Super-plasticiser	3.4		
Water	165		

Figure 3-25: Concrete pile casting.

3.7 Structural Fibres

This section describes the characterisation of the fibres used within the concrete mix design of the model piles. The concrete pile cross sectional dimensions were 40mm x 40mm with different pile embedment lengths, measuring 480mm, 680mm and 1000mm. However, two types of new fibres were used, as illustrated in Figure 3.26, and were investigated using different volume fractions to select the optimum percentage, increase the concrete performance, and to reduce the need for shear reinforcement. Additionally, these offer three-dimensional reinforcement, increase pile ductility, and overcome the limitations of casting such as concrete segregations associated with the casting of small concrete model piles. Details of the used fibres are summarised in the following sections.

3.7.1 Macro Synthetic Structural Fibres (SF) Type 1

It is well documented, by many scholars, that adding structural fibres at a specific volume fraction as reinforcement in a concrete mix, significantly enhance the mechanical properties of the concrete materials (Akdag and Özden, 2013; Mahmud et al., 2013). Randomly distributed fibres can offer a solution to low impact energy resistance and concrete cracking problems. Indeed, fibres increase the concrete energy absorption, and improve the flexural strength of the reinforced concrete pile since the applied fibres play a key role in delaying crack development (Baran et al., 2012).

In this study, two types of new SFs were utilised in different volume fractions and adopted to reduce the need for shear reinforcement. These fibres also offer three-dimensional concrete pile reinforcement and enhance the pile resistance to different types of loading systems by increasing the concrete ductility and its overall durability. They deliver high performance, cost savings, as well as health and safety advantages. The fibres have varying lengths ranging from 48mm up to 55mm with 0.7mm diameter, thus creating an improved reinforced concrete pile over the use of conventional fibres. Table 3.6 presents the chemical and physical properties of the fibres being used.

Table 3-6: Properties of the SF structural fibres used in the pile reinforcement.

Fibre property	Value	Tolerance	Remarks
Fibre length, (mm)	48-55	+/-2 mm	EN 14889-2
Equivalent diameter, (mm)	0.7	+/-0.03 mm	EN 14889-2
Slenderness ratio	69	+/-7 mm	EN 14889-2
Shape	Embossed elongated design		
Absorption rate, %	0		
Specific gravity, G_s	0.905		
Electrical conductivity, (S/mm)	0		
Colour	White		
Tensile strength, (MPa)	417	-31 MPa	EN 14889-2
Elastic modulus, (MPa)	5740	-574 MPa	EN 14889-2
Chloride content	0		

3.7.2 Micro Synthetic Structural Fibres (XT) Type 2

Micro synthetic (XT) fibre is the second type of the structural fibres that have been used in this research study. Using XT fibre leads to enhanced concrete durability and surface properties. This fibre is used as alternative to an air entraining agent (AEA), with a percentage of 1% of concrete volume, to increase the concrete’s resistance to the effect of freeze/thaw as well as to enhance the abrasion resistance of concrete in areas where high levels of chlorides will be encountered. Micro Synthetic (XT) fibre properties are illustrated in Table 3.7.

Table 3-7: Properties of the XT structural fibres that can be used as AEA.

Fibre property	Value
Material	100% Virgin Polypropylene
Fibre Length	Blended
Density, kg/m3	910
Absorption rate, %	0
Ignition Point, c˚	365
Electrical Conductivity, (S/mm)	Low
Design	Monofilament
Melt Point, c˚	160
Acid Resistance	High

Figure 3-26: Optimisation process of macro Synthetic structural fibres (SF) type 1 and Micro synthetic structural fibre (XT) type 2.

Furthermore, a series of flexural strength tests were conducted on beams with dimensions of 40 x 40 x 160mm. In total, forty-two rectangular simply supported concrete beams were tested using a three point loading configuration to provide a view of load-deformation distribution in the mid-section of the sample beams. The optimisation process involved different volume fractions, using Equation 3.3, ranging from 0.5, 0.75, 1, 1.25, 1.5 and 1.75% with 0 percent as a reference control as shown in Figure 3.27. The structural fibre was added continuously using dry-batch weights. Moreover, first crack strength, stress-strain behaviour and post cracking response were examined throughout the testing programme.

$$Absolute\ Volume = \frac{Weight\ of\ material}{Specific\ gravity\ of\ material * water\ unit\ weight} \qquad (3.3)$$

The experimental tests were run according to BSI (BS EN 12390-5:2009). It should be noted that the experimental testing programme was performed using a Tinius Olsen (TO) machine testing implementing the controlled displacement method as shown in Figure 3.28. Three beams and cubes were tested at a curing ages of 7 and 28 days. For the sake of brevity, the results of the crack propagation and the load-deflection behaviour of structural fibre reinforced concrete beams in comparison to plain concrete are shown in Figure 3.29. Figure 3.29 denotes a comparison between the average load-deflection results of structural fibre reinforced concrete (FRC) beams and plain concrete.

The results revealed that increasing the fibre percentage leads to an increase in the cracking energy capacity from 3200N to up to 5000N. In addition, the initial failure point "*first crack*" was about similar for all of the investigated mix proportions. However, the presence of fibres distributes the crack propagation after the first crack has appeared influencing the recovery and the ability to resist a higher applied load compared to the initial failure point. The use of the SFs had a remarkable influence in transforming the concrete mechanical properties from brittle to ductile behaviour. This was illustrated by the first failure crack being produced at lower loads (around 4010N) than subsequent cracks, reaching just over 5000N at deflection of 3.4mm in the optimised case of 1.25% as this fibre percentage represents the optimum fibre percentage that leads to ultimate applied load with remarkable energy absorption.

Figure 3-27: Casting process of RC beams using structural fibres (SF & XT).

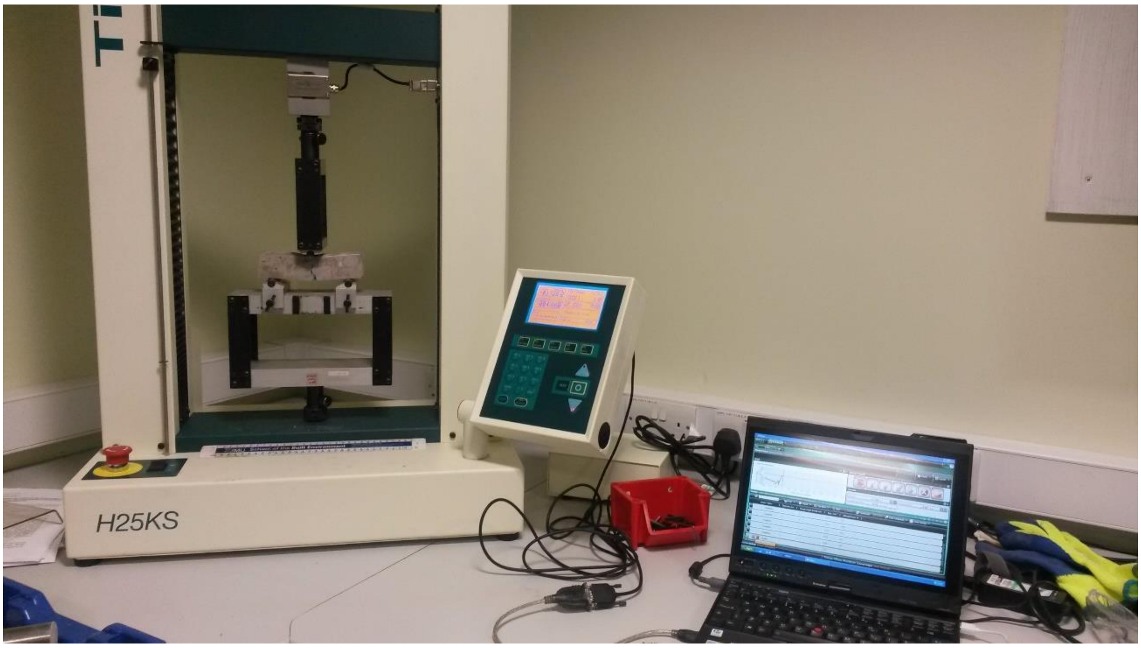

Figure 3-28: Beam testing setup using a Tinius Olsen testing machine.

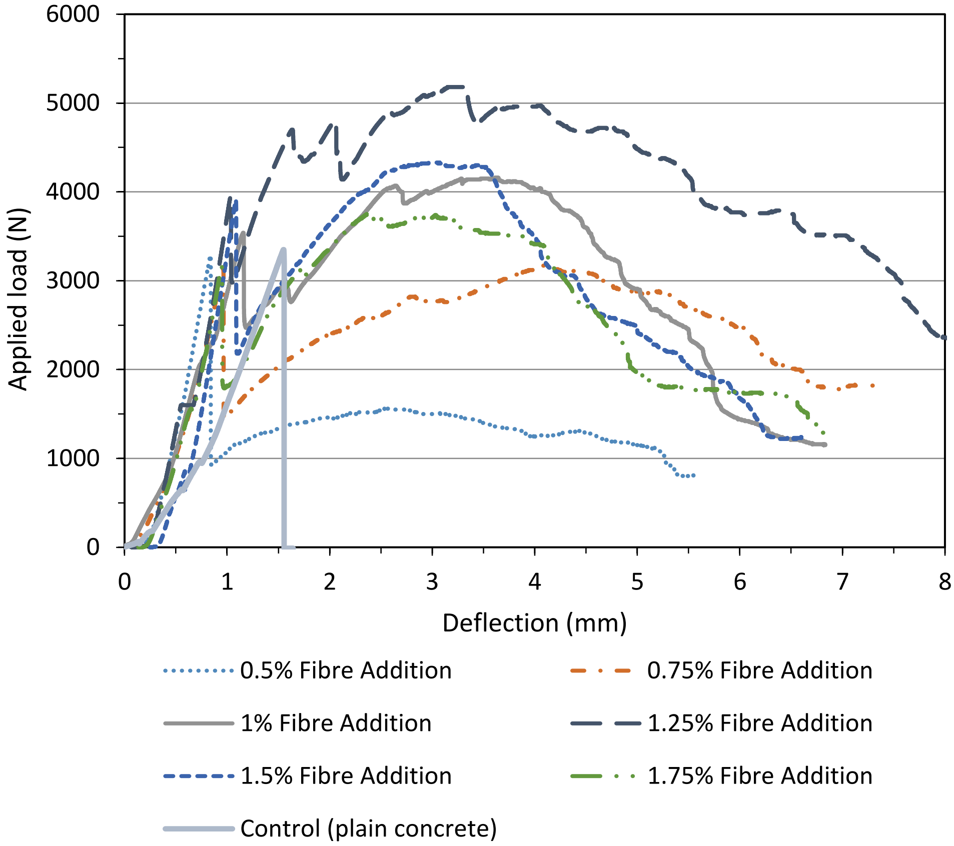

Figure 3-29: Shows the load-deflection results for the concrete beams reinforced with structural fibres at different volume fractions.

3.8 Summary

This section of the chapter described, in detail, the techniques that were used in the testing programme. It is intended to provide the reader with a concise illustration of the experimental methodology used in this study.

The overall pile testing system comprised of the following items as listed below:

- Pile testing calibration chamber.
- The testing frame.

- Pile driving system (double acting hydraulic ram).
- Loading mechanism system.
- Data acquisition system (recording data logger system with a 16-bit resolution).
- Characterisation of the sand used throughout the testing programme.
- Model piles (pile geometry, pile materials, and pile penetration length).

The dimensions of the pile-testing chamber were decided according to the soil effective stress zone from the foundation edge and it within the standard criteria (see section 3.2). The testing system also involved measurements located at the pile cap (i.e. displacement transducers) and a load cell type (DBBSM S-Beam). A 16-bit resolution data acquisition unit was utilised to record the applied load and associated pile head settlement. Moreover, details of the model piles testing were given in Table 3.2. Information regarding the sand properties and preparation methods of sand densities were summarised and discussed in section 3.3. Through the direct shear box testing, it has been proven that the sand-sand angle of friction, the peak friction angle, and the sand-pile interface friction angle depends primarily on the sand density. Regarding the use of two types of structural fibres, details in section 3.7. The utilisation of structural fibres has been proven to be advantageous in the concrete model piles as it significantly improves the shear strength behaviour and indeed promotes economy, since fibre reinforced concrete could be designed with minimum shear enforcement. The results of the load-deflection flexural tests confirmed that fibre inclusion in concrete at 1.25% by concrete volume could be recommended as the optimum fibre percentage that substantially increased the flexural strength of the concrete beam when compared to non-reinforced beams.

CHAPTER 4

Results and Discussion: Load-Settlement Curves for Precast Concrete, Steel Closed-ended and Steel Open-ended Piles Subjected to Compression Loads

4.1 Introduction

This chapter presents and discusses the experimental results of the pile-load tests along with the predicted results using the LM training algorithm. In addition, comparisons have been made between the employed training algorithm with the results of experimental pile load-test, and with those specified by a number of conventional methods. A comprehensive statistical analysis study for the dataset gathered from the experimental testing programme is also presented and discussed. The results of load distribution curves are clearly summarised in three phases; series (i) presented and discussed the results of the precast concrete piles along with the modelling and statistical approach, series (ii), and series (iii) show the graphical results of the of the steel closed-ended piles and steel open-ended piles compared with the computational methods. Additionally, details of the Levenberg-Marquardt (LM) model development, along with the assessment of the relative importance “*Beta values*”, the statistical significance “*Sig values*” study are also presented and discussed. To evaluate and verify the efficiency of the introduced approach, comparisons have been made between the results of the employed training algorithm with experimental pile load-test values, and with those specified by a number of conventional methods as detail in the following headings.

4.2 Development of the Trained LM Model for Model Piles Subjected to Compression Loads

One of the primary aims of this study is to develop and train a reliable predictive model using the LM algorithm to fully capture the pile load-settlement response with high efficiency. As mentioned previously, the proposed training algorithm is a data driven computing tool, which, could be used when the relationship between model input and output parameters is complex (Nguyen-Truong and Le, 2015). In addition, the LM algorithm has the ability to capture the nonlinear functions, and apply the substantial computer capacity to implement extremely iterated work (Yadav et al., 2014). Interest in the use of the computational intelligence has been steadily increasing in the last few years (Zhou et al., 2017). It should be stressed that one of the obvious advantages of the LM method is that no training internal parameters are required to be modified during and after the training process. This avoids many difficulties and barriers noted in the use of the classical algorithms such as the slow rate of convergence, adjusting learning epochs, learning rate and local minima (Deo and Şahin, 2015). In addition, the LM algorithm has been certified to be a faster training algorithm in comparison to other conventional machine learning algorithms. Therefore, it has been considered as a superior data-driven algorithm to provide accurate solutions for complex non-linear problems such as the one considered in the current study.

In the current study, supervised LM algorithm trained via Multilayer Feed-forward Back propagation has been developed and applied. This sort of ANNs comprises of fully interconnected parallel neurons or processing elements (PEs), which are connected in three layers, following the order: the input layer, the hidden layer(s) and finally the output layer(s), as described in Figure 4.1. One fact of significant importance is that, the optimum configuration of these layers is identified utilising a number of steps. More specifically, these phases can be summarized as: (i) the number of model input parameters, (ii) the optimum number of hidden layers, (iii) the number of model outputs, (iv) the number of processing elements (PEs), (v) the measuring performance indicators, (vi) type of the activation function (linear and/or nonlinear). One of the most important features, which plays a key role in the performance of the proposed training algorithm is the type of training algorithm (Xu et al., 2017). Indeed, after the configuration of the model, there are other important aspects that must be clearly defined such as a function of normalisation, and the method for dataset division in an attempt to avoid over fitting and to ensure good generalization ability of the trained network (Hagan et al., 1996).

The aforementioned parameters are presented and discussed as follows:

(i) The number of model input parameters: Identification of the most effective input parameters has been stated by many scholars to play a substantial role in the efficiency of the developed network (Mohammadi et al., 2016). In the present research, a comprehensive statistical analysis has been carried out in order to categorise the most significant input parameters that influence the model output as well as the contribution level of each IV, based on certain conditions recommended by Pallant (2011). It is worth noting that the statistical analysis was performed using SPSS-24 software. More details about the model input parameters and the statistical significance of each model parameter are given in sections 4.2.1 and 4.2.2.

(ii) The optimum number of hidden layers: The selection of the optimal number of the nodes or neurons is vital to a successful training process as the trained LM algorithm is sensitive to this number. If the number of neurons in the hidden layer is less than the required limit, the network is too parsimonious in the utilisation of its parameters, consequently the algorithm performance could deteriorate below that of the applicable number. Whereas, if the number of the neurons is excessive, there is danger of over fitting with no substantial improvement during the training process (Abdellatif, 2013). Following the data pre-processing, the optimal structure of the LM model has been selected at a topology of 5:10:1 (input parameters: number of hidden neurons in one hidden layer: output layer). Therefore, in this study, the developed network was trained with a single hidden layer, as illustrated in Figure 4.2. The choice was according to the fact that the reliability of such an ANN model has been well documented in several relevant studies (Mareš et al., 2016; Jebur et al., 2018b).

(iii)The number of outputs: In this study, one output was selected in the trained network.

(iv)The number of processing elements (PEs): A neuron receives input signals ($x_i^1, x_i^2, x_i^3, \ldots\ldots x_i^n$) from adjacent or an external source a neuron and transforms them to an output signal via a transfer function. 10 neurons were used to correlate the nonlinear functions between the input and output layer. This optimum number of neurons was selected by minimizing the error percentage on a testing dataset using a trial-and-error method (Stojanovic et al., 2016).

(v) Measuring performance indicators: The accuracy indicators of the trained LM algorithm were firstly assessed during the learning or training process. The optimum model performance was statistically evaluated utilising the following metric skill indicators with a minimum error between the target and predicted values. The Mean square error (MSE), correlation coefficients (R and p), and root mean square error (RMSE) functions are determined via Equations 4.1, 4.2, and 4.3. The aforementioned statistical indicators were used in this study, as they are the main standards that are frequently utilised to measure the network performance (Nejad and Jaksa, 2017; Erdal, 2013). The RMSE is the most common measure of error. It has the particular merit that small errors receive less attention than large errors (Jebur et al., 2018a). The optimum value of the correlation coefficient (R) is unity, which indicates that a perfect consistency is achieved between the measured and the predicted values (Alkroosh et al., 2015).

$$MSE = \sqrt{\frac{1}{N}\sum_{i=1}^{n}(T_i - \bar{T}_i)^2} \tag{4.1}$$

$$R = \left[\frac{\sum_{i=1}^{n}(T_i - \bar{T})(P_i - \bar{P})}{\sqrt{\sum_{i=1}^{n}(T_i - \bar{T}_i)^2 \sum_{i=1}^{n}(P_i - \bar{P})^2}}\right]^2 \tag{4.2}$$

$$RMSE = \sqrt{\frac{1}{N}\sum_{i=1}^{n}|T_i - P_i|} \tag{4.3}$$

in which N denotes the number of the dataset; T_i and P_i are the targeted and computational values; $\bar{P}$ and $\bar{T}$ are the mean of the predicted and targeted values; R is the correlation coefficient.

(vi) Type of activation function: Activation or transfer functions to simulate nonlinear relationships are necessary for transferring weighted sums from each processing element to processing elements in the next layer. In this study, tangent-sigmoid the *"tansig"* transfer function is applied in the hidden layer and a linear *"purelin"* function is employed in the output layer, this is in agreement with an earlier study (Deo et al., 2017).

(vii) The training algorithm: The supervised, self-tuning LM training algorithm was applied to train the developed network. This training algorithm is one of the fastest back-propagation algorithms and is highly recommended as the first choice of supervised algorithm. One of the distinctive features of this approach is the high rate of convergence of the constructed model (Sollazzo et al., 2017; Jebur et al., 2018b). In addition, this method is normally applied to get a quick learning time and high generalisation ability has been recommended (Stojanovic et al., 2016). To this end, the LM training algorithm was used in the present study. Moreover, the employed algorithm is that it is self-tuning (does not comprise user dependent parameters at each application) as well as being certified to be 10 to 100 times faster and a more stable training algorithm in comparison to other conventional machine learning algorithms (Wilamowski and Yu, 2010).

(viii) The function of normalisation: data normalisation, through which the IVs and the target attain values within the range (0,1), is advisable in system modelling to smooth the data, and to get a suitable rate of convergence (Gong and Ordieres-Meré, 2016). As part of this process, for each parameter with minimum and maximum values of x_{max} and x_{min}, the definition of the "normalised value" (x_i^{norm}) can be evaluated using Equation 4.4.

$$x_i^{norm} = \frac{x_{i(actual)} - x_{i(min)}}{x_{max} - x_{min}} \tag{4.4}$$

(ix) Data division: the total number of training datasets has a substantial influence on the robustness of the trained network (Stojanovic et al., 2016). The size of the training cluster is recommended as ranging between 60% and 80% of the total dataset by many scholars (Jaeel et al., 2016; Moayedi and Rezaei, 2017; Kumar and Basudhar, 2018). In the context of this research, the total dataset values were randomly divided into three main clusters; comprising of training 70%, testing at 15% and validation at 15%. The training subset goal is to determine the network strength by updating the connections weights and biases values during the learning process. The testing subset was located to check the reproducibility and the generalisation ability of the proposed algorithm. It should be noted that the testing dataset was not involved during the training and it is usually used to evaluate the reliability of the algorithm being trained (Millie et al., 2012; Sun et al., 2014). Finally, the cross-validation subset was piloted to assess the model performance, and to terminate the process of learning to avoid over fitting at a minimum value of the mean square error (MSE) (Tarawneh, 2017).

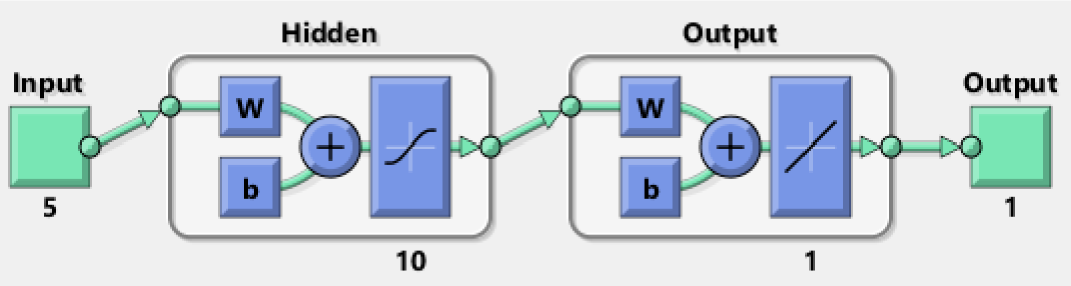

Figure 4-1: Topology of the trained LM model.

4.2.1 Model Input and Output

Identifying the most influential factors affecting pile bearing capacity and settlement is important in order to accurately develop a reliable model (Yadav et al., 2014). Introducing a large number of input parameters to any ANN model contributes in increasing the required data size to efficiently estimate the appropriate connection weights and decreases the connection speed (Maier and Dandy, 2000). Most of the traditional approaches comprise (i) pile material; (ii) pile geometry; (iii) applied load and (iv) properties of the soil. In this research, an innovative statistical significance analysis using multiple regression technique (MRT) was developed to select the most effective parameters and to underline the contribution of each IV to the dependent output. This technique has been utilised because it has many merits (Hashim et al., 2017a). For instance, it has the ability to explore the relationship between one IV to a set of independent variables (IVs) (Hashim et al., 2017c). However, based on the aforementioned method, five factors, for all model piles were considered to play a substantial role in pile settlement, with a statistical significance (Sig.) value of < 0.05, matching the statistical criteria (Field, 2008; Pallant, 2011). These parameters are (i) applied load (*P*), (ii) pile slenderness ratios (Lc/d), (iii) pile axial rigidity (EA), (iv) pile embedded length (Lc) and (v) the sand-pile interface friction angle (δ). EA was included in the model input parameters since it affects the results of the model output as demonstrated in the statistical analysis. In addition, the parameter EA has been identified to play a key role on pile settlement (see section 2.6).

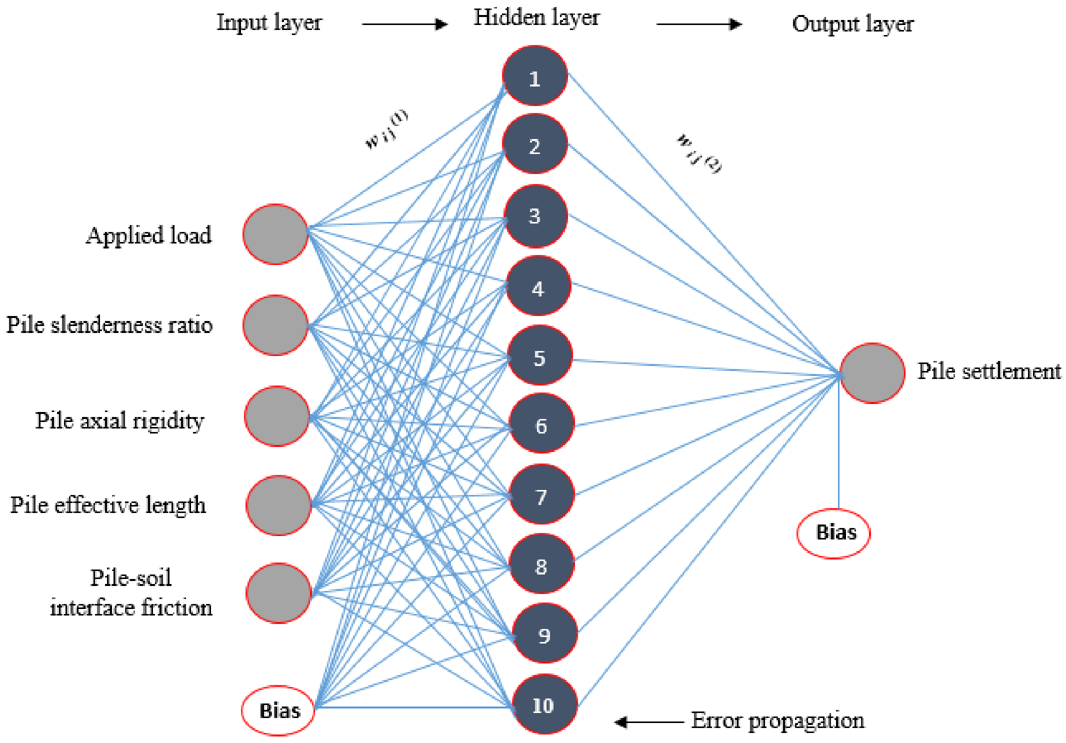

Figure 4-2: Sketch of the optimised ANN topology.

4.2.2 Statistical Significance of Independent Variables (IVs)

The level of contribution or strength of each of the independent variables (IVs) to the model output has been ascertained by calculating the relative importance parameter, or Beta value. Statistically, the closer to 1.0 the absolute Beta value is, the more significant the impact of that IV on the model being developed (Pallant, 2011; Hashim et al., 2017b). Tables 4.1, 4.2 and 4.3 display that the applied load and the sand-pile interface friction angle have been identified as making high contributions to the model output. While, the results demonstrated that pile slenderness ratios, pile length, and axial rigidity made a lesser contribution to the model output.

4.2.3 Outliers

An outlier can be defined as a case with such an extreme value for one variable (a univariate outlier) or strange combinations of scores on two or more variables (multivariate outlier) that it statistically distorts the model (Tabachnick and Fidell, 2013; Hashim et al., 2017b). The model generalisation ability can be highly influenced by the presence of such extreme points (Hashim et al., 2017c). Therefore, all IVs and dependent variables (DVs) must be statistically screened before the process of training. Based on the statistical criteria suggested by Tabachnick and Fidell (2013), the presence of outliers can be identified using the Mahalanobis distance (MD) value. In this study, the maximum MDs must be less than the critical value 20.52 as given in Table 4.4 (the maximum limit for five IVs (Pallant, 2011). For the experimental dataset, the highest MDs for the concrete piles dataset was found to be 22.83, which is higher than the values as given in Table 4.1. To check whether this exerts any influence on the results of the LM training algorithm as a whole, Tabachnick and Fidell (2013) recommended to calculate the Cook's Distance (COO_1). In any case, with COO_1 greater than 1.0 there is a potential problem. The statistical analysis results demonstrated that the Cook's Distance (COO_1) for the described point was found at 0.00344, which confirmed that the output results would not be influenced. For the steel closed-ended dataset, the max MD was determined at 21.48, while the Cook's Distance (COO_1) value for this point was found at 0.00911, which is less than the critical value. However, the presence of this point in the experimental data set will not influence the efficiency of the proposed model. Furthermore, for steel open-ended piles, the maximum MD was 17.63, which confirmed the absence of outliers in the observations being studied.

Table 4-1: Results of the statistical analysis for concrete piles.

IVs	Beta. value	MDs	COO_1
Applied load (P)	0.787	22.83	0.00344
Sand-pile angle of interface friction (δ)	0.613		
Axial rigidity (EA)	0.02		
Slenderness ratio (Lc/d)	0.139		
Pile length (L)	0.101		

Table 4-2: Results of the statistical analysis for steel closed-ended piles.

IVs	Beta. value	MDs	COO_1
Applied load (P)	0.840	21.48	0.00911
Slenderness ratio (Lc/d)	0.238		
Axial rigidity (EA)	0.015		
Pile length (L)	0.026		
Sand-pile angle of interface friction (δ)	0.718		

Table 4-3: Results of the statistical analysis for steel open-ended piles.

IVs	Beta. value	MDs
Applied load (P)	0.804	17.63
Sand-pile angle of interface friction (δ)	0.711	
Axial rigidity (EA)	0.015	
Slenderness ratio (Lc/d)	0.119	
Pile length (L)	0.088	

Table 4-4: Illustrates critical values of the MDs.

Number of model input parameters	Critical value of MDs	Number of model input parameters	Critical value of MDs
2	13.82	5	20.52
3	16.27	6	22.46
4	18.47	7	24.32

4.2.4 Data Size

The dataset size must be calculated in order to develop the best relationship between the IVs and the model output, and to obtain an efficient model performance (Pallant, 2011; Hashim et al., 2017c). For the five input parameters, according to the following formula (4.5), the minimum dataset size required to train the LM algorithm is 90 (Tabachnick and Fidell, 2013). In this study, the total number of recorded points form the experimental pile-load tests used to run the LM training algorithm are 254, 277 and 274 for concrete, steel closed-ended and steel open-ended piles, respectively. A summary of the statistical parameters for the training, testing and validation dataset, used to develop and train the LM for concrete, steel closed and open-ended piles subjected to compression loads, are given in Tables 4.3, 4.4, and 4.5, respectively.

$$N > 50 + 8 * IVs \tag{4.5}$$

where N and IVs denote the required size of the sample and number of independent factors to perform the LM training algorithm.

Table 4-5: Statistical characterisation of testing, training, and validation dataset for concrete piles.

Data Set	Statistical Parameters	**Input Variables**					**Output**
		Load (kN)	Slenderness ratio, Lc/d	Pile length, (m)	Pile axial rigidity, EA (MN)	Sand-pile friction angle, δ°	Settlement, (mm)
Training Set	Max.	6.782	25	1	47.2	36	14.416
	Min.	0.001	12	0.48	47.2	28.8	0.002
	Mean	2.13	17.28	0.72	47.2	26.26	6.14
	S.D.*	1.85	1.34	0.21	0.00	1.11	4.52
	Range	6.781	2.08	0.52	0.00	7.2	14.415
Testing Set	Max.	6.67	25	1	47.2	36	14.218
	Min.	0.001	12	0.48	47.2	28.8	0.003
	Mean	1.83	16.735	0.70	47.2	25.40	6.25
	S.D.*	1.93	1.365	0.22	0.00	1.128	4.52
	Range	5.67	13	0.52	0.00	7.2	14.215
Validation Set	Max.	6.73	25	1	47.2	36	14.30
	Min.	0.131	12	0.48	47.2	28.8	0.065
	Mean	2.39	18.06	0.68	47.2	26.32	7.13
	S.D.*	1.94	1.348	0.22	0.00	1.12	4.19
	Range	6.6	13	0.52	0.00	7.2	13.235

*Standard deviation

Table 4-6: Statistical characterisation of testing, training, and validation dataset for steel closed-ended piles.

Data Set	Statistical Parameters	**Input Variables**					**Output**
		Load (kN)	Slenderness ratio, Lc/d	Pile length, (m)	Pile axial rigidity, EA (MN)	Sand-pile friction angle, δ°	Settlement, (mm)
Training Set	Max.	4.426	25	1	251.18	19	14.461
	Min.	0.001	12	0.48	251.18	17	0.0015
	Mean	1.454	17.01	0.711	251.18	17.91	6.097
	S.D.*	1.363	1.345	0.211	0.00	1.05	4.591
	Range	4.425	2.08	0.52	0.00	2	14.49
Testing Set	Max.	4.350	25	1	251.18	19	14.215
	Min.	0.193	12	0.48	251.18	17	0.022
	Mean	0.683	18.323	0.767	251.18	17.783	5.860
	S.D.*	1.260	1.369	0.226	0.00	1.044	4.586
	Range	4.349	13	0.52	0.00	2	14.192
Validation Set	Max.	3.660	25	1	251.18	19	13.861
	Min.	0.084	12	0.48	251.18	17	0.002
	Mean	1.275	17.35	0.724	251.18	17.827	5.727
	S.D.*	1.098	1.347	0.213	0.00	1.049	4.521
	Range	3.576	13	0.52	0.00	1.117	13.814

*Standard deviation

Table 4-7: Statistical characterisation of testing, training, and validation dataset for steel open-ended piles.

		Input Variables					**Output**
Data Set	Statistical Parameters	Load (kN)	Slenderness ratio, Lc/d	Pile length, (m)	Pile axial rigidity, EA (MN)	Sand-pile friction angle, δ°	Settlement, (mm)
Training Set	Max.	4.260	25	1	251.18	19	14.450
	Min.	0.002	12	0.48	251.18	17	0.002
	Mean	1.251	17.17	0.717	251.18	17.91	5.952
	S.D.*	1.202	1.342	0.210	0.00	1.04	4.435
	Range	4.458	13	0.52	0.00	2	14.448
Testing Set	Max.	4.256	25	1	251.18	19	14.353
	Min.	0.002	12	0.48	251.18	17	0.0165
	Mean	1.233	17.24	0.724	251.18	17.836	6.207
	S.D.*	1.342	0.138	0.226	0.00	1.047	4.665
	Range	4.254	13	0.52	0.00	2	14.336
Validation Set	Max.	4.261	25	1	251.18	19	14.180
	Min.	0.211	12	0.48	251.18	17	0.449
	Mean	1.240	17.365	0.725	251.18	17.827	7.011
	S.D.*	1.118	1.352	0.216	0.00	1.049	4.609
	Range	4.050	13	0.52	0.00	1.117	13.731

*Standard deviation

4.3 Performance Analysis of the LM Algorithm for Concrete Model Piles Embedded in Loose, Medium and Dense Sandy Soil.

This part of the study details the results of the experimental versus predicted pile load-displacement and the criteria used to evaluate the performance of the proposed model. The measuring accuracy of the trained LM algorithm was firstly assessed during the learning process. To design and evaluate an optimal network topology, different statistical performance indicators were applied, for instance mean square error (MSE), coefficients of determination (R and p) and root mean square error (RMSE). They are considered as the main standards that are widely utilised to measure the network performance (Ahmadi et al., 2016; Zhang et al., 2016; Nejad and Jaksa, 2017; Erdal, 2013). However, the performance of the LM algorithm for each predictive model (concrete piles, steel closed-ended piles and steel open-ended piles) has been evaluated as clearly explained in the following sections:

4.3.1 Concrete Piles under Compression Loads

Understanding the analytical mechanism during the training process is vital for successful modelling. For this aim, the stages of testing, learning, and validation in model should be clearly described. Figure 4.3 shows the procedure of training LM through the aforementioned three stages. The results illustrated that the training process terminated when the validation errors number exceeded the allowed numbers, which were 6 sequential errors. As the learning process completed, there was a point considered by the network as the “optimal point”. At this point, although the values of training and testing errors are declining, the validation value increases from that point on. Hence, such points could be considered best validation performance; there the value of the MSE is 0.0025.

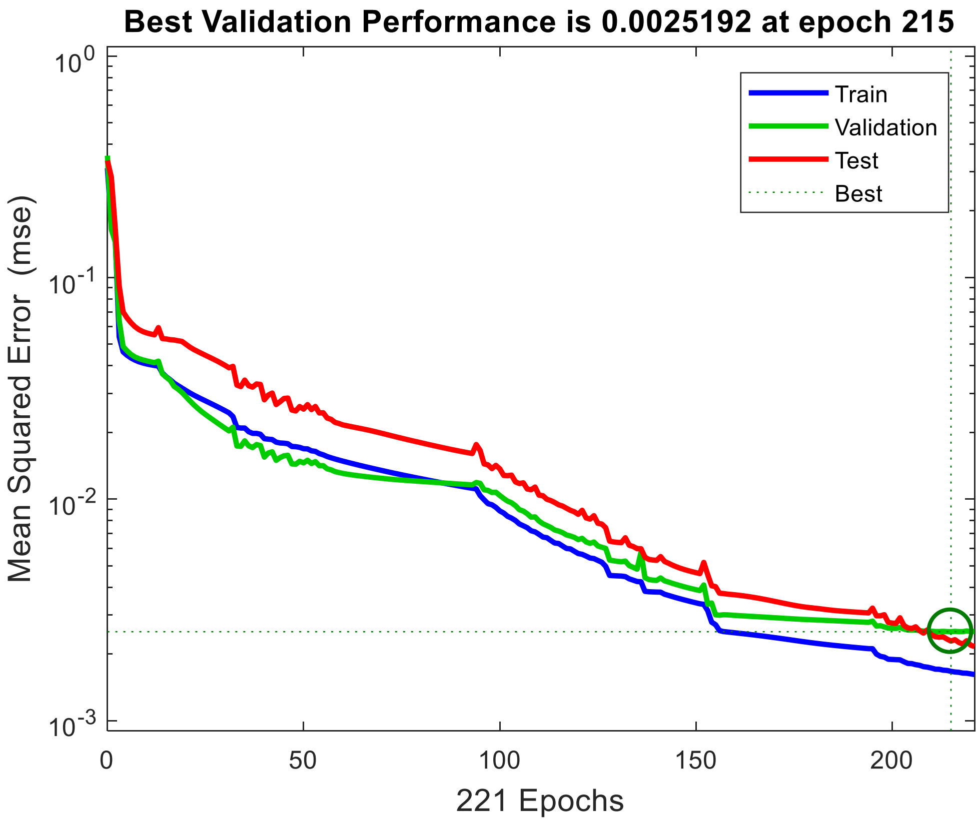

Figure 4-3: Performance plot of the LM algorithm for concrete developed model during the training process.

Furthermore, the corresponding change of gradient and the Marquardt adjustment factor (m_u), play a significant role in reduction the mean square error percentage. As revealed in Figure 4.4, the gradient error decreases and reaches 0.004. Notably, the m_u factor is decreased to negligible value ($1x10e^{-05}$) after a few epochs and the validation check increases to 6 at an epoch of 221. Moreover, Figure 4.5, presents the error histogram (EH) plot to obtain additional efficiency validation of network performance. The EH can also give an indication of outliers "*data features that appears to be inconsistent with other subsets observations*" (Yadav et al., 2014). Additionally, the conclusions drawn from the LM algorithm can be greatly affected by the presence of outliers (Tabachnick and Fidell, 2013; Hashim et al., 2017a). Thus, the training process is stopped once the validation error starts to increase. Moreover, it can be shown that the majority of data coincides with zero error line in the two central bins (-0.003 and 0.01).

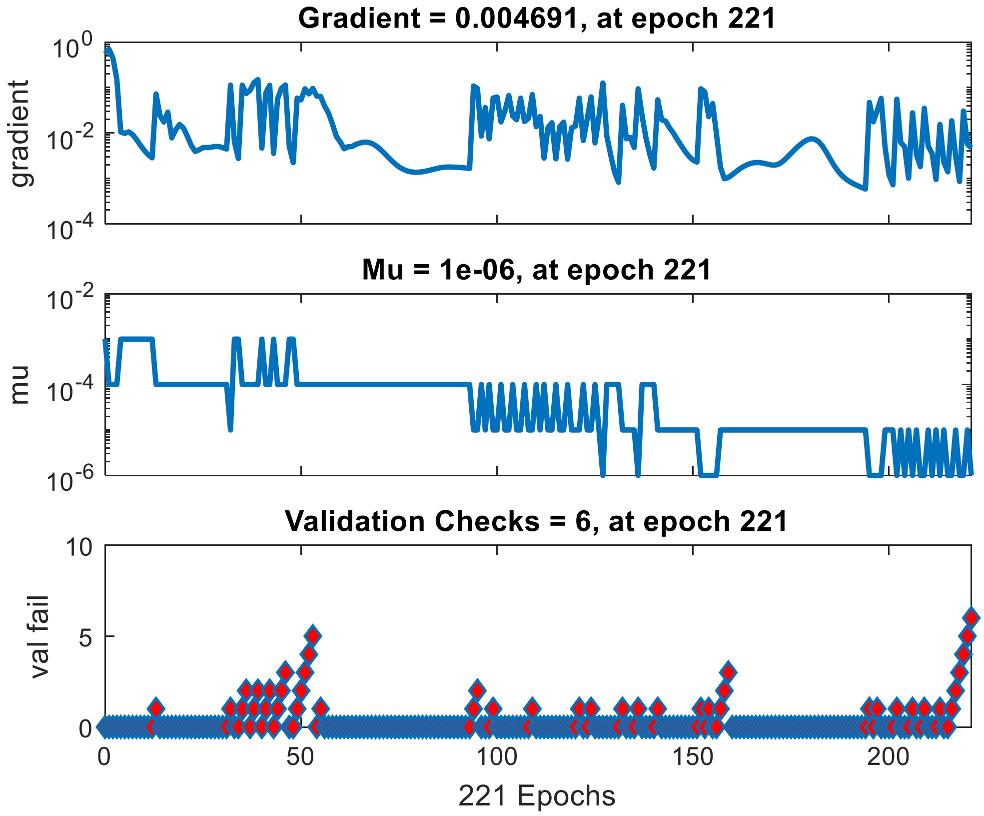

Figure 4-4: Gradient and maximum validation checks for the LM trained network.

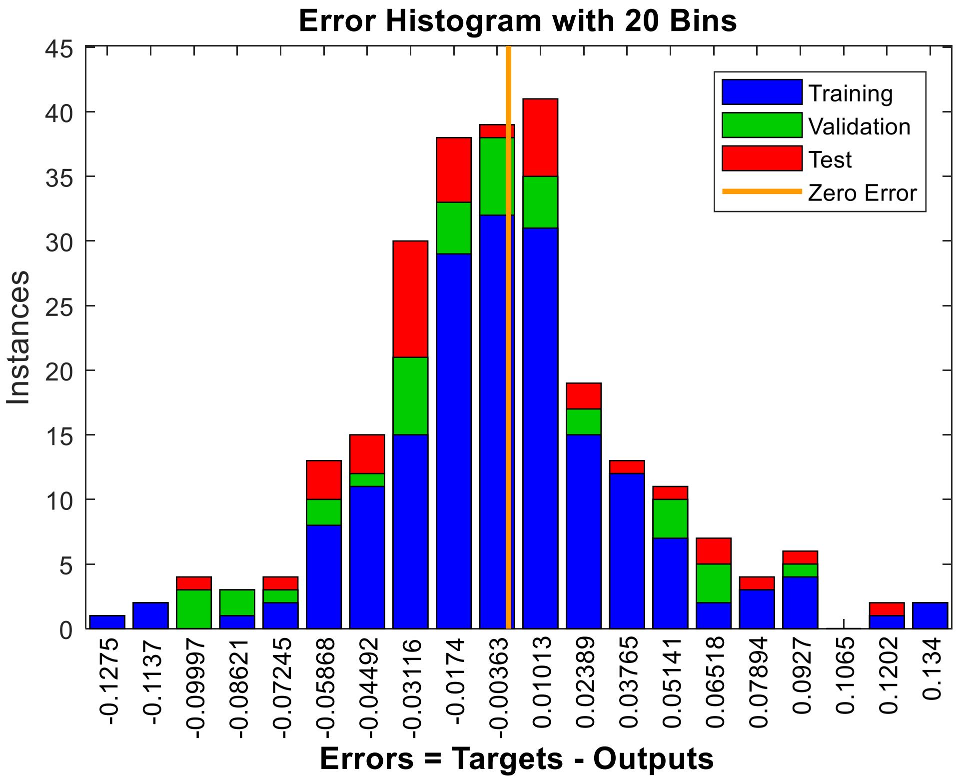

Figure 4-5: Plot of error histogram (EH) for the LM algorithm.

4.3.2 Measured Versus Predicted Pile Load Tests for Concrete Piles Subjected to Compression Load

The results of the experimental load-settlement tests and the predicted outcome using an evolutionary LM algorithm for the concrete model piles subjected to compression loads are discussed in this section. A series of experimental pile load tests were performed on model concrete piles. The testing programme consisted of three piles with slenderness ratios (Lc/d) of 12, 17 and 25 with square sections of 40mm to examine the behaviour of rigid and flexible piles. In total, 254 points were recorded from the experimental pile-load test data using a P3 strain indicator. Figures 4.6, 4.7, and 4.8 exhibit the extent of the match between the experimental and predicted load-carrying capacity of concrete piles subjected to axial load at different steps of mechanical loading. The pile load-settlement results are idealistic for pile foundations subject to axial mechanical loads, i.e., reducing from pile head to pile toe due to the increase in the developed shaft resistance and the point bearing. It is noteworthy that the plastic mechanisms involved in the effective soil surrounding the pile are the leading cause for the non-linearity of the load-settlement curves. The results revealed that the increase in the pile capacity could be clearly pronounced with an increase in the pile embedment length and sand stiffness. This is probably associated with an increase in the point bearing and the overburden pressures that lead to an increase in the mobilised skin friction resistance developed between soil-pile interactions in the adjoining zone of influence. As can be observed, the pile load carrying capacity behaviour exhibits a noticeable elastic response in the initial stages of loading until approximately 300N, 500N, and about 1000N in loose, medium, and dense sand. In addition, soil-yielding effect is clearly marked with increasing applied load, i.e., for a pile tested in loose sand, the effect of soil yielding can be underlined within the applied load ranges from 300 to 425N, 550 to 700N, and 725 to 950N for model piles in loose sand with Lc/d of 12, 17, and 25. The associated pile settlement decreases until reaching a maximum capacity at about 10% of the pile diameter following the pile load test failure criteria reported in BSI (BS EN 8004:1986).

Moreover, Figures 4.6 and 4.7 report the results of the load carrying capacity of model piles embedded in medium and dense sand. Similarly, an obvious elastic response can be seen in the initial stages of applied load until the pile settlement level is about 2.5% of the pile diameter. Beyond this settlement level, the foundation responses become non-linear, due to the occurrence of the plastic mechanism in the surrounding sand effective zone. With increasing values of applied load, the rate of pile settlement substantially increases before excessive settlement at approximately constant at loads of 1050, 1400, and over 2000N for piles embedded in medium sand and about 3200, 4400, and 6250N for piles with slenderness ratios of 12, 17, and 25 driven in dense sand. According to the graphical comparisons, for loose sand, the predicted results are slightly underestimated for the pile load-settlement curves in the case of pre-yield working settlement. It is apparent from the results that there is excellent fit between the proposed computational intelligence approach and targeted values in post-yield pile load tests responses (often the most important component for practicing engineers) This is supported with a correlation coefficient of 0.99 for all data, therefore it is plausible to conclude that the training algorithm is a reliable method to predict load-settlement curves.

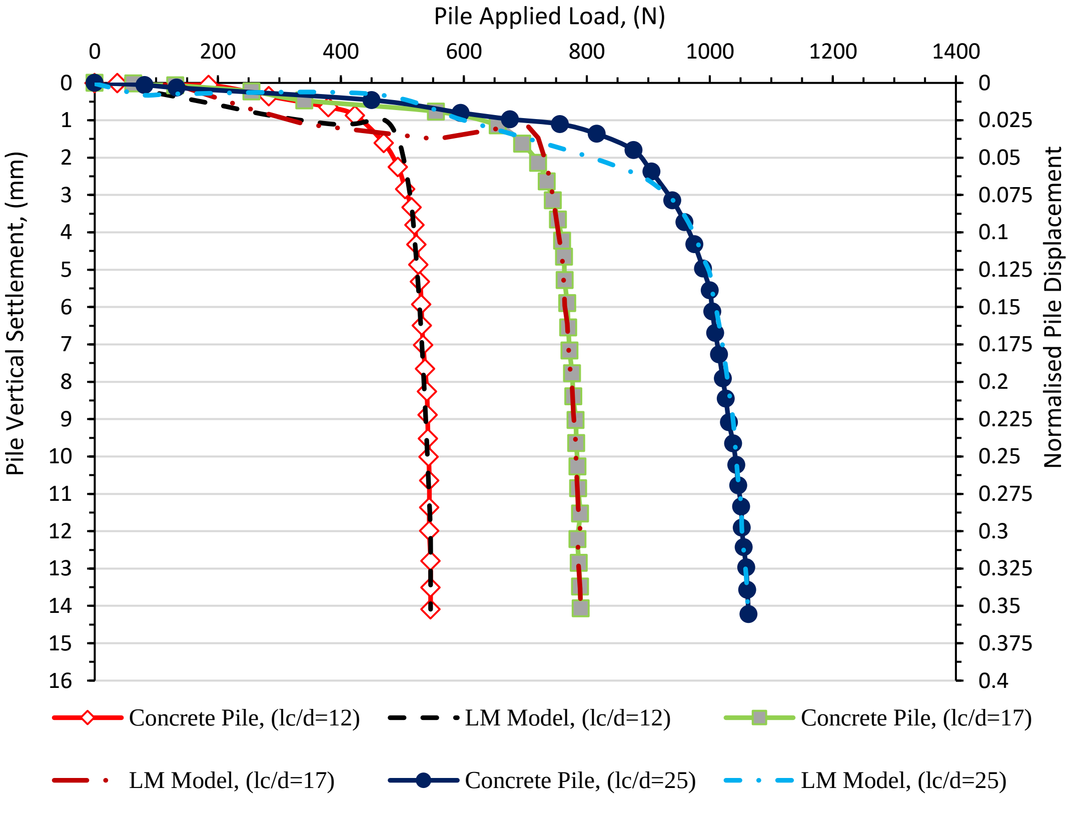

Figure 4-6: Comparison between measured versus predicted pile load-displacement tests for concrete piles embedded in loose sand.

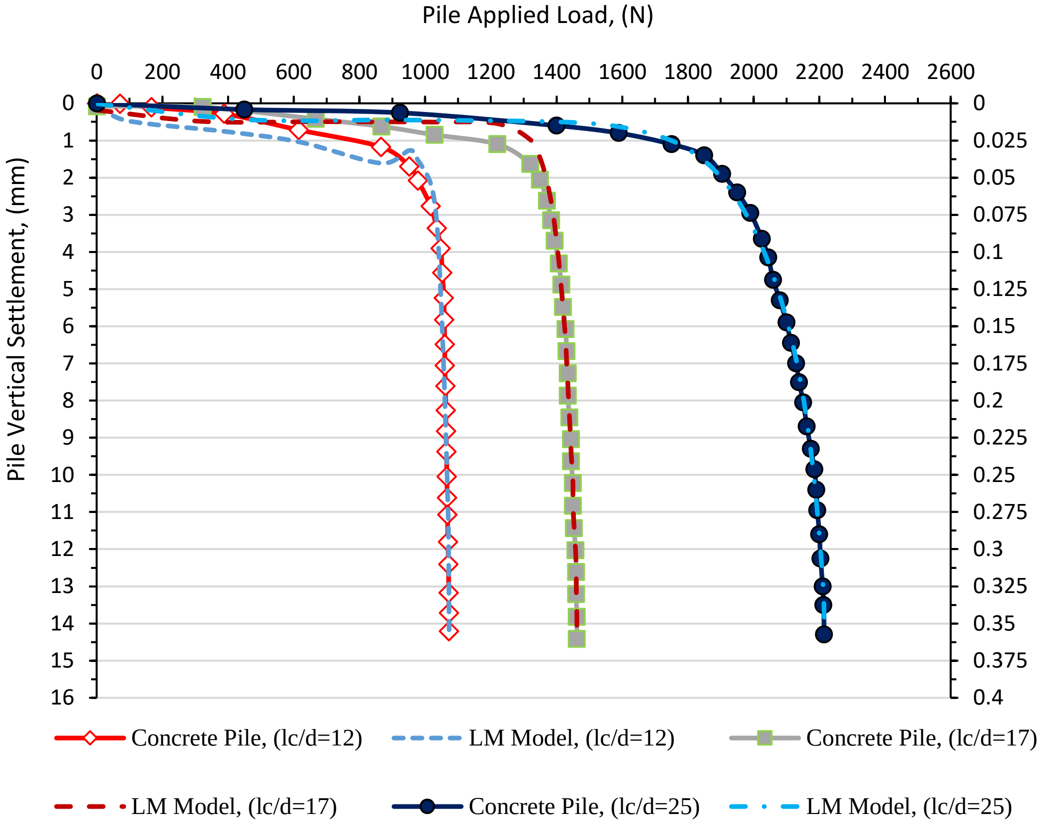

Figure 4-7: Comparison between measured versus predicted pile load-displacement tests for concrete piles embedded in medium sand.

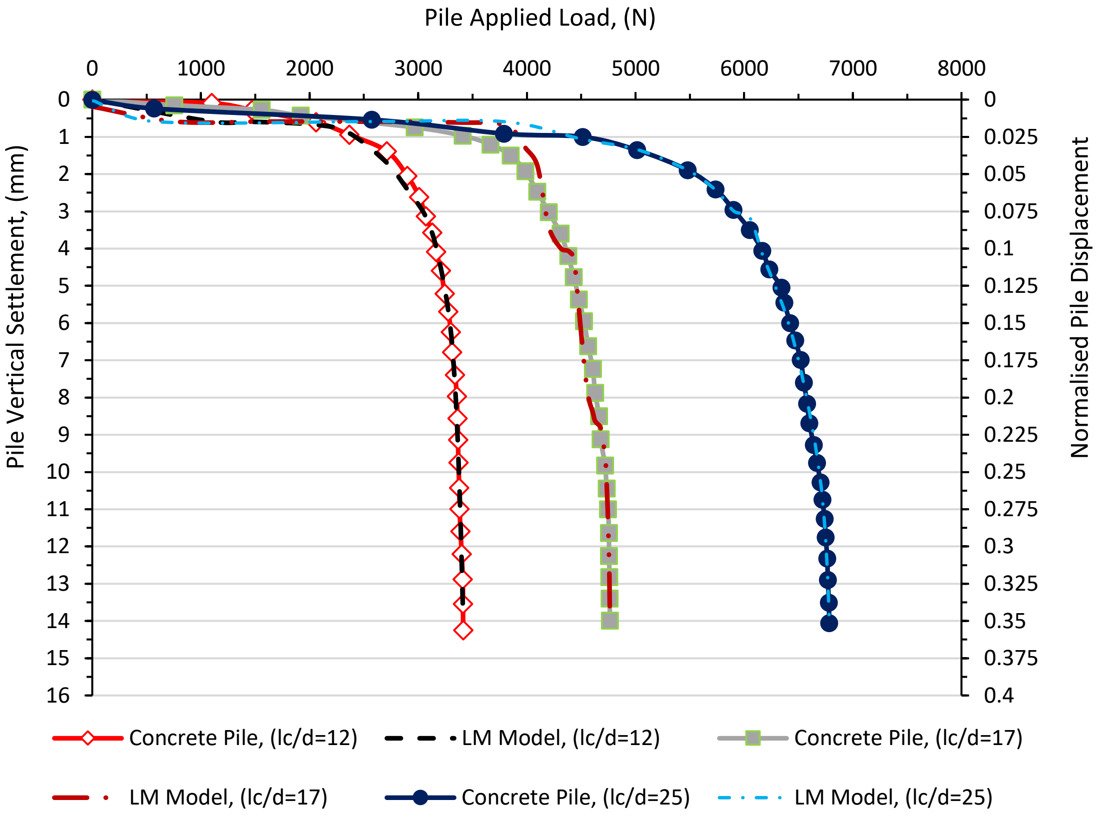

Figure 4-8: Comparison between measured versus predicted pile load-displacement tests for concrete piles embedded in dense sand.

The regression calibration plot for the training, testing and validation of all datasets to compare the measured and predicted pile settlement values, are illustrated in Figure 4.9. The points in all subdivisions (training, testing and validation) are located close to the best line of equality (Output = A x Target + C), where “A” and “C” are constant parameters, with high coefficients of determination of 0.99139, 0.98565, 0.98819 and 0.9908, for training, validation, testing and all data,

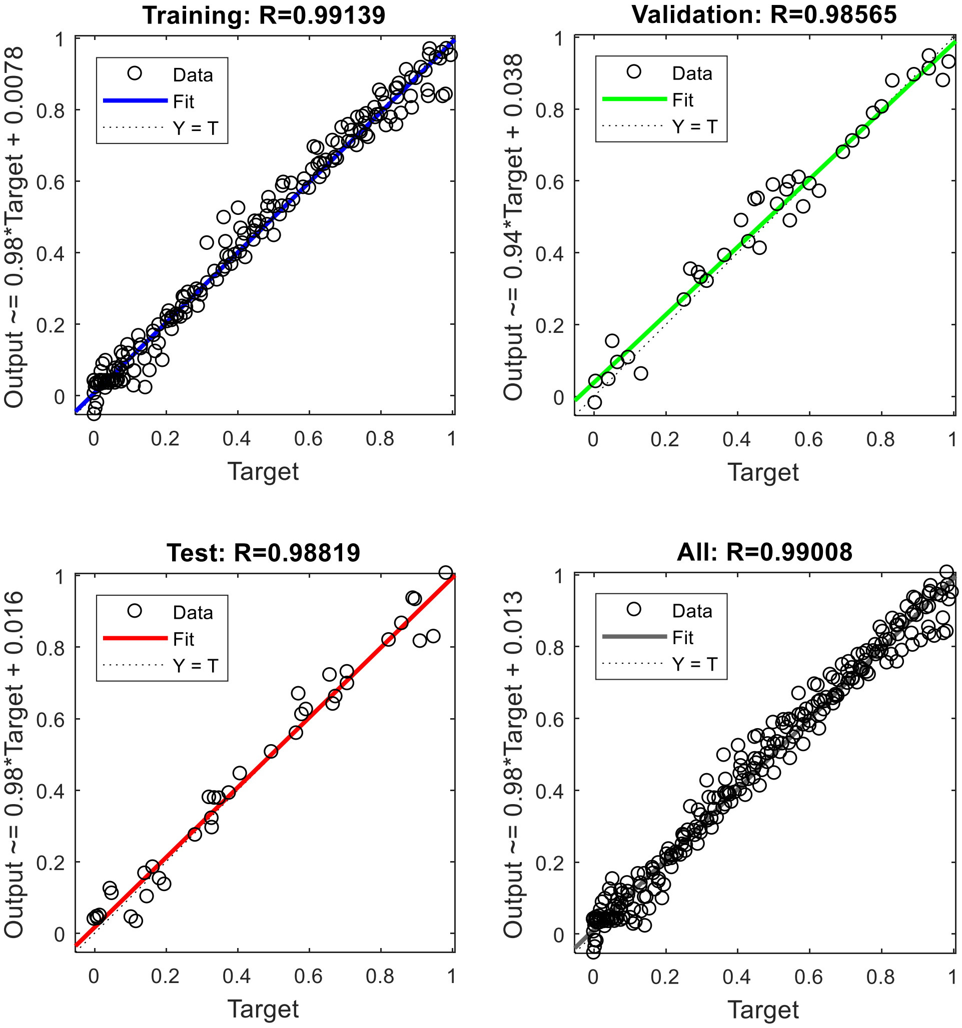

Figure 4-9: Regression graphs of the experimental results versus predicted pile settlement for concrete pile subjected to compression load.

Moreover, the performance of the LM algorithm is further examined graphically using the testing dataset as shown in Figure 4.10. It should be pointed out the testing dataset was not involved during the training process (Millie et al., 2012). It is normally used to evaluate the generalisation ability of the trained network (Sun et al., 2014). Thus, the testing dataset has been utilised to plot a regression calibration curve between measured versus predicted results, with a 95% confidence interval (CL) level of fit. According to the results, significant agreement can be observed between the measured versus predicted values with low scatter around equality line, with an RMSE and correlation coefficients (R and p) of 0.0478, 0.988, and 6.28 *10^{-31}, which confirms that the LM trained network has the ability to successfully reproduce the results of the experimental pile settlement with high consistency.

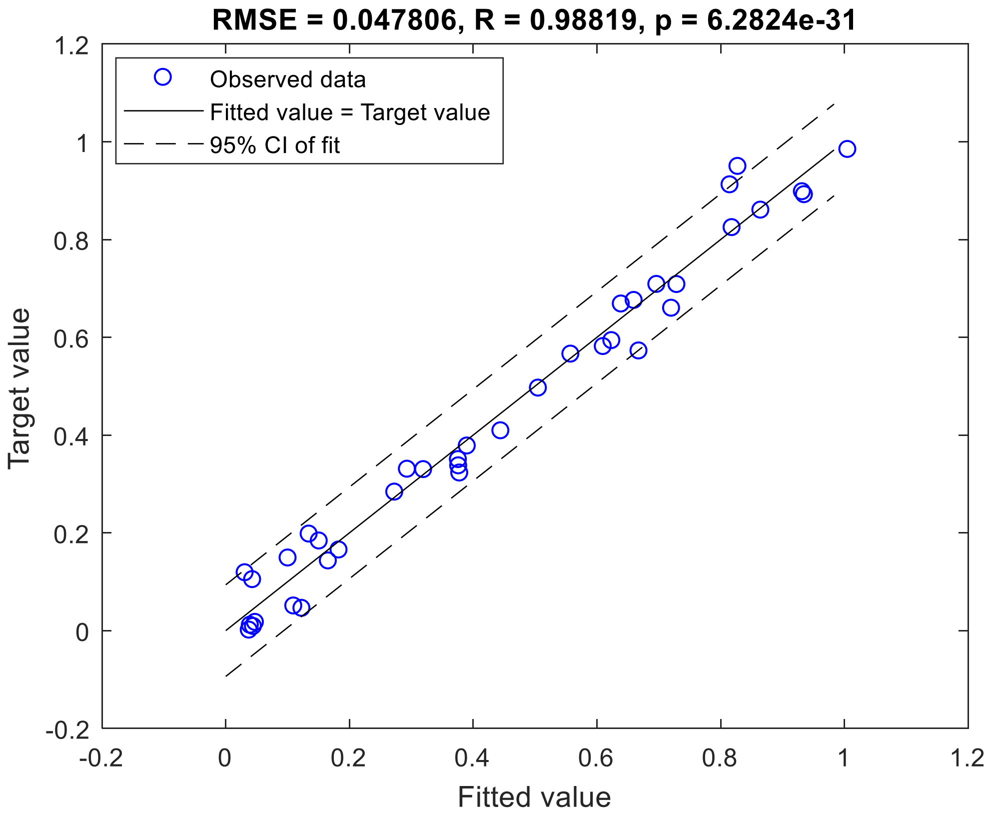

Figure 4-10: Calibration plot of the resulting model for the testing dataset at a 95% confidence interval (CI).

4.3.3 Comparison between the LM Optimum Model with the Various Traditional Methods for Concrete Piles

The full behaviour of pile load settlement needs to be well predicted, the geotechnical engineering can then, based on the applied load, be used to decide the ultimate capacity and comply with the structure serviceability and integrity requirements. Indeed, accurate simulation of the full pile-settlement curve necessitates thorough understanding of the soil-pile interaction (i.e., soil stress history, concentration of stresses and problem boundary conditions), which is complex and difficult to quantify (Comodromos et al., 2009). However, for simplification purposes and by necessity, several hypotheses and arbitrary assumptions associated with a significant set of parameters that govern pile capacity and associated settlement, have been assumed. This has resulted in the fact that the majority of current approaches fail to achieve the required levels of accuracy with respect to pile bearing capacity and the associated settlement (Momeni et al., 2014).

In this section, the reliability and the validity of the proposed method has been further checked after plotting the experimental results of the pile-load carrying capacity with the predicted results obtained from most traditional methods proposed by: Poulos and Davis (1980); Vesic (1977) and Das (1995) (see section 2.6 for more details). The comparative study results in Figures 4.11 and 4.12 clearly indicate that the predicted settlement using LM training algorithm is in remarkable agreement with the line of best fit. The predicted values proposed by Vesic and Poulos and Davis method are at the bottom of the list of performance with the later having the poorest quality of prediction accuracy, therefore, they need to be updated, if employed, in future application. Moreover, the comparison study also documented that the convergence rate for the applied algorithm is noticeably higher than the conventional methods, which confirms the feasibility of the LM training algorithm.

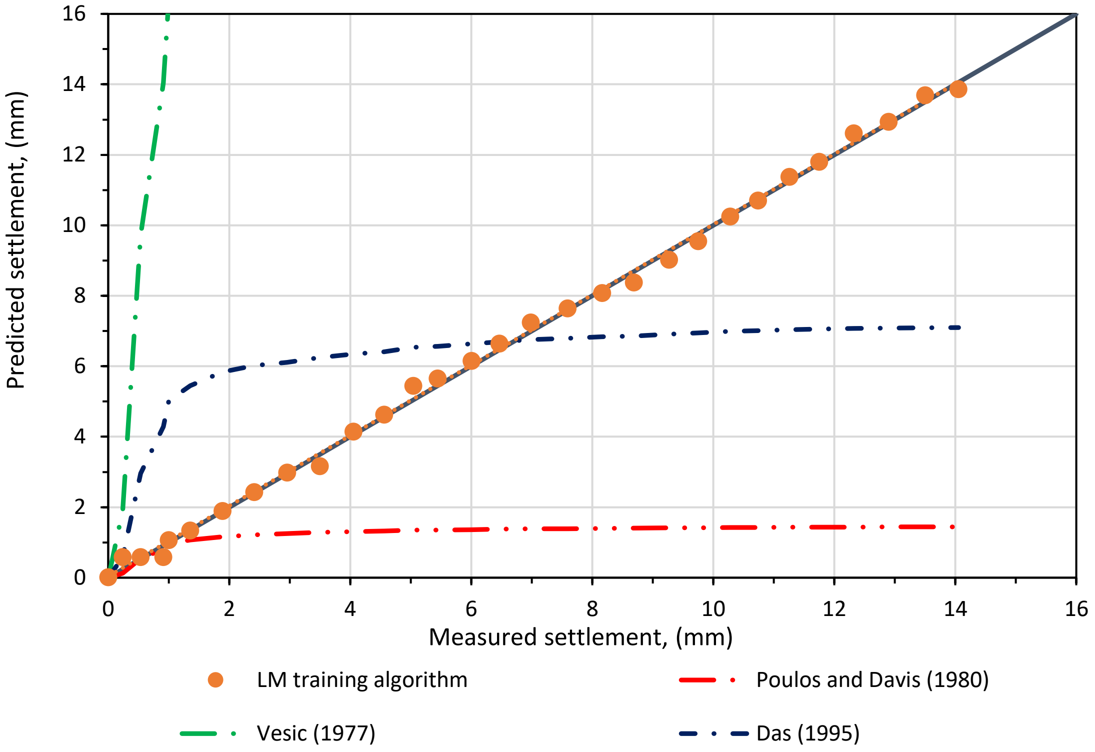

Figure 4-11: Profiles of measured versus predicted pile settlement for the proposed LM training algorithm compared with other methods for concrete piles.

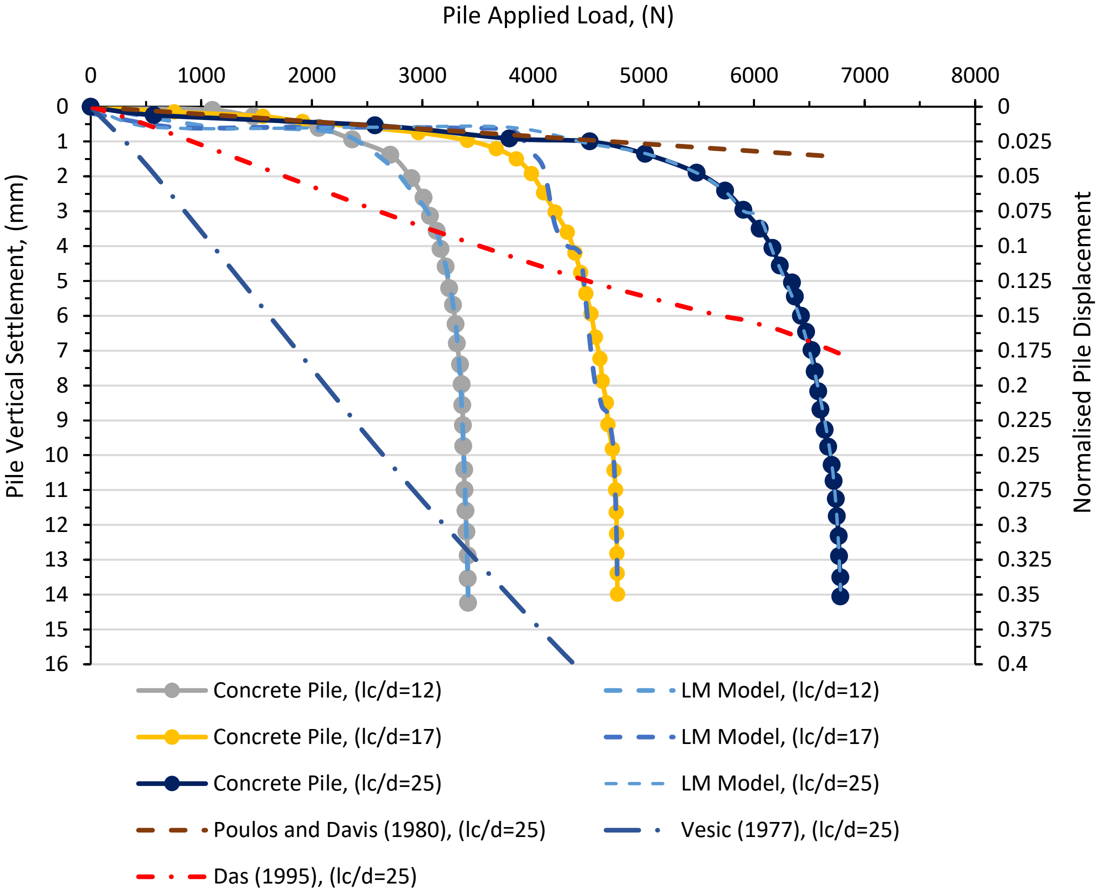

Figure 4-12: Applied load versus measured and predicted settlements for concrete piles using the optimal trained model of the proposed LM algorithm with other methods.

4.4 Factors Affecting Pile Capacity for Concrete Piles Subjected to Compression Load

The results of the load-carrying capacity discussed in section 4.3.2 provide an insight into pile capacity and allows the determination of the ultimate pile bearing capacity. Pile point bearing resistance and the developed skin friction resistance have been cited to play a key role on the total pile bearing capacity (Tomlinson and Woodward, 2014). In this section, the ultimate axial capacities for model concrete piles subjected to compression load were identified. The ultimate pile load capacity was determined from the load-displacement curves as the point when the pile continues to displace with no or very small additional applied load (post yield response), or the slope of the load displacement curves reached zero or sustained a minimum value (Jeffrey, 2012). In Figure 4.13 it can clearly be seen that the ultimate bearing capacity increases with an increase in the sand relative density and the pile embedment lengths. It is worth noting that the concrete pile square profile used in this study was 40mm (greater than the required pile diameter condition reported by Vesic (1977). For a pile slenderness ratio of 12, the ultimate axial capacity for a pile tested in dense sand is about 2 times for a pile embedded in medium sand and almost 6 times that found in loose sand. While for piles with slenderness ratio of 17, the ultimate capacity for a pile tested in dense sand is about three times that found in medium sand and 6 times in dense sand. Furthermore, for piles with Lc/d = 25, the pile ultimate capacity is about 1.75 in medium sand and 6 times in case of dense sand. This can be attributed to an increase in the pile stresses distribution around the pile, which, indeed, has a substantial effect on the pile shaft resistance in the radial effective zone and the end bearing resistance. The aforementioned results are consistent with studies such as Shanker et al. (2007).

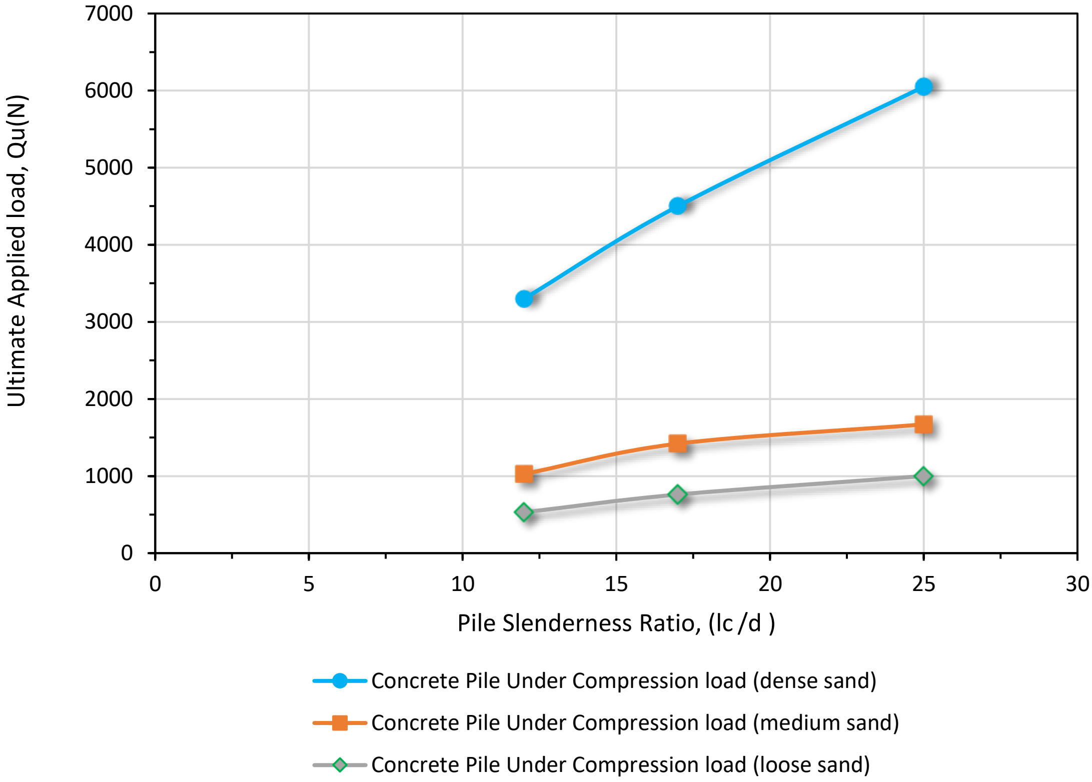

Figure 4-13: Plot shows ultimate pile capacity profile versus pile slenderness ratio for concrete piles.

4.5 Performance Analysis of the LM Algorithm for Steel Closed-ended Model Piles Embedded in Loose, Medium and Dense Sandy Soil

This part of the study is devoted to the performance of the LM training parameters to correlate pile load-settlement based on steel closed-ended piles driven in sandy soil under compression loads. As previously mentioned, the topology of the model consisted of three processing layers (input layer, hidden layer and output layer). Those processing elements or layers are a means of learning and describing the optimum network patterns controlling the dataset on which the model was constructed. Different performance indicators are available in the open literature. To overcome the highlighted barriers, the efficiency of the optimal model was statistically assessed using the performance parameters as summarised in section 4.3.

4.5.1 Steel Closed-ended Piles Subjected to Compression Loading

The performance of the trained LM network for steel closed-ended piles under training is displayed in Figure 4.14, the results revealing that the plot of validation depicts a substantial fall in minimum mean square error (MSE) with increasing iteration. The optimum network performance was identified with a relatively negligible MSE of 0.0029 at an epoch of 215. It can also be indicated that the training automatically stopped after 6 constitutive error, to avoid over fitting, once the cross-validation error started to increase, this can also be defined as early stopping criteria to avoid over fitting phenomena.

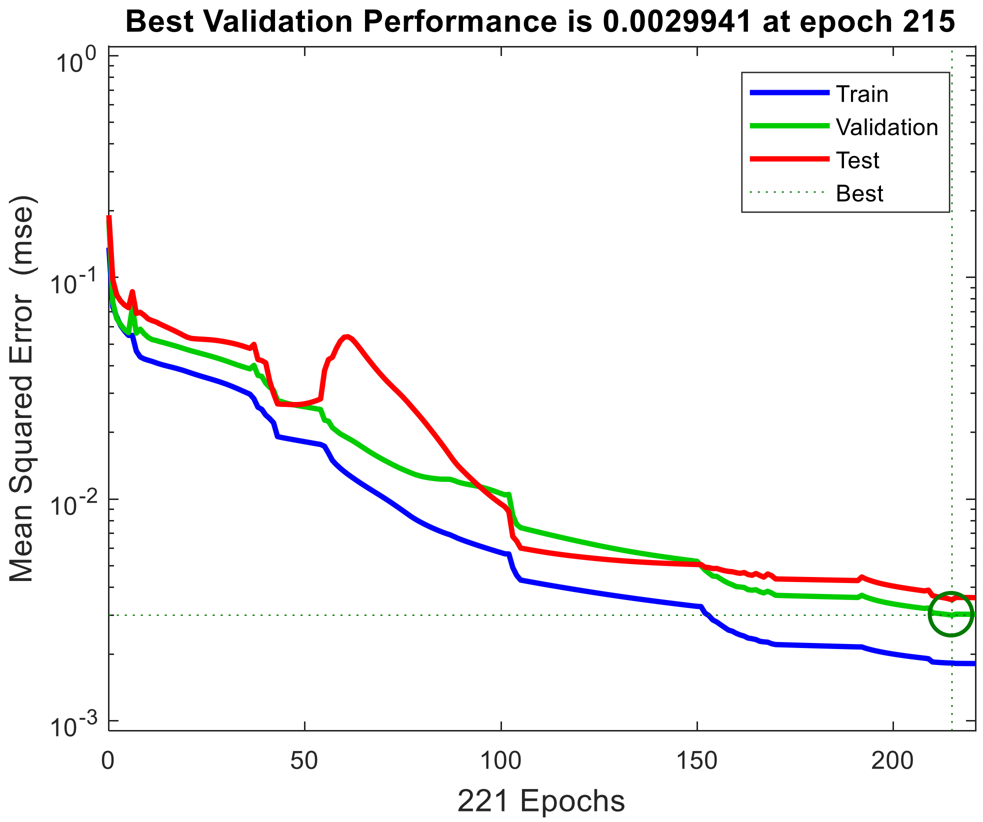

Figure 4-14: Performance plot of the LM algorithm for steel closed-ended developed model during the training process.

The variation in error gradient, the Marquardt adjustment parameter (m_u) and the validation checks for the model of steel closed-ended piles are show in Figure 4.15. It can be demonstrated that the gradient error reached a minimum value at 0.00039 at an iteration of 221, while the m_u factor and the validation check numbers are $1x10^{-05}$ and 6, respectively. Moreover, the error histogram (EH) values were plotted out against the instances in Figure 4.16. The residual plot shows normal distribution of error. It is worth pointing out that a normal distribution leads to Gaussian curve, with highest point in the middle. The analysis of the EH shows that more than 90% of the errors between the bins (-0.0148 and 0.0015).

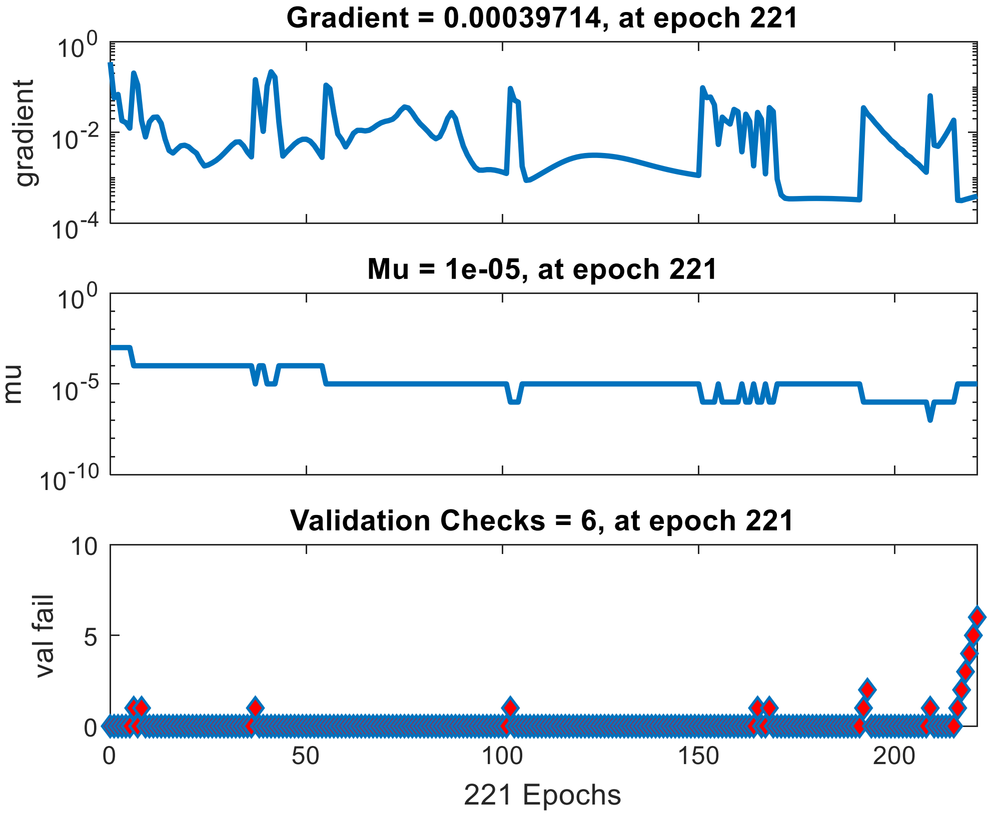

Figure 4-15: Gradient and maximum validation checks for the LM trained network.

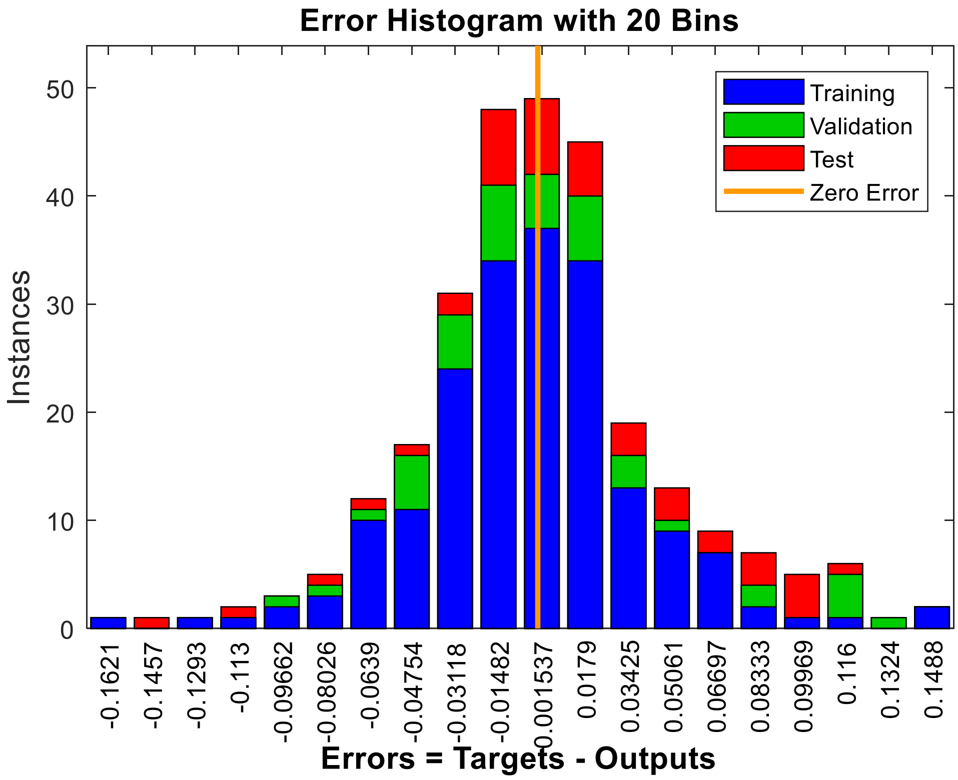

Figure 4-16: Plot of error histogram (EH) for the LM algorithm.

4.5.2 Measured Versus Predicted Pile Load Tests for Steel Closed-ended Piles Subjected to Compression Loads

In this section, the experimental and the predicted load carrying capacity results are compared along with the regression results as presented. A series of experimental pile load tests were carried out on steel, closed-ended pile models. The experimental testing programme used three piles with slenderness ratios (Lc/d) of 12, 17 and 25 where Lc is the effective pile length with a diameter (d) of 40mm, to examine the behaviour of rigid and flexible piles. 277 points in total were recorded from the experimental pile load test data, which used a P3 strain indicator with 16-bit data resolution as illustrated in the experimental setup (section 3.2). The pile head settlement was closely monitored using two full bridge strain gauge type transducers, with a 50mm stroke capacity. Figures 4.17, 4.18 and 4.19 report the extent of the fit between the experimental and predicted normalised load-carrying capacity of steel piles, subject to axial loads at different stages of mechanical loading. The results show that the elastic response can be seen in the early stages of running the pile load test until about 200, 450, and 800N for piles tested in loose, medium and, dense sand, respectively. The results also demonstrated that a soil yielding effect for axial applied loads greater than the aforementioned values was identified in the upper part of the foundation, where local nonlinearity is marked. It can be observed that the mobilised pile bearing capacity (end bearing and mobilised skin friction resistance) increases as sand stiffness and pile effective length increase. Plastic mechanisms in the soil surrounding the pile are the leading cause for the non-linearity of the load-settlement response; as the applied load increases, the pile response shows nonlinearity until reaching a maximum capacity at about 10% of pile diameter (BSI, BS EN 8004:1986). Based on the graphical comparisons, there was an excellent fit between the proposed LM training algorithm and targeted value, with a correlation coefficient of 0.988 for all data, which demonstrates that the applied algorithm is a reliable method to use to predict pile load-settlement curves for the range being investigated.

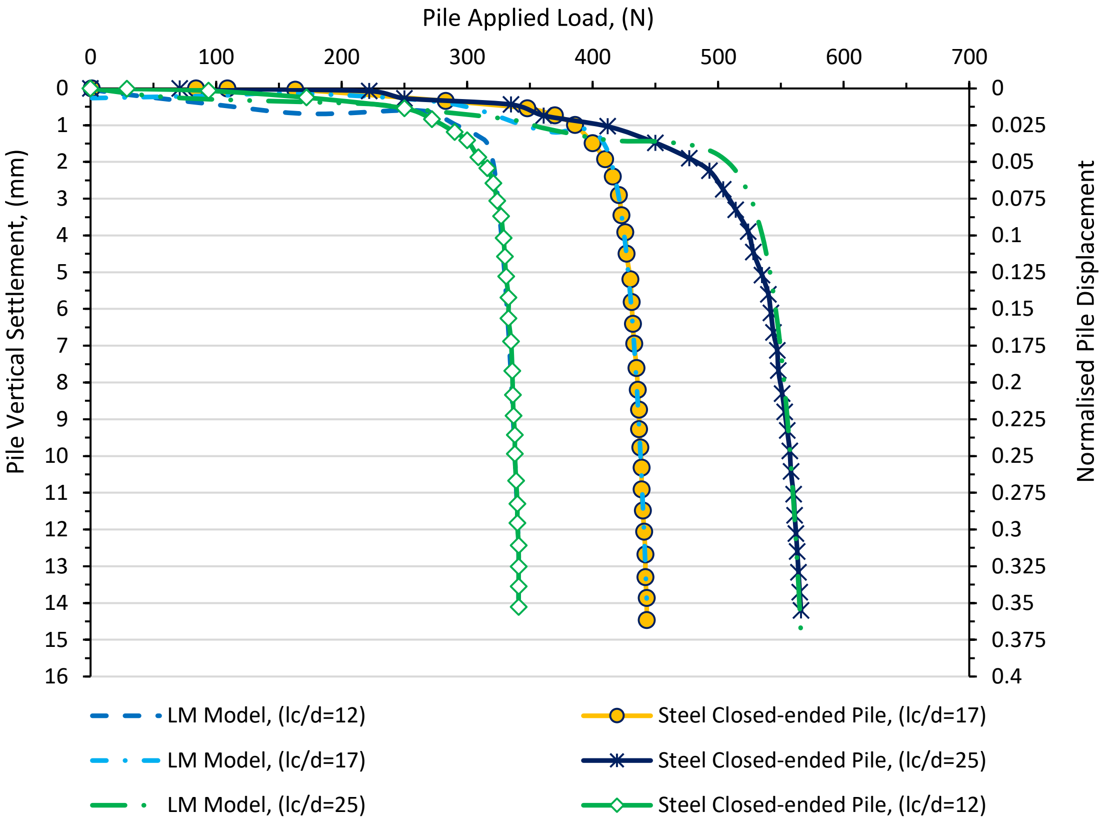

Figure 4-17: Comparison between measured versus predicted pile load-displacement tests for steel closed-ended piles embedded in loose sand.

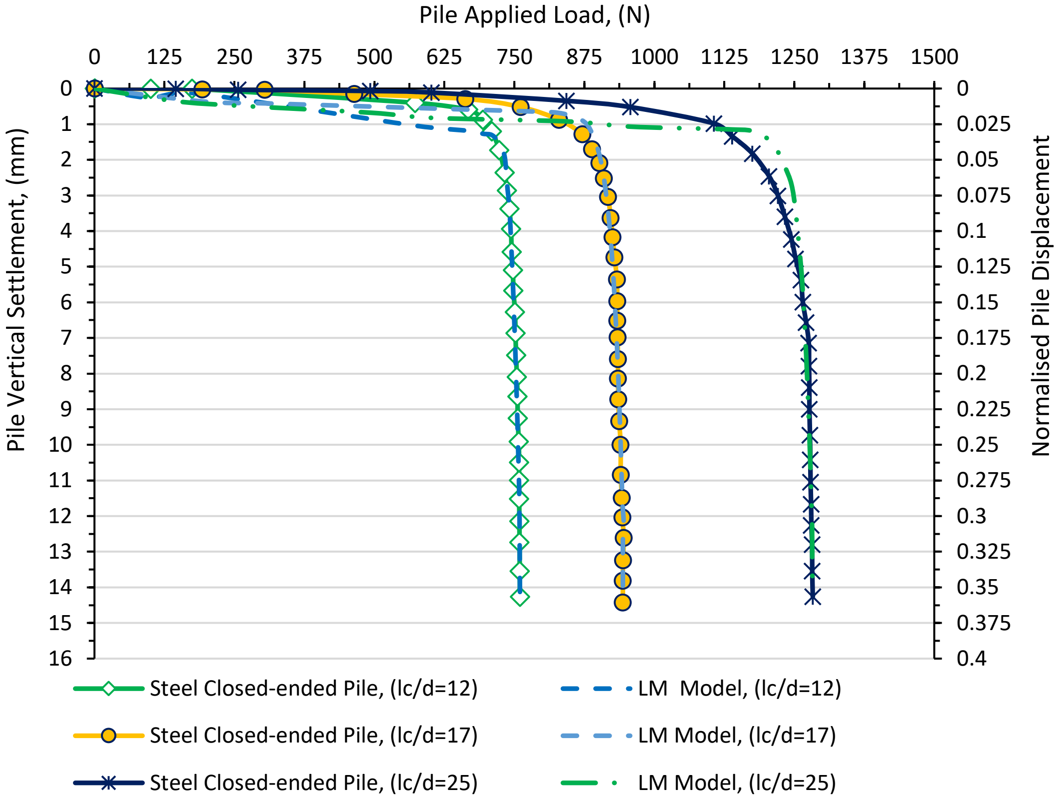

Figure 4-18: Comparison between measured versus predicted pile load-displacement tests for steel closed-ended piles embedded in medium sand.

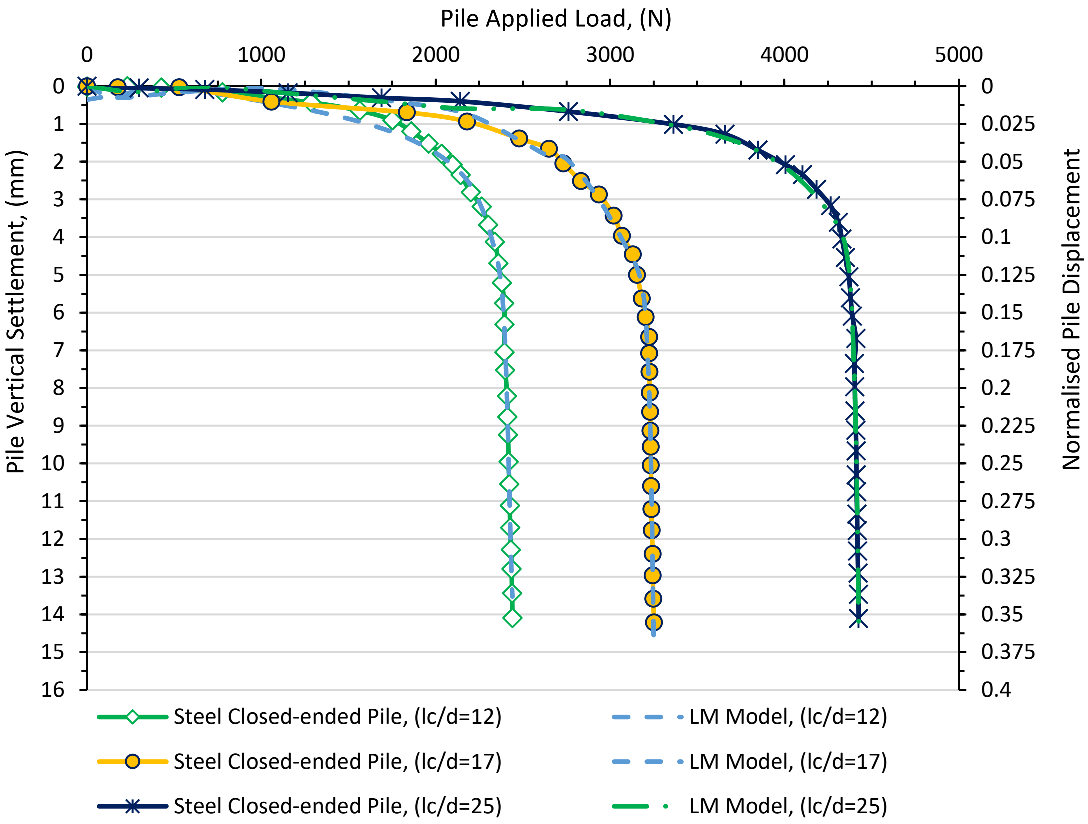

Figure 4-19: Comparison between measured versus predicted pile load-displacement tests for steel closed-ended piles embedded in dense sand.

The robustness of the LM algorithm has been further examined graphically by comparing the experimental and simulated pile settlement as shown in the following scatter plot. As can be seen in Figure 4.20, the introduced training algorithm, at topology of 5:10:1 for input layer, number of neurons and output layer, satisfies the robustness test. All the measured and predicted points are matched well with the target values and close to the best-fit line with correlation coefficients of 0.99088, 0.98436, 0.9854 and 0.98861 for training, validation, testing and all data, thus substantiating the application of the LM algorithm as an effective predictive tool.

Moreover, the reliability of the adopted algorithm has also been explored graphically, as highlighted in Figure 4.21. The testing dataset "*unseen data set* " has been used to test the generalisation ability of the employed algorithm (Mareš et al., 2016). It is worth noting that the regression calibration curve depicting actual versus predicted values was plotted using a newly developed MATLAB code, (see Appendix III), with a 95% confidence interval level. It can be concluded that substantial agreement can be seen between the measured versus predicted set, with correlation coefficients R = 0.984 and Pearson's moment correlation coefficient = 8.73x10^{-32} and an RMSE of 0.059, respectively.

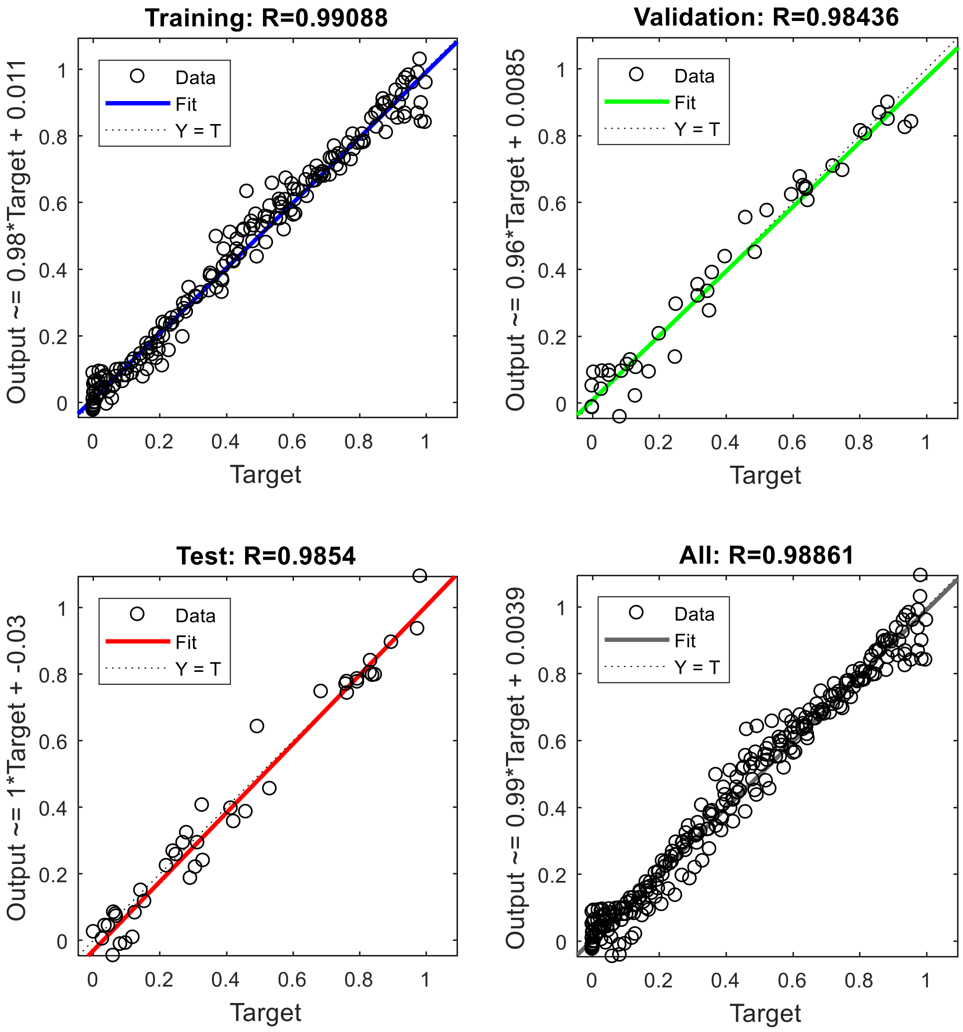

Figure 4-20: Regression graphs of the experimental results versus predicted pile settlement for steel closed-ended pile subjected to compression load.

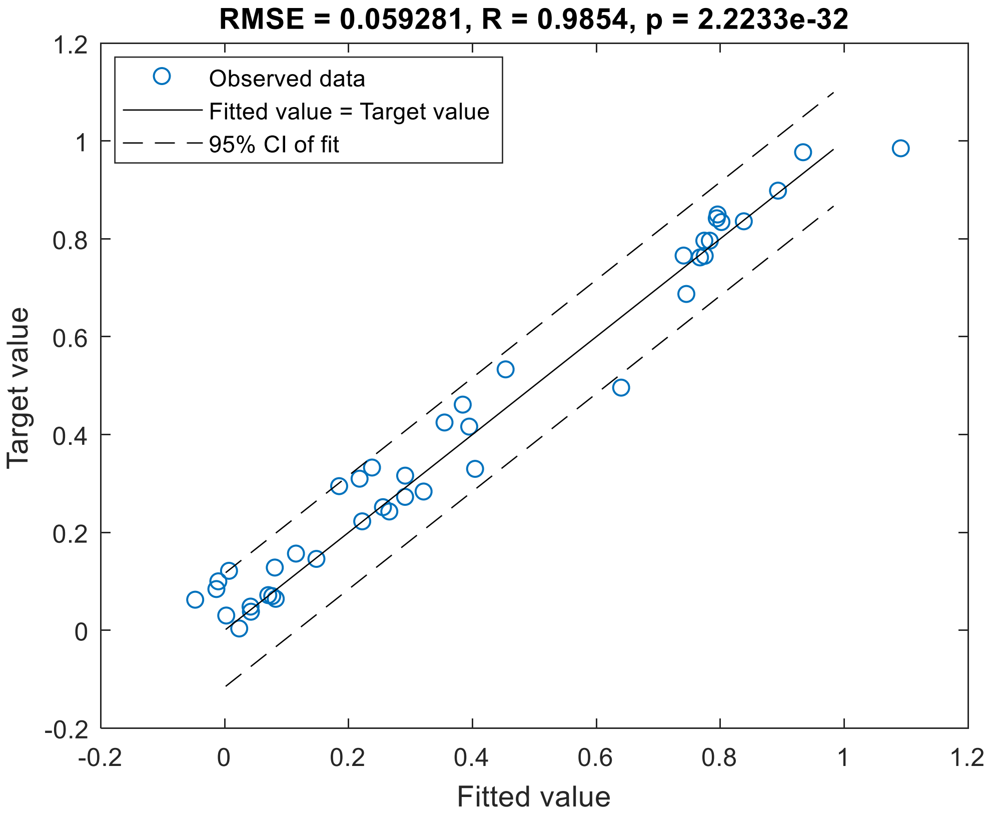

Figure 4-21: Calibration plot of the resulting model for the testing dataset at a 95% confidence interval (CI).

4.5.3 Comparison between the LM Optimum Model with the Various Traditional Methods for Steel Closed-ended Piles

Pile bearing capacity and associated settlement can be accurately determined by conducting in-situ pile-load tests. Being time consuming and with the cost considerations involved in the construction process, pile bearing capacity and settlement can be determined using many empirical approaches as detailed in section 2.6. With the aim of further exploring the validity of the proposed approach, Figures 4.22 and 4.23 characterise graphical comparisons between the predicted and measured values of pile settlement using an actual pile load carrying capacity and those estimated by most traditional methods. The comparative results indicated that pile settlement predicted using the LM training algorithm are in good agreement as per the fitted line, suggesting that the application of the LM optimal model is a high-precision tool with obvious advantages. Additionally, the results demonstrated that the predicted values using Vesic model grossly overestimated the experimental pile load test. On the other hand, the predicted values using Poulos and Davis underestimate the results of the pile load test, while it can be seen that the model proposed by Das failed to gain continuous success to capture the full response of pile load-settlement, therefore, most accurate.

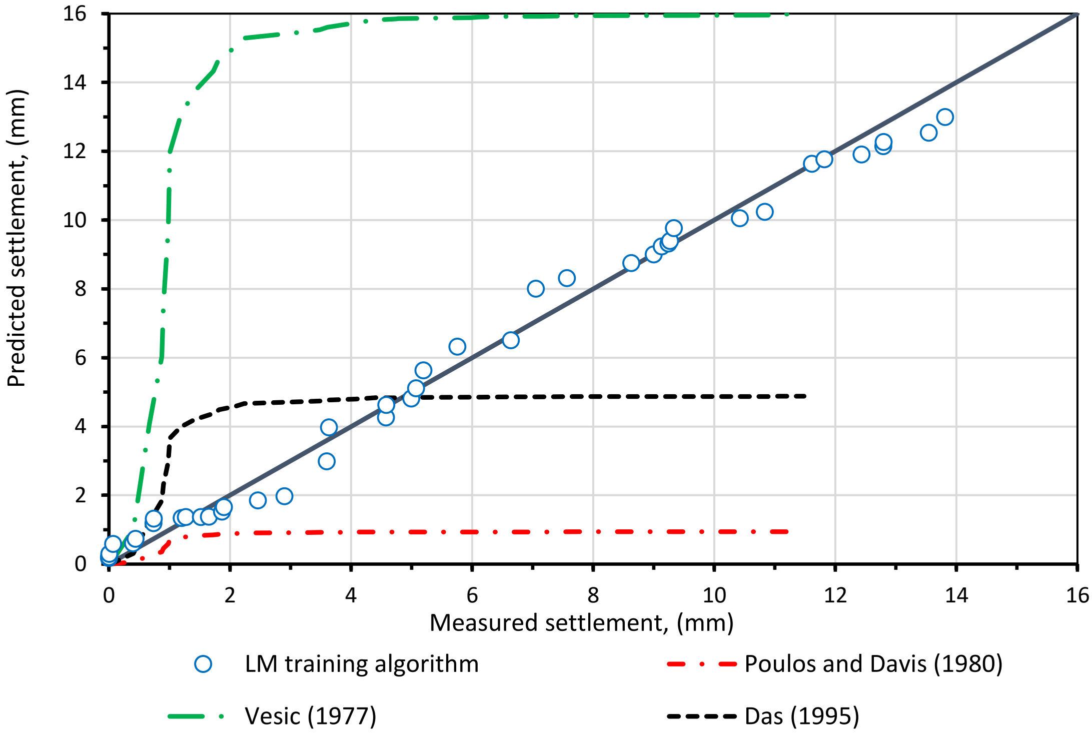

Figure 4-22: Profiles of measured versus predicted pile settlement for the proposed LM training algorithm compared with other design methods for steel closed-ended piles.

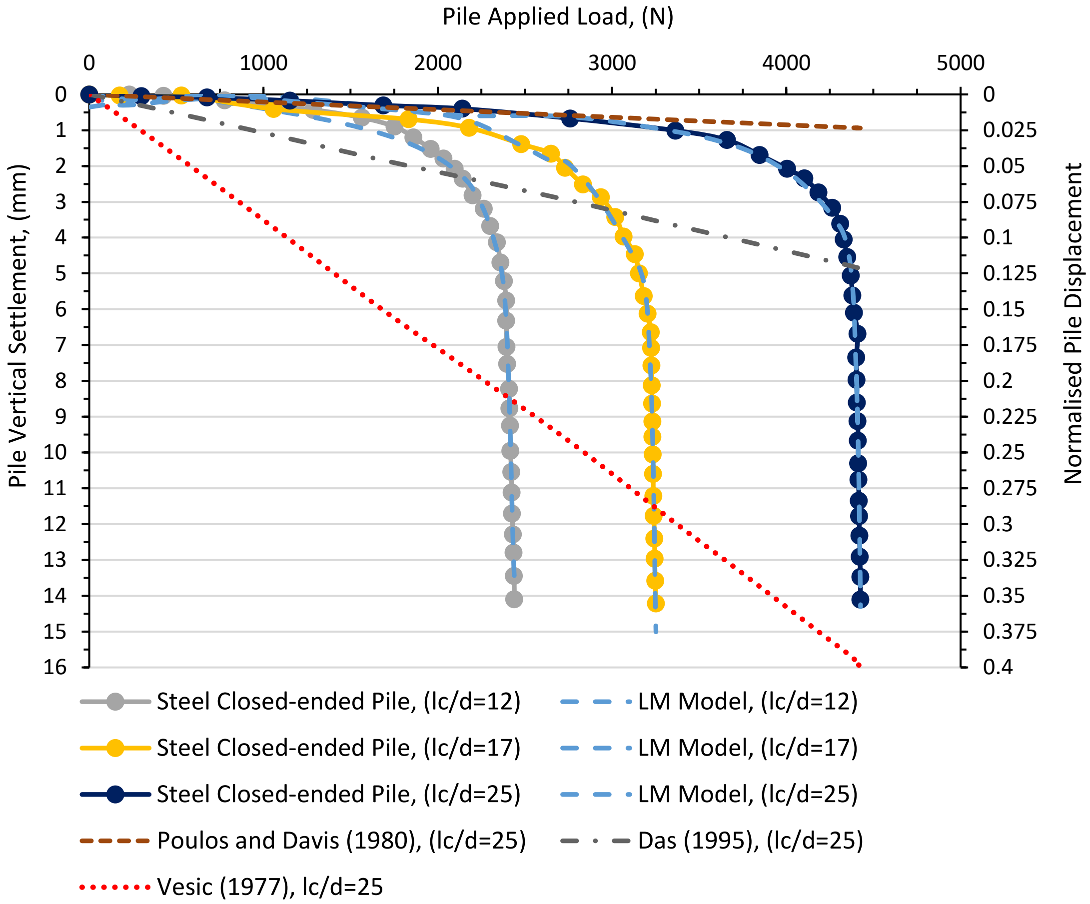

Figure 4-23: Applied load versus measured and predicted settlements for steel closed-ended piles using the optimal trained model of the proposed LM algorithm with other methods.

4.6 Factors Affecting Pile Capacity for a Steel Closed-ended Pile Subjected to Compression Load

In this part of the study, the increase in the ultimate pile load capacity with different relative densities of sand is clearly illustrated (post yield response). pile capacity can be defined as the pile capacity being reached when the slope of the load displacement curves reaches zero or sustains a minimum value (Institution of Civil Engineers, 2007). The ultimate axial capacities for steel closed-ended piles subjected to compression load were determined from pile load-displacement curves, as presented in Figure 4.24. With reference to the graphical comparisons, it can be clearly seen that the ultimate pile capacity increases with the increase in the sand relative density and the length of embedment. The results revealed that the pile ultimate capacity with a slenderness ratio Lc/d=12, in loose sand was 325N. While the maximum pile capacity is almost doubled for medium sand. In sharp contrast to that for piles penetrated in dense sand, the pile bearing capacity has been found to be several times higher than the results of pile bearing capacity for loose and medium sand.

Moreover, for a pile with length-to-diameter ratio of 17, the pile ultimate capacity in dense sand is about 6 times higher than the result for loose sand and about 3 times higher than the pile capacity in medium sand. The pile ultimate capacity with Lc/d=25 for dense sand is just under 4 and 8 times higher than the results of the medium and loose sand, respectively. This can probably be assigned to an increase in the sand stress distribution due to the increase in the radial effective stress from their initial values around the pile, which, indeed, has a substantial effect on the pile shaft resistance (q_s) and also the end bearing resistance (q_b).

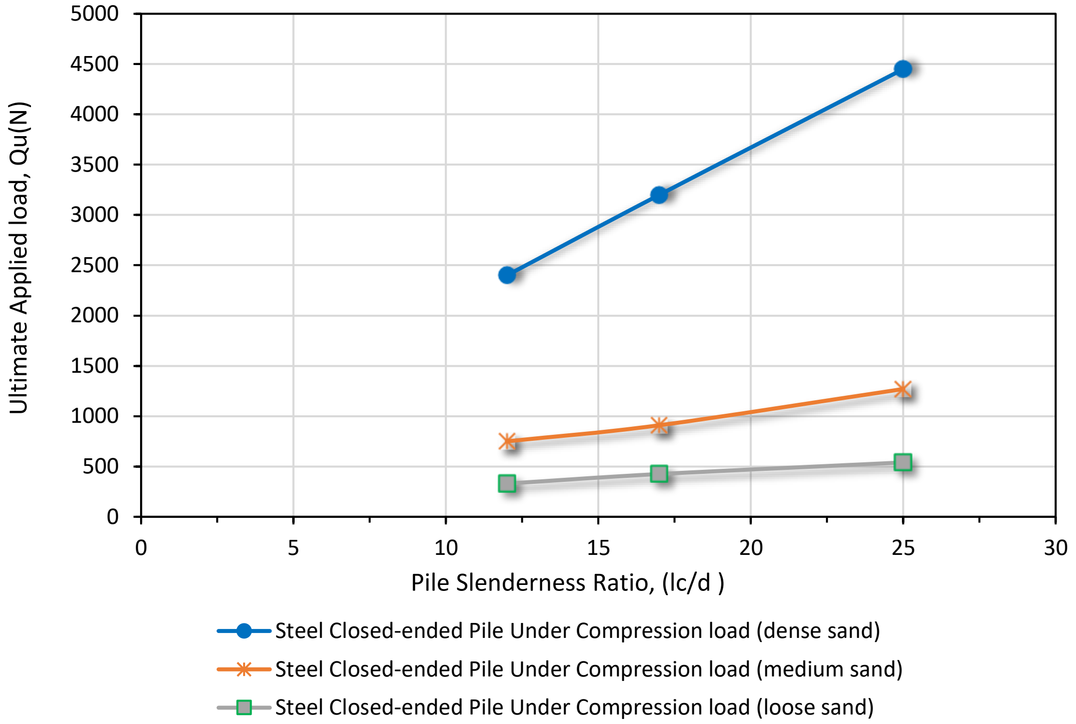

Figure 4-24: Plot shows ultimate pile capacity profile versus pile slenderness ratio for steel closed-ended piles.

4.7 Performance Analysis of the LM Algorithm for Steel Open-ended Model Piles Embedded in Loose, Medium and Dense Sandy Soil

This section of the thesis presents and discusses the performance of the trained LM algorithm using the standard measuring performance indicators; mean square error (MSE), correlations coefficients (R and p) and root mean square error (RMSE). Furthermore, a comparison between the measured, the computational values and the results of those given by the most traditional methods to simulate pile load-settlement has also been conducted. The results of targeted versus predicted behaviour of pile load carrying capacity for steel open-ended piles along with the factors affecting pile bearing capacity were also presented and discussed.

4.7.1 Feasibility of the LM Trained Model for Steel Open-ended Piles under Compression Load

As demonstrated previously, the evolving LM algorithm as a regularisation back propagation scheme was considered to train and develop the network due to its superiority over the conventional methods. The network convergence plot during the learning process has been shown in Figure 4.25. It should be noted that the network topology that provided the lowest MSE in the independent cross-validation sub-set was identified as an optimal network (Nguyen-Truong and Le, 2015). The plot of convergence reveals that the best performance occurs at 389 epochs and that the training was terminated, at the best network performance, with a relatively insignificant MSE of 0.0019.

Moreover, the distribution of the error gradient, the Marquardt adjustment factor (mu) and the validation check number are revealed in Figure 4.26. It can be demonstrated that the gradient error was 0.0001, while, the mu factor and the validation check were $1x10^{-6}$ and 6 at an epoch of 395, respectively. A more informative picture of the network profile can be seen in the error histogram (EH), as in Figure 4.27. It is worth noting that the performance of the proposed algorithm can be extremely affected by the presence of outliers. Thus, the training process is stopped once the validation error starts to increase. In addition, it can be shown that the majority of data coincides with the zero error line, which was specifically targeted.

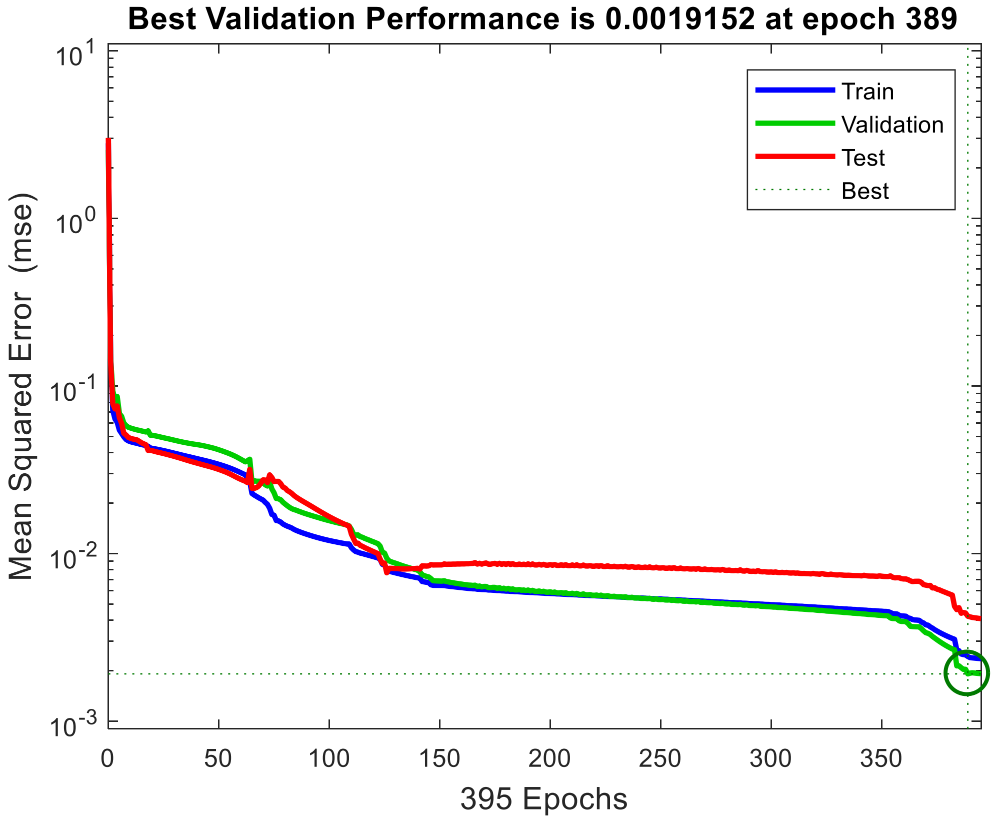

Figure 4-25: Performance plot of the LM algorithm for steel open-ended developed model during the training process.

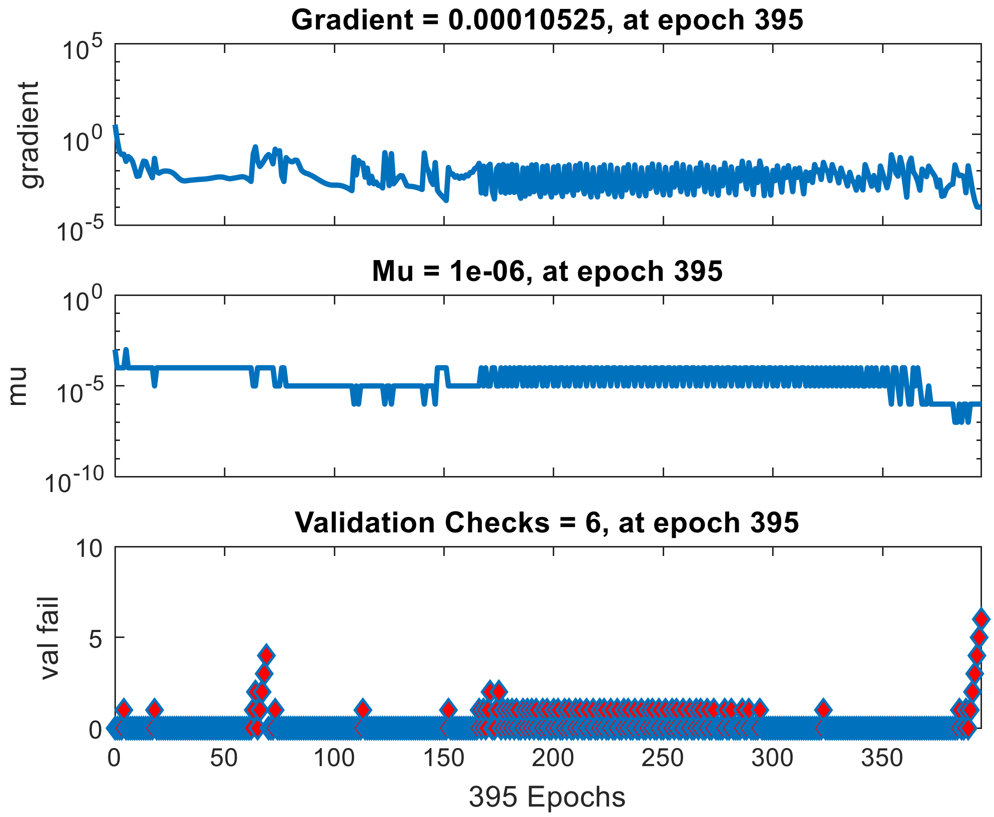

Figure 4-26: Gradiant and validation checks for the LM trained network.

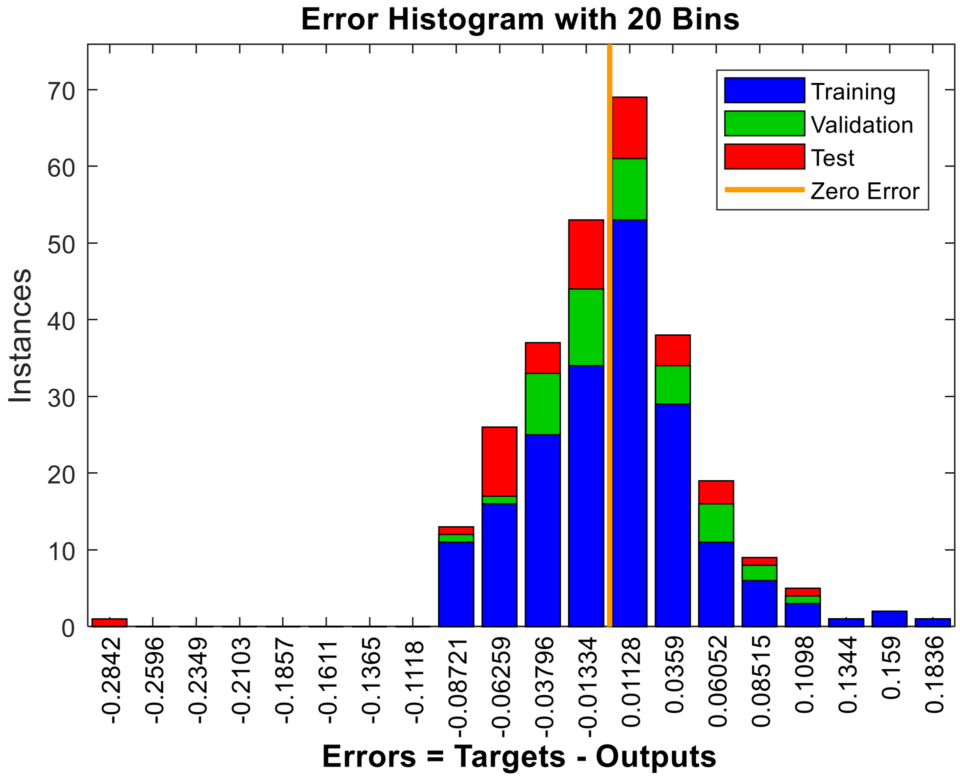

Figure 4-27: Error histogram of training, testing and validation.

4.7.2 Measured Versus Predicted Pile Load Test for Steel Open-ended Piles

Steel open-ended piles are extensively used in preference to closed-ended piles in hard soils, in an effort to facilitate the installation the penetration process to achieve the desired length (Fattah and Al-Soudani, 2016). Although many studies have been conducted concerning the pile bearing capacity of pipe piles, design approaches determining the shaft resistance developed along the length of the embedment pile rely heavily upon empirical correlations (Gavin and Gallagher, 2005). In addition, the utilisation of empirical design approaches to fully simulate the pile-load settlement have been documented as inaccurate due to many assumptions introduced in the interpretation of the pile bearing capacity.

In this part of the study, the series of experimental pile-load carrying capacity tests for model steel open-ended piles embedded in sandy soil are clearly presented and discussed as can be seen in Figures 4.28, 4.29 and 4.30, respectively. The results of the pile-load tests indicate that the pile bearing capacity increased with the increase in the sand relative density and the pile-penetrated length. This can be attributed due to an increase in the skin friction resistance and the point bearing developed within the contacted soil in the effective zone. Figure 4.28 reports the distributions of the measured versus predicted load carrying capacity at different stages of compression loading. The monitored axial applied load and the corresponding settlement is idealistic for canonical a pile foundation under compression loads, for instance, decreasing from the head of the pile to pile toe as a consequence of the mobilized shaft resistance, which is developed between pile-soil interaction in the effective soil zone. The results revealed that an obvious elastic branch is pronounced in the initial stages of the applied until a clear soil plastic response at axial applied loads of 200, 275, and 350 N for piles with Lc/d of 12, 17, and 25, respectively. It is noteworthy that the soil yielding influence for loads larger than 200 to 230 N, 275 to 315 N, and 350 to 410 N can be clearly noticed in the foundation upper part, where nonlinearity is marked.

The results also demonstrated that as the mechanical applied loads increase, the pile foundation behaviour becomes more nonlinear due to the presence of the plastic mechanisms within the soil effective zone. Pile ultimate capacities of 240, 325, and 415 N were found according to the failure criteria at 10% of pile diameter characterised by BSI (BS EN 8004:1986). Figures 4.29 and 4.30 illustrate the results of load-settlement distribution of model pile driven in medium and dense sand. Similarly, clear elastic responses can be seen in the initial stages of applied load until the pile settlement is around

3% of pile diameter. Besides, as the load increases, the foundation responses become more nonlinear, due to the existence of the plastic mechanism. As mentioned previously, ultimate pile capacities of about 600, 750, and 1000 N for piles tested in medium sand and 1900, 2800, and 4000 N for piles embedded in dense sand were demonstrated. Based on the graphical comparisons between the measured and the predicted values, the results established that there was an excellent correlation between the experimental and computational pile load-test results, with a correlation coefficient of 0.986 for all datasets, which verified that the LM trained algorithm employed, could efficiently predict the pile load-settlement behaviour with substantial accuracy.

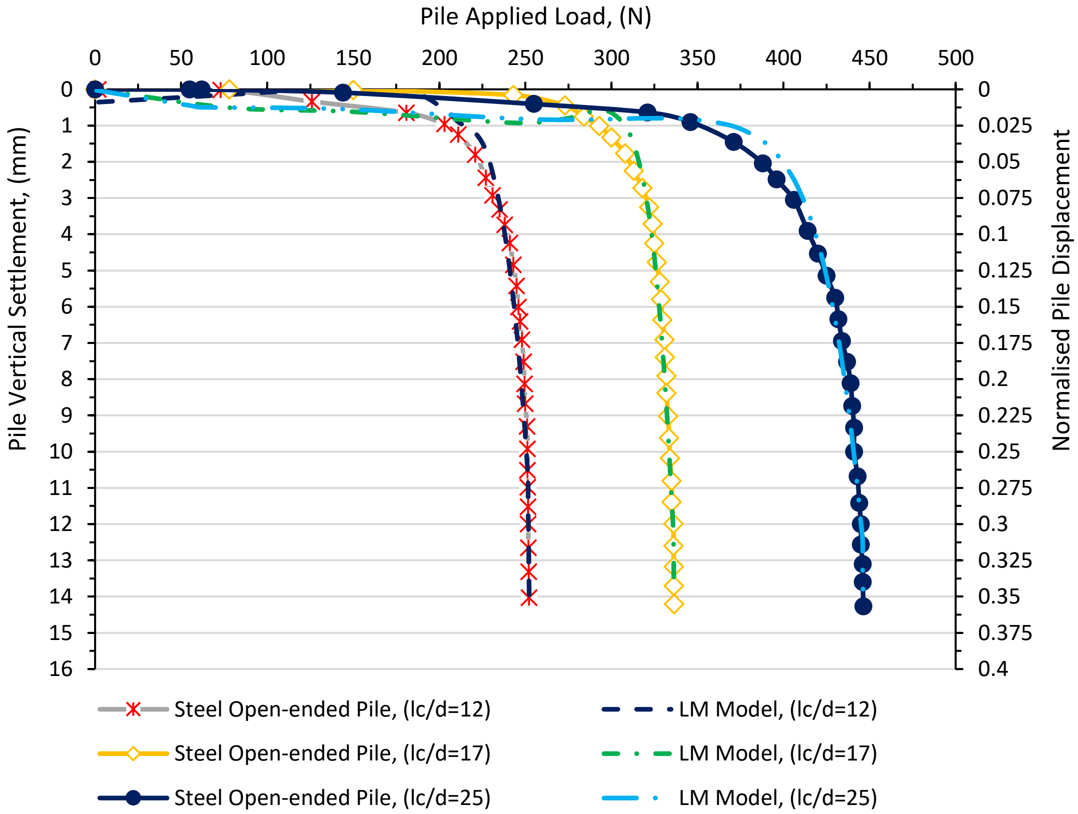

Figure 4-28: Comparison between measured versus predicted pile load-displacement tests for steel open-ended piles tested in loose sand.

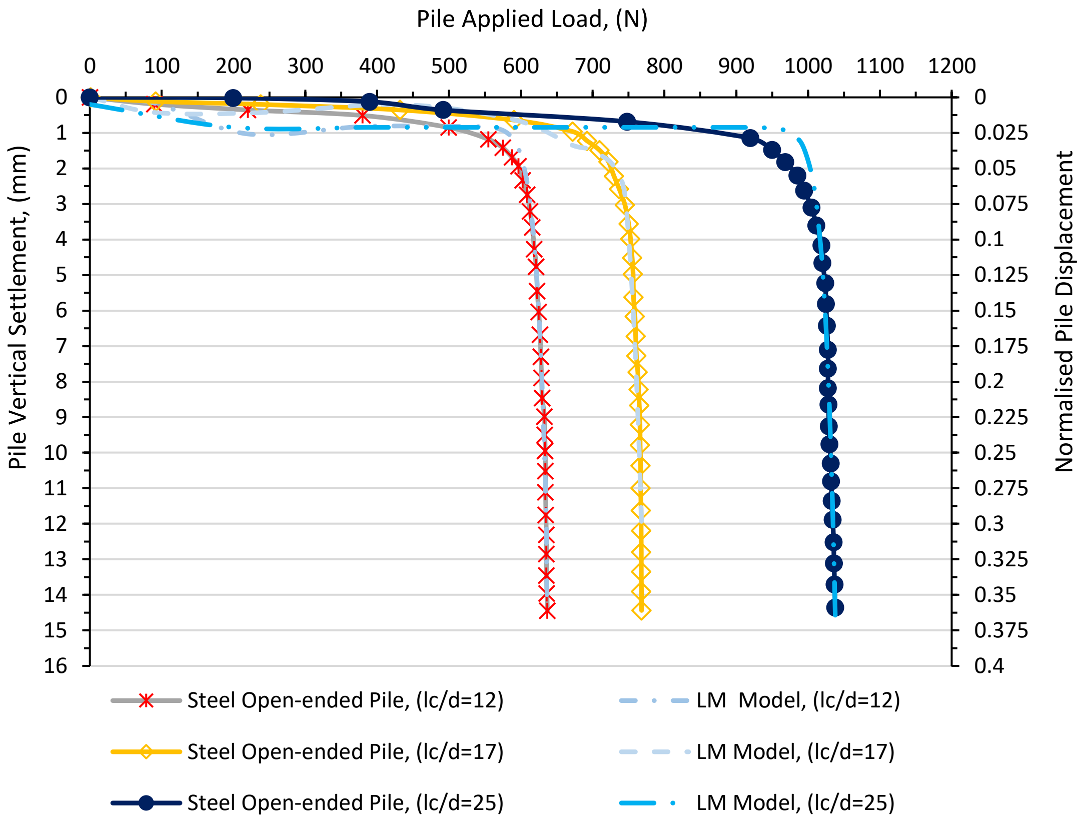

Figure 4-29: Comparison between measured versus predicted pile load-displacement tests for steel open-ended piles tested in medium sand.

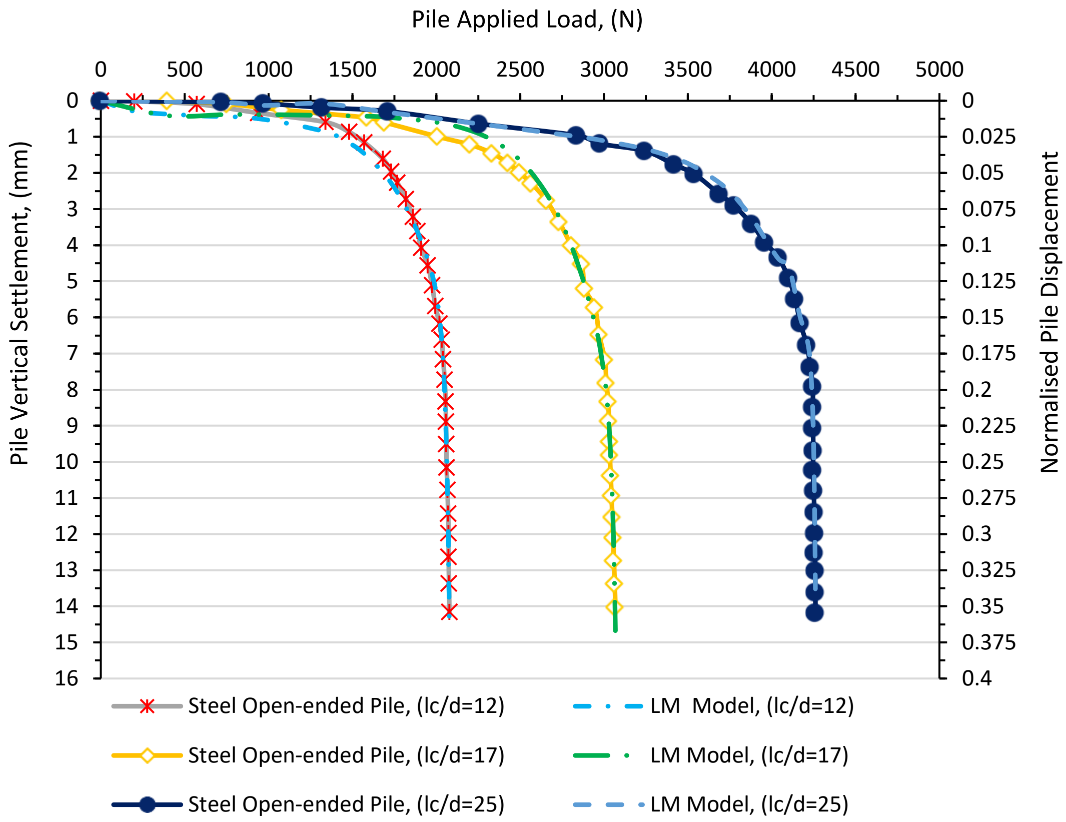

Figure 4-30: Comparison between measured versus predicted pile load-displacement tests for steel open-ended piles tested in dense sand.

To through more sight into the efficiency of the proposed self-tuning LM model, a more informative figure concerning the correlation between the measured and the computational values including; validation, training, testing and all data can be observed in the regression chart (Figure 4.31). The analysis demonstrated that a linear relationship can be seen with correlation coefficients of 0.990, 0.987, 0.980 and 0.986, respectively, substantiating that the newly implemented LM algorithm is a promising data-driven tool and has the ability to successfully learn up to 99% of the measured values.

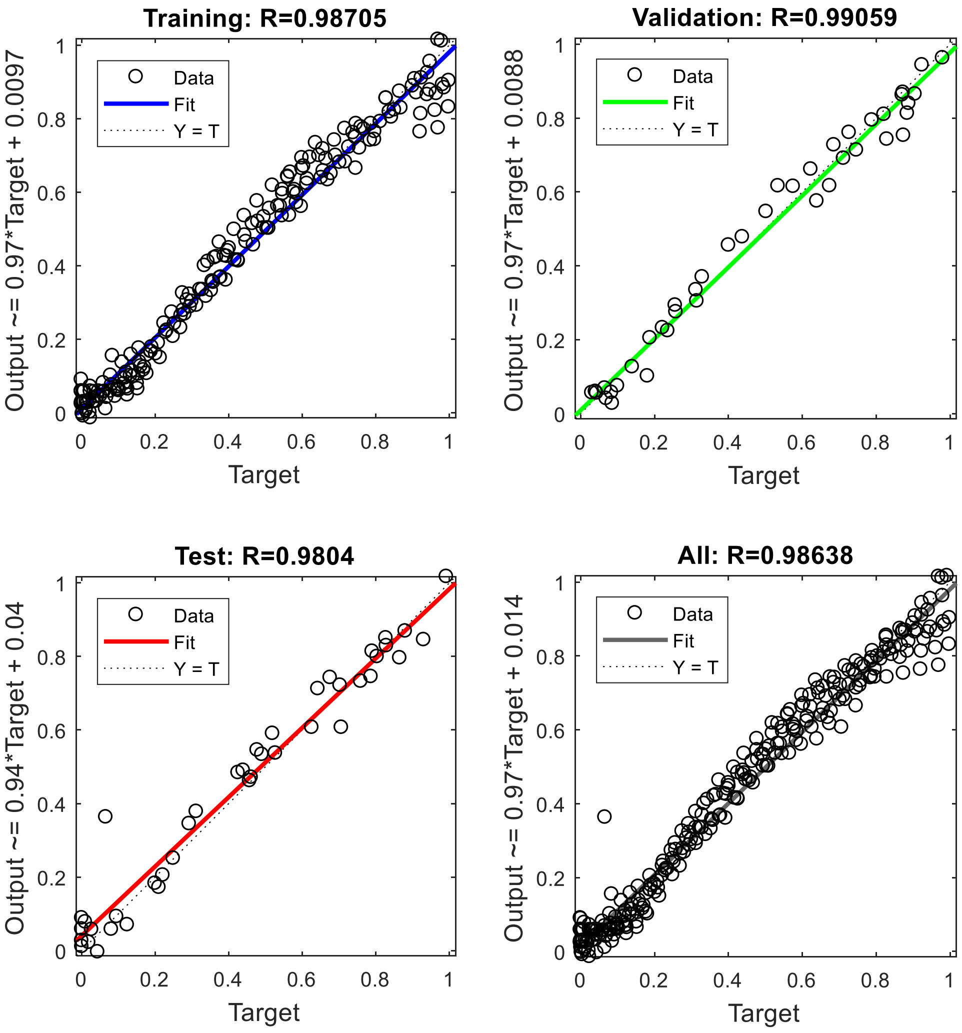

Figure 4-31: Regression graphs of the experimental versus predicted pile settlement for steel open-ended pile subjected to compression load.

Additionally, the implemented algorithm efficiency has been further examined, as emphasised in Figure 4.32. Based on the result of the scatter curve between targeted versus predicted values, significant agreement can be seen, with a coefficient of determination (R) and root mean square error (RMSE) of 0.980 and 0.065 with a relatively insignificant Pearson’s moment correlation coefficient (p) = 3.95x10^{-29}.

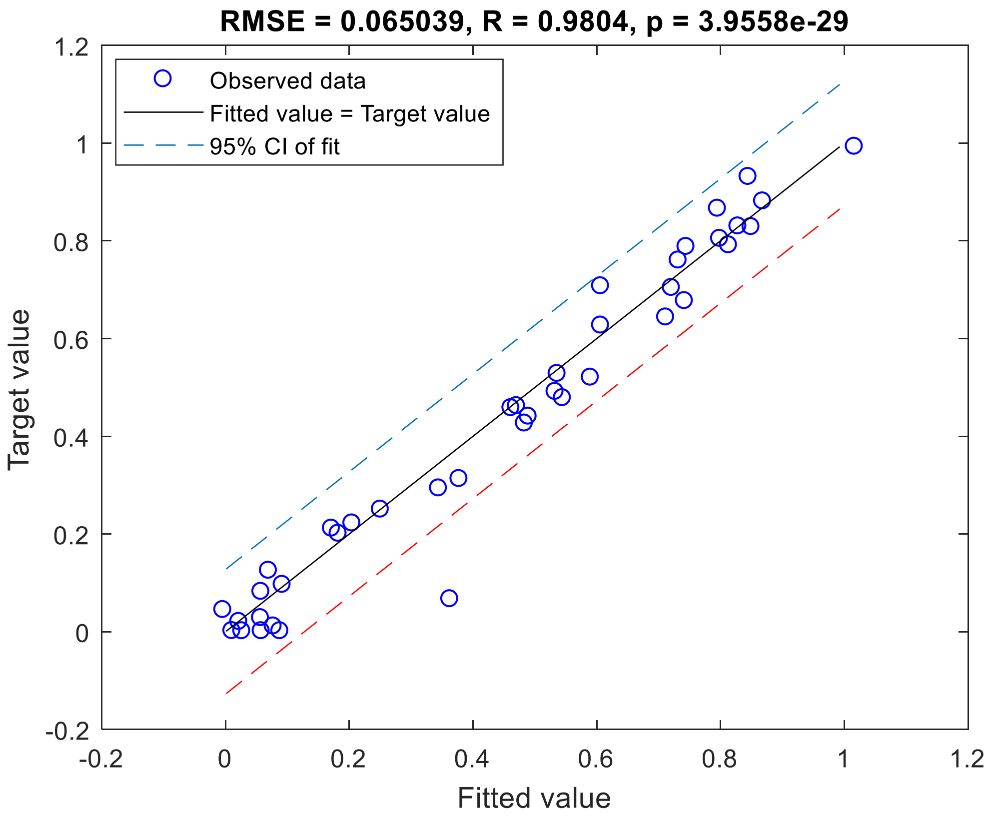

Figure 4-32: Calibration plot of the resulting model for the testing dataset at a 95% confidence interval (CI).

4.7.3 Comparison between the Trained LM Model with Traditional Design Methods for Steel Open-ended Piles

A structure's stability and safety relies largely on accurate assessment of the pile bearing capacity and associated settlement. Thus, several experimental and numerical methods have been performed to explore the behaviour of pile load-settlement. As stated previously, steel open-ended piles are normally utilised to facilitate the pile installation process and to increase soil bearing capacity in preference to closed-ended piles (Lehane and Gavin, 2001). Therefore, precise assessment of the bearing capacity of a single pile is an important aspect and plays a key role in the pile foundation design process. However, pile bearing capacity and associated settlement design procedures have traditionally been carried out separately. Moreover, it has been claimed by Fellenius (1989) that *"…the pile allowable load should be governed by a combined approach considering pile settlement and soil resistance intemperately acting together and influencing the value of each other."* On the basis of illustration for pile settlement determination, Poulos and Davis (1980); Vesic (1977) and Das (1995) demonstrated that the elastic settlement could contribute the major part of the final pile settlement. Moreover, for piles penetrated in sandy soil, elastic settlement accounts for the total final settlement (Murthy, 2002).

The reliability of the suggested approach has been further studied by comparing the experimental results of the pile-load settlement with the predicted results and comparing with most of the traditional methods proposed by: Poulos and Davis (1980); Vesic (1977) and Das (1995). The comparative study results, Figures 4.33 and 4.34 clearly illustrate that the predicted settlement using the LM training algorithm is in significant agreement with the best fitted-line (45°), and propose that the proposed model for steel open-ended piles can be implemented as an efficient highly reliable method for modelling load-settlement response with high levels of accuracy. Comparing the outcome of the LM model with the conventional design procedures (Figure 4.34), it can be realised that the level of convergence for the suggested approach is remarkably better than the proposed conventional methods.

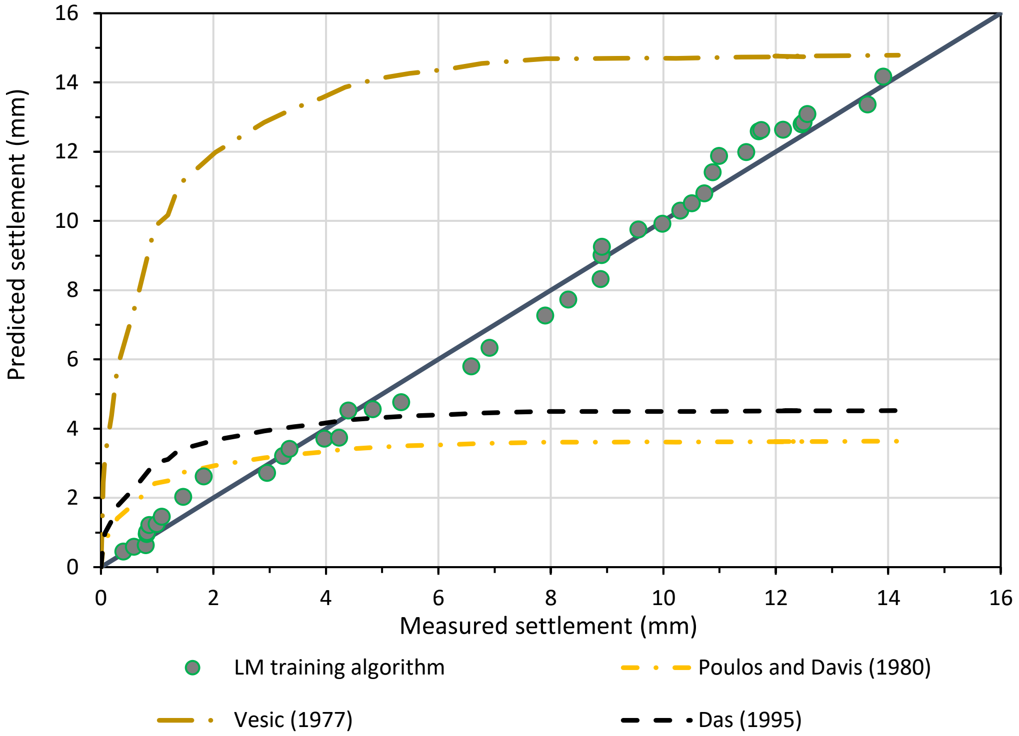

Figure 4-33: Profiles of measured versus predicted pile settlement for the proposed LM training algorithm compared with other design methods for steel open-ended piles.

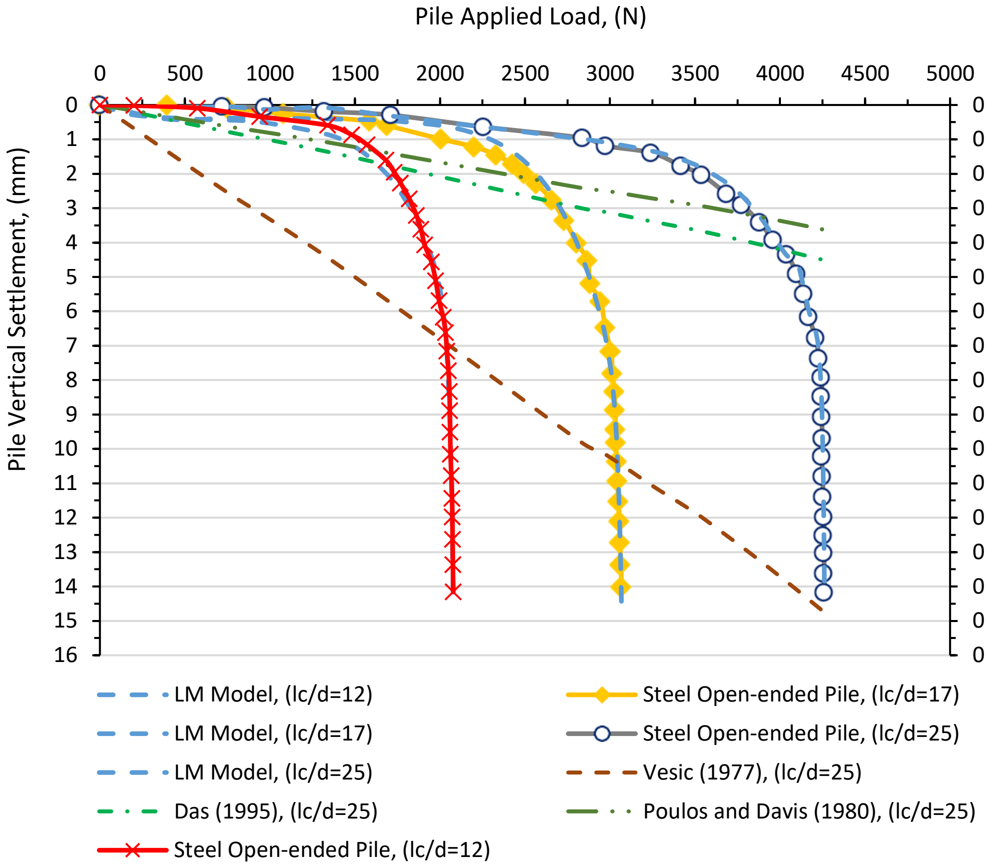

Figure 4-34: Applied load versus measured and predicted settlements for steel open-ended piles using the optimal trained model of the proposed LM algorithm with other methods.

4.8 Ultimate Bearing Capacity of a Steel Open-ended Pile under Compression Loads

The total ultimate capacity for a model pile subjected to compression loading can be developed from the combination of the end bearing and the skin friction resistance mobilised within the contacted soil. For steel open-ended piles, it has been reported by Hight et al. (1996) that the static axial capacity of a plug of sand with slenderness ratio in excess of 10 is large. The axial capacity for steel open-ended piles subjected to compression load was determined from pile load-displacement curves as presented in

Figure 4.35. With the reference to the normalised pile load-settlement, as would be anticipated, it can be observed that the ultimate pile capacity increases with the increase in the pile penetration length and the sand relative density. For model piles penetrated in dense sand with a slenderness ratio (Lc/d) equal to 12, the ultimate pile capacity is about 3 and 8 times in comparison to the ones penetrated in medium and loose sand. Moreover, for a pile with length-to-diameter ratio of 17, the pile ultimate capacity in dense sand is about 4 times the result for medium sand and about 9 times higher than the pile capacity in loose sand.

Furthermore, for a model pile with length-to-diameter ratio of 25, the ultimate pile capacity in dense sand is about 4 times higher than the result for medium sand and about 8 times higher than the pile capacity in loose sand. It is worth pointing out that the ultimate pile bearing capacity for steel open-ended (low-displacement) piles is less in comparison to the steel closed-ended and concrete piles. This can be assigned to the fact the radial effective stress distribution for steel closed-ended and precast concrete piles is higher than that for steel open-ended piles, suggesting that, as would be expected, the driving process of the open-ended piles does not considerably alter the initial sand relative density (Jeffrey, 2012).

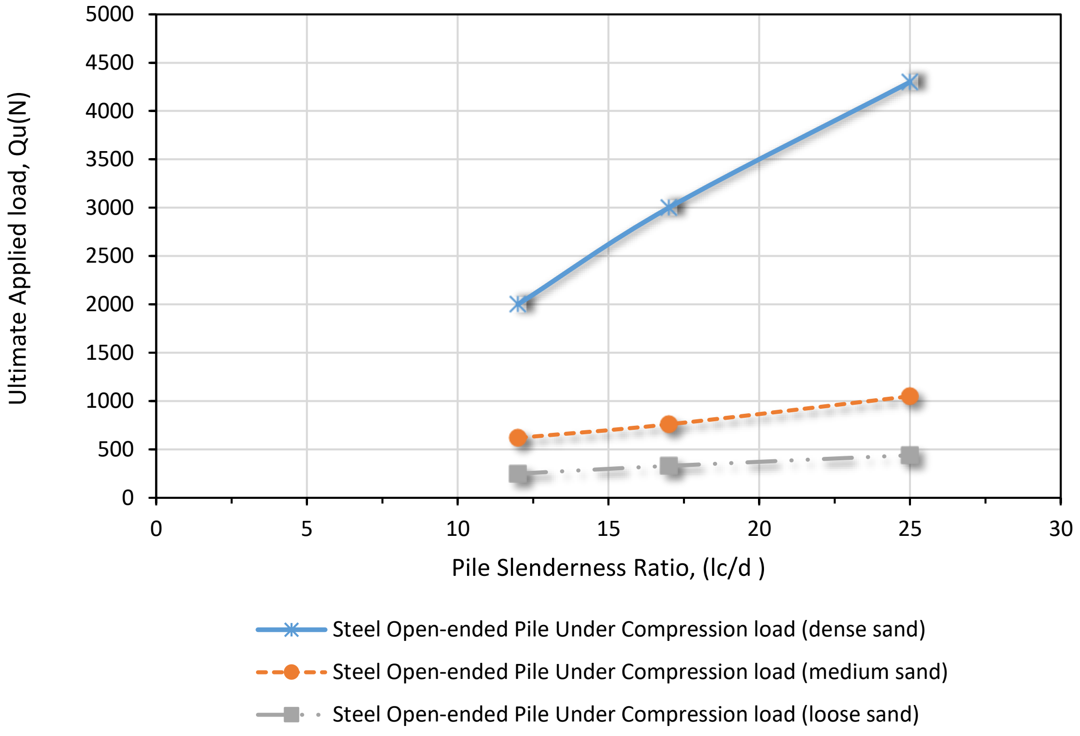

Figure 4-35: Plot shows ultimate pile capacity profile versus pile slenderness ratio for steel open-ended piles.

4.9 Summary

The results of the experimental pile load-settlement behaviour and the predicted values using the LM training algorithm performed on precast concrete piles, steel closed-ended and steel open-ended piles penetrated in three sand relative densities, covering loose, medium and dense under compression loads have been clearly presented and discussed throughout this chapter. Additionally, the feasibility of an evolutionary, self-tuning LM, enhanced by a comprehensive statistical analysis, to capture the full response of pile were also discussed. However, a summary of the findings can be found below:

- The optimum structure of the ANN model was found at a topology of 5:10:1 with a tangent sigmoid *“tansig”* transfer function between the input and hidden layer and linear *“purelin”* transfer function between the hidden and output layers.

- The statistical analyses suggest that the most influential parameters on the pile load-settlement curves, at different statistical significance level, are the pile applied load, P and the sand-pile interface friction angle, δ. Conversely, pile slenderness ratio, Lc/d, pile axial rigidity, EA and pile effective length, Lc have been identified to have least impact on the pile settlement.
- The adopted LM algorithm has several favourable features (i.e. generalisation ability, efficiency and ease of application), fast teaching speed since locally tuned neurons, and the learning process takes place without jumping over the best solution, which make it the first choice to model the complex nonlinear systems.
- The ultimate pile bearing capacity for concrete piles was found to be higher than the ultimate capacity for both steel open-ended and steel closed-ended piles. This can be attributed to the contribution of the higher skin friction resistance for concrete piles.
- To further reveal the applicability of the LM algorithm, a graphical comparison was made between the applied algorithm and conventional methods. Based on the outcomes, the newly developed approach is superior to the traditional empirical relationships as confirmed by the performance skills metric, which reveals the suitability of the algorithm and its potential in future applications.
- The graphical comparison results also revealed that the analytical methods suggested by Poulos and Davis (1980) and Das (1995) tend to underestimate the pile bearing capacity. In addition, the method offered by Vesic (1977) is at the bottom of the list of performance with the later having the poorest quality of prediction among the rest of the design methods.

CHAPTER 5

Results and Discussion: Load-Settlement Behaviour for Precast Concrete, Steel Closed-ended and Steel Open-ended Piles Subjected to Uplift Loads

5.1 Introduction

On the basis of describing the findings of the experimental and predicted load-displacement curves, this chapter comprises the results of the experimental pile-load tests for different types of model piles tested in sand, covering three relative densities of loose, medium, and dense sand. Details about the pile types, pile materials and cross-sectional dimensions are described in section 3.5. Each load-settlement response for the various types of model piles was modelled using the LM algorithm. It is worth noting that the data screening process allowed evaluation of the dataset being studied. These dataset screening test results were also utilised to check the dataset size condition and detection of outliers. Additionally, statistical analyses were used to identify the relative importance and the statistical significance of each model input parameter on the model output.

As shown in the previous chapter, the uplift pile-load carrying capacities are clearly summarised in three phases, phase (i) revealed the results of the precast concrete piles along with the modelling approach for each pile slenderness ratio and sand relative density. Series (ii) shows the results of the steel closed-ended piles, which were compared with the predicted results, and finally series (iii) indicates the results of the steel open-ended piles, which were also compared with the modelled pile load tests.

5.2 The LM Training Algorithm for Modelling Load-settlement Response of Piles Subjected to Uplift Loads

This part of the chapter describes the performance of the LM algorithm used in the modelling of load-displacement tests for model piles subjected to uplift loads. As mentioned previously, one of the obvious advantages of the introduced method is that no training parameters are required to be adjusted for the trained algorithm, thus avoiding many difficulties and limitations associated with the use of the traditional artificial intelligence methods such as convergence issues, and local minima (Deo and Şahin, 2015). In addition, the LM algorithm has been identified as the most efficient approach and is well documented as achieving a much higher performance by making training faster, more reliable, stable and converging more often than other artificial intelligence methods (Abdellatif, 2013; Jebur et al., 2018b). Details of the LM algorithm model developments, dataset pre-processing and statistical analyses are summarised in the following sub-headings.

5.2.1 Model Input and Output

Field (2008) claimed that any IV with statistical significance *"Sig."* value greater than 0.05 can be ignored form the input space as it has no potential significant influence on the suggested model output. As stated previously (section 4.2.1), based on the statistical analysis investigation, five IVs have been identified as the most influential input parameters affecting pile settlement. These factors were applied load, *P*, pile slenderness ratio, Lc/d, pile axial rigidity, EA, pile effective length, Lc and the sand-pile angle of friction, δ as revealed in the statistical analyses (Tables 5.1, 5.2, and 5.3). As with the model used in the compression pile-load tests, the optimal structure of the LM trained network has been found at structure of 5:10:1. The database values were also normalised, as this step is important in order to get high network performance, as detailed in section 4.2.1.

5.2.2 Statistical Analyses and Dataset Pre-processing

Introduction of the statistical analyses on the studied data highlights the significance of each IV on the model output. Tabachnick and Fidell (2013) demonstrated that the experimentally gathered dataset must be evaluated and passed through different steps to develop a reliable database for the applied algorithm. Therefore, the total dataset was accurately screened to determine the relative importance "*Beta.*" value, the size of the data and to explore and detect the presence of outliers.

Statistically, any IV with a relative importance *"Beta."* value close to one means this parameter exerts a high contribution level to the model output (Pallant, 2011; Hashim et al., 2017b; Hashim et al., 2017a). Results of the statistical analyses are presented in Tables 5.1, 5.2 and 5.3. According to the Beta values, the applied load and the sand-pile angle of interface friction for concrete and steel closed-ended pile models have been acknowledged to play a significant role in the model output. Whereas, for steel open-ended piles, the applied load and the pile slenderness ratio were identified to play the highest level of contribution over the five IVs.

5.2.3 Data Size Condition

The condition of the dataset size must be satisfied in order to develop a reliable model with high performance (Faber et al., 2011; Pallant, 2011). Tabachnick and Fidell (2013) documented that, by recalling Equation 4.4, for the five input parameters, the minimum dataset required to develop the model must be 90. In the present study, the dataset number for each model (concrete pile, steel closed-ended and steel open-ended) the total number of the recorded points from the experimental pile-load tests used to train the trained model were 290, 265 and 266, respectively. Therefore, the dataset condition has been met. A summary of the main statistical parameters for the training, testing and validation dataset, used to develop and train the LM for concrete, steel closed and open-ended piles subjected to uplift loads, are specified in Tables 5.4, 5.5, and 5.6, respectively.

5.2.4 Outliers

The model's generalisation ability can be highly influenced by the presence of such extreme points (Hashim et al., 2017c). Therefore, all datasets must be statistically tested and evaluated before being processed. According to the statistical criteria suggested by Pallant (2011), the presence of outliers can be detected using the Mahalanobis distances (MDs) indicator (see section 4.2.2). In the present model, the maximum MD must be less than 20.52, which is the critical value for five IVs (Pallant, 2011). For model concrete and steel closed-ended pile statistical models, the MDs were determined at 25.705 and 27.01, for one point only, these values are higher than the acceptable limit as defined previously. To explore whether this point has an influence on the model, Tabachnick and Fidell (2013) suggested to calculate the Cook's Distance (COO_1), as any case with COO_1 greater than 1.0 may influence the results of the model output. Tables 5.1 and 5.2 illustrate that the Cook's Distance (COO_1) values for both statistical models are less than 1.0, which confirmed that the model efficiency was not influenced by the presence of one extreme value only. In addition, for model steel open-ended pile statistical model, Table 5.3 reveals that the maximum detected MD was within the acceptable limit, which indicates the data reliability.

Table 5-1: Statistical analyses results for the concrete pile model.

IVs	Beta. value	Maximum detected MDs	COO_1
Applied load (P)	0.505	25.705	0.0034
Sand-pile angle of interface friction (δ)	0.401		
Axial rigidity (EA)	0.013		
Slenderness ratio (Lc/d)	0.068		
Pile effective length (Lc)	0.179		

Table 5-2: Statistical analyses results for the steel closed-ended pile model.

IVs	Beta. value	Maximum detected MDs	COO_1
Applied load (P)	0.817	27.011	0.018
Sand-pile angle of interface friction (δ)	0.568		
Axial rigidity (EA)	0.009		
Slenderness ratio (Lc/d)	0.205		
Pile effective length (Lc)	0.118		

Table 5-3: Statistical analyses results for the steel open-ended pile model.

IVs	Beta. value	Maximum detected MDs
Applied load (P)	0.545	15.211
Sand-pile angle of interface friction (δ)	0.471	
Axial rigidity (EA)	0.006	
Slenderness ratio (Lc/d)	0.700	
Pile effective length (Lc)	0.431	

Table 5-4: Statistical characterisation of testing, training, and validation dataset for concrete piles.

Data Set	Statistical Parameters	**Input Variables**					**Output**
		Load (kN)	Slenderness ratio, Lc/d	Pile length, (m)	Pile axial rigidity, EA (MN)	Sand-pile friction angle, δ°	Settlement, (mm)
Training Set	Max.	1.115	25	1	47.2	36	14.439
	Min.	0.017	12	0.48	47.2	28.8	0.0045
	Mean	0.381	17.084	0.714	47.2	26.216	6.930
	S.D.*	0.297	1.346	0.212	0.00	1.126	4.383
	Range	1.097	13	0.52	0.00	7.2	14.434
Testing Set	Max.	1.116	25	1	47.2	32.5	14.328
	Min.	0.070	12	0.48	47.2	28.8	0.045
	Mean	0.392	18.245	0.760	47.2	26.563	6.078
	S.D.*	0.290	1.345	0.215	0.00	1.128	4.291
	Range	1.045	13	0.52	0.00	3.7	14.28
Validation Set	Max.	1.117	25	1	47.2	36	13.898
	Min.	0.076	12	0.48	47.2	28.8	1.05
	Mean	0.427	17.958	0.751	47.2	26.22	7.22
	S.D.*	0.329	1.362	0.222	0.00	1.125	4.21
	Range	1.040	13	0.52	0.00	7.2	12.848

*Standard deviation

Table 5-5: Statistical characterisation of testing, training, and validation dataset for steel closed-ended piles.

Data Set	Statistical Parameters	**Input Variables**					**Output**
		Load (kN)	Slenderness ratio, Lc/d	Pile length, (m)	Pile axial rigidity, EA (MN)	Sand-pile friction angle, δ°	Settlement, (mm)
Training Set	Max.	0.497	25	1	251.18	19	14.40
	Min.	0.0001	12	0.48	251.18	17	0.001
	Mean	0.186	17.489	0.731	251.18	17.95	6.580
	S.D.*	0.139	1.351	0.216	0.00	1.049	4.468
	Range	0.4969	2.083	0.52	0.00	2	14.399
Testing Set	Max.	0.4975	25	1	251.18	19	14.152
	Min.	0.0001	12	0.48	251.18	17	0.0005
	Mean	0.1961	17.35	0.724	251.18	18.04	6.277
	S.D.*	0.147	1.341	0.210	0.00	1.048	4.825
	Range	0.497	13	0.52	0.00	2	14.151
Validation Set	Max.	0.476	25	1	251.18	19	13.604
	Min.	0.001	12	0.48	251.18	17	0.002
	Mean	0.718	17.325	0.718	251.18	17.985	5.862
	S.D.*	0.114	1.309	0.194	0.00	1.051	4.317
	Range	0.475	13	0.52	0.00	1.117	13.602

*Standard deviation

Table 5-6: Statistical characterisation of testing, training, and validation dataset for steel open-ended piles.

Data Set	Statistical Parameters	Input Variables					Output
		Load (kN)	Slenderness ratio, Lc/d	Pile length, (m)	Pile axial rigidity, EA (MN)	Sand-pile friction angle, δ°	Settlement, (mm)
Training Set	Max.	0.635	25	1	251.18	19	14.913
	Min.	0.015	12	0.48	251.18	17	0.021
	Mean	0.198	17.457	0.730	251.18	17.936	6.147
	S.D.*	0.172	1.355	0.217	0.00	1.048	4.466
	Range	0.620	13	0.52	0.00	2	14.448
Testing Set	Max.	0.6348	25	1	251.18	19	14.2705
	Min.	0.031	12	0.48	251.18	17	0.1085
	Mean	0.207	17.956	0.741	251.18	17.804	8.2963
	S.D.*	0.191	1.289	0.186	0.00	1.049	4.3544
	Range	0.6038	13	0.52	0.00	2	14.162
Validation Set	Max.	0.6326	25	1	251.18	19	14.35
	Min.	0.0205	12	0.48	251.18	17	0.0055
	Mean	0.1952	16.618	0.699	251.18	18.017	6.835
	S.D.*	0.1650	1.3761	0.226	0.00	1.052	4.671
	Range	0.6121	13	0.52	0.00	1.117	14.344

*Standard deviation

5.3 Feasibility of the LM Algorithm for Modelling Load-displacement Behaviour of Concrete Model Piles Penetrated in Loose, Medium and Dense Sandy Soil Subjected to a Wide Range Uplift Loading

The experimental uplift pile-load tests along with the application of the LM algorithm to simulate pile settlement for different types of model piles, penetrated in sandy soil and subjected to uplift loading are presented and discussed in this section. The effectiveness of the employed algorithm of the optimal model was statistically evaluated using the skill indicators listed in section 4.3, as recommended by Gordan et al. (2016). However, the robustness of the LM algorithm for each model subjected to uplift loads has been assessed, as reported in the following sections:

5.3.1 Concrete Piles under Uplift Load

The LM training scheme was applied as it has many advantages over the use of the conventional artificial neural network algorithms (Sharma et al., 2017). In the current study, the load-settlement behaviour was modelled from five easy to obtain parameters and using a high efficiency predictive model by adopting supervised feed-forward multi-layer perceptron using back-propagation training techniques. The performance analyses results during the training process are revealed in Figure 5.1. The results revealing that the plot of convergence depicts a substantial fall in mean square error (MSE) when the number of iterations increases. It can also be shown that the training process stopped at a relatively negligible MSE of 0.0039 at an epoch of 125, to avoid over fitting once the cross-validation error started to increase; this can also be defined as early stopping criteria to avoid the over fitting phenomenon. Furthermore, the profile of the error histogram (EH) for the trained network is illustrated in Figure 5.2. The majority of the training, testing and validation data sub-sets coincides with the zero error line, where more than 98% of the errors are included in the two central bins (0.01 and -0.01).

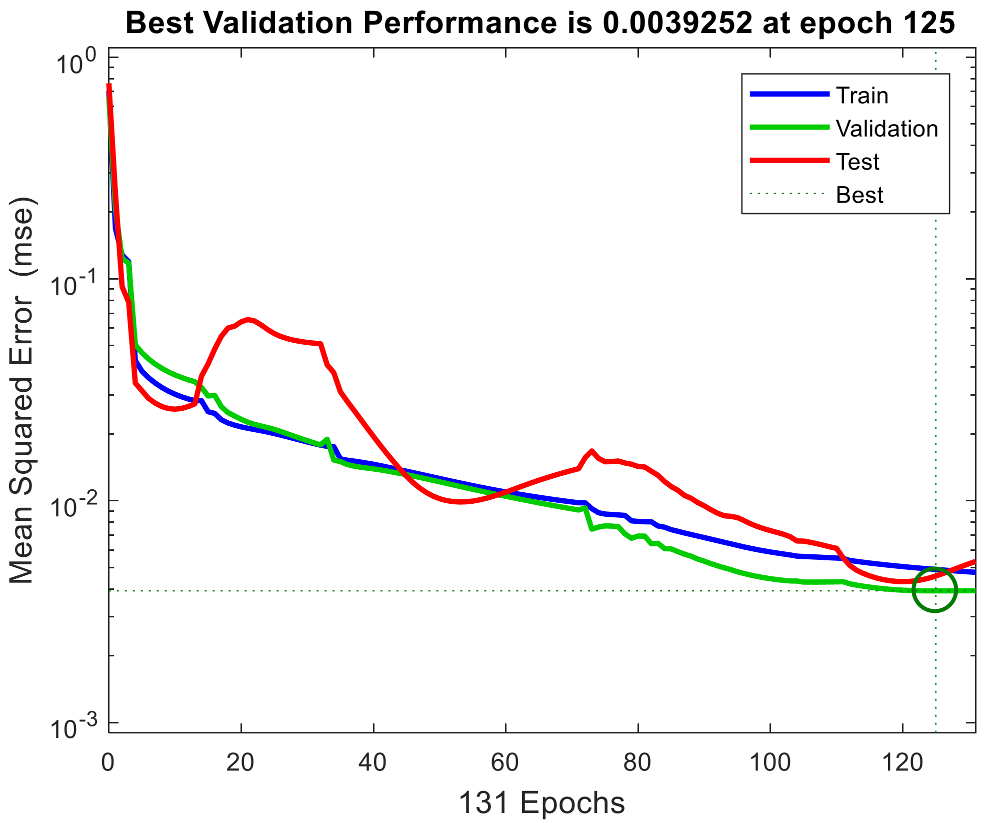

Figure 5-1: Plot of the LM analyses for concrete developed model during the training process.

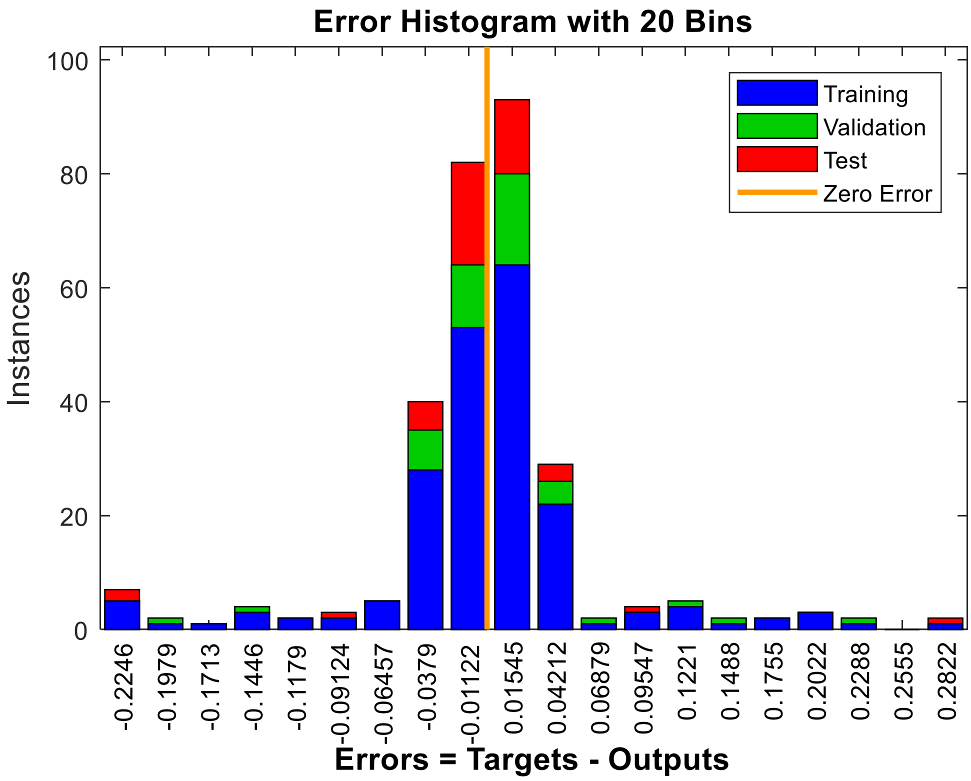

Figure 5-2: Plot of the LM algorithm error historam.

5.3.2 Measured Versus Predicted Pile Load Tests for Concrete Piles Subjected to Uplift Load

The results of the measured versus predicted load carrying capacity of piles subjected to uplift loads are graphically presented and discussed in this section. As stated previously, a series of experimental pile load tests were performed on concrete piles subjected to a wide range of axial uplift loads. The testing programme comprised of three pile slenderness ratios (Lc/d) of 12, 17, and 25) tested in different relative densities of sand – loose, medium and dense. It can be observed that all pile load-displacement curves are non-linear and failed by punching shear. Moreover, the variations of the axial load along the pile length are typical for canonical pile foundations under axial mechanical loading systems. A visual inspection of pile load tests demonstrated that the plastic conditions associated with the pile-soil interface is the main cause for the non-linearity exhibited by the pile load-displacement curves.

Figures 5.3, 5.4, and 5.5 illustrate the distribution of the axial load carrying capacity along the length of piles at different phases of mechanical uplift loads. It is noteworthy that a clear elastic behaviour can be shown in the initial stages of the applied load when the pile corresponding displacement reached about 1% of pile diameter. Moreover, it must be emphasised that the plastic mechanisms in the soil-pile interaction are the main leading source for the non-linearity of the load-displacement curve; as the uplift load increases, the soil-yielding effect can be clearly identified, where non-linearity is pronounced for uplift applied load ranges from 60 to 90 N, 100 to 140 N and 180 to 230 N for piles with slenderness ratios of 12, 17, and 25 tested in loose sand. Beyond these loads, the displacement increases rapidly, at approximately constant load, until reaching a maximum pile capacity, which equals 10% of the pile diameter, following the pile load test criteria designated by the BSI (BS EN 8004:1986). Figures 5.4 and 5.5 document the load-settlement results for the piles driven in medium and dense sand. Similarly, in the initial stages of the applied load, the load carrying capacity exhibits a noticeable elastic branch. As the range of the axial uplift applied loads increases, the non-linearity increases due to the existence of soil yielding, which can be seen within the range of 100 to 150 N, 200 to 300 N and 350 to 425 N for piles driven in medium sand, and 300 to 450 N, 600 to 750 N and 900 to 1100 N for piles embedded in dense sand. The pile load-settlement distributions denote excessive settlement beyond these loads, and continue to settle with approximately constant applied loads, indicating failure. It can also be seen that the LM training algorithm performs well for all model piles in different sand relative densities. In addition, it is apparent from the predicted response that the LM algorithm is an efficient predictive tool that has the ability to fully capture the non-linear response of pile load-displacement curves. In essence, the results show that the model performs well with a correlation coefficient of 0.9864 as noted for the testing datase, which verified that the employed LM algorithm could efficiently simulate pile load-settlement behaviour with obvious advantages.

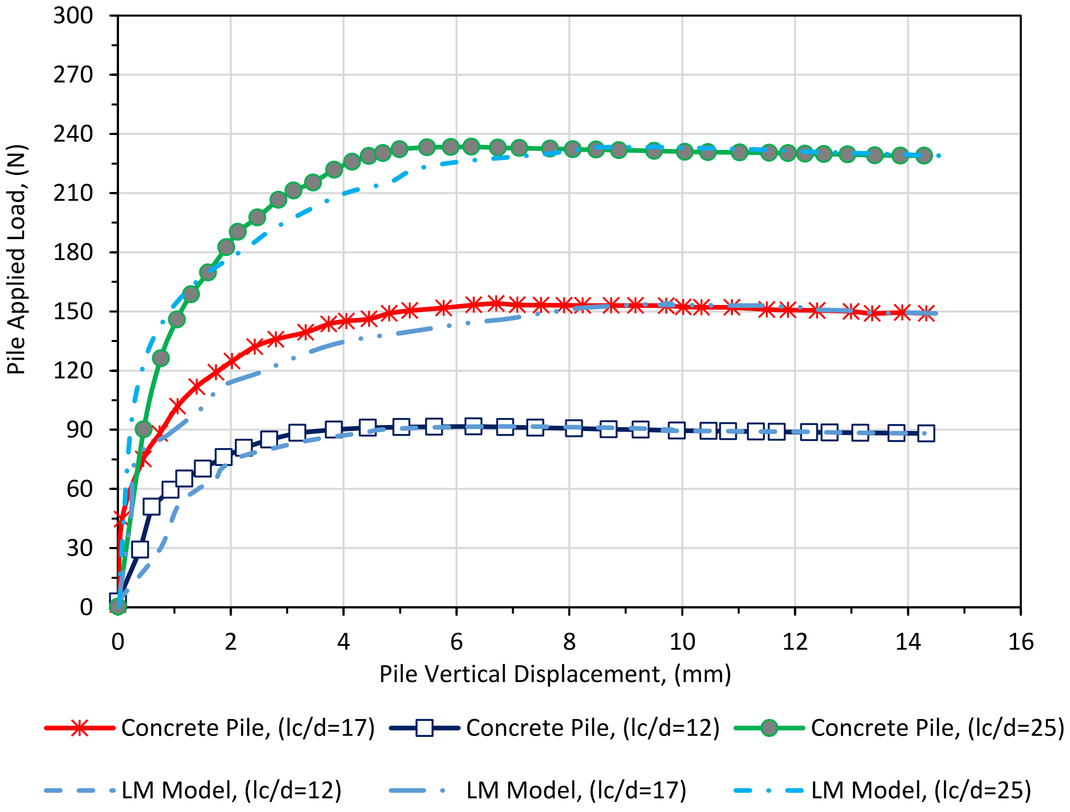

Figure 5-3: Profiles of measured versus predicted uplift pile load tests for concrete piles embedded in loose sand.

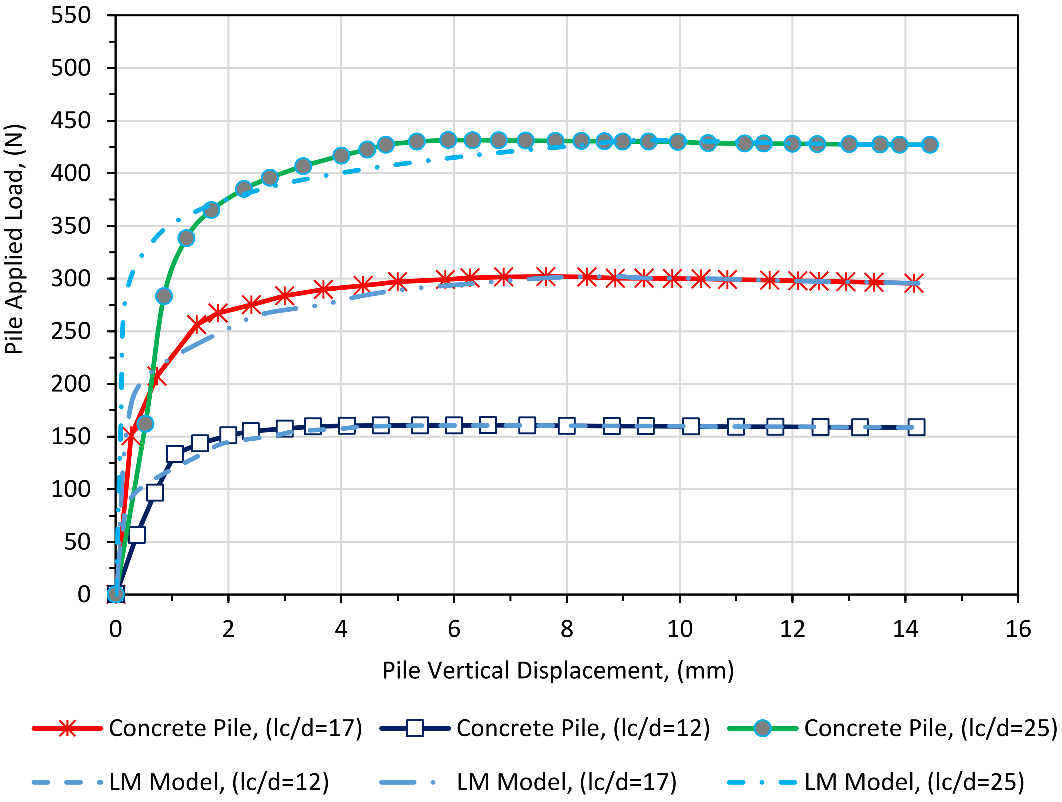

Figure 5-4: Profiles of measured versus predicted uplift pile load tests for concrete piles embedded in medium sand.

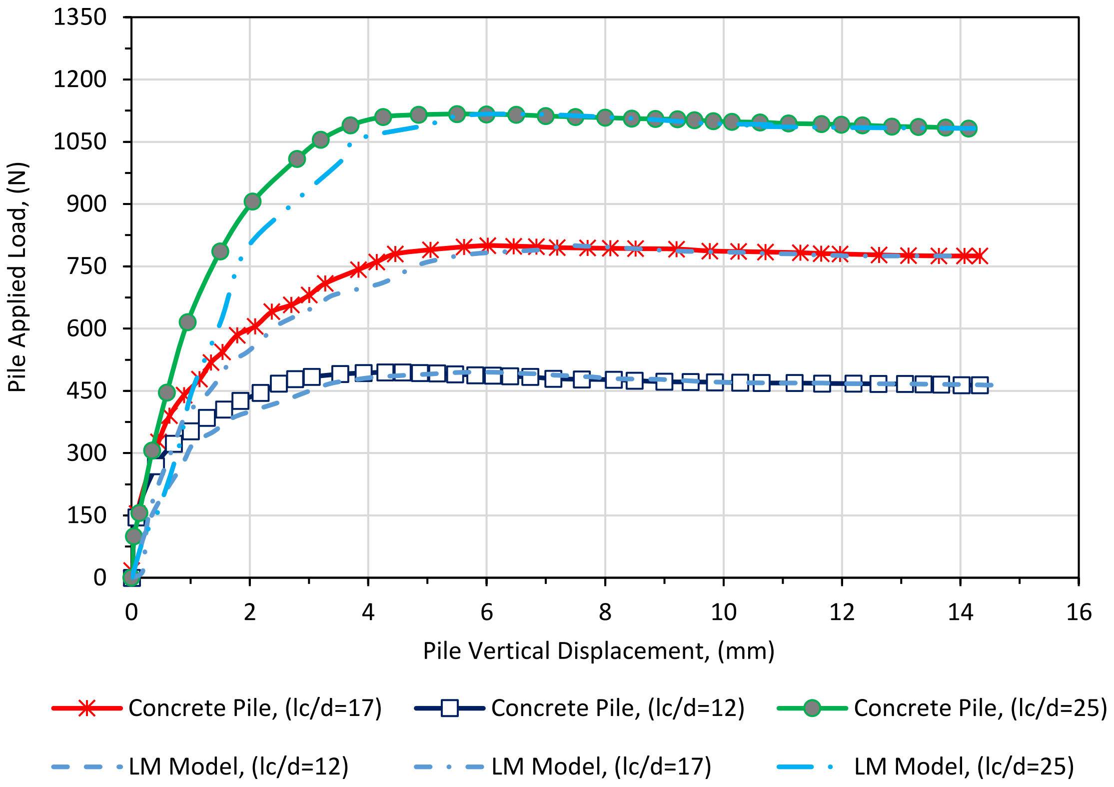

Figure 5-5: Profiles of measured versus predicted uplift pile load tests for concrete piles embedded in dense sand.

Furthermore, regression plots between the measured and the computational values of pile settlement for training, validation, testing and all data of the developed model denotes high consistency between the measured and the predicted values (Figure 5.6) and this was supported by the higher correlation coefficient the lower percentage error. This could also indicate that the developed prediction model has a good confidence level in modelling the model output and gives a close approximation of actual versus predicted pile settlement compared to the best-fit line.

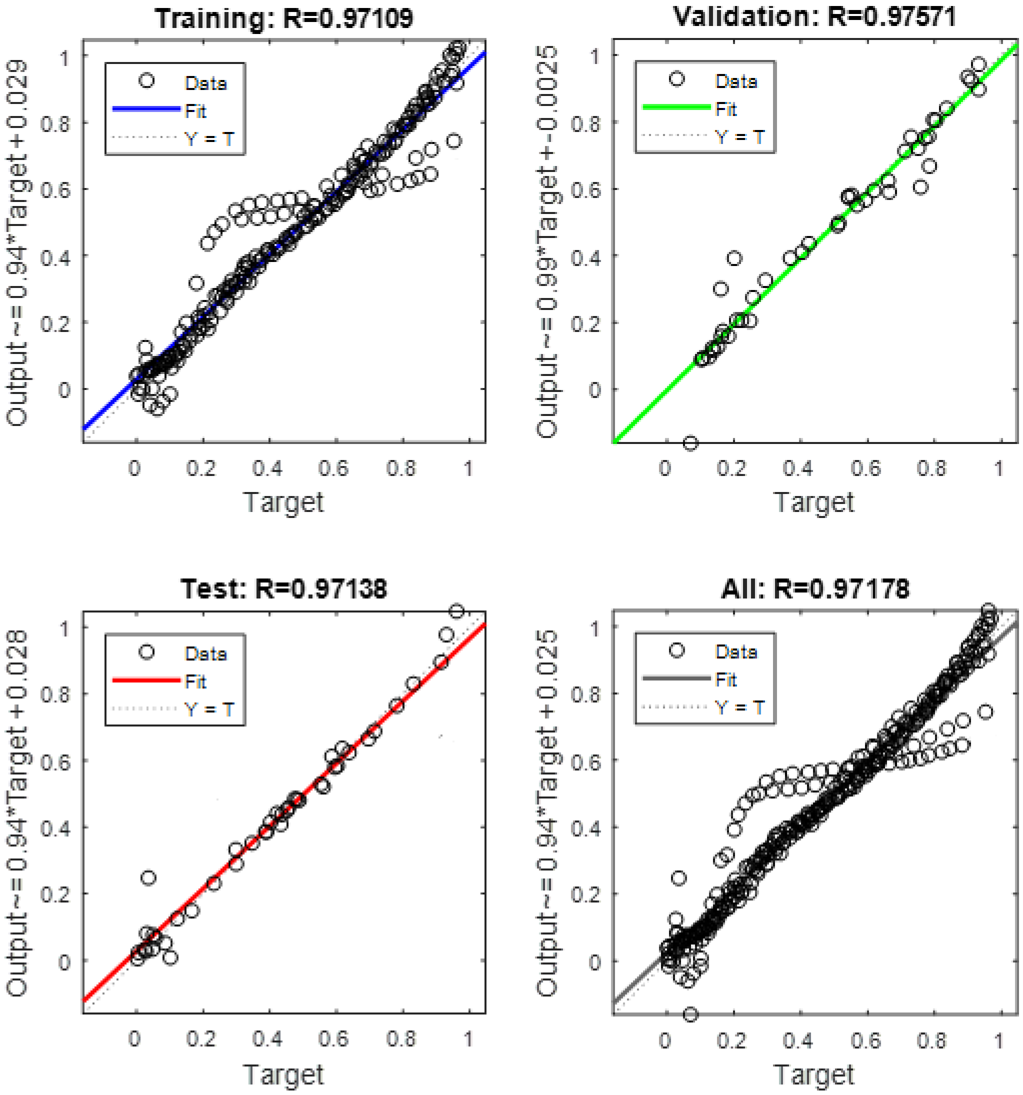

Figure 5-6: Regression graphs of the experimental versus predicted pile settlement for concrete pile subjected to uplift load.

Moreover, the assigned testing dataset (15% of the dataset) has been applied to further evaluate the generalisation ability of this approach with a 95% confidence interval level. The advantage of the testing dataset is to check and assess the network efficiency in the developed model where an independent dataset cannot be afforded (Armaghani et al., 2016). Significant consistency can be shown (Figure 5.7) between the actual versus predicted pile settlement, with a correlation coefficient (R) and a root mean square error (RMSE) of 0.971 and 0.067. This means that the proposed model for the range of the dataset being studied has the capability to model pile load-settlement with a low error percentage.

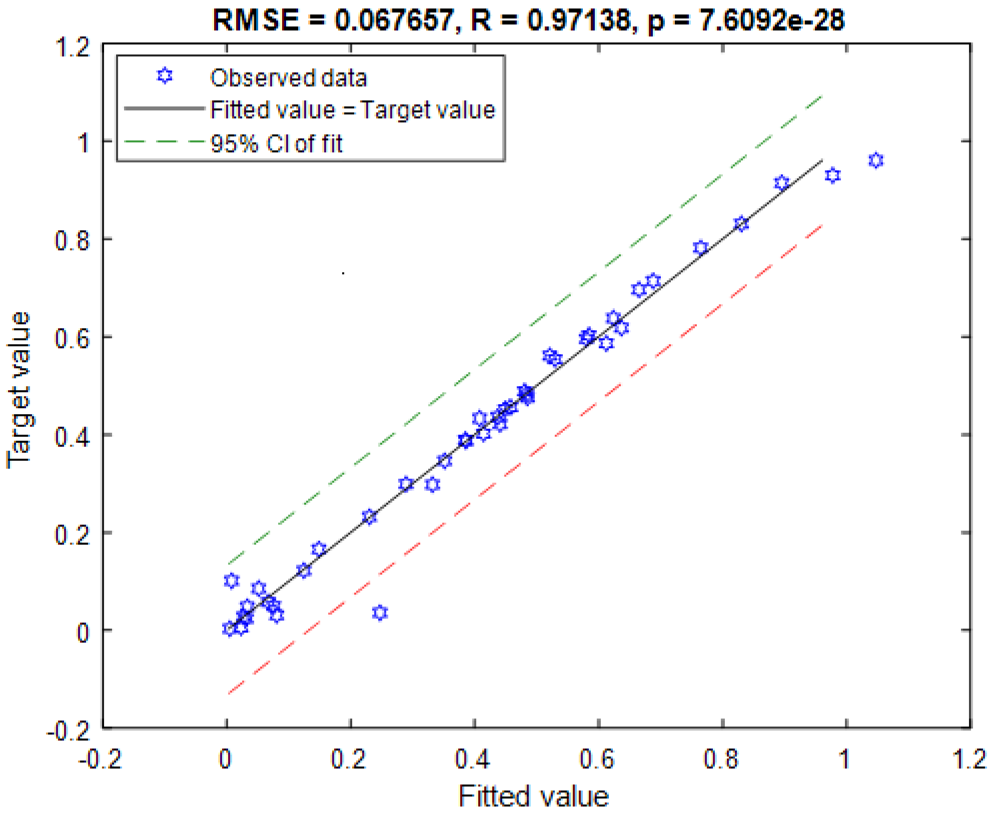

Figure 5-7: Calibration plot of the resulting model for the testing dataset at a 95% confidence interval (CI).

5.3.3 Assessment of the LM Model Performance for Concrete Piles under Uplift Load with the Existing Predictive Approaches

The increasing utilisation of straight skin frictional piles to resist pull-out loads requires accurate evaluation of ultimate uplift capacity for cost effective and safe pile foundation design reasons. In this section, the efficiency of the proposed approach has been further examined by providing a comparison of LM fitting accuracy of the current study with unseen experimental dataset and with those obtained using the commonly applied models that are documented by Meyerhof (1973), Das (1983), and Truncated cone model (see section 2.7), which is used by most geotechnical engineers (Shanker et al., 2007). It is notable that the pile ultimate uplift capacity was selected based on the pile failure criterion of 10% of pile diameter/cross-section (BSI, BS EN 8004:1986). The numerical comparative study results (Table 5.7) demonstrate the integrity and robustness of the proposed method as it is in good agreement with the experimental results and performs better than the recognised methods discussed. In addition, as depicted, the Truncated cone and Das models provide inaccurate prediction values for all piles slenderness ratios. As demonstrated numerically in Table 5.4, this study's results revealed that the Meyerhof (1973) model is by far the best, giving good agreement compared to the results of the experimental and predicted models for all pile slenderness ratios in the described soil stiffness.

Table 5-7: Measured and predicted uplift capacity of the precast concrete piles.

Lc/d ratio	Truncated cone's model, (N)	Meyerhof's model, (N)	Das's model, (N)	Experimental results, (N)	The proposed LM model, (N)
Dense sand, D_r (83%)					
12	268	378	1246	490	485
17	752	613	1941	750	710
25	2392	851	2757	1100	1055
Medium sand, D_r (51%)					
12	183	124	397	160	159
17	506	228	733	300	295
25	1609	344	1080	420	400
Loose sand, D_r (18%)					
12	136	143	231	90	87
17	369	117	367	150	140
25	1174	184	581	225	210

5.4 Factors Affecting Pile Capacity for a Concrete Pile Subjected to Uplift Loads

The ultimate applied load for a concrete model pile subjected to uplift load has been determined with reference to the pile slenderness ratio and sand relative density (Institution of Civil Engineers, 2007). When a model pile is penetrated in a dry sand and subjected to uplift load, the major source for increasing the uplift pile capacity is the mobilised skin friction developed between sand and pile in the radial effective zone (Jebur et al., 2016). Therefore, based on a given formula (Eq. 2.3), the pile embedment length, sand-pile interface friction angle and the sand relative density can be considered as the main factors that govern the pile capacity subjected to uplift loads.

The ultimate uplift pile capacity is the applied load after which the load-displacement response slope reaches zero or a constant value. The results illustrated that the pile bearing capacity increases as the sand relative density and pile penetration length increase, as reported in Figure 5.8. For a pile slenderness ratio of 12 penetrated in loose sand, the rate of increase in the ultimate axial capacity is about 2 times in medium sand and about 5 times in dense sand. While, for pile slenderness ratio of 17, the pile ultimate capacity is about twice in medium sand and just over 7 times in dense sand. For the pile slenderness ratio of 25, the pile ultimate capacity is also about 2 times in medium sand and just under 5 times higher in the case of dense sand. The reasons for this increment could be associated with an increase in the sand density together with the increasing overburden pressures in the effective radial zone, which have a significant effect on the mobilised pile shaft resistance.

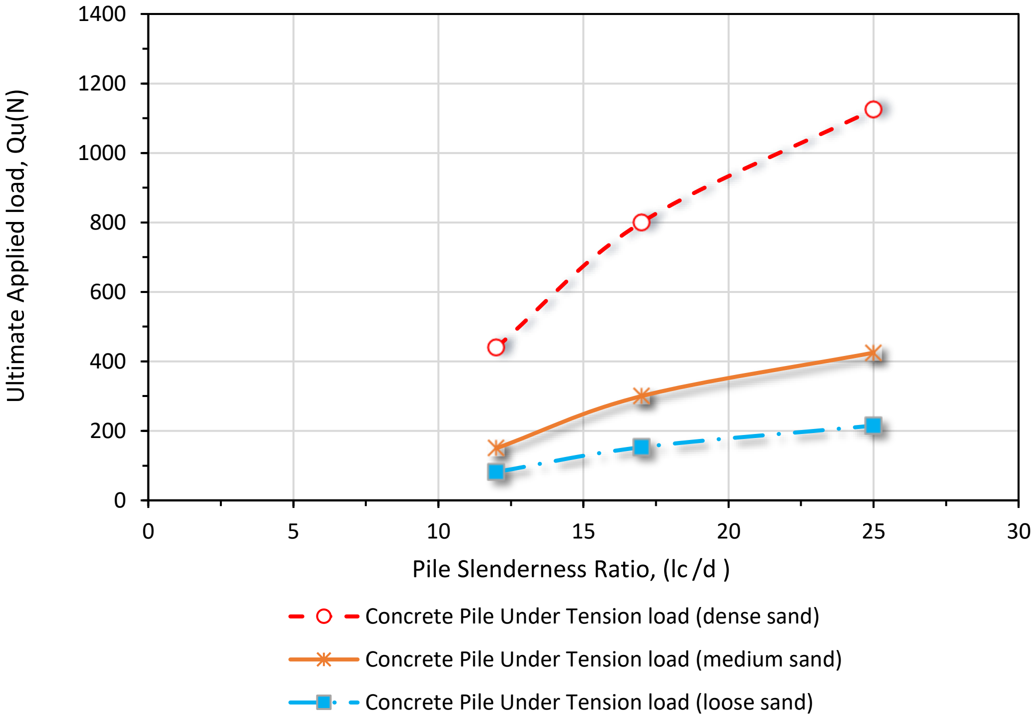

Figure 5-8: Distribution of the ultimate pile capacity with pile slenderness ratio for concrete piles under uplift load.

5.5 Feasibility of the LM Algorithm to Simulate Load-displacement Response of Steel Closed-ended Piles Penetrated in Loose, Medium and Dense Sandy Soil subjected to a Wide Range of Uplift Loading

This part of the study presents the experimental pile load-displacement curves for model steel closed-ended piles subjected to uplift loading system. In addition, the applicability of the proposed approach to model the experimental pile load-settlement is also discussed. The competence of the LM model was evaluated using the metric skill indicators as clearly reported in the previous section. For validation aspects, a comparison between the proposed model and the most conventional design procedures are also discussed.

5.5.1 Performance Evaluation of the Proposed LM Algorithm

Figure 5.9 reports the LM network performance analyses for steel closed-ended model piles under uplift loads during the training process. It should be mentioned that the learning process is stopped either when the number of iterations reaches its selected maximum value or if the prediction error between the targeted and the computational values reached its minimum value. To this end, it can be realised that there is a gradual fall in the MSE with an increase in the iteration process and the training terminated, at a best performance (epoch 34), with a relatively insignificant MSE of 0.004. The error histogram is documented in Figure 5.10, this provides further confirmation of network performance and reliability of the established dataset. It can be observed that the optimal network performance was achieved when most of the dataset (training, testing and validation) fell within a relatively negligible error value between -0.011 to 0.012.

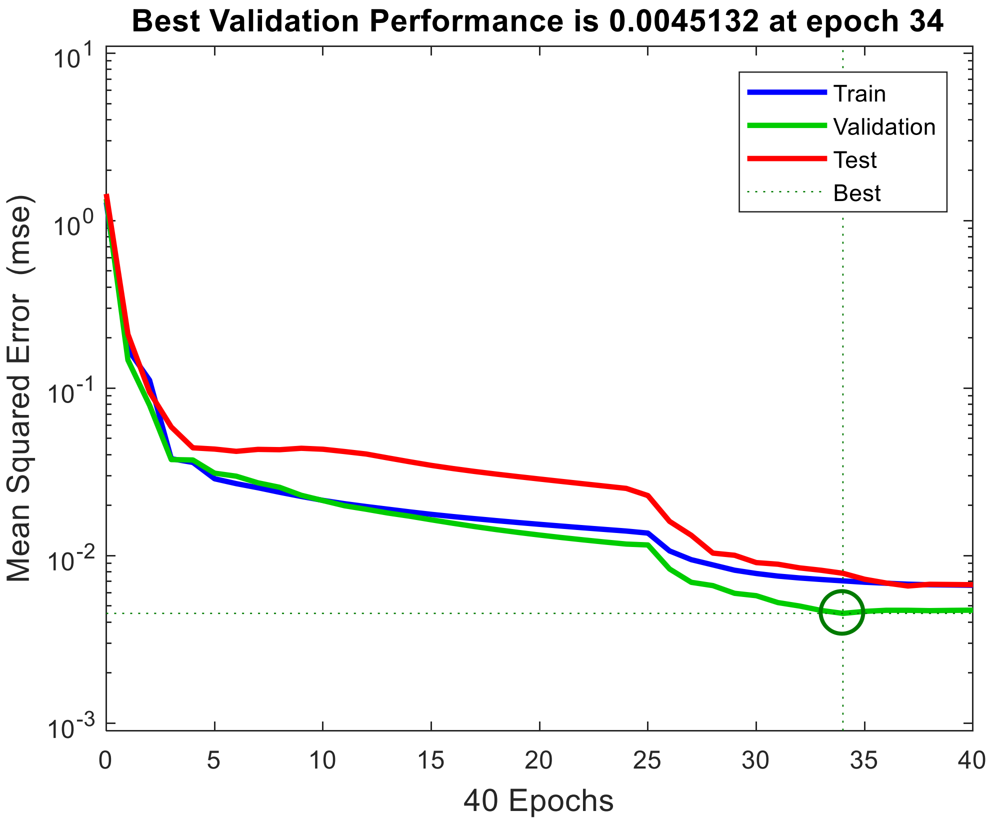

Figure 5-9: Plot of the LM analyses for steel closed-ended developed model during the training process.

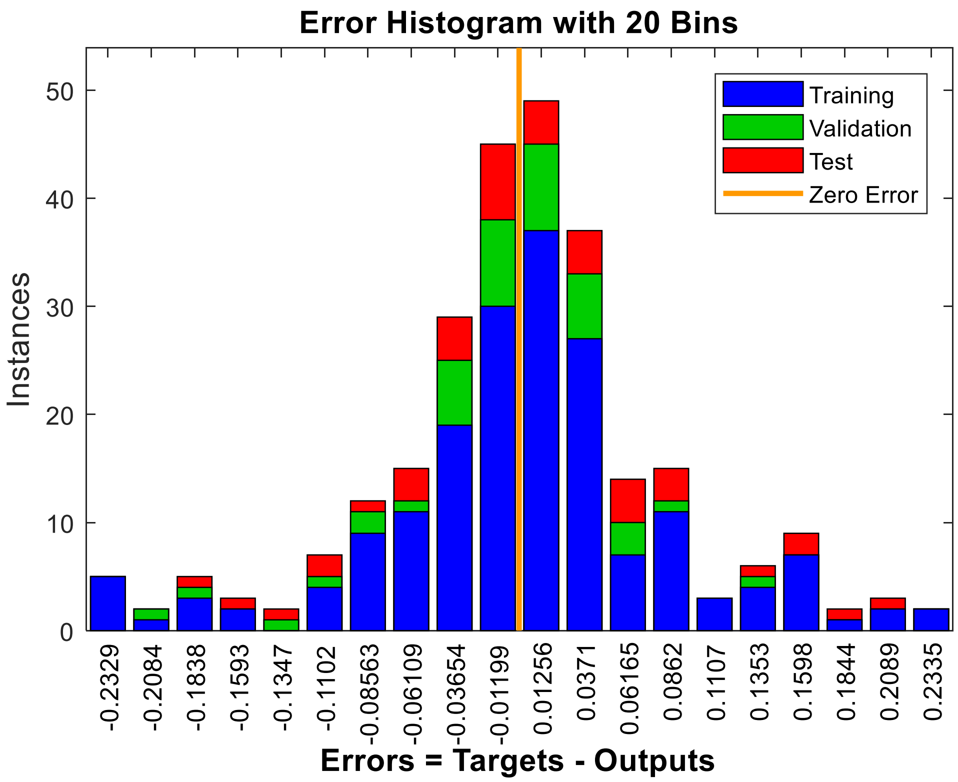

Figure 5-10: Histogram of error during the training, testing and validation.

5.5.2 Evaluation of the Experimental and the Predicted Load-settlement Response for Steel Closed-ended Piles Subjected to uplift Load

Figures 5.11, 5.12 and 5.13 report the measured versus predicted pile-load tests for steel closed-ended model piles subjected to independent uplift loads. The results revealed that the mobilised uplift pile bearing capacity increases with increases in the sand stiffness and the overburden pressure. The graphical results demonstrated that a noticeable soil elastic response could be seen in the initial stages when the applied uplift axial load is about 20, 50, and 80 N, for piles embedded in loose, medium, and dense sand, respectively. Moreover, the influence of soil yielding for the applied uplift load higher than the aforementioned values can be clearly observed in the upper part of the foundation, where non-linearity is marked. When the applied uplift load increases, the non-linearity associated with the foundations is substantially increased until reaching a maximum pile capacity. This can probably be attributed to the effect of plastic mechanisms occurring within the effective soil-pile interaction . To give a suitable reference point, on the load carrying capacity curve, the ultimate pile bearing capacity can be calculated based on pile uplift deformation equal to 10% of pile diameter, which is considered as the applied load equivalent to the ultimate state (BSI, BS EN 8004:1986). According to the graphical comparisons, good agreement can be seen between the experimental results and the computational values with correlation coefficients of (R = 0.99 and p = 6.282 x 10^{-31}) for all datasets with a relatively small percentage of error. This is a demonstration of the high efficiency of the proposed approach to provide accurate predictions.

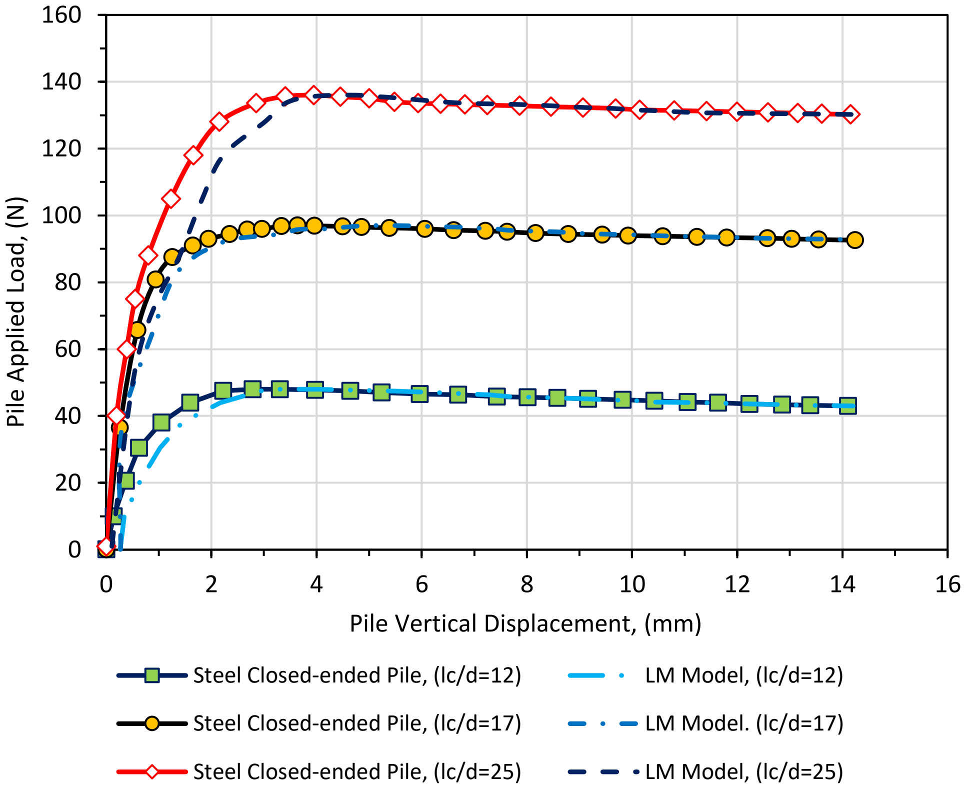

Figure 5-11: Comparisons of load-displacement response between the targeted and simulation results for steel closed-ended pile penetrated in loose sand under uplift loads.

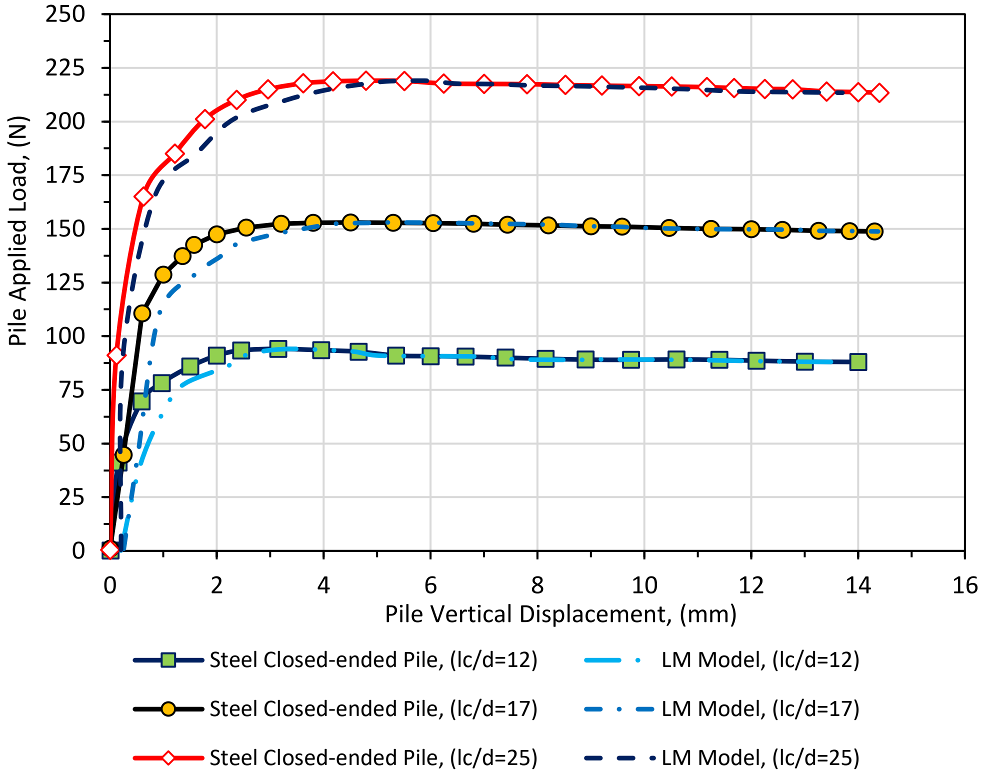

Figure 5-12: Comparisons of load-displacement response between the targeted and simulation results for steel closed-ended pile penetrated in medium sand under uplift loads.

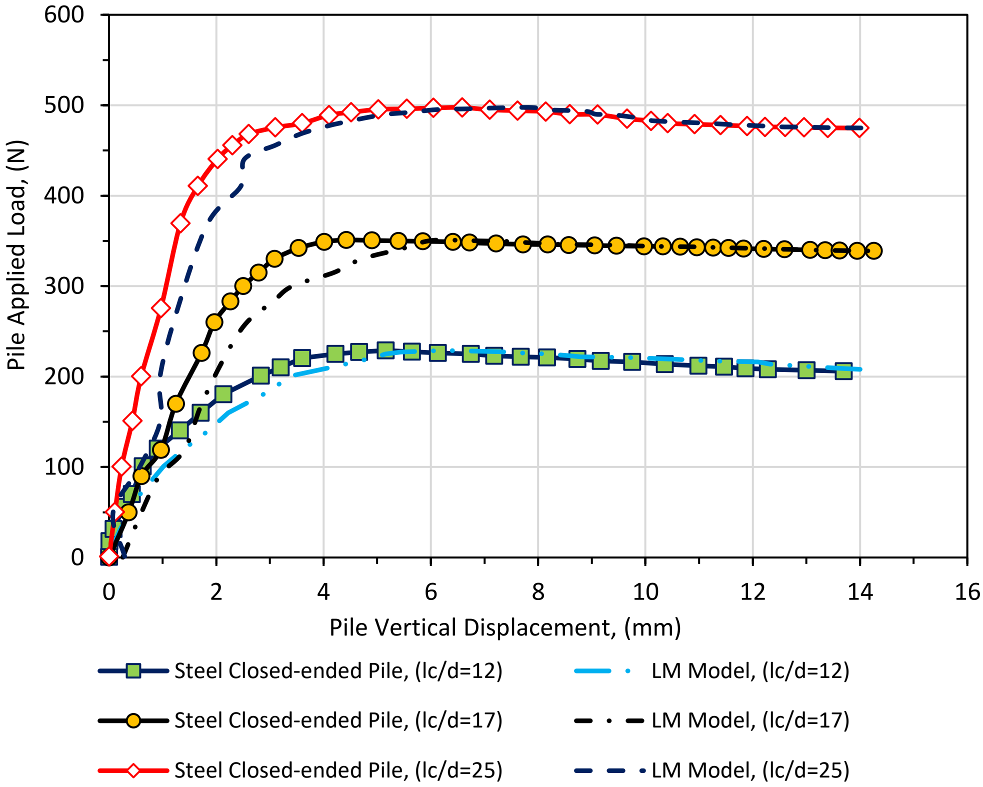

Figure 5-13: Comparisons of load-displacement response between the targeted and simulation results for steel closed-ended pile penetrated in dense sand under uplift loads.

The predicted versus targeted values of pile uplift deformation for training, testing, validation, and all dataset are illustrated in Figure 5.14. The determination coefficient of the experimental vs. predicted values (according to the best-fit line equation as Output = A x Target + C) and residuals analysis were considered for all datasets, training, testing, and validation. The points in all subdivisions (training, testing, validation, and all datasets) are located close to the best line of equality with high coefficient of determinations of 0.959, 0.963, 0.973 and 0.961, confirming that the LM algorithm has efficaciously learnt the non-linearity involved in the pile load-settlement with a continuous degree of success.

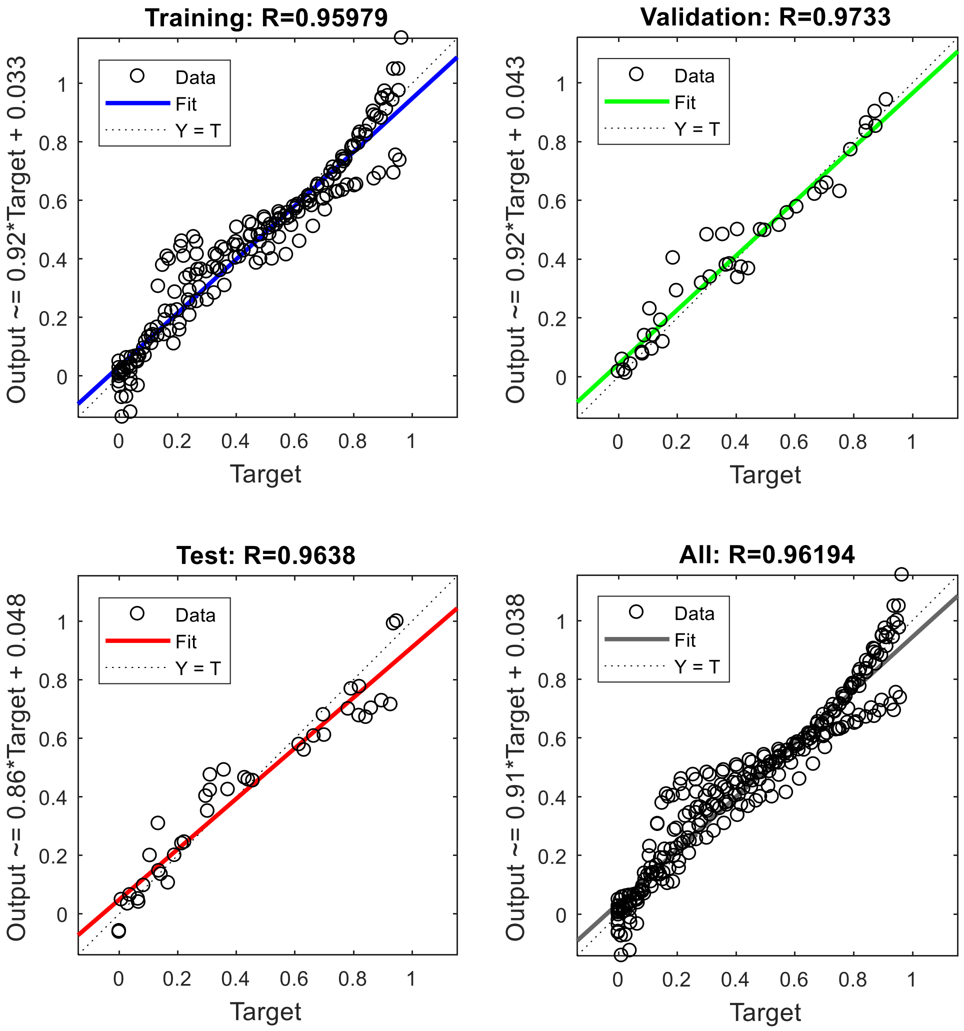

Figure 5-14: Regression graphs of the experimental results versus predicted pile settlement for steel closed-ended pile subjected to uplift load.

The performance of the LM algorithm is further tested graphically using a testing dataset. The high performance of the training dataset reveals that the process of learning is successful if those of the testing dataset show that the generalisation ability of the proposed model is satisfactory (Gordan et al., 2016). Given that, the testing dataset has been utilised to plot a regression calibration curve between measured versus predicted results of pile uplift deformation, with a 95% CI. The low scatter level along the 45° line seen in Figure 5.15 is indicative of the constructive response of the trained model to the process of learning. This in parallel with a root mean square error (RMSE) of 0.088 and Pearson correlation coefficients, R = 0.963 and p = 2.03x10^{-23}, respectively, confirms that the performed model, can successfully reproduce the results of the experimental pile settlement and behaves in a fashion as would be expected.

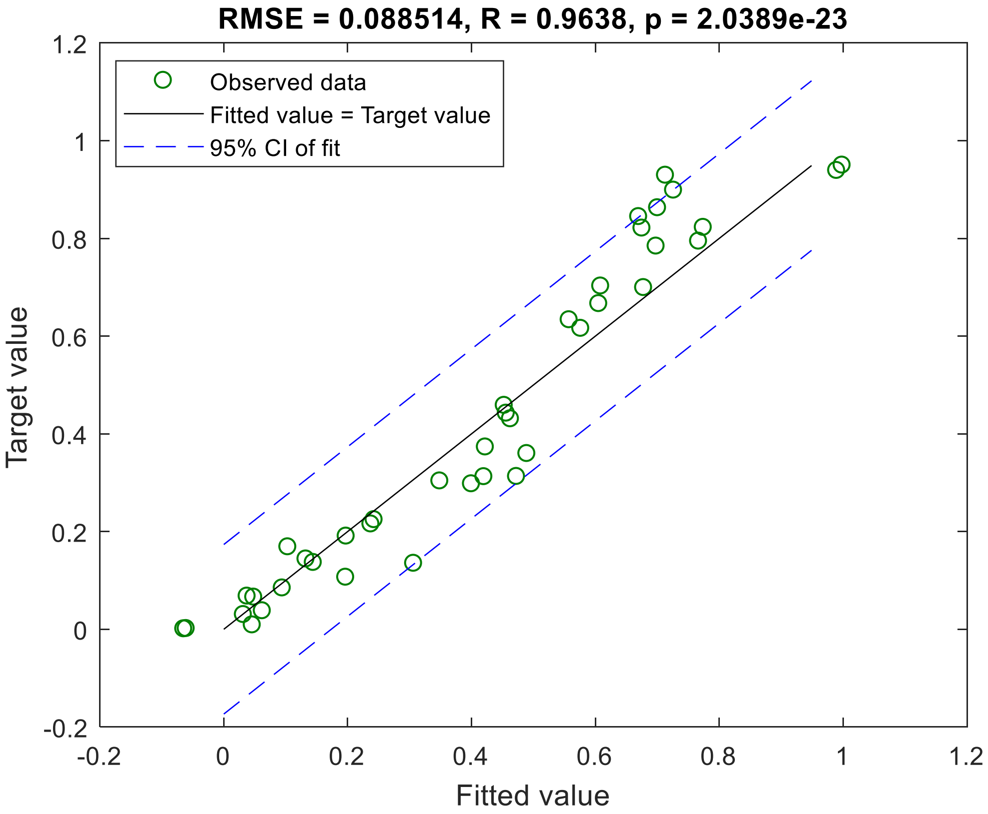

Figure 5-15: Calibration plot of the resulting model for the testing dataset at a 95% confidence interval (CI).

5.5.3 Comparison between the LM Model for Steel Closed-ended Piles with the Various Traditional Methods

Several approaches have been introduced, as detailed in section 2.7, for estimating pile capacity subjected to uplift loads. Nevertheless, the reliability and efficiency level of the predicted bearing capacity is of prime importance in the pile foundation design process (Unsever et al., 2015). Table, 5.8 illustrates the numerical results of the measured and the predicted pile capacity for steel piles subjected to axial uplift load. It can be seen that the level of agreement between the experimental and the applied LM algorithm is satisfactory. Therefore, the comparisons suggest that the proposed approach has the ability to provide fair assessments of pile bearing capacity and outperformed the traditional methods. While, as previously discussed, the comparison study confirmed that the results provided by Das and the Truncated Cone model tended to overestimate the pile capacity for the described soil. Whereas, the model performed by Meyerhof (1973) is the best prediction model, giving good agreement compared to the results of the experimental and predicted models for all pile slenderness ratios in the described soil.

Table 5-8: Measured and predicted uplift capacity of the steel closed-ended piles.

Lc/d ratios	Truncated cone's model, (N)	Meyerhof's model, (N)	Das's model, (N)	Experimental results, (N)	The proposed LM model, (N)
Dense sand, D_r (83%)					
12	264	214	622	225	210
17	2033	333	978	350	320
25	2392	487	1399	495	485
Medium sand, D_r (51%)					
12	178	88	124	93	93
17	506	146	426	150	150
25	1609	214	619	220	218
Loose sand, D_r (18%)					
12	129	46	136	50	50
17	369	92	266	95	95
25	1174	197	373	135	135

5.6 Factors Affecting Pile Capacity for Steel Closed-ended Piles Subjected to Uplift Loads

The pile embedment-length-to-diameter-ratio and the sand relative density have been cited to play a significant role in the uplift pile capacity (Das, 2015; Faizi et al., 2015). To examine the influence of the aforementioned factors on the uplift pile bearing capacity, three different pile slenderness ratios of 12, 17 and 25 penetrated in sandy soil of various densities were investigated. As mentioned previously, the pile diameter used in this research is 40mm (higher than the minimum size criterion for a model pile reported by Vesic (1977). Figure 5.16 reports the results of the ultimate uplift capacity with reference to pile slenderness ratio and sand relative density. The graphical results revealed that with the increase in the sand relative density and pile effective length, the ultimate uplift capacity increases by almost double for piles with a slenderness ratio less than 25. While, for a flexible pile the ultimate uplift capacity in dense sand is about 2.3 and 3.8 higher than the ultimate capacity for model piles penetrated in medium and loose sand. This could be assigned to several reasons as follows: (i) the overburden pressure increasing with depth, thus the mobilised skin friction for a pile increases with pile penetration length. (ii) the sand stiffness increases with the increase in the density, this leads to higher earth pressure coefficients (K), this can also contribute to the increase in the uplift resistance for a model pile within the contacted soil in the radial effective region.

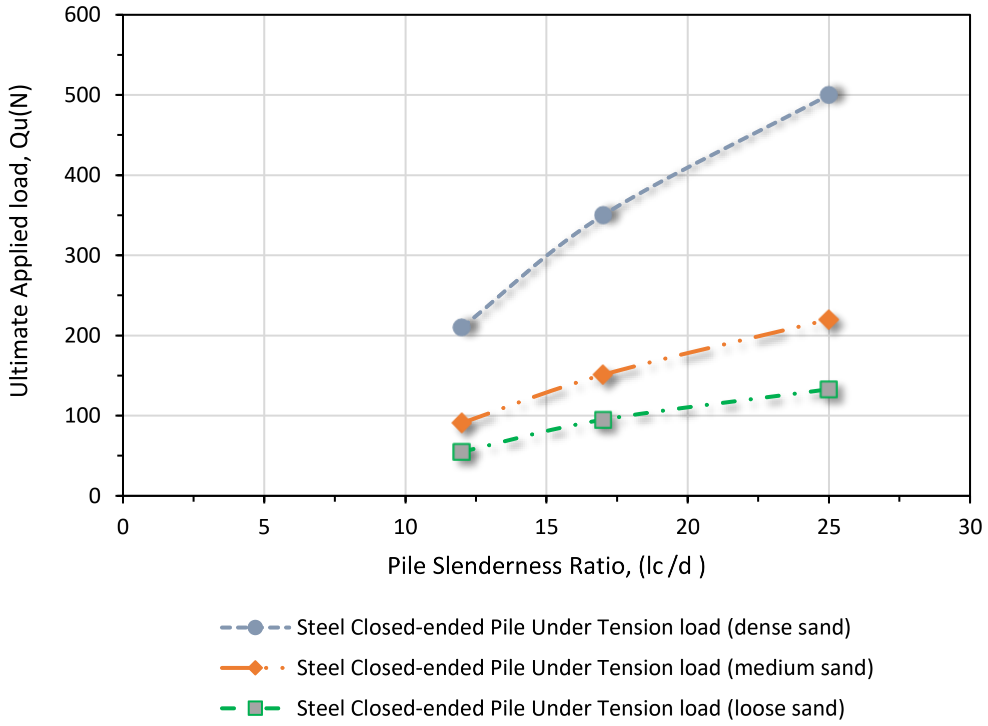

Figure 5-16: Variations of ultimate pile capacity with pile slenderness ratio for steel closed-ended piles subjected to uplift.

5.7 Performance Analyses of LM Model for Modelling of Uplift Load-deformation of Steel Open-ended Model Piles Penetrated in Loose, Medium and Dense Sandy Soil

The applicability of the LM algorithm to simulate pile load-deformation for steel open-ended piles subjected to independent uplift loads has been reported in this section. The accuracy of the aforementioned approach was assessed in different stages with reference to the experimental pile load-displacement results. In order to develop the LM algorithm, the total 266 recorded dataset values were randomly divided into three sets; covering training at 70% (186 data points), testing at 15% (40 data points) and validation at 15% (40 data points). In addition, the LM optimal structure was identified as one hidden layer with transfer functions of tangent sigmoid *"tansig"* and linear *"pruelin"* for the hidden and output layers, respectively. Comprehensive details about the MATLAB codes and the neural network functions for all model piles for compression and uplift loads, including the optimum synaptic connection weights are provided in the supplementary information (see Appendices I to VIII).

5.7.1 Performance Evaluation of the Proposed LM Algorithm

The network performance graph, based on the mean square error (MSE) of the LM trained algorithm is exhibited in Figure 5.17. It can be observed that a gradual decrease in the MSE level in the first stages from the learning process and the training was stopped when the network reached the optimum performance at the desired level with relatively negligible mean squared error (0.0068) at epoch of 47. A more informative figure about the residual error between the measured and the predicted can be seen in the error histogram (Figure 5.18). The results revealed that the majority of the data subsets (training, testing and validation) coincides with zero error line between the central bines of -0.0008 and 0.030, which further demonstrates the reliability of the trained network together with the absence of outliers from the gathered dataset.

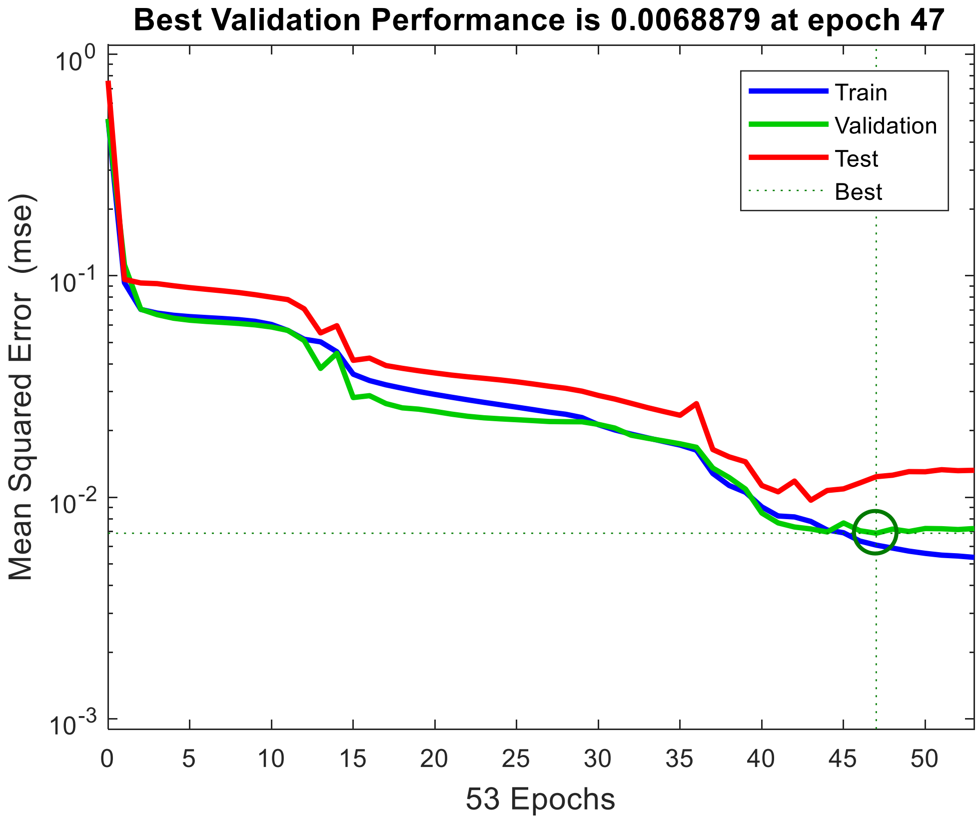

Figure 5-17: Convergence graph illustrates the effectiveness of the proposed LM algorithm for steel open-ended developed model during the learning process.

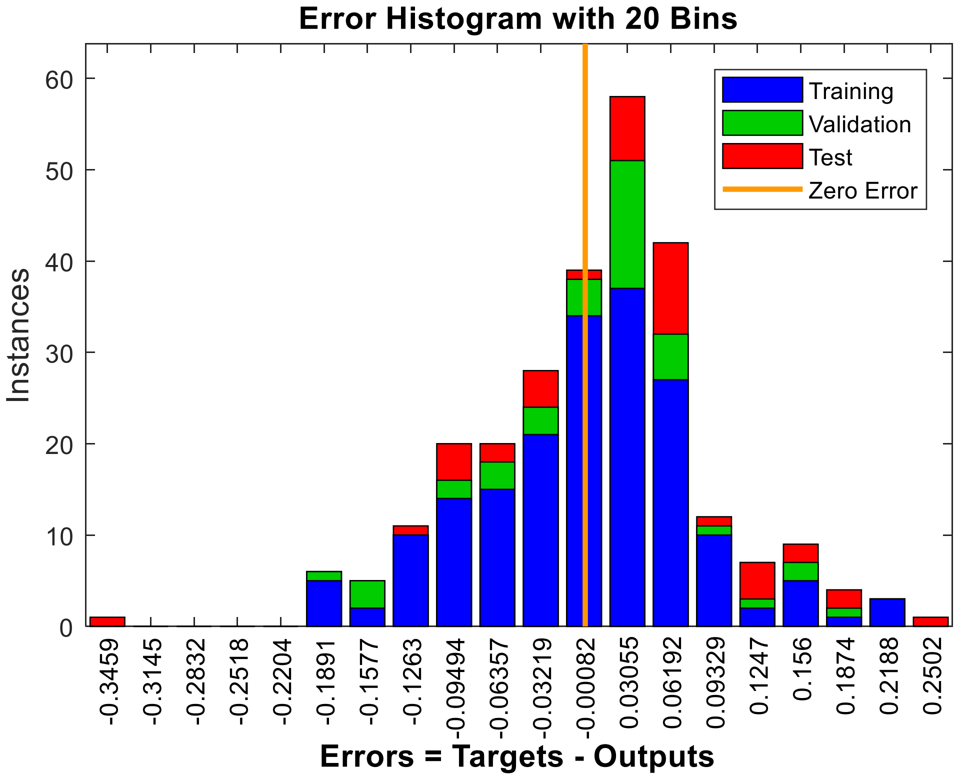

Figure 5-18: Error histogram plot of training, testing and validation for the LM algorithm.

5.7.2 Measured Versus Predicted Pile Load Tests for Steel Open-ended Piles Subjected to Uplift Loads

In this section, comparisons between the results of the pile load tests for steel open-ended piles subjected to uplift loads are reported. In addition, the feasibility of the proposed self-tuning LM model to map the response of pile load-deformation are also presented and discussed. Figures 5.19, 5.20 and 5.21 show the uplift load-settlement curves of circular open-ended piles with three slenderness ratios tested in three sand relative densities obtained by experimental pile load testing and were plotted. Generally, as observed in the experimental results, the piles take about 80% of the fully mobilised load at early stages of the loading procedures. A clear elastic branch can be seen in the earlier stages from running the test at applied load of approximately 25, 40, and 70N for piles driven in loose, medium and dense. The soil yielding effect is obvious with increasing in the applied load. With the range of 25 to 60N, 40 to 80N, and 75 to 120N for piles with Lc/d =12, 17, and 25 tested in loose sand and between 40 to 75N, 120, and 710N for piles driven in medium sand. In addition, for piles driven in dense sand an obvious elastic branch can be observed within the range of applied loads of about 70N to 200, 400, and 600N, respectively. Uplift pile capacity was identified according to the failure criteria at 10% of pile diameter (BSI, BS EN 8004:1986). In the context of comparing the experimental results with the LM training algorithm, the graphical results revealed that good agreement can be observed between the measured and the computational values, with a correlation coefficient of 0.96 for all datasets, which reveal the feasibility of the introduced method to learn up to 90% of the experimental dataset.

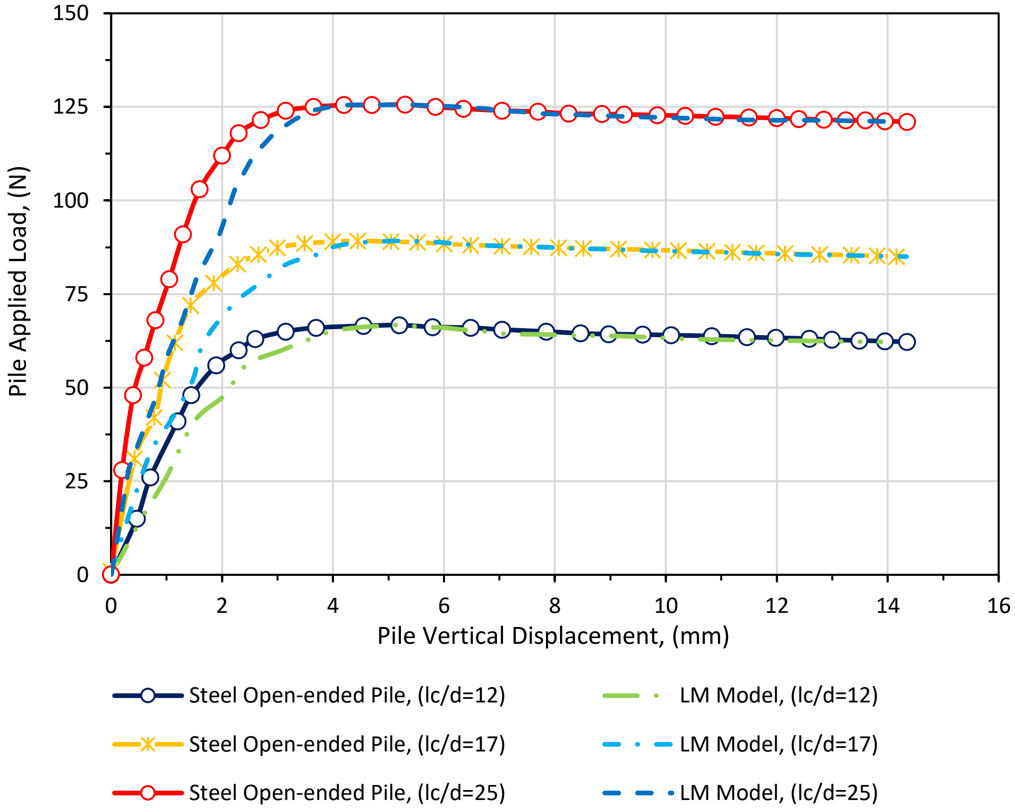

Figure 5-19: Comparisons of load-displacement response between the targeted and simulation results for steel open-ended pile penetrated in loose sand under uplift loads.

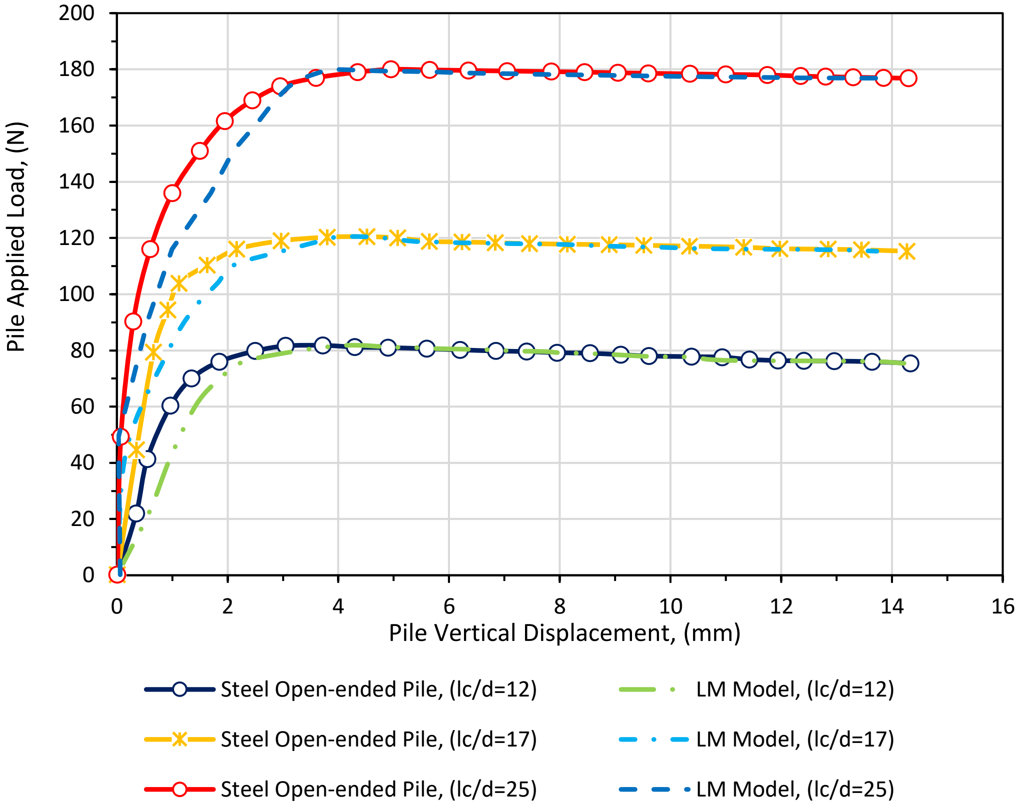

Figure 5-20: Comparisons of load-displacement response between the targeted and simulation results for steel open-ended pile penetrated in medium sand under uplift loads.

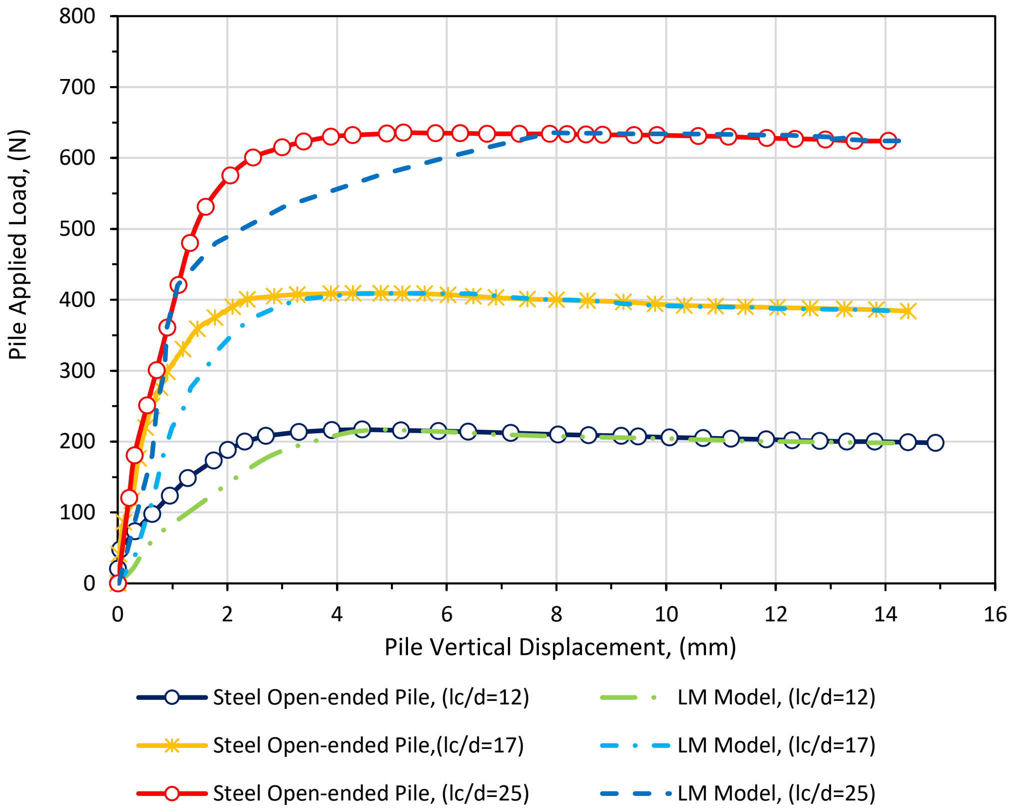

Figure 5-21: Comparisons of load-displacement response between the targeted and simulation results for steel open-ended pile penetrated in dense sand under uplift loads.

For further analysis, the generalisation ability and the performance of the LM algorithm was evaluated. Figure 5.22 exhibits the extent of the consistency between the predicted and the experimental pile settlement for training, testing and validation datasets in terms of scatter plots. As clearly presented, the LM prediction is in agreement with relevant measured values. The simulations that match the corresponding settlement experimental values should fall on the line y = x at 45°. As reported, all of the data (training, testing and validation) for the measured and simulated values lie around the best-fit line, which attests to the superiority of the proposed approach to capture the targeted values.

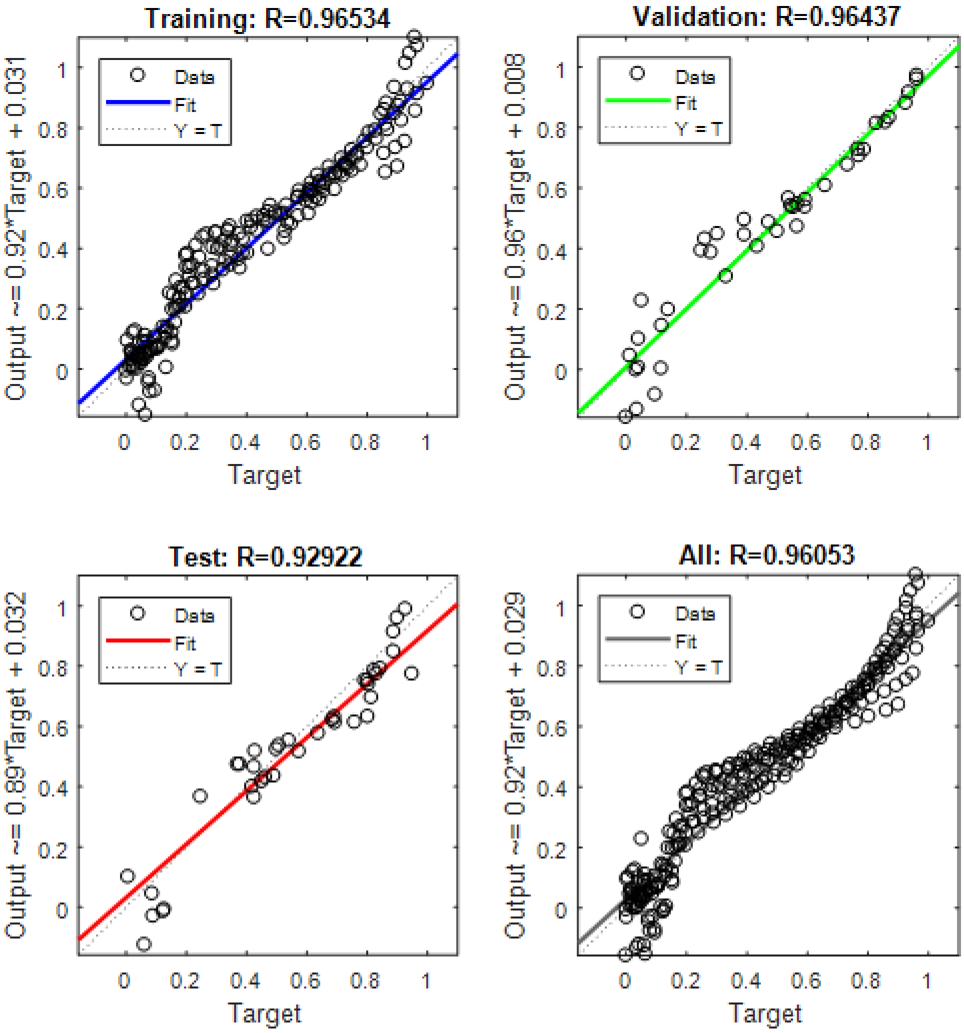

Figure 5-22: Regression graph of the experimental results versus predicted pile settlement for steel open-ended pile subjected to uplift load.

5.7.3 Ultimate Uplift Capacity for Steel Open-ended Piles Subjected to Uplift Loads

In this section, for verification purposes, the predictive abilities of the LM training algorithm has been re-evaluated with the corresponding experimental pile load tests for model piles subjected to uplift loads and associated theories available to predict the ultimate uplift capacity in the absence of pile load tests suggested by Das (1983), Meyerhof (1973) and the Truncated Cone model. The comparison results are presented numerically, as depicted in Table 5.9. It can be seen that the Meyerhof (1973) model is the best model to predict the ultimate uplift capacity when assessed with the experimental result and with those given by the trained LM model. While, the numerical results proposed by Das (1983) and the Truncated Cone models tend to overestimate the ultimate uplift pile capacity for the described soil densities. Therefore, it can be concluded that the conventional design procedures are not reliable to predict the ultimate uplift capacity and this can be attributed to the many uncertainties and hypotheses associated with the soil pile interaction.

Table 5-9: Measured and predicted uplift capacity of the steel open-ended piles.

Lc/d ratio	**Truncated cone's model, (N)**	**Meyerhof's model , (N)**	**Das's model, (N)**	**Experimental results, (N)**	**The proposed LM model, (N)**
Dense sand, D_r (83%)					
12	269	209	587	205	202
17	752	390	1121	400	400
25	2392	613	2309	635	600
Medium sand, D_r (51%)					
12	183	74	180	80	80
17	506	118	341	120	120
25	1609	192	530	180	179
Loose sand, D_r (18%)					
12	136	47	160	65	64
17	369	84	231	88	86
25	1174	122	347	125	124

5.8 Influence of Pile Effective Length and Sand Relative Density on the Ultimate Uplift Capacity

Skin frictional resistance that develops between the soil-pile interface in the radial effective zone is identified as a major capacity source and a design factor for a pile subjected to uplift loads (Nasr, 2013; Jebur et al., 2016). Sand relative density, pile effective length and the pile surface roughness also play a substantial role in the value of the mobilised shaft resistance. Therefore, in the current study, different types of pile surface roughness, pile effective length and sand relative densities have been used to explore the effect of the aforementioned parameters on the ultimate pile capacity. Figure 5.23 summarises the profiles of the ultimate uplift capacity for steel open-ended piles for the described slenderness ratios, penetrated in loose, medium and dense sand. Generally, it can be seen that the increase in sand density leads to a significant increase in the ultimate capacity. For a pile with Lc/d equal to 12, the uplift capacity in dense sand is just over double that in medium and loose sand. In addition, the ultimate uplift capacity in dense sand is three times higher than that in medium sand and about five times higher than the uplift capacity for a model pile with Lc/d = 17 penetrated in loose sand. Whereas, in dense sand, the percentage of the increase in the ultimate uplift capacity is about 3.4 and almost 5 times for model piles with Lc/d = 25 penetrated in medium and loose sand, respectively. In essence, the rate of increase of the uplift capacity is high for dense sand compared to smaller factors in medium and loose sand.

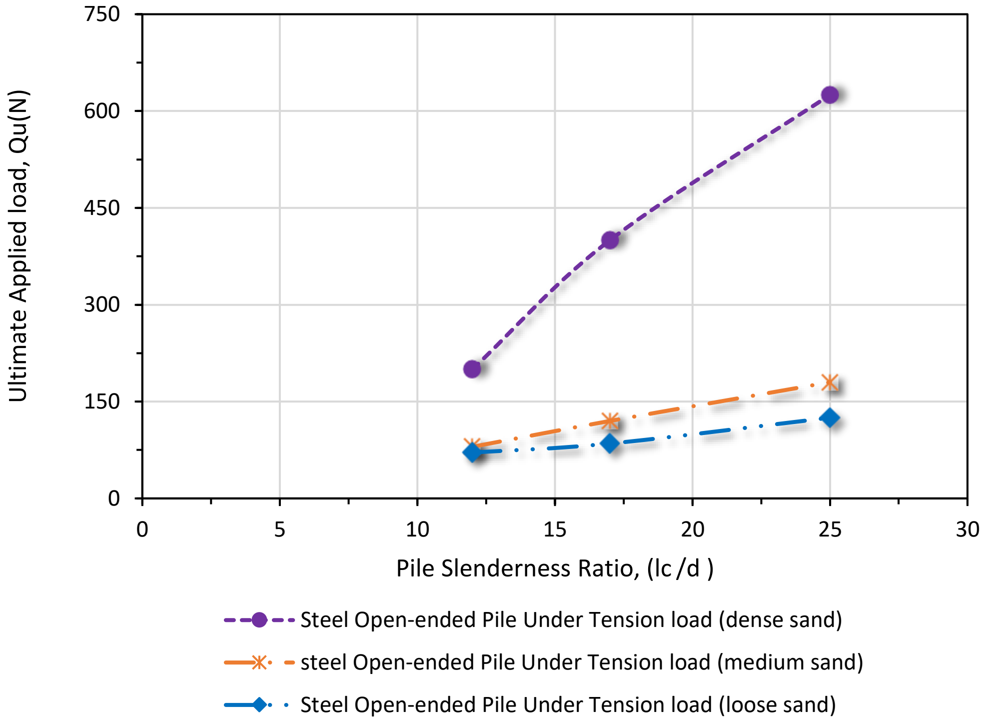

Figure 5-23: Distribution of the ultimate pile capacity with pile slenderness ratio for steel open-ended piles under uplift load.

5.9 Summary

The load-displacement characteristics, ultimate pile uplift capacity, and failure mechanism of precast concrete piles, steel closed-ended and steel open-ended piles embedded in pre-prepared sand relative densities of loose, medium and dense, subjected to uplift loads were explored. The choice of the input parameter in the space of the model input parameters for the developed model, statistical reliability of the dataset being studied, and the contribution level of each input parameter were also discussed. Moreover, for verification purposes, comparisons have been made between the introduced approaches with most commonly available methods used to predict pile-bearing capacity. The following conclusions, on the basis of the achieved outputs, can be drawn:

- Increasing the sand relative density and the pile slenderness ratio remarkably decreases pile uplift deformation and increases the ultimate uplift capacity. This can be attributed to the increase in the developed skin friction resistance due to an increase in the overburden pressure.
- The employed computational intelligence approach has attracted growing attention due to its comprehensive adaptability and notably powerful capacity for solving problems of this type.
- Comparing the experimental results to the predicted values demonstrates that the LM concept can be applied successfully, with enhanced prediction performance, to simulate pile-load settlement with high efficiency.
- The load-displacement curves show a clear elastic branch, in the initial stages of loading, when the normalised pile settlement is about 1% of pile diameter.
- The plastic mechanism associated with the soil-pile interaction is the leading cause for the presence of the non-linearity in the load-settlement response.
- Pile effective length, Lc, pile material roughness, δ and sand relative density, D_r have been considered, according to the sensitivity analysis, as being the most effective on the ultimate uplift capacity, following the order D_r > Lc > δ.
- According to the comparative study, the results introduced by the Truncated Cone and Das (1983) models do not exhibit acceptable precision and desired integrity in predicting pile capacity subjected to axial uplift loads in the described test environment. However, there is satisfactory agreement between the results of the proposed approach and the outputs attained from application of the Meyerhof (1973) model when compared with test results of the steel closed-ended piles under uplift load, thus most precise compared to the aforementioned methods.

CHAPTER 6

Analysis of the Load-transfer for Precast Concrete, Steel Closed-ended and Steel Open-ended Piles Embedded in Sandy Soil

6.1 Introduction

In this chapter, an attempt has been made with the aim of developing new and reliable design charts that can be used to determine the main significant parameters that influence pile-bearing capacity for different types of model piles, having three slenderness ratios, subjected to uplift and compression loading. Recalling Equations 2.3 and 2.5, the earth pressure coefficient (K) and the bearing capacity parameters (N_q) are marked to be the most influential design factors that govern the individual contributions of pile skin friction and end-bearing capacity. However, the aforementioned parameters are found to be substantially influenced by sand stiffness, pile materials, overburden pressure and the embedment length-to-diameter ratio (Lc/d) (Manandhar and Yasufuku, 2013; Tomlinson and Woodward, 2014; Das, 2015; Kampitsis et al., 2015; Loria et al., 2015). Thus, the effect of these factors on pile bearing capacity is presented in the following section. In addition, for verification purposes, the obtained results are further compared with those suggested traditional design methods proposed by Tomlinson and Woodward (2014); Poulos and Davis (1980); American Petroleum Institute (1993); Coyle and Castello (1981); and Meyerhof (1976).

6.2 Bearing Capacity Factor (N_q) for Concrete Piles

Figures 6.1, 6.2 and 6.3 illustrate the N_q distribution with the sand relative density. The results show that the bearing capacity factor (N_q) increases with the increase in the sand relative density. The proposed design charts can be easily used during the pile foundation design process, to precisely determine the N_q factor for a concrete pile subjected to compression load. For instance, for piles with a slenderness ratio of 12, the N_q factor (y-axis) can be determined based on the in-situ sand relative density (x-axis). In all cases, the design charts proposed by Meyerhof (1976) tend to grossly overestimate the bearing capacity factor for all piles slenderness ratios. While, the methodology reported by the American Petroleum Institute (1993) and Coyle and Castello (1981) are found to significantly underestimate the N_q values. This can be properly assigned due to several hypothesis and arbitrary assumption associated with the soil-pile interaction, i.e., method of pile installation, critical effective length concept, initial boundary conditions, and etc. The results also exposed that good agreement can be seen between the current study and the results suggested by Poulos and Davis (1980) in dense sand and Tomlinson and Woodward (2014) in loose and medium sands.

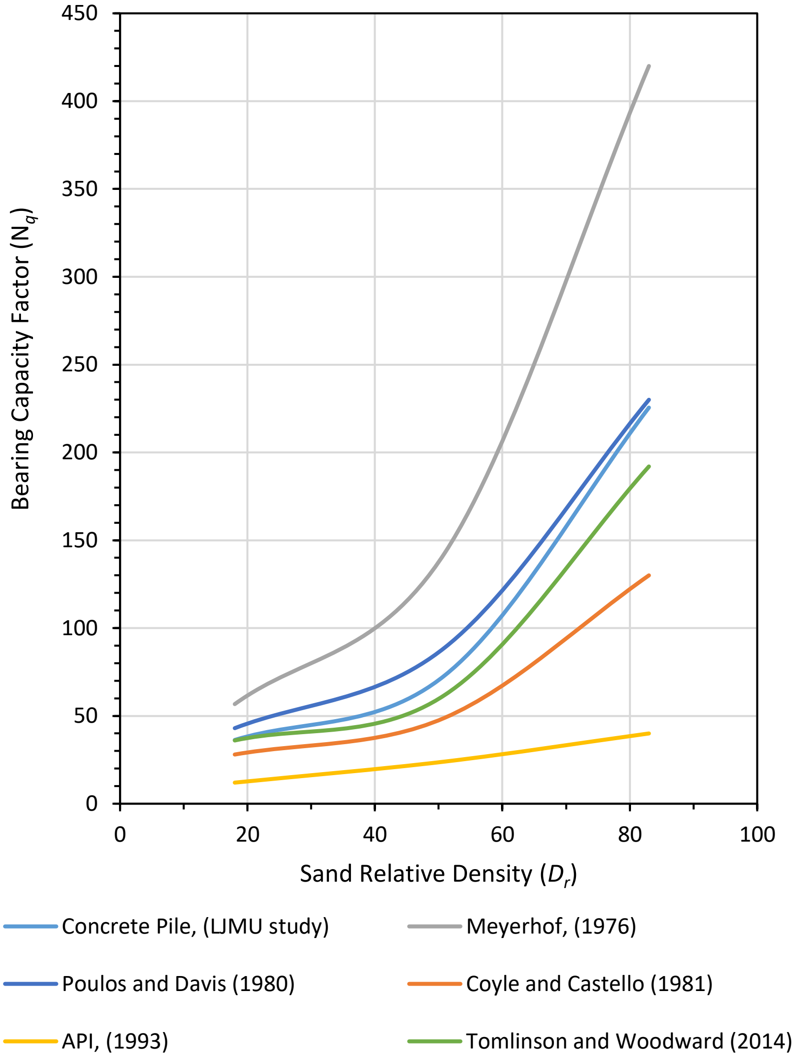

Figure 6-1: Bearing capacity factor for a concrete pile with slenderness ratio of 12.

For a pile with slenderness ratio of 17, the approach proposed by Tomlinson and Woodward (2014) approach indicates higher prediction accuracy than the rest of the conventional design procedures in evaluating the bearing capacity factor, as can be seen in Figure 6.2.

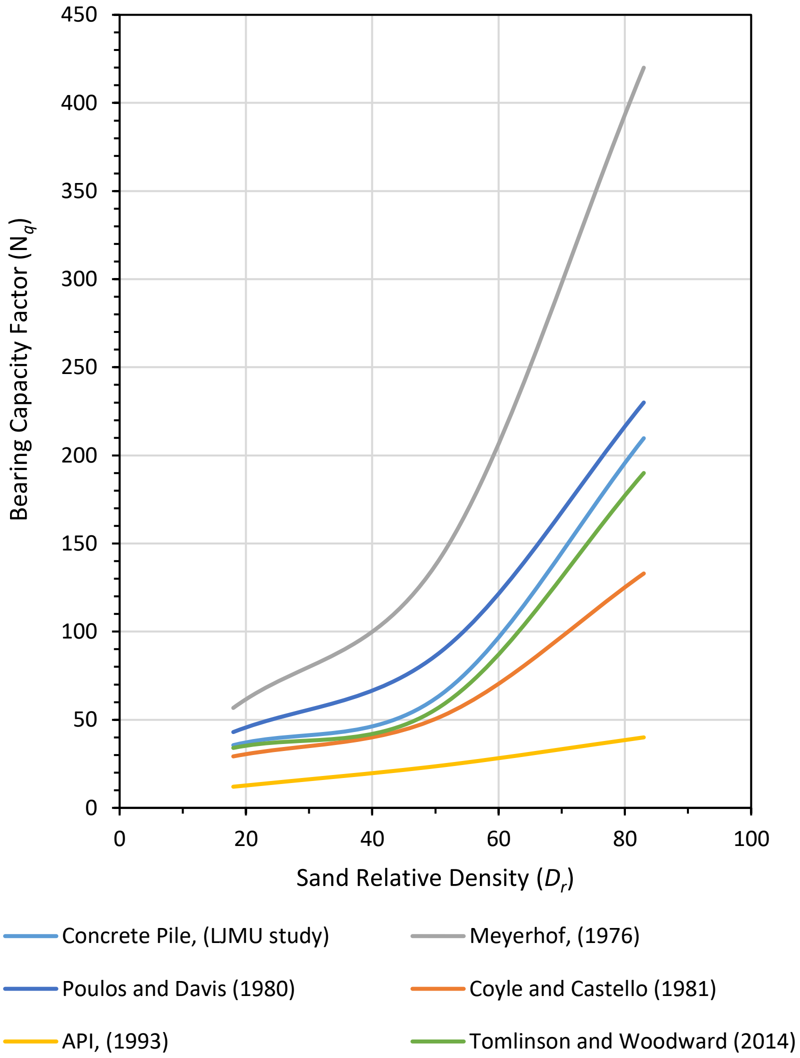

Figure 6-2: Bearing capacity factor for a concrete pile with slenderness ratio of 17.

For a long pile with a slenderness ratio of 25, it can be demonstrated, for all sand relative densities, that the end bearing capacity design procedures with significant agreement are achieved between the N_q values of the current study and those proposed by Tomlinson and Woodward (2014) . Additionally, the method suggested by Coyle and Castello (1981) shows a significant consistency with the current study to determine the pile bearing capacity in loose and medium sands respectively.

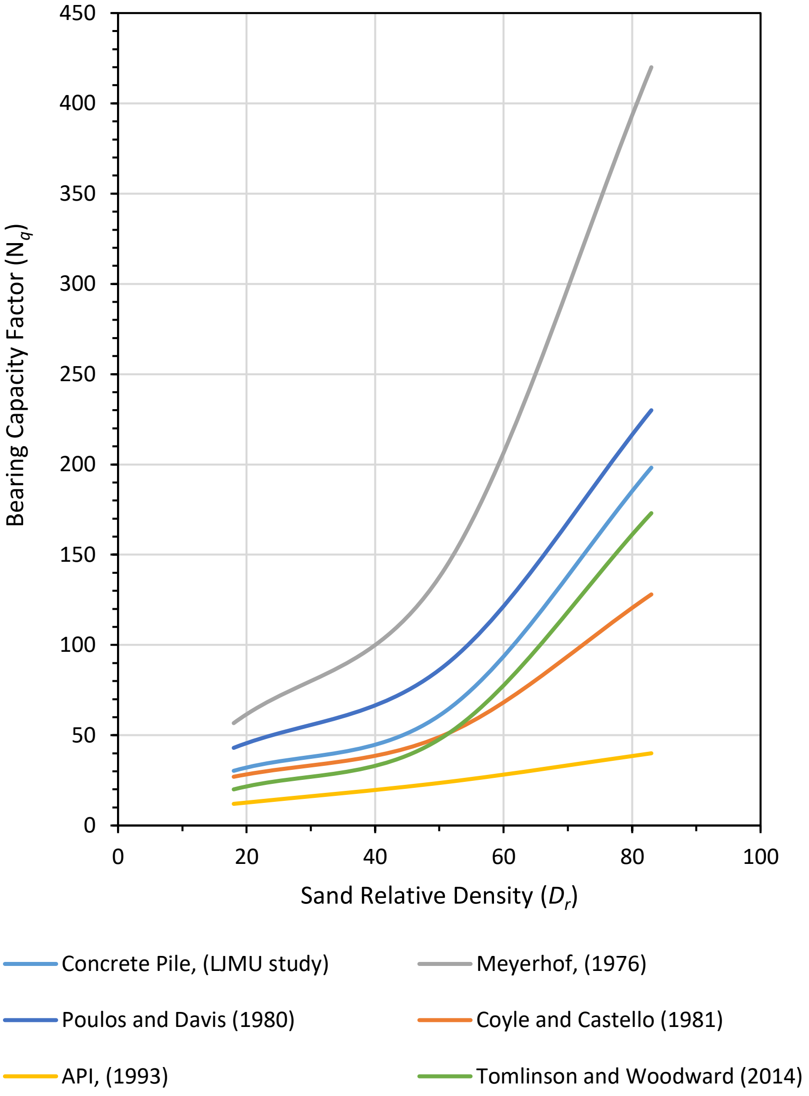

Figure 6-3: Bearing capacity factor for a concrete pile with slenderness ratio of 25.

6.3 Earth Pressure Coefficient (K) for Concrete Piles

The profiles of the earth pressure coefficient, K for concrete model piles, covering three pile slenderness ratios are clearly presented in Figures 6.4, 6.5 and 6.6 along with a comparison between newly developed design charts and traditional design criteria proposed by Poulos and Davis (1980); American Petroleum Institute (1993) and Broms (1964). The results reveal that the coefficient of earth pressure increases with the increase in the soil density. It can be seen that the K values proposed by Poulos and Davis (1980) remarkably overestimated for all cases of a model pile penetrated in medium and dense sands. The K values reported by the American Petroleum Institute (1993) and Broms (1964) are observed to be conservative for model piles penetrated in medium and dense sands. A visual inspection confirmed that all design methods are well fitted to the current study in the case of loose sand.

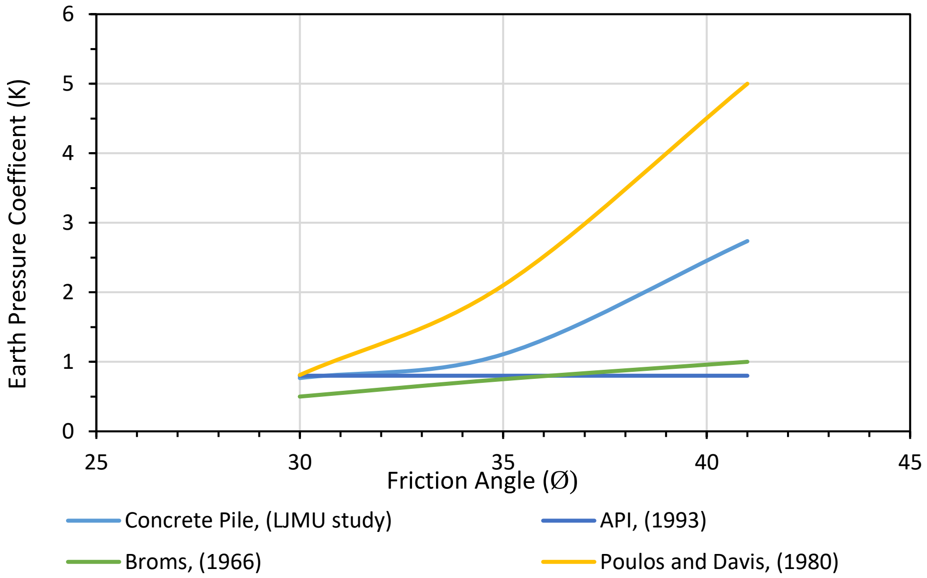

Figure 6-4: Variation of earth pressure coefficient (K) with angle of friction (Ø) for concrete piles with a slenderness ratio of 12.

The variation of Ø versus the earth pressure coefficient, K for model piles with a slenderness ratio of 17 is denoted in Figure 6.5. The K values reported by the American Petroleum Institute (1993) and Broms (1964) are revealed to underestimate the K value for piles driven in dense sand only. Furthermore, consistent agreement can be observed for the K values proposed by the current study with the aforementioned methods for a pile embedded in loose and medium sands respectively.

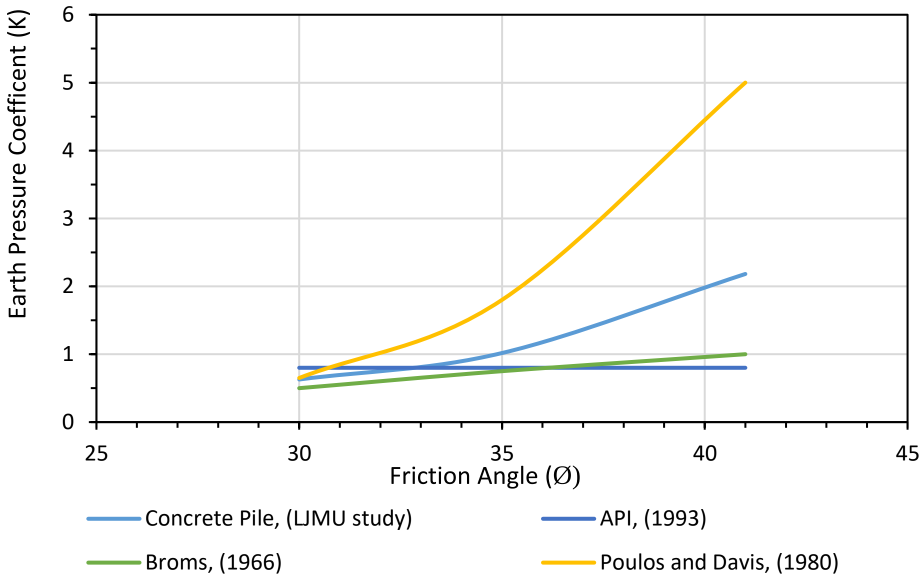

Figure 6-5: Variation of earth pressure coefficient (K) with angle of friction (Ø) for concrete piles with a slenderness ratio of 17.

Moreover, for a pile with slenderness ratio of 25, it can be observed that the design chart recommended by Poulos and Davis (1980) seems to overestimate the K values for piles in medium and dense sands. Good agreement can be achieved for the values developed by the current study with those models offered by the American Petroleum Institute (1993), and Broms (1964), demonstrating that the design charts suggested by the aforementioned methods can be successfully utilised to determine the earth pressure coefficient for concrete piles with Lc/d equal to 25.

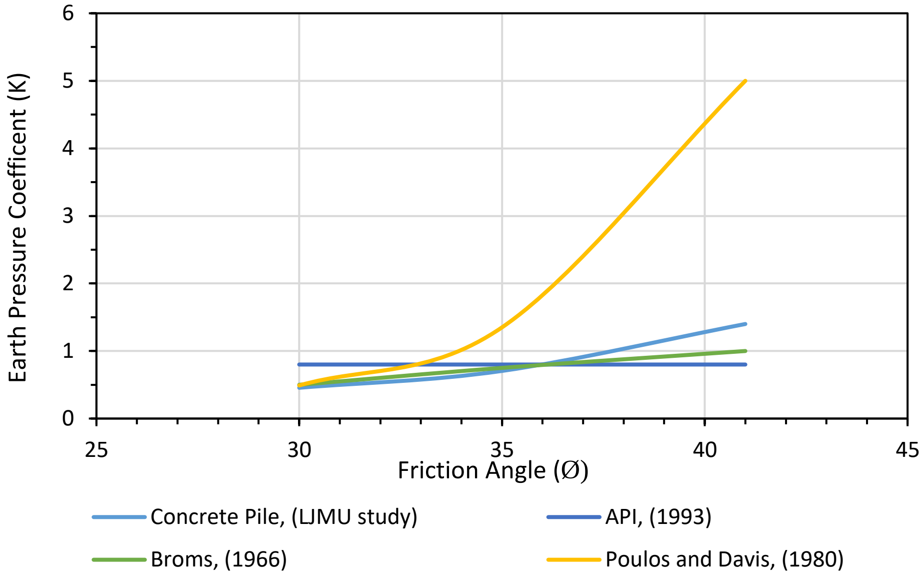

Figure 6-6: Variation of earth pressure coefficient (K) with angle of friction (Ø) for concrete piles with a slenderness ratio of 25.

6.4 Bearing Capacity Factor (N_q) for Steel Closed-ended Piles

For point bearing piles, the N_q parameter is a major design factor for piles subjected to axial compression loads (Igoe et al., 2014). The N_q values along with those obtained from the conventional design procedures for steel closed-ended piles are summarised in Figures 6.7, 6.8 and 6.9 for slenderness ratios of 12, 17 and 25 respectively. As clearly presented, for particular soil densities, the suggested design procedures provided by Meyerhof (1976) are unreliable and overestimate the N_q values for piles, whereas, the N_q values reported by the American Petroleum Institute (1993) are found to substantially underestimate the N_q values. It is worth pointing out that the suggested design curves offered by Coyle and Castello (1981) are in good agreement and seem to be efficient to predict the N_q values for piles penetrated in loose sand only. Additionally, the Poulos and Davis (1980) recommended values are found to be slightly overestimated. A substantial similarity can be seen between the N_q values developed from the current experimental tests (LJMU) and those proposed by Tomlinson and Woodward (2014) for all sand stiffness and pile slenderness ratios. This indicates the reliability of the aforementioned model to evaluate the steel bearing capacity factor in the described soil.

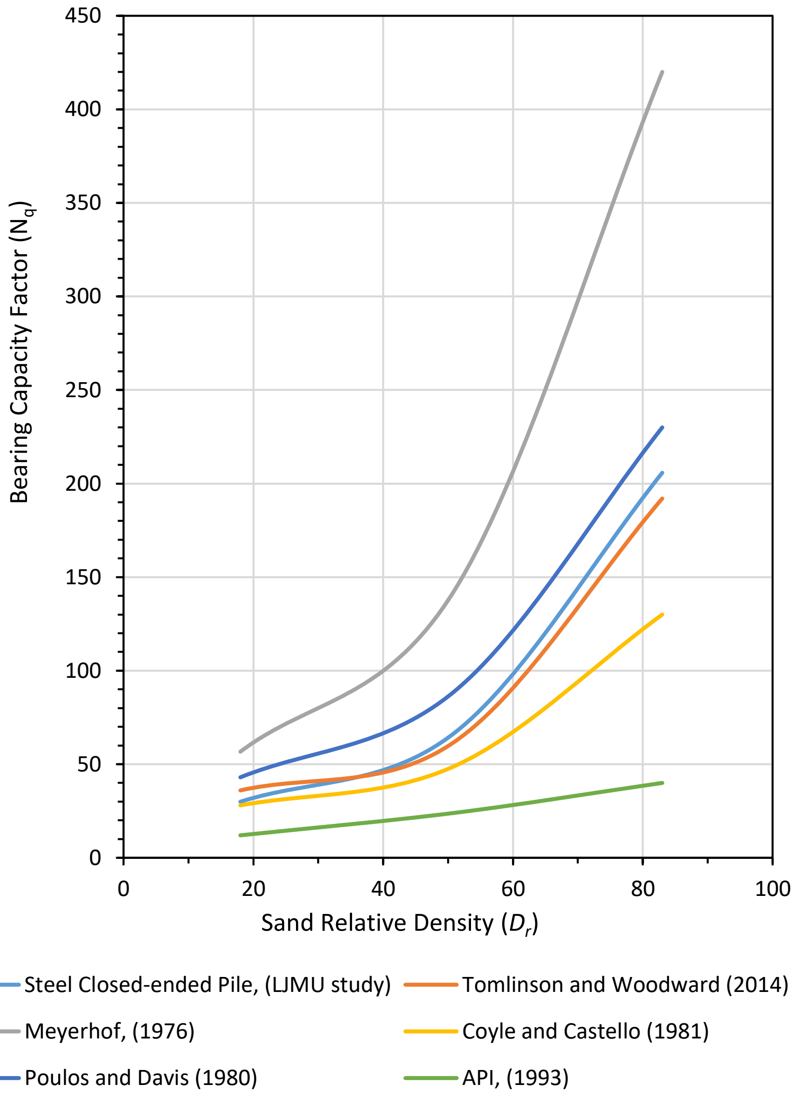

Figure 6-7: Bearing capacity factor for steel closed-ended pile with a slenderness ratio of 12.

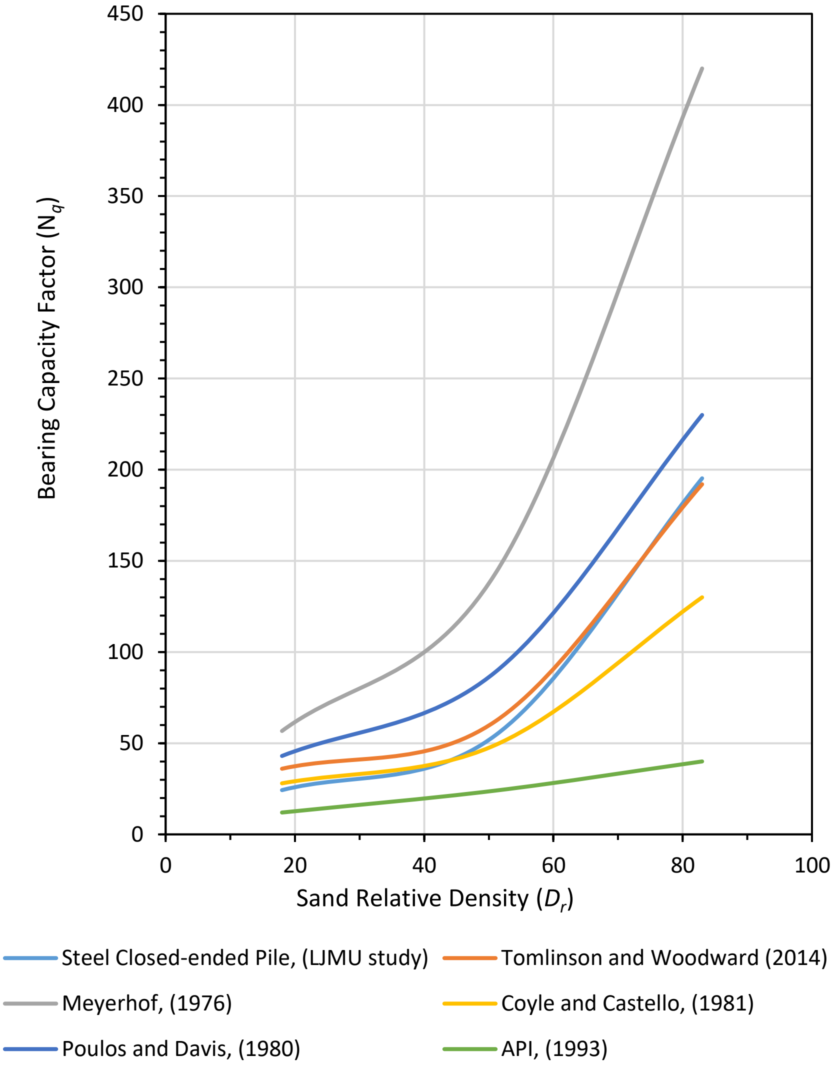

Figure 6-8: Bearing capacity factor for steel closed-ended pile with a slenderness ratio of 17.

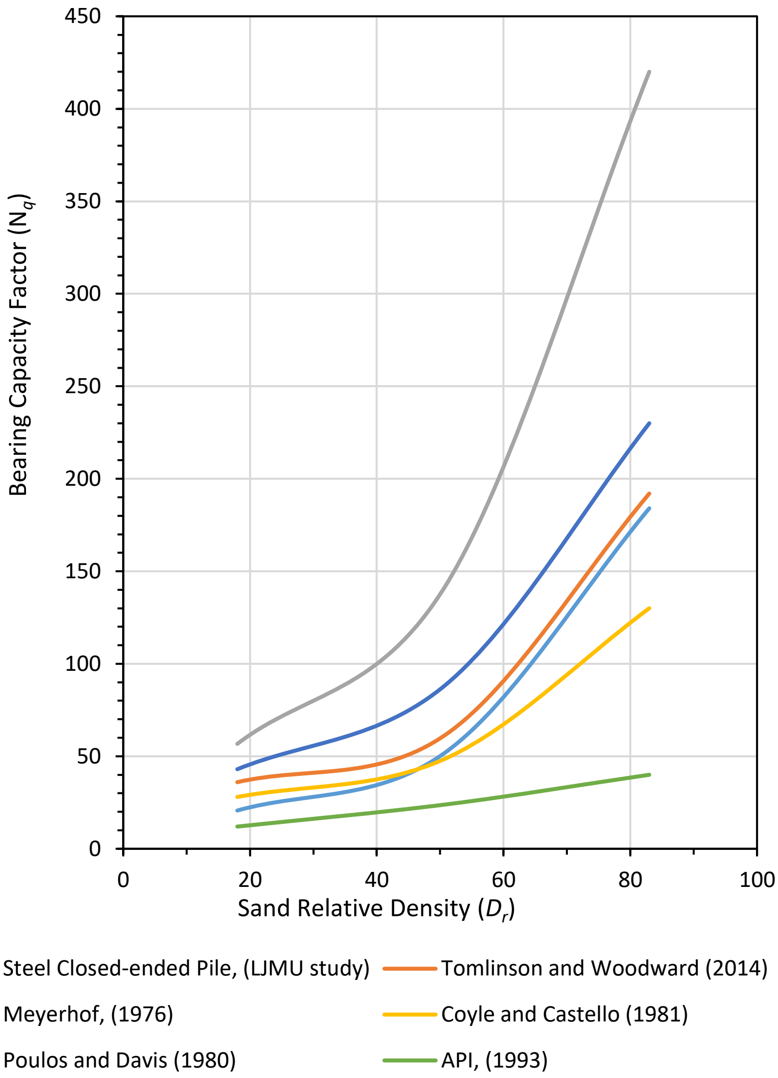

Figure 6-9: Bearing capacity factor for steel closed-ended piles with a slenderness ratio of 25.

6.5 Earth Pressure Coefficient (K) for Steel Closed-ended Piles

For steel piles penetrated in sandy soil, shaft resistance developed between the soil-pile interfaces in the radial effective zone are considered, based on the effective stress design approach, as a major design parameter for piles subjected to axial uplift load. Recalling Equation 2.3, sand relative density and the earth pressure coefficient have been identified as playing a significant role in pile mobilised shaft capacity. Therefore, in the current study, the variations of the K parameter with the sand angle of friction, Ø for steel piles are reported. Based on the graphical comparison presented in Figures 6.10, 6.11, and 6.12, the design chart proposed by Poulos and Davis (1980) tends to overestimate the K parameters for piles driven in medium and loose sands. Whereas, the methods suggested by American Petroleum Institute (1993), and Broms (1964) tend to be more conservative with the K values for piles with slenderness ratios of 12, and 17, especially in case of medium and dense sands. The results also demonstrated that the American Petroleum Institute (1993) and Broms (1964) models are by far the best when applied to piles with a length-to-diameter-ratio of 25 penetrated in sandy soil, and therefore most accurate. This gives remarkable agreement with reference to the reported experimental K values established in the current study, demonstrating the applicability and the reliability of the method in future applications.

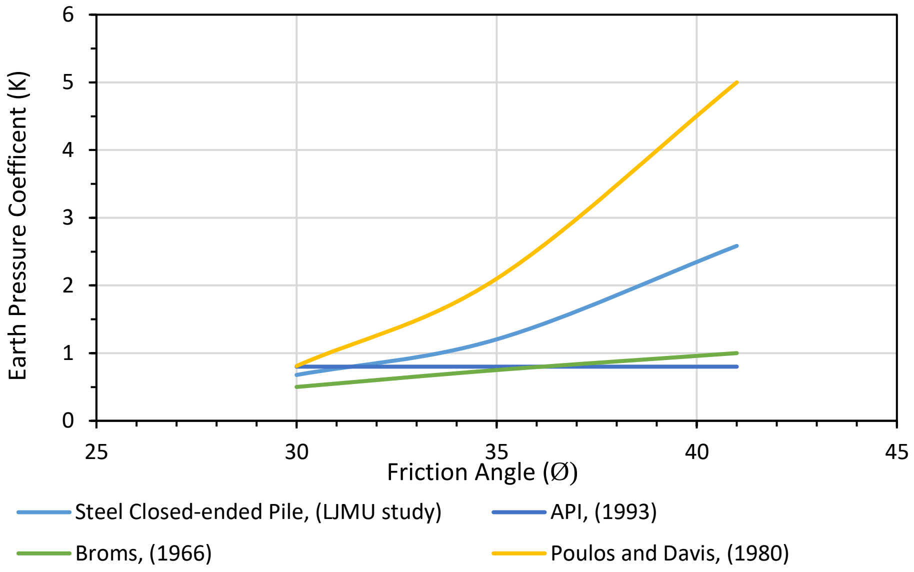

Figure 6-10: Effect of angle of friction (Ø) on earth pressure coefficient (K) for steel closed-ended piles with a slenderness ratio of 12.

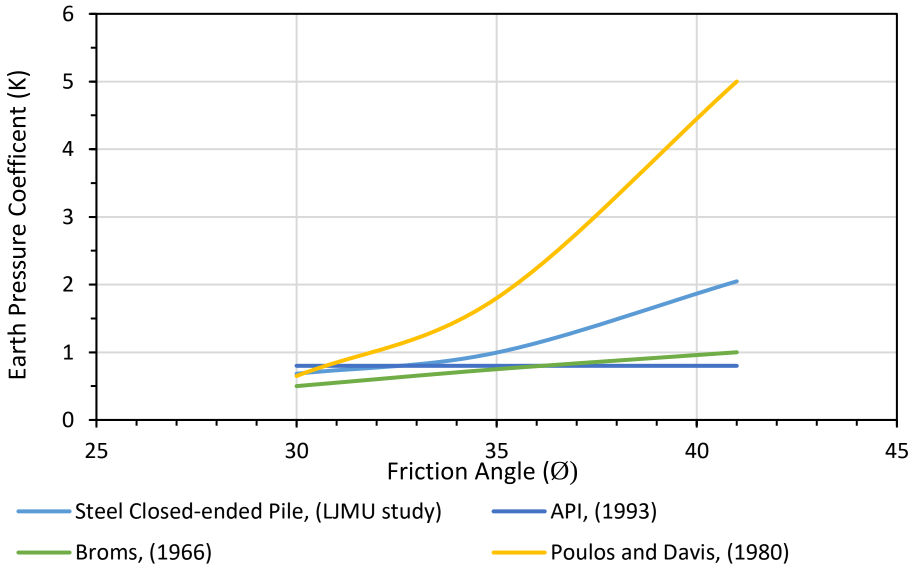

Figure 6-11: Effect of angle of friction (Ø) on earth pressure coefficient (K) for steel closed-ended piles with a slenderness ratio of 17.

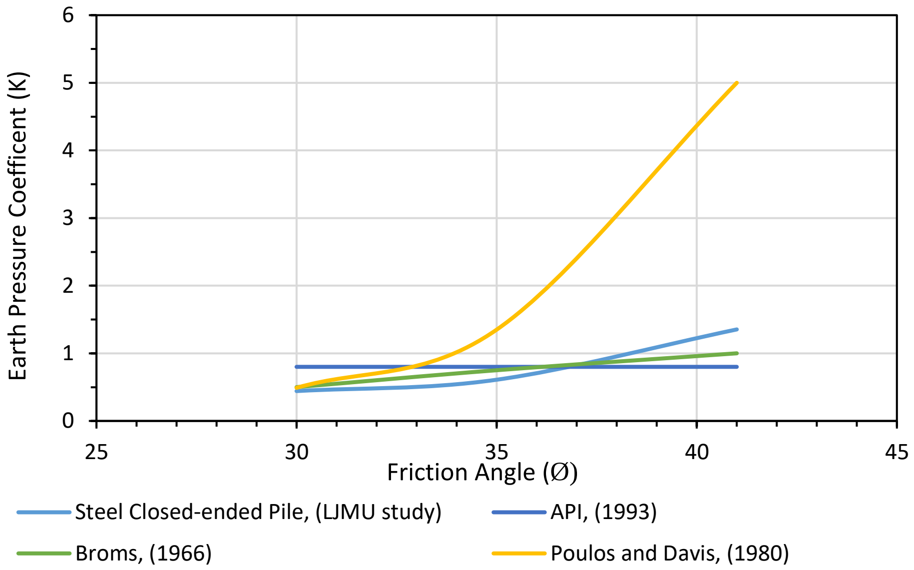

Figure 6-12: Effect of angle of friction (Ø) on earth pressure coefficient (K) for steel closed-ended piles with a slenderness ratio of 25.

6.6 Bearing Capacity Factor (N_q) for Steel Open-ended Piles

On the basis of comparing the bearing capacity factors with the most popular procedures used to estimate the pile bearing capacity, the variation of the bearing capacity factor (N_q) with sand relative density (D_r) concerning three piles slenderness ratios of 12, 17 and 25 for open-ended piles are presented and discussed in this section. As demonstrated in Figures 6.13, 6.14 and 6.15, the N_q factor is highly influenced by the sand stiffness. The bearing capacity factor for dense sand is markedly higher than that for loose sand and becomes more pronounced for medium sand. Based on the graphical comparison, it can be seen that the results proposed by Poulos and Davis (1980), and Meyerhof (1976) tend to overestimate the bearing capacity factor for all cases. The results also revealed that the predicted bearing capacity factor using the American Petroleum Institute (1993)'s design procedures is observed to underestimate the N_q design parameter, especially for piles constructed in medium and dense sands. It should be mentioned that this is compatible with the findings stressed by Fattah and Al-Soudani (2016). In addition, good agreement can be observed between the N$_q$ values obtained using the Tomlinson and Woodward (2014) model with reference to the experimental results. Moreover, the results proposed by Coyle and Castello (1981) are also reliable to estimate the bearing capacity for model piles penetrated in loose and medium sands, respectively.

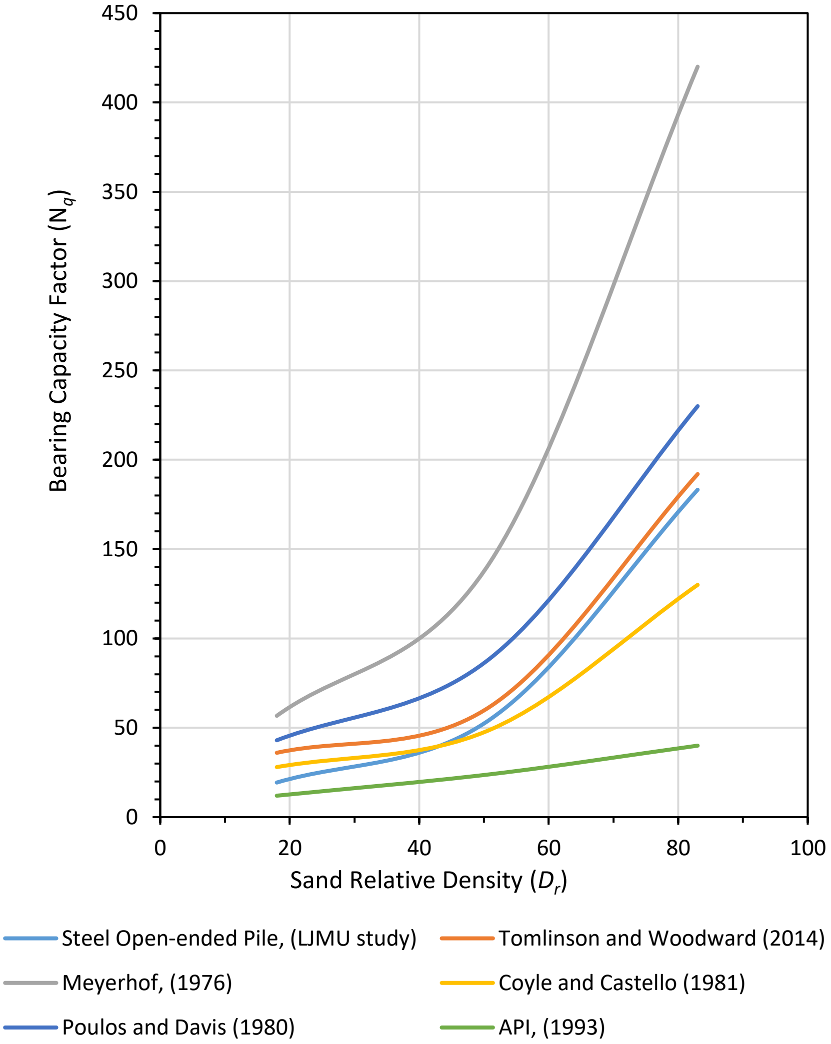

Figure 6-13: Variation of pile bearing capacity factor for steel open-ended piles with a slenderness ratio of 12.

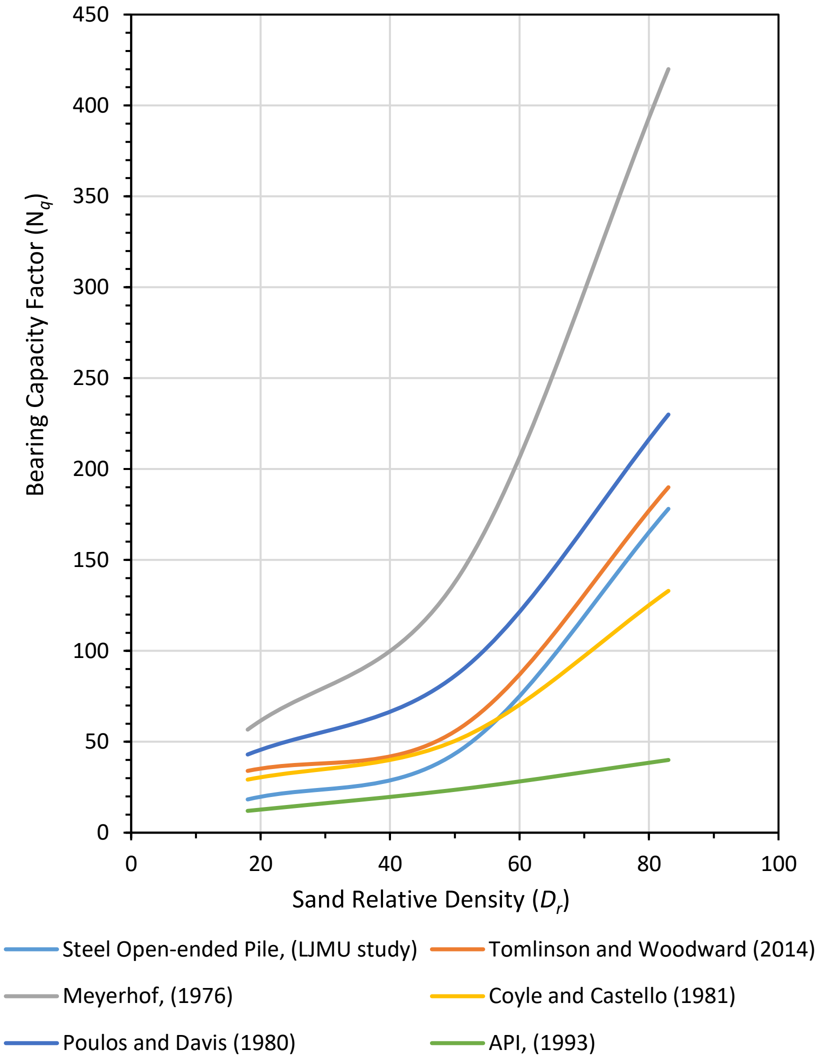

Figure 6-14: Variation of pile bearing capacity factor for steel open-ended piles with a slenderness ratio of 17.

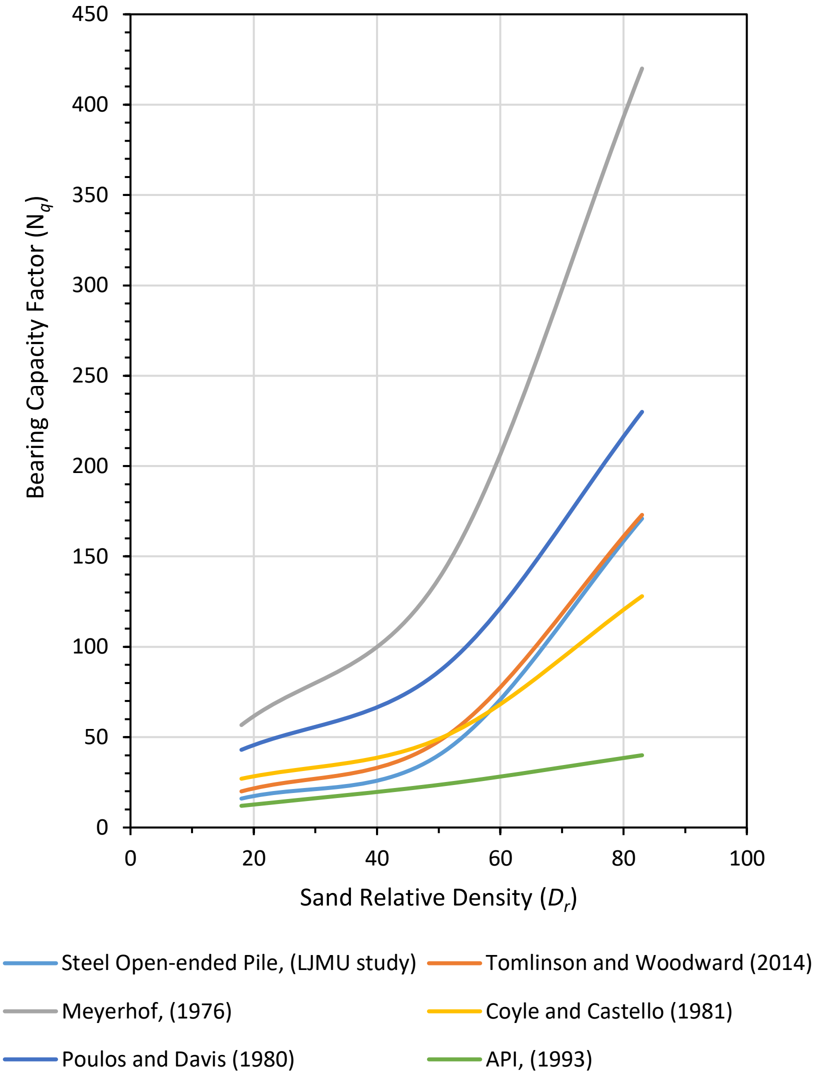

Figure 6-15: Variation of pile bearing capacity factor for steel open-ended piles with a slenderness ratio of 25.

6.7 Earth Pressure Coefficient (K) for Steel Open-ended Piles

As mentioned previously, the sand relative density, D_r, pile effective length, Lc, and pile surface roughness have been underlined to play a fundamental role in the value of the earth pressure coefficient, K. Mobilised skin friction resistance, however, is also highly influenced by the aforementioned factors. Figures 6.16, 6.17, and 6.18 indicate comparisons between the actual measured earth pressure coefficients and the predicted values utilising different approaches, with various angles of friction at three pile slenderness ratios. According to the graphical comparisons, design charts proposed by Poulos and Davis (1980) provide unreliable predicted values for the skin friction resistance of steel piles embedded in medium and dense sands. While, the American Petroleum Institute (1993) and Broms (1964) models reveal themselves to be inefficient and tend to overestimate the earth pressure coefficient, especially for piles with a slenderness ratio of 25 driven in dense sand. On the other hand, the latest suggested design charts have a better estimation performance with good accuracy to predict the skin friction resistance for piles driven in loose and medium sands with slenderness ratios of 12 and 17, respectively. There is a reasonable error rate to predict the K values for piles with a slenderness ratio of 25 driven in dense sand.

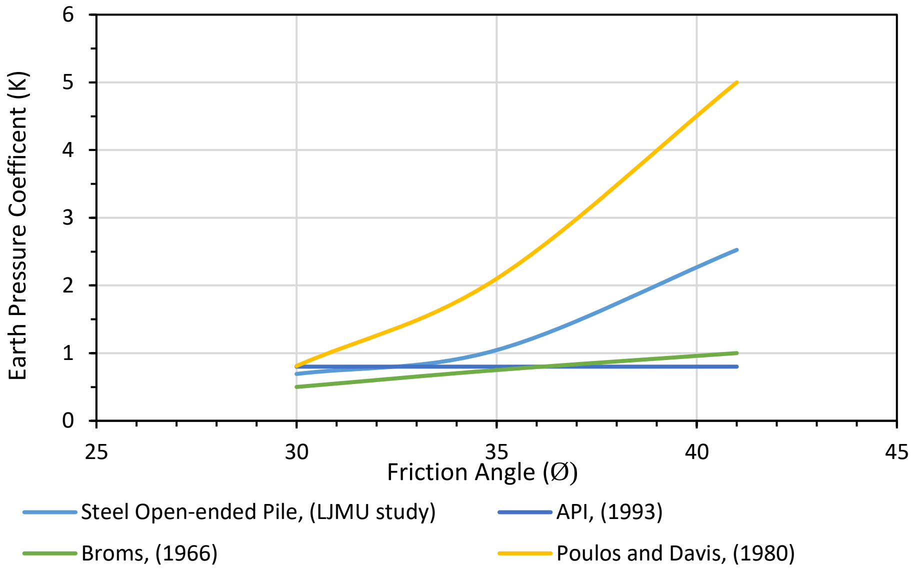

Figure 6-16: Effect of angle of friction (Ø) on earth pressure coefficient (K) for steel open-ended piles with a slenderness ratio of 12.

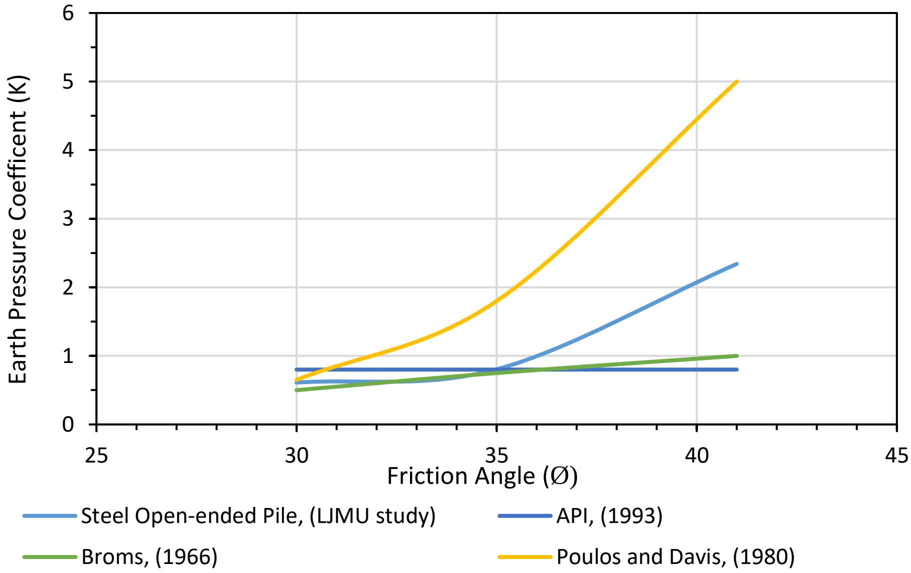

Figure 6-17: Effect of angle of friction (Ø) on earth pressure coefficient (K) for steel open-ended piles with a slenderness ratio of 17.

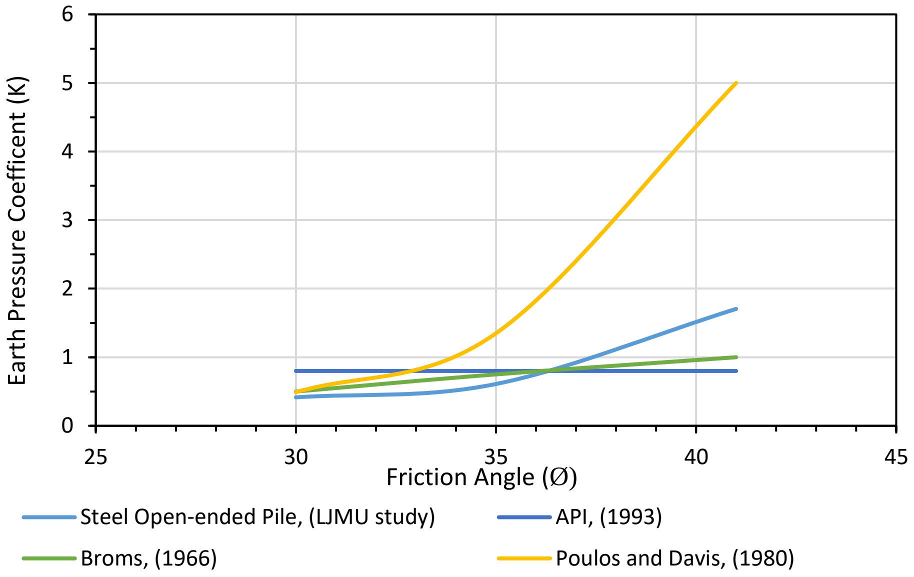

Figure 6-18: Effect of angle of friction (Ø) on earth pressure coefficient (K) for steel open-ended piles with a slenderness ratio of 25.

6.8 Summary

Accurate determination of pile bearing capacity is a prerequisite for structural stability and effective insurance against failure. A methodology allowing an economical and efficient form of new pile foundation design charts in comparison with the most used conventional design charts is introduced in this chapter. Pile bearing capacity factors ($N_q$values) and earth pressure coefficients (K values) for the described piles and sand densities were determined by back calculation from the experimental pile load tests. For the described soil profile, it was clearly observed that the suggested design charts proposed by the conventional methods have revealed shortcomings to accurately define the pile bearing capacity design factors. Accordingly, errors on the unsafe side can be obtained with the application of such methods. In essence, from what has been presented and discussed, the following conclusions can be drawn:

- Pile penetrated length-to-diameter ratio, pile surface roughness, effective overburden pressure, and the sand relative density have been identified to play significant roles in the governing pile bearing capacity design procedure.
- For concrete piles, using the bearing capacity design charts, the N_q values obtained by the current study seem to be in good agreement with those proposed by Tomlinson and Woodward (2014) and Poulos and Davis (1980).
- For piles with a slenderness ratio of 12, the described conventional design charts are revealed to be unreliable to predict the k factor for piles embedded in medium and dense sands. While, for piles with Lc/d equal to 17, consistent agreement can be observed between the predicted and actual K values proposed by the current study and those offered by the American Petroleum Institute (1993), and Broms (1964) for piles driven in loose and medium sands, respectively. Whereas, the aforementioned suggested analysis charts seem to be in good agreement for piles with Lc/d equal to 25.
- For steel piles, the N_q design charts proposed by Tomlinson and Woodward (2014) demonstrated remarkable agreement with reference to the developed design charts. Additionally, the American Petroleum Institute (1993) and Broms (1964) methods are by far the best for predicting the K coefficient for piles with a length-to-diameter-ratio of 25, giving substantial consistency with reference to the reported K values evaluated by the current study. Whereas, the rest of the described suggested design procedures tend to be unreliable in assessing the pile bearing capacity design factors.

CHAPTER 7

Conclusions and Recommendations for Future Works

7.1 Conclusions

In the introductory chapter, the utilisation of the pile foundations was clearly presented. The uncertainty associated with the existing pile bearing capacity approaches and simulation of the combined soil-pile interaction, led to the study of the objectives in an effort to overcome the limitations of the pile design and analysis under compression and uplift loading systems. The investigation was aimed at better understanding the behaviour and performance of model piles embedded in sandy soil. Moving the existing knowledge forward, a body of research was developed at Liverpool John Moores University. The work was optimised in different stages conducting a series of comprehensive experimental load-carrying capacity tests on different types of model piles tested in three sand relative densities, namely loose, medium and dense, and subjected to uplift and compression loads. The feasibility of applying a new, self-tuning computational intelligence system, enhanced by a comprehensive statistical analysis study, has been explored and discussed in relation to the stated aim and objectives.

A summary of the main conclusions from the current research is presented below:

Objective One

1. The higher the values of the pile effective length, sand density, and the soil-pile angle of shearing resistance, the higher the axial load magnitudes to reach the yield limit.
2. The load-displacement curves show a clear elastic response when the normalised pile settlement is between 1 to 2% of pile diameter.
3. For all cases, as the applied load increases, the response of the pile load-settlement curves increases in its nonlinearity until the maximum pile capacity is reached. This can be attributed to the plastic mechanism behaviour associated with the soil-pile interaction, where local nonlinearity is obvious.
4. Through the direct shear test, the peak angle of friction and the sand-pile angle of interface friction were found to be influenced by the initial sand stiffness and pile material roughness.
5. The ultimate bearing capacity for concrete piles is revealed greater than the capacity for steel piles. This can be assigned to the contribution of end bearing and higher mobilised skin friction resistance developed within the contacted soil in the adjoining zone of influence.

Objective Two

6. The fibre optimisation process shows that the addition of 1.25% (out of seven percentages) structural fibres by concrete volume has been identified as the optimum percentage to enhance concrete efficiency beyond the elastic limit. Additionally, the flexural test results revealed that the mechanical performance of the fibre reinforced concrete provides a better energy absorption capacity by delaying and controlling crack formation compared with the plain concrete.

Objective Three

7. Five independent variables (IVs) namely, applied load, *P*, pile slenderness ratio, Lc/d, pile axial rigidity, EA, pile effective length, Lc and sand-pile interface friction angle, δ were identified, according to the dataset screening process, to play a significant role, at different contribution levels, on pile-load settlement response, following the order *P*> δ > Lc/d > L > EA.
8. The optimal structure for the trained network was found at a topology of 5:10:1 with a "*tangent sigmoid*" transfer function between the first and second layers and a "*linear*" transfer function in the third (output) layers.
9. Based on the graphical comparisons between the targeted pile load-settlement versus the computational values, substantial consistency has been identified for all training, testing and validation elements, demonstrating that the proposed approach can be utilised with a continuous degree of success.

Objective Four

10. The applied supervised, evolutionary Levenberg-Marquardt (LM) training algorithm has several favourable features, for instance (generalisation ability, efficiency, ease of application, and faster), which make it a good choice to map complex nonlinear systems.
11. According to the defined performance skill indicators, the developed algorithm is superior to the reviewed empirical approaches, indicating that the conventional design methods are inaccurate and need to be updated, if used, in future applications.

Objective Five

12. The Truncated Cone and Das (1983) models do not exhibit acceptable precision in predicting ultimate uplift pile capacity in the described test environment. While, the Meyerhof (1973) model indicates an acceptable level of error with better proficiency when compared with results of the steel closed-ended piles.
13. Comparing the results of the developed pile bearing capacity design charts proposed by the current study with most conventional design procedures used in the absence of pile load tests yielded interesting findings. For precast concrete piles, Tomlinson and Woodward (2014) and Poulos and Davis (1980) models are by far the best at predicting the bearing capacity factor, N_q, while the rest are inefficient to accurately predict the $\mathrm{N}_q$design factor. Regarding the earth pressure coefficient, K, the results proposed by Poulos and Davis (1980) model substantially overestimate the K values for concrete piles driven in medium and dense sands and are not recommend to be applied in practice. While, the results proposed by the American Petroleum Institute (1993) and Broms (1964) models are in good consistency with the new design charts to predict the K values for concrete piles with slenderness ratio of 25 in the described soil stiffness.
14. The Tomlinson and Woodward (2014) model is demonstrated to be efficient to predict the pile bearing capacity (N_q) for steel piles. Moreover, the design chart documented by the American Petroleum Institute (1993) and Broms (1964) display consistent prediction accuracy, to evaluate the k factor for piles with a slenderness ratio of 25.

In essence, the study aim was to explore pile-bearing capacity driven at different relative densities of sand subjected to compression and uplift loads, examine the feasibility of an enhanced self-tuning computational intelligence approach, and to develop an improved design guidance, which permits us to determine the individual contribution of the most influential pile bearing capacity design factors. The main limitation of this study lies in the fact that the piles were tested in cohesionless soil only. Considering this limitation, a new set of recommendations for further studies are summarised as detailed in the following section:

7.2 Recommendations for Future Work

In light of the results reported in this study and based on the experience gained during the course of this research, a number of possible future studies are recommended as follows:

1. Explore the effect of ground water content on pile bearing capacity under independent uplift loads by varying the degree of saturation, and with different types of piles embedded in cohesive soils.
2. Examine the performance of different types of model piles (precast concrete, steel closed-ended and steel open-ended) subjected to combined loading (compression, uplift, and lateral) loads driven in cohesive soils.
3. Apply a novel Particle Image Velocity (PIV) technique to investigate the stress distribution of the test media by changing the following parameters: pile material types, soil stiffness, loading mechanism and pile slenderness ratio.
4. Investigate the feasibility of the finite element applications to simulate load-displacement curves and compare it with conventional pile bearing capacity design procedures.
5. Study the effect of oil contaminated soil on pile bearing capacity subjected to combined loading systems.

References

Abdellatif, M. E. M. 2013. Modelling The Impact Of Climate Change On Urban Drainage System. *PhD thesis, Faculty of Engineering and Technology, Liverpool John Moores University, Liverpool, UK*.

Ahmadi, M. A., Zendehboudi, S., Dusseault, M. B. & Chatzis, I. 2016. Evolving Simple-To-Use Method To Determine Water-Oil Relative Permeability In Petroleum Reservoirs. *Petroleum,* 2(1)**,** 67-78.

Akdag, C. T. & Özden, G. 2013. Nonlinear Behavior Of Reinforced Concrete (RC) And Steel Fiber Added RC (WS-SFRC) Model Piles In Medium Dense Sand. *Construction and Building Materials,* 48**,** 464-472.

Al-Janabi, K. R. 2006. Laboratory Leaching Process Modeling In Gypseous Soils Using Artificial Neural Networks (ANNs). *PhD thesis, Building and Construction Engineering Department, University of Technology, Iraq*.

Alizadeh, B., Najjari, S. & Kadkhodaie-Ilkhchi, A. 2012. Artificial Neural Network Modeling And Cluster Analysis For Organic Facies And Burial History Estimation Using Well Log Data: A Case Study Of The South Pars Gas Field, Persian Gulf, Iran. *Computers and Geosciences,* 45**,** 261-269.

Alkroosh, I. & Nikraz, H. 2011. Simulating Pile Load-Settlement Behavior From CPT Data Using Intelligent Computing. *Central European Journal of Engineering,* 1(3)**,** 295-305.

Alkroosh, I. & Nikraz, H. 2014. Predicting Pile Dynamic Capacity Via Application Of An Evolutionary Algorithm. *Soils and Foundations,* 54(2)**,** 233-242.

Alkroosh, I. S., Bahadori, M., Nikraz, H. & Bahadori, A. 2015. Regressive Approach For Predicting Bearing Capacity Of Bored Piles From Cone Penetration Test Data. *Journal of Rock Mechanics and Geotechnical Engineering,* 7(5)**,** 584-592.

Alrashydah, E. I. & Abo-Qudais, S. A. 2018. Modeling Of Creep Compliance Behavior In Asphalt Mixes Using Multiple Regression And Artificial Neural Networks. *Construction and Building Materials,* 159**,** 635-641.

American Petroleum Institute 1987. Recommended Practice For Planning Designing And Constructing Of Fixed Offshore Platforms: 2A (RP 2A). *17th edition; Washington*.

American Petroleum Institute 1993. Recommended Practice For Planning, Designing And Construction Of Fixed Offshore Platforms-Load And Resistance Factor Design: RP2A-LRFD. *20th edition; Washington*.

American Petroleum Institute 2007. Recommended Practice For Planning, Designing And Constructing Of Fixed Offshore Platforms-Working Stress Design: API RP 2A. *22nd edition; Washington*.

American Society for Testing and Materials 2013. D1143M-13 Standard Test Methods For Deep Foundations Under Static Axial Compressive Load. *ASTM, West Conshohocken, USA*.

Armaghani, D. J., Mohamad, E. T., Hajihassani, M., Yagiz, S. & Motaghedi, H. 2016. Application Of Several Non-Linear Prediction Tools For Estimating Uniaxial Compressive Strength Of Granitic Rocks And Comparison Of Their Performances. *Engineering with Computers,* 32(2)**,** 189-206.

Baran, E., Akis, T. & Yesilmen, S. 2012. Pull-Out Behavior Of Prestressing Strands In Steel fiber Reinforced Concrete. *Construction and Building Materials,* 28**,** 362-371.

Baziar, M. H., Azizkandi, A. S. & Kashkooli, A. 2015. Prediction Of Pile Settlement Based On Cone Penetration Test Results: An ANN Approach. *KSCE Journal of Civil Engineering,* 19(1)**,** 98-106.

Bowles, J. E. 1992. Engineering Properties Of Soils And Their Measurement. *McGraw-Hill International Book Company, New York*.

Broms, B. B. 1964. Lateral Resistance Of Piles In Cohesive Soils. *Journal of the Soil Mechanics and Foundations Division ASCE* 90(2)**,** 27-64.

BSI BS EN 196-1:2005. Methods Of Testing Cement. Determination Of Strength. *British Standards Institution, London*.

BSI BS EN 410-2:2000. Test Sieves - Technical Requirements And Testing. *British Standards Institution, London*.

BSI BS EN 1377-7:1990. Methods Of Test For Soils For Civil Engineering Purposes, Part 7: Shear Strength Tests. *British Standards Institution, London*.

BSI BS EN 8004:1986. Code Of Practice For Foundations. *British Standards Institution, London*.

BSI BS EN 12390-2:2009. Testing Hardened Concrete. Making And Curing Specimens For Strength Tests. *British Standards Institution, London*.

BSI BS EN 12390-5:2009. Testing Hardened Concrete: Flexural Strength Of Test Specimens. *British Standards Institution, London*.

Burland, J. B. 1973. Shaft Friction Of Piles In Clay-A Simple Fundamental Approach. *Ground Engineering,* 6(3)**,** 30-42.

Caudill, M. 1988. Neural Networks Primer. *Part III. AI Expert,* 3(6)**,** 53-59.

Cho, S. E. 2009. Probabilistic Stability Analyses Of Slopes Using The ANN-Based Response Surface. *Computers and Geotechnics,* 36(5)**,** 787-797.

Comodromos, E. M., Papadopoulou, M. C. & Rentzeperis, L. K. 2009. Pile Foundation Analysis And Design Using Experimental Data And 3-D Numerical Analysis. *Computers and Geotechnics,* 36(5)**,** 819-836.

Coyle, H. M. & Castello, R. R. 1981. New Design Correlations For Piles In Sand. *Journal of Geotechnical and Geoenvironmental Engineering,* 107(7)**,** 965-986.

Das, B. M. 1983. A Procedure For Estimation Of Uplift Capacity Of Rough Piles. *Soils and Foundations,* 23(3)**,** 122-126.

Das, B. M. 1995. Principles Of Foundation Engineering. *PWS Publishing Company, USA.*

Das, B. M. 2015. Principles Of Foundation Engineering. *Cengage Learning, USA*.

Deo, R. C., Downs, N., Parisi, A. V., Adamowski, J. F. & Quilty, J. M. 2017. Very Short-Term Reactive Forecasting Of The Solar Ultraviolet Index Using An Extreme Learning Machine Integrated With The Solar Zenith Angle. *Environmental Research,* 155**,** 141–166.

Deo, R. C. & Şahin, M. 2015. Application Of The Extreme Learning Machine Algorithm For The Prediction Of Monthly Effective Drought Index In Eastern Australia. *Atmospheric Research,* 153**,** 512–525.

Ebrahimian, B. & Movahed, M. 2016. Application Of An Evolutionary-Based Approach In Evaluating Pile Bearing Capacity Using CPT Results. *Ships and Offshore Structures,* 12(7)**,** 937-953.

Erdal, H. I. 2013. Two-Level And Hybrid Ensembles Of Decision Trees For High Performance Concrete Compressive Strength Prediction. *Engineering Applications of Artificial Intelligence* 26(7)**,** 1689-1697.

Erdem, H. 2015. Predicting The Moment Capacity Of RC Beams Exposed To Fire Using ANNs. *Construction and Building Materials,* 101**,** 30-38.

Faber, M., Koehler, J. & Nishijima, K. 2011. Applications Of Statistics And Probability In Civil Engineering. *CRC Press, Florida*.

Faizi, K., Armaghani, D. J., Sohaei, H., Rashid, A. S. A. & Nazir, R. 2015. Deformation Model Of Sand Around Short Piles Under Pullout Test. *Measurement,* 63**,** 110-119.

Fattah, M. Y. & Al-Soudani, W. H. 2014. Bearing Capacity Of Closed And Open Ended Pipe Piles Installed In Loose Sand With Emphasis On Soil Plug. *Indian Journal of Geo-Marine Science,* 45(5)**,** 703-724.

Fattah, M. Y. & Al-Soudani, W. H. 2016. Bearing Capacity Of Open-Ended Pipe Piles With Restricted Soil Plug. *Ships and Offshore Structures,* 11**,** 501-516.

Fattah, M. Y., Al-Soudani, W. H. & Omar, M. 2016. Estimation Of Bearing Capacity Of Open-Ended Model Piles In Sand. *Arabian Journal of Geosciences,* 9(242)**,** 1-14.

Fellenius, B. H. 1989. Unified Design Of Piles And Pile Groups. *Transportation Research Record,* 1169**,** 75-82.

Feng, Y., Barr, W. & Harper, W. F. 2013. Neural Network Processing Of Microbial Fuel Cell Signals For The Identification Of Chemicals Present In Water. *Journal of Environmental Management,* 120**,** 84-92.

Field, A. 2008. Multiple Regression Using SPSS. *Research Methods in Psychology. C8057, University of Sussex, UK***,** 1-11.

Fleming, K., Weltman, A., Randolph, M. & Elson, K. 2009. Piling Engineering. *Taylor & Francis, London*.

Gaaver, K. E. 2013. Uplift Capacity Of Single Piles And Pile Groups Embedded In Cohesionless Soil. *Alexandria Engineering Journal,* 52(3)**,** 365-372.

Gavin, K. & Gallagher, D. 2005. Development Of Shaft Friction On Driven Piles In Sand And Clay. *Paper presented to the Geotechnical Society of the Institution of Civil Engineers of Ireland. Dublin: Institution of Civil Engineers of Ireland***,** 1-16.

Gere, J. M. & Timoshenko, S. P. 1997. Mechanics Of Materials XVI. *PWS Publishing Company, USA.*

Gong, B. & Ordieres-Meré, J. 2016. Prediction Of Daily Maximum Ozone Threshold Exceedances By Preprocessing And Ensemble Artificial Intelligence Techniques: Case Study Of Hong Kong. *Environmental Modelling and Software,* 84**,** 290-303.

Gordan, B., Armaghani, D. J., Hajihassani, M. & Monjezi, M. 2016. Prediction Of Seismic Slope Stability Through Combination Of Particle Swarm Optimization And Neural Network. *Engineering with Computers,* 32**,** 85-97.

Hagan, M. T., Demuth, H. B., Beale, M. H. & Jesús, O. D. 1996. *Neural Network Design* [Online]. PWS Publishing Co, Boston. Available: http://hagan.okstate.edu/NNDesign.pdf [Accessed 20 July 2018].

Han, F., Zhao, M. R., Zhang, J. M. & Ling, Q. H. 2017. An Improved Incremental Constructive Single-Hidden-Layer Feedforward Networks For Extreme Learning Machine Based On Particle Swarm Optimization. *Neurocomputing,* 228**,** 133-142.

Handley, B., Ball, J., Bell, A. & Suckling, T. 2006. Handbook on Pile Load Testing. *Federation of Piling Specialists, Beckenham, UK***,** 1-29.

Hashim, K. S., Shaw, A., Al Khaddar, R., Pedrola, M. O. & Phipps, D. 2017a. Defluoridation Of Drinking Water Using A New Flow Column Electrocoagulation Reactor (FCER) - Experimental, Statistical, And Economic Approach. *Journal of Environmental Management,* 197**,** 80-88.

Hashim, K. S., Shaw, A., Al Khaddar, R., Pedrola, M. O. & Phipps, D. 2017b. Energy Efficient Electrocoagulation Using A New Flow Column Reactorto To Remove

Nitrate From Drinking Water - Experimental, Statistical, And Economic Approach. *Journal of Environmental Management,* 196**,** 224-233.

Hashim, K. S., Shaw, A., Al Khaddar, R., Pedrola, M. O. & Phipps, D. 2017c. Iron Removal, Energy Consumption And Operating Cost Of Electrocoagulation Of Drinking Water Using A New Flow Column Reactor. *Journal of Environmental Management,* 189**,** 98-108.

Hight, D. W., Lawrence, D. M., Farquhar, G. B., Milligan, G. W., Gue, S. S. & Potts, D. M. 1996. Evidence For Scale Effects In The Bearing Capacity Of Open-Ended Piles In Sand. *In: Proceedings of the 28th International Conference of Offshore Technology, Houston,OTC 7975* 181-192.

Hornik, K., Stinchcombe, M. & White, H. 1989. Multilayer Feedforward Networks Are Universal Approximators. *Neural Networks,* 2(5)**,** 359-366.

Hu, J., Zhang, J., Zhang, C. & Wang, J. 2016. A New Deep Neural Network Based On A Stack Of Single-Hidden-Layer Feed Forward Neural Networks With Randomly Fixed Hidden Neurons. *Neurocomputing,* 171**,** 63-72.

Igoe, D., Gavin, K. & O'Kelly, B. 2011. Shaft Capacity Of Open-Ended Piles In Sand. *Journal of Geotechnical and Geoenvironmental Engineering,* 137(10)**,** 903-913.

Igoe, D., Spagnoli, G., Doherty, P. & Weixler, L. 2014. Design Of A Novel Drilled-and-Grouted Pile In Sand For Offshore Oil And Gas Structures. *Marine Structures,* 39**,** 39-49.

Institution of Civil Engineers 2007. Specification For Piling And Embedded Retaining Walls, ICE Publishing. *London, UK.*

Ismail, A., Jeng, D. S. & Zhang, L. L. 2013. An Optimised Product-Unit Neural Network With A Novel PSO-BP Hybrid Training Algorithm: Applications To Load Deformation Analysis Of Axially Loaded Piles. *Engineering Applications of Artificial Intelligence,* 26(10)**,** 2305-2314.

Jaeel, A. J., Al-wared, A. I. & Ismail, Z. Z. 2016. Prediction Of Sustainable Electricity Generation In Microbial Fuel Cell By Neural Network: Effect Of Anode Angle With Respect To Flow Direction. *Journal of Electroanalytical Chemistry,* 767**,** 56-62.

Jebur, A. A., Atherton, W. & Al Khaddar, R. M. 2018a. Feasibility Of An Evolutionary Artificial Intelligence (AI) Scheme For Modelling Of Load Settlement Response Of Concrete Piles Embedded In Cohesionless Soil. *Ships and Offshore Structures,* 13(7)**,** 705-718.

Jebur, A. A., Atherton, W., Al Khaddar, R. M. & Loffill, E. 2016. Simulation Of Soil-Pile Interaction Of Steel Batter Piles Penetrated In Sandy Soil Subjected To Pull-Out Loads. *International Journal of Civil and Environmental Engineering,* 10(5)**,** 605-610.

Jebur, A. A., Atherton, W., Al Khaddar, R. M. & Loffill, E. 2018b. Settlement Prediction Of Model Piles Embedded In Sandy Soil Using The Levenberg–Marquardt (LM) Training Algorithm. *Geotechnical and Geological Engineering,* 36(5)**,** 2893-2906.

Jeffrey, J. 2012. Investigating The Performance Of Continuous Helical Displacement Piles. *PhD thesis, College of Art, Science & Engineering, University of Dundee,UK.*

Juncai, X., Qingwen, R. & Zhenzhong, S. 2015. Prediction Of The Strength Of Concrete Radiation Shielding Based On LS-SVM. *Annals of Nuclear Energy,* 85**,** 296-300.

Kabiri-Samani, A. R., Aghaee-Tarazjani, J., Borghei, S. M. & Jeng, D. S. 2011. Application Of Neural Networks And Fuzzy Logic Models To Long-Shore Sediment Transport. *Applied Soft Computing,* 11(2)**,** 2880–2887.

Kampitsis, A. E., Giannakos, S., Gerolymos, N. & Sapountzakis, E. J. 2015. Soil-Pile Interaction Considering Structural Yielding: Numerical Modeling And Experimental Validation. *Engineering Structures,* 99**,** 319-333.

Kézdi, Á. & Rétháti, L. 1974. Handbook Of Soil Mechanics. *Elsevier. Amsterdam*.

Kishida, H. 1963. Stress Distribution By Model Piles In Sand. *Soils and Foundations,* 4(1)**,** 1–23.

Kosmatka, S. H. & Panarese, W. C. 1994. Design And Control Of Concrete Mixtures. *Portland Cement Association, Illinois, USA.*

Kriesel, D. 2011. *Brief Introduction To Neural Networks* [Online]. University of Bonn, Germany. Available: http://www.dkriesel.com/_media/science/neuronalenetze-en-zeta2-2col-dkrieselcom.pdf [Accessed 20 July 2018].

Kulhawy, F. H. 1984. Limiting Tip And Side Resistance: Fact Or Fallacy? In Symposium Of Analysis And Design Of Pile Foundation. *ASCE, New York***,** 80-98.

Kumar, S. & Basudhar, P. K. 2018. A Neural Network Model For Slope Stability Computations. *Géotechnique Letters,* 8**,** 149-154.

Lehane, B. M. & Gavin, K. G. 2001. Base Resistance Of Jacked Pipe Piles In Sand. *Journal Of Geotechnical And Geoenvironmental Engineering,* 127(6)**,** 473-480.

Letsios, C., Lagaros, N. D. & Papadrakakis, M. 2014. Optimum Design Methodologies For Pile Foundations In London. *Case Studies in Structural Engineering,* 2**,** 24-32.

Loria, A. F. R., Orellana, F., Minardi, A., Fürbringer, J. M. & Laloui, L. 2015. Predicting The Axial Capacity Of Piles In Sand. *Computers and Geotechnics,* 69**,** 485-495.

Mahmud, G. H., Yang, Z. & Hassan, A. M. 2013. Experimental And Numerical Studies Of Size Effects Of Ultra High Performance Steel Fibre Reinforced Concrete (UHPFRC) Beams. *Construction and Building Materials,* 48**,** 1027-1034.

Maier, H. R. & Dandy, G. C. 2000. Applications Of Artificial Neural Networks To Forecasting Of Surface Water Quality Variables: Issues, Applications And Challenges. *Environmental Modelling and Software,* 15(1)**,** 101-124.

Majdi, M. & Beiki, M. 2010. Evolving Neural Network Using A Genetic Algorithm For Pre- Dicting The Deformation Modulus Of Rock Masses. *International Journal of Rock Mechanics and Mining Sciences,* 47(2)**,** 246–253.

Majeed, A. H., Mahmood, K. R. & Jebur, A. A. 2013. Simulation Of Hyperbolic Stress-Strain Parameters Of Soils Using Artificial Neural Networks. *In: Proceedings of the 23rd International Conference on Geotechnical Engineering,* Hammamet, Tunisia**,** 105-115.

Manandhar, S. & Yasufuku, N. 2013. Vertical Bearing Capacity Of Tapered Piles In Sands Using Cavity Expansion Theory. *Soils and Foundations,* 53(6)**,** 853-867.

Mareš, T., Janouchová, E. & Kuˇcerová, A. 2016. Artificial Neural Networks In The Calibration Of Nonlinear Mechanical Models. *Advances in Engineering Software,* 95**,** 68-81.

Master, T. 1993. Practical Neural Networks Recipes In C ++. *Academic Press, San Diego, USA.*

Meyerhof, G. G. 1973. Uplift Resistance Of Inclined Anchors And Piles. *In: Proceedings of the 8th International Conference on Soil Mechanics and Foundation Engineering, Moscow,* 2**,** 167–172.

Meyerhof, G. G. 1976. Bearing Capacity And Settlement Of Pile Foundations. *Journal of Geotechnical and Geoenvironmental Engineering,* 102, GT3**,** 195-228.

Millie, D. F., Weckman, G. R., Young II, W. A., Ivey, J. E., Carrick, H. J. & Fahnenstiel, G. L. 2012. Modeling Microalgal Abundance With Artificial Neural Networks: Demonstration Of A Heuristic 'Grey-Box' To Deconvolve And Quantify Environmental Influences. *Environmental Modelling and Software,* 38**,** 27-39.

Mirabdolazimi, S. M. & Shafabakhsh, G. 2017. Rutting Depth Prediction Of Hot Mix Asphalts Modified With Forta Fiber Using Artificial Neural Networks And Genetic Programming Technique. *Construction and Building Materials,* 148**,** 666-674.

Moayedi, H. & Rezaei, A. 2017. An Artificial Neural Network Approach For Under-Reamed Piles Subjected To Uplift Forces In Dry Sand. *Neural Computing and Applications***,** DOI 10.1007/s00521-017-2990-z, 1-10.

Mohammadi, E. G. & Ashour, A. 2016. A Feasibility Study Of BBP For Predicting Shear Capacity Of FRP Reinforced Concrete Beams Without Stirrups. *Advances in Engineering Software,* 97**,** 29-39.

Mohammadi, K., Shamshirband, S., Kamsin, A., Lai, P. C. & Mansor, Z. 2016. Identifying The Most Significant Input Parameters For Predicting Global Solar

Radiation Using An ANFIS Selection Procedure. *Renewable and Sustainable Energy Reviews,* 63**,** 423-434.

Mohammed, M. A., Ghani, M. K. A. & Hamed, R. I. 2017. Analysis Of An Electronic Methods For Nasopharyngeal Carcinoma:Prevalence, Diagnosis, Challenges And Technologies. *Journal of Computational Science*, 21**,** 241-254.

Momeni, E., Nazir, A., Armaghani, D. J. & Maizir, H. 2014. Prediction Of Pile Bearing Capacity Using A Hybrid Genetic Algorithm-Based ANN. *Measurement,* 57**,** 122-131.

Morfidis, K. & Kostinakis, K. 2017. Seismic Parameters' Combinations For The Optimum Prediction Of The Damage State Of R/C Buildings Using Neural Networks. *Advances in Engineering Software*, 106**,** 1-16.

Murthy, V. N. S. 2002. Geotechnical Engineering: Principles And Practices Of Soil Mechanics And Foundation Engineering. *CRC Press, USA.*

Nasr, A. M. 2013. Uplift Behavior Of Vertical Piles Embedded In Oil-Contaminated Sand. *Journal of Geotechnical and Geoenvironmental Engineering,* 139(1)**,** 162-174.

Nazir, A. & Nasr, A. 2013. Pullout Capacity Of Batter Pile In Sand. *Journal of Advanced Research,* 4(2)**,** 147-154.

Nejad, F. P. & Jaksa, M. B. 2017. Load-Settlement Behavior Modeling Of Single Piles Using Artificial Neural Networks And CPT Data. *Computers and Geotechnics,* 89**,** 9-21.

Nguyen-Truong, H. T. & Le, H. M. 2015. An Implementation Of The Levenberg–Marquardt Algorithm Forsimultaneous-Energy-Gradient Fitting Using Two-Layer Feed Forwardneural Networks. *Chemical Physics Letters*, 629**,** 40-45.

Nunez, I. L., Hoadley, P. J., Randolph, M. F. & Hulett, J. M. 1988. Driving And Tension Loading Of Piles In Sand On A Centrifuge. *In: Proceedings of the International Conference Centrifuge. Paris, France,* 88**,** 353–362.

Ornek, M., Laman, M., Demir, A. & Yildiz, A. 2012. Prediction Of Bearing Capacity Of Circular Footings On Soft Clay Stabilized With Granular Soil. *Soils and Foundations* 52(1)**,** 69-80.

Paik, K. & Salgado, R. 2003. Determination of Bearing Capacity of Open-Ended Piles In Sand. *Journal of Geotechnical and Geoenvironmental Engineering,* 129(1)**,** 46-57.

Pallant, J. 2011. SPSS Survival Manual: A Step By Step Guide To Data Analysis Using SPSS. *Maidenhead, Berkshire. Open University Press, UK.*

Peiris, T., Thambiratnam, D., Perera, N. & Gallage, C. 2014. Soil-Pile Interaction Of Pile Embedded In Deep Layered Marine Sediment Under Seismic Excitation. *Structural Engineering International*, 24(2)**,** 521-531.

Poulos, H. G. & Davis, E. H. 1980. Pile Foundation Analysis And Design. *John Wiley & Sons, New York*.

Premalatha, N. & Valan, A. A. 2016. Prediction Of Solar Radiation For Solar Systems By Using ANN Models With Different Back Propagation Algorithms. *Journal of Applied Research and Technology,* 14(3)**,** 206-214.

Rajasvaran, K. N. 2007. Comparison Of Ultimate Bearing Capacity Obtained By Pile Driving Analyzer And Maintained Load Test. *PhD thesis, Faculty of Civil Engineering. Universiti Teknologi Malaysia*.

Ramasamy, G., Dey, B. & Indrawan. E. 2004. Studies Of Skin Friction In Piles Under Tensile And Compressive Load. *Indian Geotechnical Journal*, 34(3) 276–289.

Rao, S. N., Ramakrishna, V. G. S. T. & Rao, M. B. 1998. Influence Of Rigidity On Laterally Loaded Pile Groups In Marine Clay. *Journal of Geotechnical and Geoenvironmental Engineering,* 124(6)**,** 542–549.

Ravuri, S. & Stolcke, A. 2016. A Comparative Study Of Recurrent Neural Network Models For Lexical Domain Classification. *In: Proceedings of the International Conference on Acoustics, Speech and Signal Processing (ICASSP), Shanghai, IEEE***,** 6075-6079.

Reddy, K. M. & Ayothiraman, R. 2015. Experimental Studies On Behavior Of Single Pile Under Combined Uplift And Lateral Loading. *Journal of Geotechnical and Geoenvironmental Engineering,* 141(7)**,** 1-10.

Remaud, D. 1999. Pieux Sous Charges Latérales: Etude Expérimentale De L'effet De Groupe [Lateral Loads Piles: Experimental Study Of The Group Effect]. *PhD thesis. University of Nantes. France*.

Robinsky, E. I. & Morrison, C. F. 1964. Sand Displacement And Compaction Around Model Friction Piles. *Canadian Geotechnical Journal,* 1(2)**,** 81-93.

Rumelhart, D. E., Hinton, G. E. & Williams, R. J. 1986. Learning Internal Representation By Error Propagation. In: Rumelhart, D. E., James, L., & McClelland (Eds.), Parallel Distributed Processing: Explorations in the Microstructure of Cognition. *MIT Press, Cambridge,* 1**,** 318-362.

Schawmb, T. 2009. The Continuous Helical Displacement Pile In Comparison To Conventional Piling Techniques. *Masters thesis. University of Dundee, UK*.

Shahin, M. A. 2014. Load–Settlement Modeling Of Axially Loaded Steel Driven Piles Using CPT-Based Recurrent Neural Networks. *Soils and Foundations,* 54(3)**,** 515-522.

Shahin, M. A. 2016. State-Of-The-Art Review Of Some Artificial Intelligence Applications In Pile Foundations. *Geoscience Frontiers,* 7(1)**,** 33-44.

Shahin, M. A. & Jaksa, M. B. 2005. Neural Network Prediction Of Pullout Capacity Of Marquee Ground Anchors. *Computers and Geotechnics,* 32(3)**,** 153-163.

Shaia, H. A. 2013. Behaviour Of Fibre Reinforced Polymer Composite Piles: Experimental And Numerical Study. *PhD thesis, School of Mechanical, Aerospace and Civil Engineering, The University of Manchester, Manchester, UK*.

Shanker, K., Basudhar, P. K. & Patra, N. R. 2007. Uplift Capacity Of Single Piles: Predictions And Performance. *Geotechnical and Geological Engineering,* 25(2)**,** 151-161.

Sharma, L. K., Singh, R., Umrao, R. K., Sharma, K. M. & Singh, T. N. 2017. Evaluating The Modulus Of Elasticity Of Soil Using Soft Computing System. *Engineering with Computers,* 33(3)**,** 497-507.

Sitton, J. D., Zeinali, Y. & Story, B. A. 2017. Rapid Soil Classification Using Artificial Neural Networks For Use In Constructing Compressed Earth Blocks. *Construction and Building Materials,* 138**,** 214-221.

Sollazzo, G., Fwa, T. F. & Bosurgi, G. 2017. An ANN Model To Correlate Roughness And Structural Performance In Asphalt Pavements. *Construction and Building Materials,* 134**,** 684–693.

Stojanovic, B., Milivojevic, M., Milivojevic, N. & Antonijevic, D. 2016. A Self-Tuning System For Dam Behavior Modeling Based On Evolving Artificial Neural Networks. *Advances in Engineering Software,* 97**,** 85-95.

Sun, S., Yan, H. & Kouyi, G. L. 2014. Artificial Neural Network Modelling In Simulation Of Complex Flow At Open Channel Junctions Based On Large Data Sets. *Environmental Modelling and Software,* 62**,** 178-187.

Tabachnick, B. G. & Fidell, L. S. 2013. Using Multivariate Statistics. *Allyn and Bacon, USA.*

Tarawneh, B. 2013. Pipe Pile Setup: Database And Prediction Model Using Artificial Neural Network. *Soils and Foundations,* 53(4)**,** 607-615.

Tarawneh, B. 2017. Predicting Standard Penetration Test N-Value From Cone Penetration Test Data Using Artificial Neural Networks. *Geoscience Frontiers,* 8(1)**,** 199-204.

Taylor, R. N. 1995. Centrifuges In Modeling: Principles And Scale Effects. *Geotechnical Centrifuge Technology, Blackie Academic & Professional, London***,** 19–33.

Terzaghi, K. 1951. Theoretical Soil Mechanics. *Chapman And Hall, Limited, London*.

Tomlinson, M. & Woodward, J. 2014. Pile Design And Construction Practice. *CRC Press, London*.

Tschuchnigg, F. & Schweiger, H. F. 2015. The Embedded Pile Concept – Verification Of An Efficient Tool For Modelling Complex Deep Foundations. *Computers and Geotechnics*, 63**,** 244-254.

Ueno, K. 2001. Methods For Preparation Of Sand Samples. *In: Proceedings of the International Conference Centrifuge 98, ISSMFE,* Tokyo, 2**,** 1047-1055.

Unsever, Y. S., Matsumoto, T. & Özkan, M. Y. 2015. Numerical Analyses Of Load Tests On Model Foundations In Dry Sand. *Computers and Geotechnics,* 63**,** 255-266.

Vesic, A. S. 1977. Design Of Pile Foundations. *NCHRP Synthesis of Highway Practice, Rep. No. 42, Transportation Research Board, Washington*.

Whitaker, T. 1963. The Constant Rate Of Penetration Test For The Determination Of The Ultimate Bearing Capacity Of A Pile. *In: Proceedings of the Institutions of Civil Engineering*, 26**,** 119-123.

Wilamowski, B. M. & Yu, H. 2010. Improved Computation For Levenberg-Marquardt. *IEEE Transaction on Neural Network*, 21**,** 930-737.

Xu, W. Z., Li, C. B., Choung, J. & Lee, J. M. 2017. Corroded Pipeline Failure Analysis Using Artificial Neural Network Scheme. *Advances in Engineering Software,* 112**,** 255-266.

Yadav, A. K., Malik, H. & Chandel, S. S. 2014. Selection Of Most Relevant Input Parameters Using WEKA For Artificial Neural Network Based Solar Radiation Prediction Models. *Renewable and Sustainable Energy Reviews,* 31**,** 509-519.

Young, H. D. & Freedman, R. A. 2000. Sears And Zemansky's University Physics. *Addison-Wesley, San Francisco*.

Yu, H. & Wilamowski, B. M. 2011. Levenberg–Marquardt Training. *Industrial Electronics Handbook, chapter 12, CRC Press, USA***,** 12-1 to 12-15.

Zhang, L., Wu, X., Ji, W. & AbouRizk, S. M. 2016. Intelligent Approach To Estimation Of Tunnel-Induced Ground Settlement Using Wavelet Packet And Support Vector Machines. *Journal of Computing in Civil Engineering,* 31(2)**,** 04016053.

Zhou, Y., Su, W., Ding, L., Luo, H. & Love, P. E. 2017. Predicting Safety Risks In Deep Foundation Pits In Subway Infrastructure Projects: Support Vector Machine Approach. *Journal of Computing in Civil Engineering,* 31(5)**,** 04017052.

Appendices

Appendix I: %MATLAB code, including the optimum number of hidden layers, the data dividing process for each sub-set, used to run the LM algorithm for all ANN developed models%

```
% This script assumes these variables are defined:
%
%   input - input data.
%   Output - target data.

x = input;
t = Output;

% Choose a Training Function
% For a list of all training functions type: help nntrain
% 'trainlm' is usually fastest.
% 'trainbr' takes longer but may be better for challenging problems.
% 'trainscg' uses less memory. Suitable in low memory situations.
trainFcn = 'trainlm';  % Levenberg-Marquardt backpropagation.

% Create a Fitting Network
hiddenLayerSize = 10;
net = fitnet(hiddenLayerSize,trainFcn);

% Choose Input and Output Pre/Post-Processing Functions
% For a list of all processing functions type: help nnprocess
net.input.processFcns = {'removeconstantrows','mapminmax'};
net.output.processFcns = {'removeconstantrows','mapminmax'};

% Setup Division of Data for Training, Validation, Testing
% For a list of all data division functions type: help nndivide
net.divideFcn = 'dividerand';  % Divide data randomly
net.divideMode = 'sample';  % Divide up every sample
net.divideParam.trainRatio = 70/100;
net.divideParam.valRatio = 15/100;
net.divideParam.testRatio = 15/100;

% Choose a Performance Function
% For a list of all performance functions type: help nnperformance
net.performFcn = 'mse';  % Mean Squared Error

% Choose Plot Functions
% For a list of all plot functions type: help nnplot
net.plotFcns = {'plotperform','plottrainstate','ploterrhist', ...
    'plotregression', 'plotfit'};

% Train the Network
```

```
[net,tr] = train(net,x,t);

% Test the Network
y = net(x);
e = gsubtract(t,y);
performance = perform(net,t,y)

% Recalculate Training, Validation and Test Performance
trainTargets = t .* tr.trainMask{1};
valTargets = t .* tr.valMask{1};
testTargets = t .* tr.testMask{1};
trainPerformance = perform(net,trainTargets,y)
valPerformance = perform(net,valTargets,y)
testPerformance = perform(net,testTargets,y)

% View the Network
view(net)
% Plots
% Uncomment these lines to enable various plots.
%figure, plotperform(tr)
%figure, plottrainstate(tr)
%figure, ploterrhist(e)
%figure, plotregression(t,y)
%figure, plotfit(net,x,t)
% Deployment
% Change the (false) values to (true) to enable the following code blocks.
% See the help for each generation function for more information.
if (false)
   % Generate MATLAB function for neural network for application
   % deployment in MATLAB scripts or with MATLAB Compiler and Builder
   % tools, or simply to examine the calculations your trained neural
   % network performs.
   genFunction(net,'myNeuralNetworkFunction');
   y = myNeuralNetworkFunction(x);
end
if (false)
   % Generate a matrix-only MATLAB function for neural network code
   % generation with MATLAB Coder tools.
   genFunction(net,'myNeuralNetworkFunction','MatrixOnly','yes');
   y = myNeuralNetworkFunction(x);
end
if (false)
   % Generate a Simulink diagram for simulation or deployment with.
   % Simulink Coder tools.
   gensim(net);
end
```

Appendix II: %MATLAB Neural Network Function, including the optimum connection weights, and details about the transfer function for the concrete pile model tested in three relative densities and subjected to compression loads%

```
function [Y,Xf,Af] = myNeuralNetworkFunction(X,~,~)
%MYNEURALNETWORKFUNCTION neural network simulation function.
%
% Generated by Neural Network Toolbox function genFunction, 01-Mar-2017
12:21:52.
%
% [Y] = myNeuralNetworkFunction(X,~,~) takes these arguments:
%
%   X = 1xTS cell, 1 inputs over TS timesteps
%   Each X{1,ts} = 5xQ matrix, input #1 at timestep ts.
%
% and returns:
%   Y = 1xTS cell of 1 outputs over TS timesteps.
%   Each Y{1,ts} = 1xQ matrix, output #1 at timestep ts.
%
% where Q is number of samples (or series) and TS is the number of timesteps.

%#ok<*RPMT0>

% ===== NEURAL NETWORK CONSTANTS =====

% Input 1
x1_step1.keep = [1 2 3 5];
x1_step2.xoffset = [0;1.079181246;0.48;1.357934847];
x1_step2.gain = [2;6.27433731131652;3.84615384615385;16.5793970038493];
x1_step2.ymin = -1;

% Layer 1
b1 = [-6.2915381947175995;0.74943262710818803;0.34284371478414316;-
2.8937598504046855;16.098742731474367;1.3940501196830313;-
1.3923256184385597;6.0429795565785289;-
5.2741693006469985;4.0069124043344511];
IW1_1 = [20.113152074358318 -0.47069286949554839 -0.92437334137699478 -
3.56242547690373;17.442656143939537 -3.4911070530498631 -2.505061290440227
-6.5876187709626466;-7.5348811658274384 1.2668001418278467
2.746984442898841 4.3432386270004226;-13.874428501864097
5.7995274048966321 -1.3371386007645083
7.0915511412590888;39.604878666201166 3.1264948628322009 -
10.248595377771435 -50.638290465233865;-12.46610761176599 -
1.6991415333081872 -3.5453113635067064 9.6443839605932613;-
22.442799372021401 2.8078392341031506 5.241219243500006
9.133484670062149;42.535138189244897 -2.9719964203023568 -
0.4923080488223785 -25.089993333660637;-18.488182732882091
0.8874559965642751 4.4149577946751251
```

```
20.1494234815435579;0.21793583149216855 0.58611821809289444 -
0.66906326444519493 4.1484483346177905];

% Layer 2
b2 = 3.4930621377025908;
LW2_1 = [-18.623889048647495 14.372778978349071 -8.8696910889824849
7.8567667573836522 19.160602503794447 -1.079719340708148 6.843960875710386
18.096164011204937 12.063890565352011 11.778880188600718];

% Output 1
y1_step1.ymin = -1;
y1_step1.gain = 2.0061741232409;
y1_step1.xoffset = 0;

% ===== SIMULATION ========

% Format Input Arguments
isCellX = iscell(X);
if ~isCellX, X = {X}; end;

% Dimensions
TS = size(X,2); % timesteps
if ~isempty(X)
  Q = size(X{1},2); % samples/series
else
  Q = 0;
end

% Allocate Outputs
Y = cell(1,TS);

% Time loop
for ts=1:TS

    % Input 1
    temp = removeconstantrows_apply(X{1,ts},x1_step1);
    Xp1 = mapminmax_apply(temp,x1_step2);

    % Layer 1
    a1 = tansig_apply(repmat(b1,1,Q) + IW1_1*Xp1);

    % Layer 2
    a2 = repmat(b2,1,Q) + LW2_1*a1;

    % Output 1
    Y{1,ts} = mapminmax_reverse(a2,y1_step1);
end

% Final Delay States
```

```
Xf = cell(1,0);
Af = cell(2,0);

% Format Output Arguments
if ~isCellX, Y = cell2mat(Y); end
end

% ===== MODULE FUNCTIONS ========

% Map Minimum and Maximum Input Processing Function
function y = mapminmax_apply(x,settings)
  y = bsxfun(@minus,x,settings.xoffset);
  y = bsxfun(@times,y,settings.gain);
  y = bsxfun(@plus,y,settings.ymin);
end

% Remove Constants Input Processing Function
function y = removeconstantrows_apply(x,settings)
  y = x(settings.keep,:);
end

% Sigmoid Symmetric Transfer Function
function a = tansig_apply(n,~)
  a = 2 ./ (1 + exp(-2*n)) - 1;
end

% Map Minimum and Maximum Output Reverse-Processing Function
function x = mapminmax_reverse(y,settings)
  x = bsxfun(@minus,y,settings.ymin);
  x = bsxfun(@rdivide,x,settings.gain);
  x = bsxfun(@plus,x,settings.xoffset);
end
```

Appendix III: %Regression Calibration Curve Code, which has been developed and used to individually determine and draw the testing dataset for each case of pile loading tests with 95% confidence interval (CI) level of fit%

```
function [binMeans,confIntervals,binMids,binStdErrs] =
regressioncalibrationcurve(targets,fits,varargin)
%INPUTS
%targets              A vector of target values
%fits                 A vector of fitted values
%bins (optional)      Number of intervals
%xLab (optional)      label on the x axis
%yLab (optional)      label on the y axis
%customTitle (optional) custom title for graphs
%
%OUTPUTS
%binMeans             The mean target value for each interval
%confIntervals        Upper and lower limits of 95% CIs for each interval
%binMids              Mid point of each interval
%binStdErrs           Standard error for each interval

defaultBins = 10;
defaultXLabel = 'Fitted value';
defaultYLabel = 'Target value';
defaultTitle = 'Calibration plot';
p = inputParser;
addRequired(p, 'targets', @isnumeric);
addRequired(p, 'fits', @isnumeric);
addOptional(p, 'bins', defaultBins, @isscalar);
addOptional(p, 'xLab', defaultXLabel);
addOptional(p, 'yLab', defaultYLabel);
addOptional(p, 'customTitle', defaultTitle);
parse(p,targets,fits,varargin);
bins = p.Results.bins;
xLab = p.Results.xLab;
yLab = p.Results.yLab;
customTitle = p.Results.customTitle;

if isrow(targets)
    targets = targets';
end

if isrow(fits)
    fits = fits';
end

binMids = zeros(1,bins);
binMeans = zeros(1,bins);
binCounts = zeros(1,bins);
```

```
binStdErrs = zeros(1,bins);
binCiSize = zeros(1,bins);

figure;
hold on;
plot([min(targets),max(targets)],[min(targets),max(targets)],'--black');
legend([xLab ' = ' yLab]);
for i = 1:bins
    binStart = min(fits) + ((i - 1) * range(fits)/bins);
    binEnd = min(fits) + (i * range(fits)/bins);
    binMids(i) = (binStart + binEnd)/2;
    binIndices = and(fits>=binStart,fits<=binEnd);
    binMeans(i) = mean(targets(binIndices));
    binCounts(i) = sum(binIndices);
    binStdErrs(i) = sqrt(var(targets(binIndices))./sum(binIndices));
    tVal = tinv(0.975,sum(binIndices)-1);
    binCiSize(i) = tVal * binStdErrs(i);
    quiver(binMids(i),binMeans(i),0,binCiSize(i),'blue');
    quiver(binMids(i),binMeans(i),0,-binCiSize(i),'blue');
end
plot(binMids,binMeans,'ored');
xlabel(xLab);
ylabel(yLab);
title(customTitle);
hold off;

confIntervals = [binMeans + binCiSize;binMeans - binCiSize];

rmse = rms(fits - targets);
[pearsonR, pearsonP] = corr(fits,targets);

if ~strcmp(customTitle,defaultTitle)
    fullTitle = [customTitle ', RMSE = ' num2str(rmse) ', R = ' num2str(pearsonR) ', p = '
num2str(pearsonP)];
else
    fullTitle = ['RMSE = ' num2str(rmse) ', R = ' num2str(pearsonR) ', p = '
num2str(pearsonP)];
end

ciWidth = 1.96 * rmse;

figure;
hold on;
plot(fits,targets,'.');
plot([min(targets),max(targets)],[min(targets),max(targets)],'-black');
plot([min(targets),max(targets)],[min(targets) + ciWidth,max(targets) + ciWidth],'--
black');
plot([min(targets),max(targets)],[min(targets) - ciWidth,max(targets) - ciWidth],'--
black');
```

```
legend('Observed data',[xLab ' = ' yLab],'95% CI of fit');
title(fullTitle);
xlabel(xLab);
ylabel(yLab);
hold off;
end
```

Appendix IV: %MATLAB Neural Network Function, including the optimum connection weights, and details about the transfer function for the steel closed-ended pile model tested in three relative densities and subjected to compression loads%

```
function [Y,Xf,Af] = myNeuralNetworkFunction(X,~,~)
%MYNEURALNETWORKFUNCTION neural network simulation function.
%
%
% [Y] = myNeuralNetworkFunction(X,~,~) takes these arguments:
%
%   X = 1xTS cell, 1 inputs over TS timesteps
%   Each X{1,ts} = 5xQ matrix, input #1 at timestep ts.
%
% and returns:
%   Y = 1xTS cell of 1 outputs over TS timesteps.
%   Each Y{1,ts} = 1xQ matrix, output #1 at timestep ts.
%
% where Q is number of samples (or series) and TS is the number of timesteps.

%#ok<*RPMT0>

% ===== NEURAL NETWORK CONSTANTS =====

% Input 1
x1_step1.keep = [1 2 3 5];
x1_step2.xoffset = [0;1.079181246;0.48;1.230448921];
x1_step2.gain =
[3.06485875552452;6.27433731131652;3.84615384615385;41.4038556926575];
x1_step2.ymin = -1;

% Layer 1
b1 = [-4.7335000699190015;-
7.0639533463320809;4.1329970301250638;5.2470851647772401;-
0.49227829607045082;17.491927161783888;2.962410419851687;-
0.075691370168353297;-4.4230433789804389;0.379362475981039];
IW1_1 = [40.275585304284341 0.32535030055269659 -0.33857322930673334
0.12689449793776311;65.276140627305267 -15.166378815812726 -
11.417494963815884 -34.358163491476176;-27.96056354871078
```

```
3.2556014384437058 10.208090305622321 13.138295023393006;-
23.946281707200036 14.547864899382382 10.221682125718425
21.782345522834859;-46.365170762142789 9.0537663061064126
12.456034894971674 26.970253774100573;60.929154019673533
14.239906103222786 -15.203964715750491 -27.306292032687029;-
3.5020529913278198 -1.7241109178922789 3.2265337530702305 -
0.0724555981006762;22.77102786325954 -4.1392970754615579 -
5.3495204850693883 -16.019238024374047;-0.16198698703837058 -
0.28686383636971086 -2.6130816016474028 -1.0346597572084379;-
0.038784284388606011 0.32236284218144723 -0.27807372320806967
0.032449889665935643];

% Layer 2
b2 = 5.1265822059816966;
LW2_1 = [-20.964564880177161 24.45965083434989 9.5452237750905251 -
1.6450079524465526 -17.167329296331793 20.951698184852045 -
1.6102248477073193 -12.900386503726693 -18.059560828709721 -
3.9289506134717684];
% Output 1
y1_step1.ymin = -1;
y1_step1.gain = 2;
y1_step1.xoffset = 0;

% ===== SIMULATION ========

% Format Input Arguments
isCellX = iscell(X);
if ~isCellX, X = {X}; end;

% Dimensions
TS = size(X,2); % timesteps
if ~isempty(X)
  Q = size(X{1},2); % samples/series
else
  Q = 0;
end

% Allocate Outputs
Y = cell(1,TS);

% Time loop
for ts=1:TS

    % Input 1
    temp = removeconstantrows_apply(X{1,ts},x1_step1);
    Xp1 = mapminmax_apply(temp,x1_step2);

    % Layer 1
    a1 = tansig_apply(repmat(b1,1,Q) + IW1_1*Xp1);
```

```
    % Layer 2
    a2 = repmat(b2,1,Q) + LW2_1*a1;

    % Output 1
    Y{1,ts} = mapminmax_reverse(a2,y1_step1);
end

% Final Delay States
Xf = cell(1,0);
Af = cell(2,0);

% Format Output Arguments
if ~isCellX, Y = cell2mat(Y); end
end

% ===== MODULE FUNCTIONS ========

% Map Minimum and Maximum Input Processing Function
function y = mapminmax_apply(x,settings)
  y = bsxfun(@minus,x,settings.xoffset);
  y = bsxfun(@times,y,settings.gain);
  y = bsxfun(@plus,y,settings.ymin);
end

% Remove Constants Input Processing Function
function y = removeconstantrows_apply(x,settings)
  y = x(settings.keep,:);
end

% Sigmoid Symmetric Transfer Function
function a = tansig_apply(n,~)
  a = 2 ./ (1 + exp(-2*n)) - 1;
end

% Map Minimum and Maximum Output Reverse-Processing Function
function x = mapminmax_reverse(y,settings)
  x = bsxfun(@minus,y,settings.ymin);
  x = bsxfun(@rdivide,x,settings.gain);
  x = bsxfun(@plus,x,settings.xoffset);
end
```

Appendix V: %MATLAB Neural Network Function, including the optimum connection weights, and details about the transfer function for the steel open-ended piles tested in three relative densities and model subjected to compression loads%

```
function [Y,Xf,Af] = myNeuralNetworkFunction(X,~,~)
%MYNEURALNETWORKFUNCTION neural network simulation function.
%
% Generated by Neural Network Toolbox function genFunction, 02-Mar-2017
14:53:08.
%
% [Y] = myNeuralNetworkFunction(X,~,~) takes these arguments:
%
%   X = 1xTS cell, 1 inputs over TS timesteps
%   Each X{1,ts} = 5xQ matrix, input #1 at timestep ts.
%
% and returns:
%   Y = 1xTS cell of 1 outputs over TS timesteps.
%   Each Y{1,ts} = 1xQ matrix, output #1 at timestep ts.
%
% where Q is number of samples (or series) and TS is the number of timesteps.

%#ok<*RPMT0>

% ===== NEURAL NETWORK CONSTANTS =====

% Input 1
x1_step1.keep = [1 2 3 5];
x1_step2.xoffset = [0.000147471;1.079181246;0.48;1.230448921];
x1_step2.gain =
[3.18431556959602;6.27433731131652;3.84615384615385;41.4038556926575];
x1_step2.ymin = -1;

% Layer 1
b1 = [-3.3196959635135275;7.8103855814089282;-
19.439771600205646;17.03036467633704;7.5023489273931441;7.2689008363564076
;4.5284400639994367;5.4488829135101806;-61.620993405554515;-
7.4649934731947347];
IW1_1 = [3.8391721257269782 -0.50733490725615371 -1.4445797680330934
0.47694646653617823;0.16006364777888576 0.7020359325761647 -
3.5076233949453761 -3.3367985407169987;-37.740367145714742
25.97043613833155 35.840537198763649 -
5.8907900370573039;46.148795171066276 -26.555162457875621
4.7272165209105577 -39.67977950365303;16.683534151088789 5.797717350761352
17.1907616831678 -17.059654879785324;26.692788293287244 -
10.477345449896802 -3.1258314817778245 -
24.95019792946329;50.044539880331897 -12.37924470448983 -
6.1554649024941552 -34.188770827544829;75.195974898844952 -
8.496920805236881 -23.204437422548317 -50.821780786261186;-
```

```
78.91713065335496 30.30675618042681 -11.41710388503142 -
12.075402335723002;-0.73275907266874662 2.8114180499481907
6.5991083777129163 -14.411560475242718];

% Layer 2
b2 = 4.0803391408865233;
LW2_1 = [3.4333621818930378 7.8772256424019567 9.7317463188872999
27.439402981276821 -9.4485556438291631 -27.409680337858806 -
18.150887716279193 27.560566484940949 -9.729740808703367
9.4785784313141477];

% Output 1
y1_step1.ymin = -1;
y1_step1.gain = 2.00159191669162;
y1_step1.xoffset = 3.45793e-05;

% ===== SIMULATION ========

% Format Input Arguments
isCellX = iscell(X);
if ~isCellX, X = {X}; end;

% Dimensions
TS = size(X,2); % timesteps
if ~isempty(X)
  Q = size(X{1},2); % samples/series
else
  Q = 0;
end

% Allocate Outputs
Y = cell(1,TS);

% Time loop
for ts=1:TS

    % Input 1
    temp = removeconstantrows_apply(X{1,ts},x1_step1);
    Xp1 = mapminmax_apply(temp,x1_step2);

    % Layer 1
    a1 = tansig_apply(repmat(b1,1,Q) + IW1_1*Xp1);

    % Layer 2
    a2 = repmat(b2,1,Q) + LW2_1*a1;

    % Output 1
    Y{1,ts} = mapminmax_reverse(a2,y1_step1);
end
```

```
% Final Delay States
Xf = cell(1,0);
Af = cell(2,0);

% Format Output Arguments
if ~isCellX, Y = cell2mat(Y); end
end

% ===== MODULE FUNCTIONS ========

% Map Minimum and Maximum Input Processing Function
function y = mapminmax_apply(x,settings)
  y = bsxfun(@minus,x,settings.xoffset);
  y = bsxfun(@times,y,settings.gain);
  y = bsxfun(@plus,y,settings.ymin);
end

% Remove Constants Input Processing Function
function y = removeconstantrows_apply(x,settings)
  y = x(settings.keep,:);
end

% Sigmoid Symmetric Transfer Function
function a = tansig_apply(n,~)
  a = 2 ./ (1 + exp(-2*n)) - 1;
end

% Map Minimum and Maximum Output Reverse-Processing Function
function x = mapminmax_reverse(y,settings)
  x = bsxfun(@minus,y,settings.ymin);
  x = bsxfun(@rdivide,x,settings.gain);
  x = bsxfun(@plus,x,settings.xoffset);
end
```

Appendix VI: %MATLAB Neural Network Function, including the optimum connection weights, and details about the transfer function for the concrete pile model tested in three relative densities and subjected to uplift loads%

```
function [Y,Xf,Af] = myNeuralNetworkFunction(X,~,~)
%MYNEURALNETWORKFUNCTION neural network simulation function.
%
% Generated by Neural Network Toolbox function genFunction, 02-Mar-2017
14:53:08.
%
```

```
% [Y] = myNeuralNetworkFunction(X,~,~) takes these arguments:
%
%   X = 1xTS cell, 1 inputs over TS timesteps
%   Each X{1,ts} = 5xQ matrix, input #1 at timestep ts.
%
% and returns:
%   Y = 1xTS cell of 1 outputs over TS timesteps.
%   Each Y{1,ts} = 1xQ matrix, output #1 at timestep ts.
%
% where Q is number of samples (or series) and TS is the number of timesteps.

%#ok<*RPMT0>

% ===== NEURAL NETWORK CONSTANTS =====

% Input 1
x1_step1.keep = [1 2 3 5];
x1_step2.xoffset = [0.000147471;1.079181246;0.48;1.230448921];
x1_step2.gain =
[3.18431556959602;6.27433731131652;3.84615384615385;41.4038556926575];
x1_step2.ymin = -1;

% Layer 1
b1 = [-3.3196959635135275;7.8103855814089282;-
19.439771600205646;17.03036467633704;7.5023489273931441;7.2689008363564076
;4.5284400639994367;5.4488829135101806;-61.620993405554515;-
7.4649934731947347];
IW1_1 = [3.8391721257269782 -0.50733490725615371 -1.4445797680330934
0.47694646653617823;0.16006364777888576 0.7020359325761647 -
3.5076233949453761 -3.3367985407169987;-37.740367145714742
25.97043613833155 35.840537198763649 -
5.8907900370573039;46.148795171066276 -26.555162457875621
4.7272165209105577 -39.67977950365303;16.683534151088789 5.797717350761352
17.1907616831678 -17.059654879785324;26.692788293287244 -
10.477345449896802 -3.1258314817778245 -
24.950197929463299;50.044539880331897 -12.37924470448983 -
6.1554649024941552 -34.188770827544829;75.195974898844952 -
8.496920805236881 -23.204437422548317 -50.821780786261186;-
78.917130653354696 30.30675618042681 -11.41710388503142 -
12.075402335723002;-0.73275907266874662 2.8114180499481907
6.5991083777129163 -14.411560475242718];

% Layer 2
b2 = 4.0803391408865233;
LW2_1 = [3.4333621818930378 7.8772256424019567 9.7317463188872999
27.439402981276821 -9.4485556438291631 -27.409680337858806 -
18.150887716279193 27.560566484940949 -9.729740808703367
9.4785784313141477];
```

```
% Output 1
y1_step1.ymin = -1;
y1_step1.gain = 2.00159191669162;
y1_step1.xoffset = 3.45793e-05;

% ===== SIMULATION ========

% Format Input Arguments
isCellX = iscell(X);
if ~isCellX, X = {X}; end;

% Dimensions
TS = size(X,2); % timesteps
if ~isempty(X)
  Q = size(X{1},2); % samples/series
else
  Q = 0;
end

% Allocate Outputs
Y = cell(1,TS);

% Time loop
for ts=1:TS

    % Input 1
    temp = removeconstantrows_apply(X{1,ts},x1_step1);
    Xp1 = mapminmax_apply(temp,x1_step2);

    % Layer 1
    a1 = tansig_apply(repmat(b1,1,Q) + IW1_1*Xp1);

    % Layer 2
    a2 = repmat(b2,1,Q) + LW2_1*a1;

    % Output 1
    Y{1,ts} = mapminmax_reverse(a2,y1_step1);
end

% Final Delay States
Xf = cell(1,0);
Af = cell(2,0);

% Format Output Arguments
if ~isCellX, Y = cell2mat(Y); end
end

% ===== MODULE FUNCTIONS ========
```

```
% Map Minimum and Maximum Input Processing Function
function y = mapminmax_apply(x,settings)
  y = bsxfun(@minus,x,settings.xoffset);
  y = bsxfun(@times,y,settings.gain);
  y = bsxfun(@plus,y,settings.ymin);
end

% Remove Constants Input Processing Function
function y = removeconstantrows_apply(x,settings)
  y = x(settings.keep,:);
end

% Sigmoid Symmetric Transfer Function
function a = tansig_apply(n,~)
  a = 2 ./ (1 + exp(-2*n)) - 1;
end

% Map Minimum and Maximum Output Reverse-Processing Function
function x = mapminmax_reverse(y,settings)
  x = bsxfun(@minus,y,settings.ymin);
  x = bsxfun(@rdivide,x,settings.gain);
  x = bsxfun(@plus,x,settings.xoffset);
end
```

Appendix VII: %MATLAB Neural Network Function, including the optimum connection weights, and details about the transfer function for the steel closed-ended pile model tested in three relative densities and subjected to uplift loads%

```
function [Y,Xf,Af] = myNeuralNetworkFunction(X,~,~)
%MYNEURALNETWORKFUNCTION neural network simulation function.
%
% Generated by Neural Network Toolbox function genFunction, 15-Jun-2017 09:35:08.
%
% [Y] = myNeuralNetworkFunction(X,~,~) takes these arguments:
%
%   X = 1xTS cell, 1 inputs over TS timesteps
%   Each X{1,ts} = 5xQ matrix, input #1 at timestep ts.
%
% and returns:
%   Y = 1xTS cell of 1 outputs over TS timesteps.
%   Each Y{1,ts} = 1xQ matrix, output #1 at timestep ts.
%
% where Q is number of samples (or series) and TS is the number of timesteps.
```

```
%#ok<*RPMT0>

% ===== NEURAL NETWORK CONSTANTS =====

% Input 1
x1_step1.keep = [1 2 3 5];
x1_step2.xoffset = [0;1.079181246;0.48;1.230448921];
x1_step2.gain =
[4.35616621339015;6.27433731131652;3.84615384615385;41.4038556926575];
x1_step2.ymin = -1;

% Layer 1
b1 = [3.3292689538915234;-3.3051814273023781;-
2.1986897865241875;1.6570286686173747;-
0.40742137641892107;0.91295618297191039;-3.0444751310350804;-
5.3739077915921856;-3.8709278466889581;-2.5217673676433474];
IW1_1 = [-1.4575742200789055 1.7439121748091484 -0.31479477903963538 -
1.1025739140935069;2.6565474940491072 -2.1618805072730303 -
0.69995552861964916 1.0078851176706947;8.3723873665284252
2.8303627163494607 -6.0892578028661797 -
3.3189226046778098;1.4848616543672182 -1.0419054423197376 -
2.0572549870000061 1.2180012961951772;4.1230276102419987
2.5861159535251557 1.6016832612478069 -0.060701104194385805;-
2.5978843101248272 0.37693791629206908 1.1748570633104309
0.07261236938495455;13.151748526408575 -5.9055751348726293
3.4487510635689436 -10.186853292561402;-9.7923745226242964
2.3834998015546809 0.29605417125415662 -9.3976381204689829;-
2.0338309138189192 -0.67779687069680083 1.7577051445306719
4.9304893249435366;0.021107901158951288 -1.6052957029236841 -
0.23171872625584192 1.7539645432929456];

% Layer 2
b2 = 2.9848018891996637;
LW2_1 = [3.6619638716336822 2.4225131414977725 3.3347160418874497 -
0.017413325405720069 0.029562184331260587 4.2472756000355183
6.0727174153121837 -4.9395312192006502 -4.9814427494112792
0.01382847501142101];

% Output 1
y1_step1.ymin = -1;
y1_step1.gain = 2.07125247494864;
y1_step1.xoffset = 0;

% ===== SIMULATION ========

% Format Input Arguments
isCellX = iscell(X);
if ~isCellX
  X = {X};
```

```
end

% Dimensions
TS = size(X,2); % timesteps
if ~isempty(X)
  Q = size(X{1},2); % samples/series
else
  Q = 0;
end

% Allocate Outputs
Y = cell(1,TS);

% Time loop
for ts=1:TS

    % Input 1
    temp = removeconstantrows_apply(X{1,ts},x1_step1);
    Xp1 = mapminmax_apply(temp,x1_step2);

    % Layer 1
    a1 = tansig_apply(repmat(b1,1,Q) + IW1_1*Xp1);

    % Layer 2
    a2 = repmat(b2,1,Q) + LW2_1*a1;

    % Output 1
    Y{1,ts} = mapminmax_reverse(a2,y1_step1);
end

% Final Delay States
Xf = cell(1,0);
Af = cell(2,0);

% Format Output Arguments
if ~isCellX
  Y = cell2mat(Y);
end
end

% ===== MODULE FUNCTIONS ========

% Map Minimum and Maximum Input Processing Function
function y = mapminmax_apply(x,settings)
  y = bsxfun(@minus,x,settings.xoffset);
  y = bsxfun(@times,y,settings.gain);
  y = bsxfun(@plus,y,settings.ymin);
end
```

```
% Remove Constants Input Processing Function
function y = removeconstantrows_apply(x,settings)
  y = x(settings.keep,:);
end

% Sigmoid Symmetric Transfer Function
function a = tansig_apply(n,~)
  a = 2 ./ (1 + exp(-2*n)) - 1;
end

% Map Minimum and Maximum Output Reverse-Processing Function
function x = mapminmax_reverse(y,settings)
  x = bsxfun(@minus,y,settings.ymin);
  x = bsxfun(@rdivide,x,settings.gain);
  x = bsxfun(@plus,x,settings.xoffset);
end
```

Appendix VIII: %MATLAB Neural Network Function, including the optimum connection weights, and details about the transfer function for the steel open-ended pile tested in three relative densities and model subjected to uplift loads%

```
function [Y,Xf,Af] = myNeuralNetworkFunction(X,~,~)
%MYNEURALNETWORKFUNCTION neural network simulation function.
%
% Generated by Neural Network Toolbox function genFunction, 15-Jun-2017 10:34:02.
%
% [Y] = myNeuralNetworkFunction(X,~,~) takes these arguments:
%
%   X = 1xTS cell, 1 inputs over TS timesteps
%   Each X{1,ts} = 5xQ matrix, input #1 at timestep ts.
%
% and returns:
%   Y = 1xTS cell of 1 outputs over TS timesteps.
%   Each Y{1,ts} = 1xQ matrix, output #1 at timestep ts.
%
% where Q is number of samples (or series) and TS is the number of timesteps.

%#ok<*RPMT0>

% ===== NEURAL NETWORK CONSTANTS =====

% Input 1
x1_step1.keep = [1 2 3 5];
x1_step2.xoffset = [0.013340496;1.079181246;0.48;1.230448921];
x1_step2.gain =
[3.4659425901304;6.27433731131652;3.84615384615385;41.4038556926575];
```

```
x1_step2.ymin = -1;

% Layer 1
b1 = [2.0267101954959159;-
1.5087309258155894;2.095838297514407;0.96572887444104416;-
1.0492957909871108;1.2353570696881908;-0.29911286927592629;-
0.41254869953850659;-2.3720572374595101;6.1186838201698617];
IW1_1 = [-1.8620913466872988 0.1175940535346955 -1.7548765633698249
1.8676170032509016;5.3894115118074275 0.4329579505109078 -
0.47449698753625918 -4.3807362331663198;-0.8506172051249894
3.1432450369550495 0.24693434795409963 -0.34291564820481241;-
7.0844502259990723 -1.0480638328464862 -2.486532276644287
1.3630147947263065;1.1287101798939168 -0.1774198526460993
1.7463735524760855 1.5721615559775857;4.687323352222422 -
2.2873478615966154 -4.1483365785656643 -
0.31340377458438157;5.2640207963372516 1.0984627935348097 -
2.0162153734024297 2.2181636289100042;2.0832323708462694
0.46906910758403281 2.1214682394301314 1.5109717485019716;-
1.2255888098926138 0.45252445407353598 2.4204189894337187
1.2892560843799932;3.9502753260275498 2.3196850141681553
1.7641030544807115 -0.47876460736652315];

% Layer 2
b2 = 1.3831167496710244;
LW2_1 = [1.2494510481267598 3.12791187208239 -2.2245859375877917 -
2.9089703824837061 0.89637800312147842 3.8889192456677821 -
3.1742046221871369 -1.3379762746318939 1.0775090445342772
5.5858503994567466];

% Output 1
y1_step1.ymin = -1;
y1_step1.gain = 2.00067080291284;
y1_step1.xoffset = 0.000335289;

% ===== SIMULATION ========

% Format Input Arguments
isCellX = iscell(X);
if ~isCellX
   X = {X};
end

% Dimensions
TS = size(X,2); % timesteps
if ~isempty(X)
   Q = size(X{1},2); % samples/series
else
   Q = 0;
end
```

```
% Allocate Outputs
Y = cell(1,TS);

% Time loop
for ts=1:TS

    % Input 1
    temp = removeconstantrows_apply(X{1,ts},x1_step1);
    Xp1 = mapminmax_apply(temp,x1_step2);

    % Layer 1
    a1 = tansig_apply(repmat(b1,1,Q) + IW1_1*Xp1);

    % Layer 2
    a2 = repmat(b2,1,Q) + LW2_1*a1;

    % Output 1
    Y{1,ts} = mapminmax_reverse(a2,y1_step1);
end

% Final Delay States
Xf = cell(1,0);
Af = cell(2,0);

% Format Output Arguments
if ~isCellX
    Y = cell2mat(Y);
end
end

% ===== MODULE FUNCTIONS ========

% Map Minimum and Maximum Input Processing Function
function y = mapminmax_apply(x,settings)
y = bsxfun(@minus,x,settings.xoffset);
y = bsxfun(@times,y,settings.gain);
y = bsxfun(@plus,y,settings.ymin);
end

% Remove Constants Input Processing Function
function y = removeconstantrows_apply(x,settings)
y = x(settings.keep,:);
end

% Sigmoid Symmetric Transfer Function
function a = tansig_apply(n,~)
a = 2 ./ (1 + exp(-2*n)) - 1;
end
```

```
% Map Minimum and Maximum Output Reverse-Processing Function
function x = mapminmax_reverse(y,settings)
x = bsxfun(@minus,y,settings.ymin);
x = bsxfun(@rdivide,x,settings.gain);
x = bsxfun(@plus,x,settings.xoffset);
end
```

Appendix IX: List of Journal Publications

Published Journal Papers:

1. Ameer A. Jebur, William Atherton, Rafid M. Al Khaddar, and Ed Loffill (2016) "*Simulation of Soil Pile Interaction of a Steel Batter Pile Penetrated in Sandy Soil subjected to Pull-out Loads*" International Journal of Civil, Environmental, Structural, Construction and Architectural Engineering, Vol:10, No:5, pp. 623-628.

2. Ameer A. Jebur, William Atherton, Rafid M. Al Khaddar, and Ed Loffill (2017) "*Nonlinear Analysis of Single Model Piles Subjected to Lateral Load in Sloping Ground*" Journal of Procedia Engineering, Elsevier Vol:196, pp 52-59. https://doi.org/10.1016/j.proeng.2017.07.172.

3. Ameer A. Jebur, William Atherton, Rafid M. Al Khaddar, and Ed Loffill (2017) "*Piles in Sandy Soil: A Numerical Study and Experimental Validation*" Journal of Procedia Engineering, Elsevier Vol:196, pp 60-67. https://doi.org/10.1016/j.proeng.2017.07.173.

4. Ameer A. Jebur, William Atherton, Rafid M. Al Khaddar, and Ed Loffill (2018) "*Settlement Prediction of Model Piles Embedded in Sandy Soil Using the Levenberg-Marquardt (LM) Training Algorithm*" Geotechnical and Geological Engineering, pp 1-14, https://doi.org/10.1007/s10706-018-0511-1.

5. Ameer A. Jebur, William Atherton, and Rafid M. Al Khaddar (2018) "*Feasibility of an Evolutionary Artificial Intelligence (AI) Scheme for Modelling of Load Settlement Response of Concrete Piles Embedded in Cohesionless Soil*" Ships and Offshores Structures, pp 1-14, https://doi.org/10.1080/17445302.2018.1447746.

6. Ameer A. Jebur, William Atherton, and Rafid M. Al Khaddar (2018) *"Artificial Neural Network (ANN) for Modelling of Pile Settlement of Closed-ended Steel Piles Subjected to Compression Load"* European Journal of Environmental and Civil Engineering. Accepted, in Press.

Journal Papers under Review:

1. Ameer A. Jebur, William Atherton, and Rafid M. Al Khaddar (2018) *"Performance analysis of an evolutionary LM algorithm to model the load-settlement response of steel piles embedded in sandy soil"* Journal of Measurements.

2. Ameer A. Jebur, William Atherton, and Rafid M. Al Khaddar (2018) *"A self-tuning system for modelling the load distribution of concrete piles under uplift loading using an evolutionary LM training algorithm"* Ships and Offshores Structures.

Appendix X: List of Conference Publications

Presented Conference papers:

1. Ameer A. Jebur, William Atherton, Rafid M. Alkhaddar, and Ed Loffill (2015). "*Deep Foundations: An Empirical and Theoretical Study of Pile Foundations Embedded in Sand Soil*" Proceeding of the 8th Innovation International Conference, Manchester Metropolitan University, 5th November, UK.

2. Ameer A. Jebur, William Atherton, Rafid M. Alkhaddar, and Ed Loffill (2016). "*Deep Foundations: Analysis of the Lateral Response of Closed Ended Steel Tubular Piles Embedded in Sandy Soil Using p-y Curves*" Proceeding of the 15th Asphalt, Pavement Engineering and Infrastructure Conference; 24th -25th February, Liverpool, UK. ISBN: 978-0-9571804-9-9.

3. Ameer A. Jebur; William Atherton; Rafid M. Alkhaddar, and Ed Loffill (2016). "Analysis *of the Lateral Response of a Reinforced Concrete Pile Penetrated in Sand Soil Using Finite Element"* The 2nd International BDRC Conference, British University in Dubai (BUiD). Dubai, UAE. ISBN: 978-9948-02-481-1.

4. Ameer A. Jebur; William Atherton; Rafid M. Alkhaddar, and Ed Loffill (2017). "*Modelling of Pile-Soil Interaction of Concrete Model Piles Penetrated in Sandy Soil"* The 3rd International BDRC Conference, British University in Dubai (BUiD). Dubai, UAE.

5. Ameer A. Jebur; William Atherton; Rafid M. Alkhaddar, and Ed Loffill (2017). "*Computational Intelligence Applications in Geotechnical Engineering*" Cutting Edge Postgraduate Conference, Edge Hill University, 27th April, Lancashire, UK. Poster Presentation.

6. Ameer A. Jebur; William Atherton; Rafid M. Alkhaddar, and Ed Loffill (2017). "*Development of an Experimental and Numerical Study for Piles Penetrated in Sandy Soil*" Proceeding of the 12th Annual Faculty Research Week. Liverpool, UK. ISBN: 2398-6611.

7. Ameer A. Jebur, William Atherton, Rafid M. Alkhaddar, and Ed Loffill (2018). *"An experimental study to investigate the use of novel structural fibres as shear reinforcement in concrete beams"* Proceeding of the 17th Asphalt, Pavement Engineering and Infrastructure Conference; 21st -22nd February, Liverpool, UK. Vol, 17, ISBN 978-0-9957519-2-7.

8. Ameer A. Jebur, William Atherton, Rafid M. Alkhaddar, and Ed Loffill (2018). *"An Enhanced Neural Network Scheme to Model of Pile Load-deformation under uplift loading"* The 11th IEEE International Conference on Development in e-System Engineering, 2nd-5th September 2018, Cambridge, UK.

Appendix XI: Awards and Recognitions

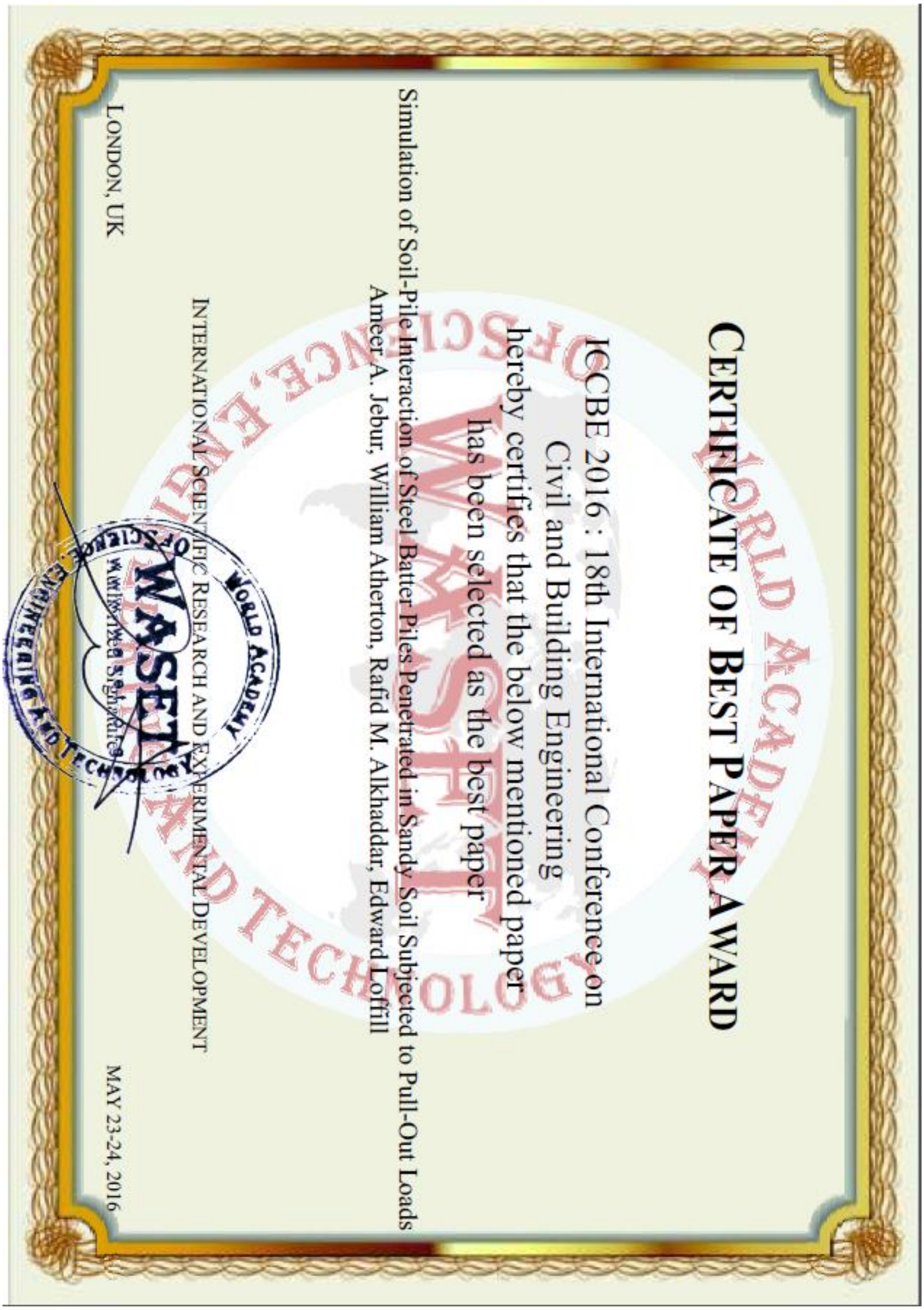

CERTIFICATE OF BEST PAPER AWARD

ICCBE 2016 : 18th International Conference on
Civil and Building Engineering
hereby certifies that the below mentioned paper
has been selected as the best paper

Simulation of Soil-Pile Interaction of Steel Batter Piles Penetrated in Sandy Soil Subjected to Pull-Out Loads
Ameer A. Jebur, William Atherton, Rafid M. Alkhaddar, Edward Loffill

INTERNATIONAL SCIENTIFIC RESEARCH AND EXPERIMENTAL DEVELOPMENT

LONDON, UK

MAY 23-24, 2016

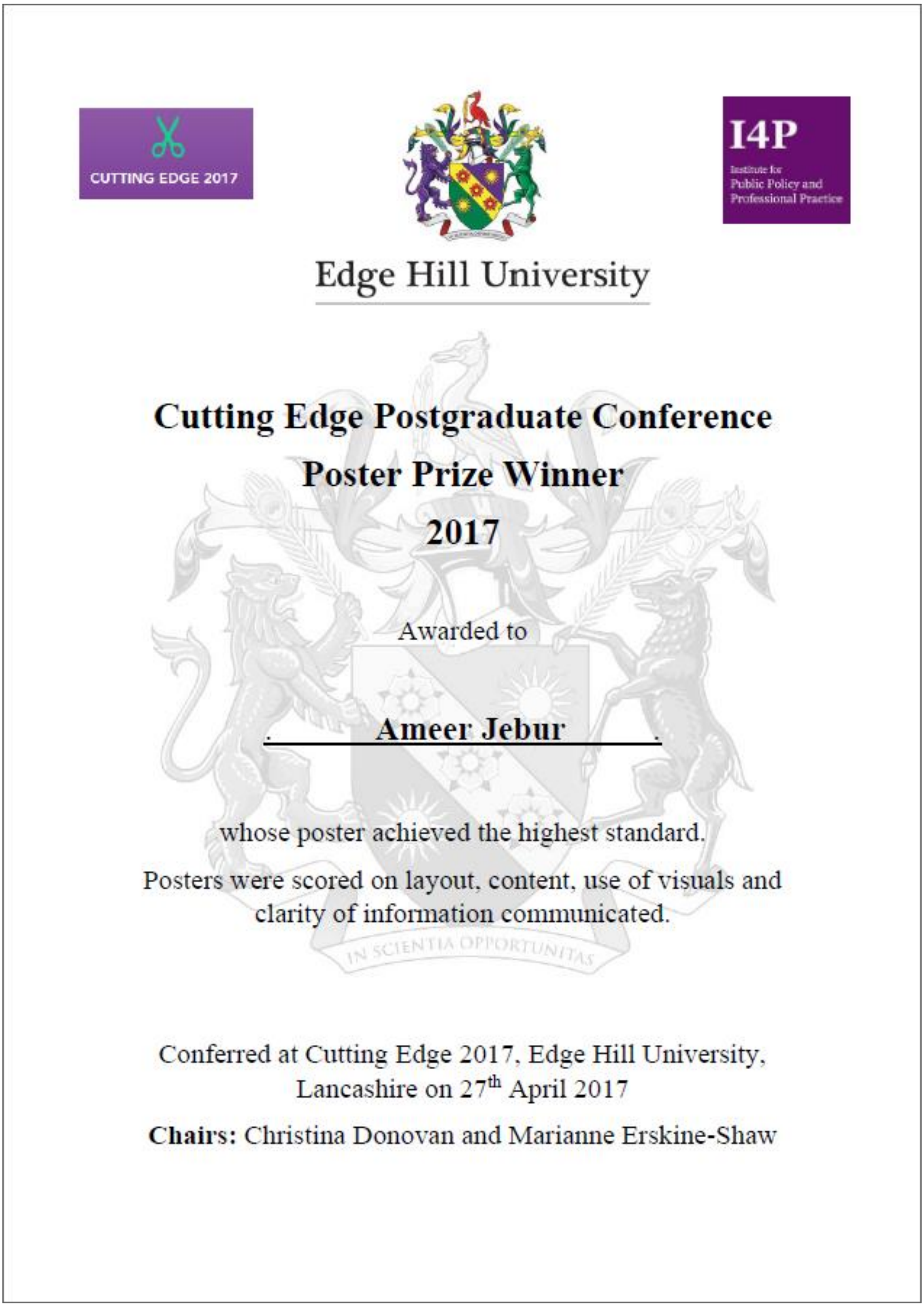

CUTTING EDGE 2017

I4P
Institute for
Public Policy and
Professional Practice

Edge Hill University

Cutting Edge Postgraduate Conference
Poster Prize Winner
2017

Awarded to

Ameer Jebur

whose poster achieved the highest standard.

Posters were scored on layout, content, use of visuals and clarity of information communicated.

IN SCIENTIA OPPORTUNITAS

Conferred at Cutting Edge 2017, Edge Hill University, Lancashire on 27th April 2017

Chairs: Christina Donovan and Marianne Erskine-Shaw

CERTIFICATE *of* EXCELLENCE

AWARDED TO

Ameer Ashour Jebur

TO RECOGNISE HIS OUTSTANDING ACADEMIC ACHIEVEMENTS DURING HIS STUDY IN THE UK

MARCH 05
2017

H.E. DR SALIH HUSAIN ALI
AMBASSADOR OF THE REPUBLIC OF IRAQ TO
THE UNITED KINGDOM - LONDON

IRAQI STUDENTS SOCIETY

Certificate of Excellence

This certificate is awarded to

Ameer Ashour Jebur

TO RECOGNISE HIS OUTSTANDING ACADEMIC ACHIEVEMENTS DURING HIS STUDY IN THE UK
on 05 March, 2017
London – United Kingdom

Zeyad Yousif Al-Shibaany
Chair of Iraqi Students Society

This Event is sponsored by the Embassy of the Republic of Iraq in the United Kingdom

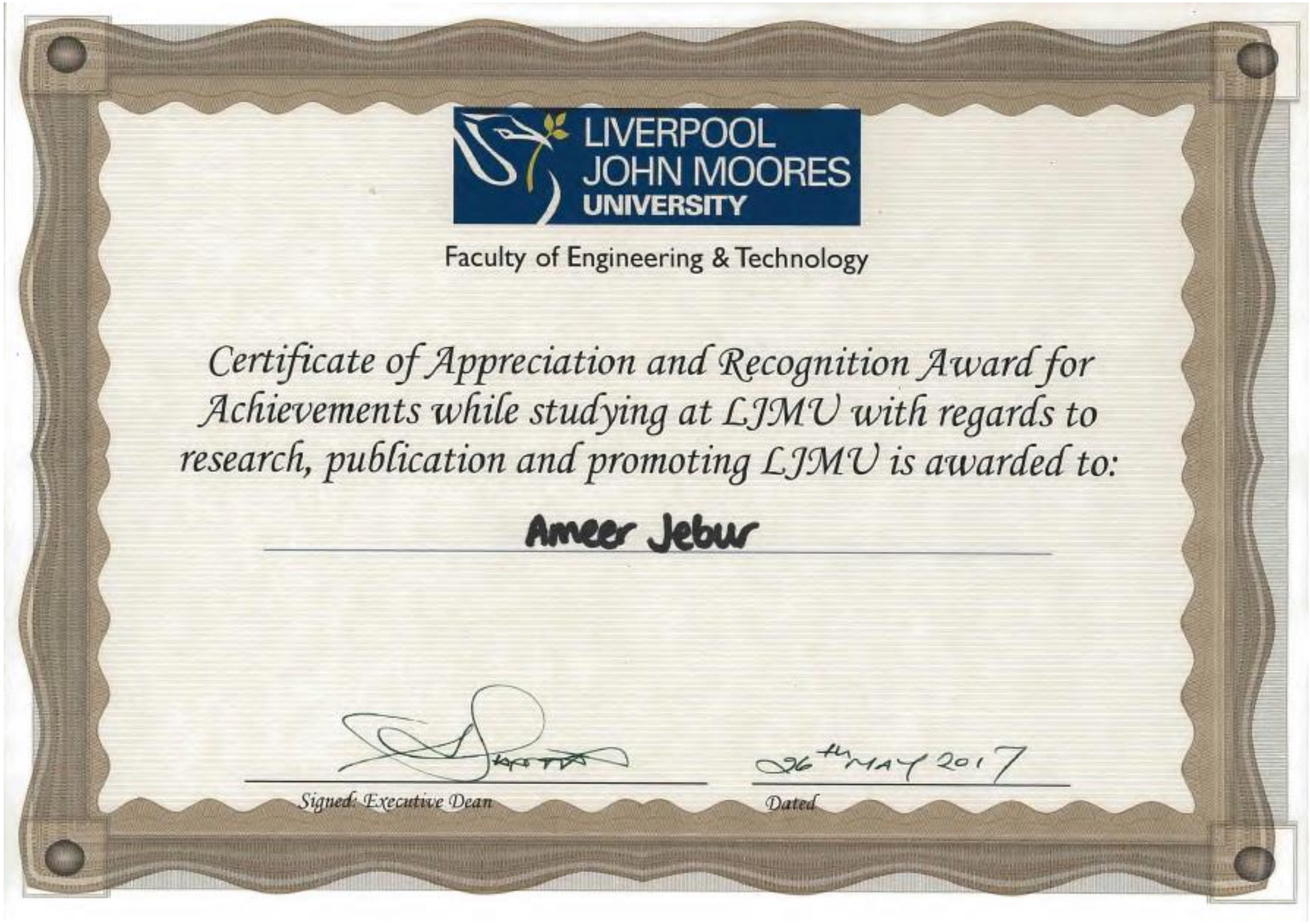

LIVERPOOL
JOHN MOORES
UNIVERSITY

Faculty of Engineering & Technology

Certificate of Appreciation and Recognition Award for Achievements while studying at LJMU with regards to research, publication and promoting LJMU is awarded to:

Ameer Jebur

Signed: Executive Dean

26th MAY 2017

Dated

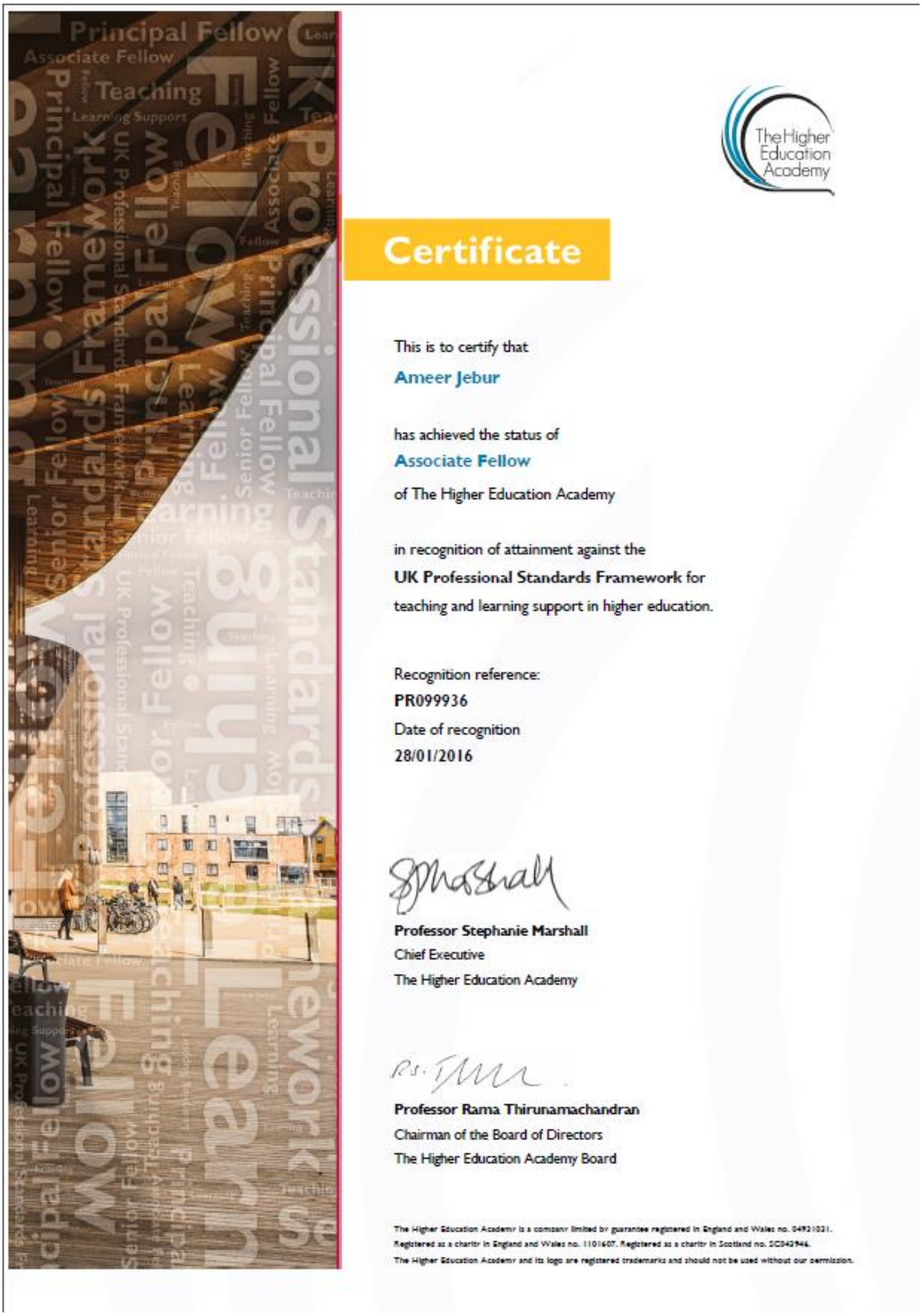

The Higher Education Academy

Certificate

This is to certify that

Ameer Jebur

has achieved the status of

Associate Fellow

of The Higher Education Academy

in recognition of attainment against the

UK Professional Standards Framework for

teaching and learning support in higher education.

Recognition reference:

PR099936

Date of recognition

28/01/2016

Professor Stephanie Marshall

Chief Executive

The Higher Education Academy

Professor Rama Thirunamachandran

Chairman of the Board of Directors

The Higher Education Academy Board

The Higher Education Academy is a company limited by guarantee registered in England and Wales no. 04931031.
Registered as a charity in England and Wales no. 1101607. Registered as a charity in Scotland no. SC043946.
The Higher Education Academy and its logo are registered trademarks and should not be used without our permission.